



LOW-MOLECULAR WEIGHT ORGANIC SEMICONDUCTORS FOR ORGANIC AND PEROVSKITE SOLAR CELLS

Cristina Rodríguez Seco

ADVERTIMENT. L'accés als continguts d'aquesta tesi doctoral i la seva utilització ha de respectar els drets de la persona autora. Pot ser utilitzada per a consulta o estudi personal, així com en activitats o materials d'investigació i docència en els termes establerts a l'art. 32 del Text Refós de la Llei de Propietat Intel·lectual (RDL 1/1996). Per altres utilitzacions es requereix l'autorització prèvia i expressa de la persona autora. En qualsevol cas, en la utilització dels seus continguts caldrà indicar de forma clara el nom i cognoms de la persona autora i el títol de la tesi doctoral. No s'autoritza la seva reproducció o altres formes d'explotació efectuades amb finalitats de lucre ni la seva comunicació pública des d'un lloc aliè al servei TDX. Tampoc s'autoritza la presentació del seu contingut en una finestra o marc aliè a TDX (framing). Aquesta reserva de drets afecta tant als continguts de la tesi com als seus resums i índexs.

ADVERTENCIA. El acceso a los contenidos de esta tesis doctoral y su utilización debe respetar los derechos de la persona autora. Puede ser utilizada para consulta o estudio personal, así como en actividades o materiales de investigación y docencia en los términos establecidos en el art. 32 del Texto Refundido de la Ley de Propiedad Intelectual (RDL 1/1996). Para otros usos se requiere la autorización previa y expresa de la persona autora. En cualquier caso, en la utilización de sus contenidos se deberá indicar de forma clara el nombre y apellidos de la persona autora y el título de la tesis doctoral. No se autoriza su reproducción u otras formas de explotación efectuadas con fines lucrativos ni su comunicación pública desde un sitio ajeno al servicio TDR. Tampoco se autoriza la presentación de su contenido en una ventana o marco ajeno a TDR (framing). Esta reserva de derechos afecta tanto al contenido de la tesis como a sus resúmenes e índices.

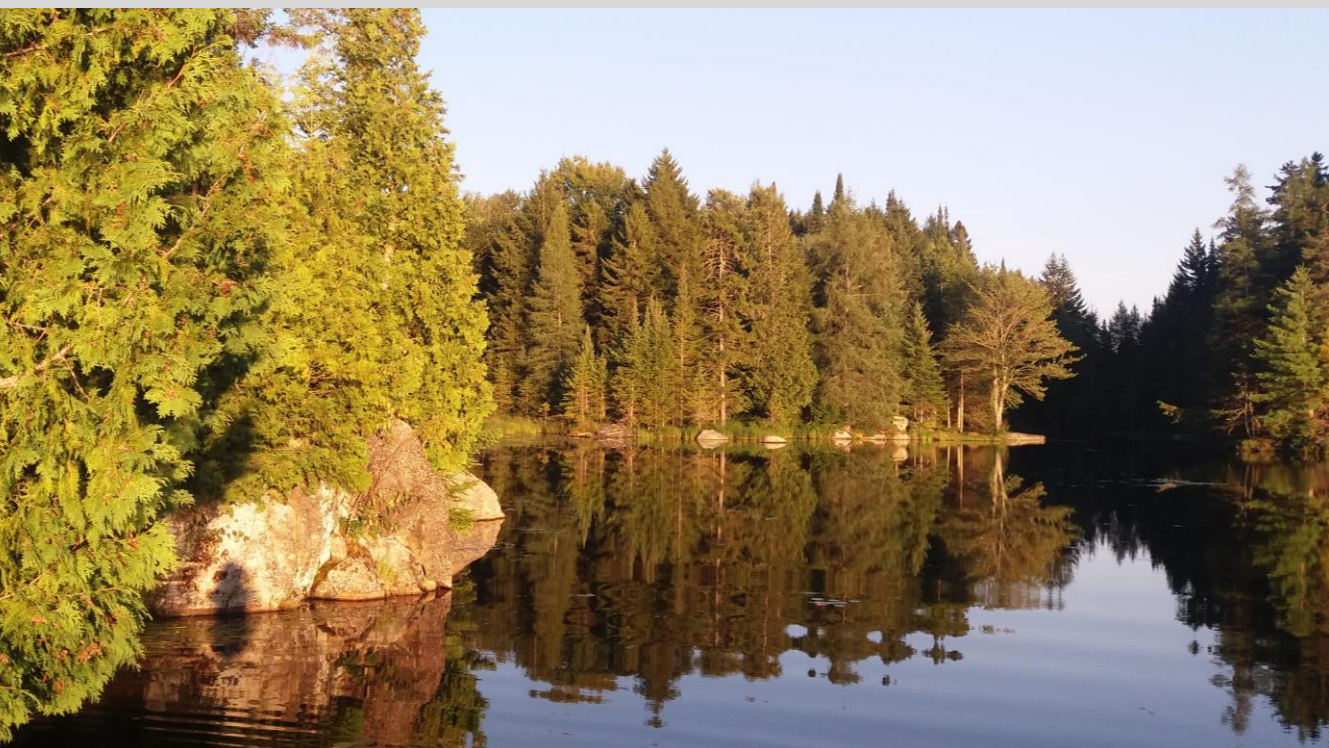
WARNING. Access to the contents of this doctoral thesis and its use must respect the rights of the author. It can be used for reference or private study, as well as research and learning activities or materials in the terms established by the 32nd article of the Spanish Consolidated Copyright Act (RDL 1/1996). Express and previous authorization of the author is required for any other uses. In any case, when using its content, full name of the author and title of the thesis must be clearly indicated. Reproduction or other forms of for profit use or public communication from outside TDX service is not allowed. Presentation of its content in a window or frame external to TDX (framing) is not authorized either. These rights affect both the content of the thesis and its abstracts and indexes.



UNIVERSITAT
ROVIRA i VIRGILI

Low-Molecular Weight Organic Semiconductors for Organic and Perovskite Solar Cells

CRISTINA RODRÍGUEZ SECO



**TESI DOCTORAL – TESIS DOCTORAL- DOCTORAL THESIS
2019**

UNIVERSITAT ROVIRA I VIRGILI

LOW-MOLECULAR WEIGHT ORGANIC SEMICONDUCTORS FOR ORGANIC AND PEROVSKITE SOLAR CELLS

Cristina Rodríguez Seco

UNIVERSITAT ROVIRA I VIRGILI

LOW-MOLECULAR WEIGHT ORGANIC SEMICONDUCTORS FOR ORGANIC AND PEROVSKITE SOLAR CELLS

Cristina Rodríguez Seco

UNIVERSITAT ROVIRA I VIRGILI

LOW-MOLECULAR WEIGHT ORGANIC SEMICONDUCTORS FOR ORGANIC AND PEROVSKITE SOLAR CELLS

Cristina Rodríguez Seco

Doctoral Thesis

Low-Molecular Weight Organic Semiconductors for Organic and Perovskite Solar Cells

Cristina Rodríguez Seco

Supervised by Prof. Emilio Palomares Gil.

ICIQ – URV

Tarragona – June 2019



UNIVERSITAT ROVIRA I VIRGILI

LOW-MOLECULAR WEIGHT ORGANIC SEMICONDUCTORS FOR ORGANIC AND PEROVSKITE SOLAR CELLS

Cristina Rodríguez Seco

Emilio Palomares Gil, Group Leader of the Institute of Chemical Research of Catalonia (ICIQ) in Tarragona, and Research Professor of the Catalan Institution for Research and Advanced Studies (ICREA) in Barcelona

Certify:

That the present thesis entitled “Low-Molecular Weight Organic Semiconductors for Organic and Perovskite Solar Cells” presented by Cristina Rodríguez Seco for the award of the degree of Doctor, has been carried out under my supervision at ICIQ and that she fulfils the requirements to obtain a ‘European Doctorate Mention’.

Tarragona, June 21st 2019.

Prof. Dr. Emilio Palomares Gil.



UNIVERSITAT ROVIRA I VIRGILI

LOW-MOLECULAR WEIGHT ORGANIC SEMICONDUCTORS FOR ORGANIC AND PEROVSKITE SOLAR CELLS

Cristina Rodríguez Seco

Agradecimientos / Acknowledgments.

En estos cuatro años de tesis han sido un viaje lleno de experiencias donde he aprendido mucho, no solo acerca de la investigación en celdas solares también a nivel personal. Ha sido un periodo con algunas dificultades, pero lo recordaré porque ha estado lleno de momentos maravillosos. Por eso, me gustaría agradecer aquí a todas las personas que me han apoyado y han hecho que este viaje haya sido inolvidable. Siempre que una etapa se termina una nueva comienza.

Primero de todo, quiero agradecer a mi supervisor de tesis, Emilio, el haberme dado la oportunidad de hacer la tesis en su grupo y a entender que a aprender se aprende equivocándose. También por haberme dado la oportunidad de irme de estancia dos veces y entender que no solo es ciencia, sino también experiencias en la vida.

Al Ministerio de Economía y Competitividad (MINECO) y al ICIQ por el soporte económico. Al personal del área de soporte del ICIQ por haber hecho más fácil llevar a cabo la investigación. En especial a Xavi y al área de cromatografía análisis térmico y electroquímica.

El hacer la tesis en un grupo de investigación como este, implica trabajar y ayudarnos entre todos los compañeros y compañeras. He aprendido mucho de todos vosotros en todos los niveles. Me llevo conmigo los momentos haciendo un café, escuchando música y riendo en el laboratorio lleno de gente peluda, anarquista y radical. Quiero agradecer especialmente a María todo su apoyo y paciencia (hasta para ir a nadar!), eres un sol, t'estimo molt!, a Alba y Beloqui por haberme ayudado a despegar en Tarragona y a Laia por haberme dado la oportunidad de disfrutar enseñando química a los más pequeños. Siempre habrá un sitio para ti en mi casa donde quiera que esté! Gracias Lydia por introducirme en el mundo de la síntesis orgánica. Rajesh, it was a pleasure to meet you. See you somewhere in the future!

During these four years I have worked abroad in two different laboratories, where I had the opportunity of discovering other sides of the chemistry and meeting people from all around the world. For that, I would like to thank Neil Robertson and his group. Going to Edinburgh made me enjoy doing organic synthesis. Furthermore, I also want to thank M. K. Nazeeruddin and his group for all the support in the long days making devices. The Spanish team! Hicisteis de Sion un lugar acogedor.

Quería aprovechar también para agradecer a Roberto por haber hecho de soporte durante los primeros años de tesis. Gracias por creer en mí.

No puedo pasar por alto el sitio de donde siento tengo mis raíces: Palacios Rubios. Allí es donde siempre puedo volver y encontrar descanso. Vivan las Valkirias! Siempre es un placer compartir momentos con vosotras. Gracias Leticia por el apoyo y las visitas exprés en Salamanca. Te deseo lo mejor en esta nueva etapa que comienzas. Seguiremos pidiendo un poquito de pop-rock!

Yaro, I am glad we have shared many amazing moments. I discovered with you the other side of the Moon. Life is a long path full of surprises.

Delia, nunca te he dicho lo importante que fuiste para mí. Espero que el futuro nos dé más momentos juntas. Te animo a que sigas siendo fuerte y decidida. El mundo te está esperando para que lo descubras.

Mis niñas y compañeras de batalla de Coitus! Muchas gracias por formar parte de mi vida, desde que os conozco siento que he encontrado mi sitio. Me encanta hacer planes y hablar con vosotras de política, feminismo o de cualquier otras cosas, que siempre acaban en risas y cervezas. Bárbara, amiga y compañera de piso, es un placer llegar a casa y hablar del mundo con palomitas. Me siento afortunada de haberte conocido! Creo que nos queda todavía mucho camino por recorrer. Irene, eres un sol con un brillo infinito. Cuando hablas es porque realmente tienes algo que aportar. Eres muy especial, me alegro que estés en mi vida! Sofía, conocerte fue un punto de inflexión en mi vida y me gustaría que siguieras formando parte de ella. Tardé en descubrirte, pero no importa

porque queda toda una vida por delante. Os quiero mucho a todas! Sigamos creando tribu.

Leyre! Me es difícil resumir en un párrafo todo lo que tengo dentro, hemos crecido juntas durante todos estos años. Esas llamadas interminables y las visitas... Me das la vida y la llenas de alegría! Da igual en qué punto del mundo estemos (Palacios, Granada, Tarragona, Sion, Leipzig o Australia!) siempre siento que estás a mi lado. Gracias por todo lo que hemos vivido y por todo lo que nos queda! Te quiero, te estimo y te todo!

Esta tesis no habría sido posible sin el apoyo incondicional de toda mi familia. Gracias a mis padres por haberme educado a ser una persona libre e independiente que piensa por sí misma; especialmente por todas las veces que me has dicho, no dependas de nadie. Sé que siempre habéis estado y estaréis ahí. A mis abuelos por todo el amor incondicional que me habéis dado. Abuela Claudia, eres el sol que ilumina mis días, estás llena de alegría y bondad. Siempre te llevo conmigo. Y a mi primo Alejandro, te deseo todo lo mejor en tu nueva etapa. Os quiero mucho a todos.

UNIVERSITAT ROVIRA I VIRGILI

LOW-MOLECULAR WEIGHT ORGANIC SEMICONDUCTORS FOR ORGANIC AND PEROVSKITE SOLAR CELLS

Cristina Rodríguez Seco

A todos los míos, a los que están y a los que ya marcharon.

A mi primo y a mi abuela.

UNIVERSITAT ROVIRA I VIRGILI

LOW-MOLECULAR WEIGHT ORGANIC SEMICONDUCTORS FOR ORGANIC AND PEROVSKITE SOLAR CELLS

Cristina Rodríguez Seco

Abstract

Nowadays, renewable energy sources are attracting a lot of attention due to the undesired environmental impact that fossil fuels are causing to the Earth. Solar energy is a sustainable alternative to the increasing world energy demand.

The main aim of this work was to design and synthesize novel molecules that could replace the polymers widely used as absorbers in organic solar cells and to replace spiro-OMeTAD used as a hole transporting material (HTM) in perovskite solar cells.

On the one hand, polymers are known for their good hole transporting properties, high solubility and good film forming abilities but they have a poor batch-to-batch reproducibility. Furthermore, spiro-OMeTAD is the best molecule to achieve reproducible and highly efficient perovskite solar cells. However, its complex and expensive synthesis and purification hinder its usage in industrial scale photovoltaics.

In order to overcome these problems, the rational design, synthesis and characterization of a variety of small molecules for both applications have been the focus of this thesis.

UNIVERSITAT ROVIRA I VIRGILI

LOW-MOLECULAR WEIGHT ORGANIC SEMICONDUCTORS FOR ORGANIC AND PEROVSKITE SOLAR CELLS

Cristina Rodríguez Seco

Resumen

Actualmente, las fuentes de energía renovables están atrayendo mucha atención debido al impacto negativo que los combustibles fósiles están causando al planeta. Las tecnologías basadas en las celdas fotovoltaicas son una alternativa sostenible para cubrir la demanda energética mundial.

El principal objetivo de este trabajo fue el diseño y la síntesis de nuevas moléculas que reemplacen los polímeros comúnmente utilizados como moléculas captadoras de luz en celdas solares orgánicas y el spiro-OMeTAD usado como transportador de huecos (HTM por sus siglas en inglés “hole transporting material”) en dispositivos solares de perovskita.

Por una parte, los polímeros son conocidos por ser buenos transportadores de huecos, su alta solubilidad y su favorable habilidad en la formación de capas, pero tienen muy poca reproducibilidad entre distintos lotes. Por otra parte, el spiro-OMeTAD es la molécula que mejor reproducibilidad y eficiencia presenta en celdas solares de perovskita. Sin embargo, su síntesis compleja y de alto coste impide la posibilidad de escalado a nivel industrial.

Con el fin de solucionar estos problemas, esta tesis se ha enfocado en el diseño, síntesis y caracterización de un conjunto de moléculas pequeñas de bajo peso molecular para su aplicación en dichos dispositivos.

UNIVERSITAT ROVIRA I VIRGILI

LOW-MOLECULAR WEIGHT ORGANIC SEMICONDUCTORS FOR ORGANIC AND PEROVSKITE SOLAR CELLS

Cristina Rodríguez Seco

List of abbreviations

A: Acceptor.

ACN: Acetonitrile.

AM: Air mass coefficient.

AZO: aluminium-doped zinc oxide.

BHJ: Bulk heterojunction.

BT: Benzothiadiazole.

^tBuONa: Sodium *tert*-butoxide.

CB: chlorobenzene.

CBZ: carbazole.

CsI: Cesium iodide.

Cs-mix perovskite / triple cation perovskite: $\text{Cs}_{0.1}(\text{MA}_{0.15}\text{FA}_{0.85})\text{Pb}(\text{I}_{0.85}\text{Br})_3$.

CS₂: carbon disulphide.

Cs₂CO₃: Cesium carbonate.

CV: cyclic voltammetry.

D: Donor.

DCM / CH₂Cl₂: Dichloromethane.

DINI: 5,10-dihydroindolo [3,2-b]indole.

DMF: Dimethyl formamide.

DMSO: Dimethyl sulfoxide.

DPP: diketopyrrolopyrrole.

DSC: Differential Scanning Calorimetry.

DSSCs: Dye-sensitized solar cells.

EA: Ethylammonium.

E_g: Energy of the optical bandgap.

E_{loss}: Energy loss.

EPFL: École Polytechnique Fédérale de Lausanne.

EQE: External quantum efficiency.

ETL: Electron transport layer.

EtOAc: Ethyl acetate

EtOH: Ethanol.

FAI: Formamidineum iodide.

FETs: Field effect transistors.

FF: Fill factor.

FK209: tris(2-(1H-pyrazol-1-yl)-4-tert-butylpyridine)cobalt(III)
tri[bis(trifluoromethane)sulfonimide].

FTO: Fluorine-doped Tin Oxide.

GaAs: Gallium arsenide silicon solar cells.

G_{\max} : Maximum exciton generation rate.

HOMO: Highest Occupied Molecular Orbital.

HR-MS: High Resolution Mass Spectrometry.

HTM: Hole transporting material.

HTL: Hole transporting layer.

H₂O: Water.

ICIQ: Institute of Chemical Research of Catalonia.

ICT: Intermolecular charge transfer.

IPCE: Incident photon-to-current conversion efficiency.

ITO: Indium tin oxide.

J_{light} : Photogenerated current.

J_{dark} : Current in the dark.

J_{ph} : Photocurrent density.

J_{sc} : Current density/Short circuit current.

kV: Kilovolts.

L: thickness of the active layer.

LEDs: Light emitting diodes.

Li-TFSI: Bis(trifluoromethane)sulfonimide lithium salt.

LMW: Low Molecular Weight.

LUMO: Lowest Unoccupied Molecular Orbital.

M: Molar.

m -: Meta-.

MABr: Methylammonium bromide.

mA/cm²: Milliamperes per centimetre square.

MAI: Methylammonium iodide.

MAPBr₃: Methyl ammonium lead bromide perovskite.

MAPI₃: Methyl ammonium lead iodide perovskite.

MeOH: Methanol.

MgSO₄: Magnesium sulphate.

MPU3: 2,2'-((5*Z*,5'*Z*)-((((2,5-bis(2-ethylhexyl)-3,6-dioxo-2,3,5,6-tetrahydropyrrolo[3,4-*c*]pyrrole-1,4-diyl)bis(thiophene-5,2-diyl))bis(ethyne-2,1-diyl))bis(3,4-dihexylthiophene-5,2-diyl))bis(methaneylylidene))bis(3-ethyl-4-oxothiazolidine-5,2-diylidene))dimalononitrile.

n: Parameter that indicates the degree of bimolecular recombination in OSCs.

N₂: Nitrogen gas.

NBS: N-Bromosuccinimide.

(*n*-C₄H₉)₄NBr₃: *n*-tetrabutylammonium tribromide.

NaHSO₄: Sodium bisulphate.

Na₂SO₄: Sodium sulphate.

NMR: Nuclear magnetic resonance.

NREL: National Renewable Energy Labs.

o -: Ortho-.

OPV: Organic photovoltaics.

OSC: Organic solar cells.

p -: Para-.

PbBr₂: Lead(II) bromide.

PbI₂: Lead(II) iodide.

PC₇₁BM: [6,6]-Phenyl C₇₁ butyric acid methyl ester.

PCE: Power conversion efficiency.

Pd(PPh₃)₂Cl₂: Bis(triphenylphosphine)palladium(II) dichloride.

Pd(OAc)₂: Palladium acetate.

PE: Petroleum ether.

PHJ: Planar heterojunction.

ppm: Parts per million.

PSC: Perovskite solar cells.

PEDOT: PSS: poly (3,4-ethylenedioxythiophene):(polystyrene sulfonate).

PFN: poly [(9,9-bis(3'-(N,N-dimethylamino)propyl)-2,7-fluorene)-alt-2,7-(9,9-dioctylfluorene)].

PTAA: Poly[bis(4-phenyl)(2,4,6-trimethylphenyl)amine].

PTB7: Poly({4,8-bis[(2-ethylhexyl)oxy]benzo[1,2-b:4,5-b']dithiophene-2,6-diyl}{3-fluoro-2-[(2-ethylhexyl)carbonyl]thieno[3,4-b]thiophenediyl}).

PV: Photovoltaic.

P3HT: Poly(3-hexylthiophene-2,5-diyl).

q: Elementary charge.

P_{in}: Power of the incident light.

P_{diss}: Probability of exciton dissociation.

P_{coll}: Probability of charge collection.

PL: Photoluminescence.

rpm: Revolutions per minute.

s: Seconds.

SC: Short circuit.

SCLC: Space-Charge Limited Current method.

SEM: Scanning electron microscopy.

SMs: Small molecules.

SMOSC: Small molecules organic solar cells.

Spiro-OMeTAD: 2,2',7,7'-Tetrakis-[N,N'-di-p-methoxyphenylamine]-9,9'-spirobifluorene.

ss-DSSCs: Solid state dye-sensitized solar cells.

SVA: Solvent vapor annealing.

TAA: Titanium diisopropoxide bis(acetylacetonate).

tBP: 4-*tert*-butylpyridine.

[(*t*-Bu)₃PH]BF₄: Tri-*tert*-butylphosphonium tetrafluoroborate.

TCO: Transparent conducting electrode.

TEM: Transmission Electron Microscopy.

TGA: Termogravimetric analysis.

T_g: Glass transition temperature.

V_{oc}: Open circuit voltage.

PCE: Power conversion efficiency.

T: Absolut temperature.

TAA: Titanium diisopropoxide bis(acetylacetonate).

TBAPF₆: Tetrabutylammonium hexafluorophosphate.

T_c: Crystal temperature.

T_{des}: Decomposition temperature.

T_g: Glass transition temperature.

T_m: Melting temperature.

TiO₂: Titania dioxide.

TGA: Termogravimetry analysis.

THF: Tetrahydrofuran.

Tol : Toluene.

UPS: Ultraviolet photoelectron spectroscopy.

V: Volts.

V_{eff} : Effective voltage.

V_{ext} : External voltage applied.

V_{OC} : Open-circuit voltage.

V_0 : Voltage when J_{sc} is zero.

XRD: X-Ray Diffraction.

γ : Parameter that indicates the degree of bimolecular recombination in OSCs.

κ : Boltzmann constant.

λ : Wavelength.

λ_{em} : Emission wavelength.

$\lambda_{\text{max, abs}}$: Maxim absorption wavelength.

τ : Charge extraction time.

List of publications resulting from this Thesis.

- C. Rodríguez-Seco, L. Cabau, A. Vidal, E. Palomares. *Advances on the Synthesis of Small Molecules as Hole Transport Materials for Lead Halide Perovskite Solar Cells*. Acc. Chem. Res., 2018, 51 (4), 869–880.
- C. Rodríguez-Seco, S. Biswas, G. D. Sharma, A. Vidal-Ferran, E. Palomares. *Benzothiadiazole Substituted Semiconductor Molecules for Organic Solar Cells: The Effect of the Solvent Annealing Over the Thin Film Hole Mobility Values*. J. Phys. Chem. C 2018, DOI: 10.1021/acs.jpcc.8b00840.
- C. Rodríguez-Seco, A. Vidal-Ferran, R. Misra, G. D. Sharma, E. Palomares. ACS Applied Energy Materials, *Efficient Non-Polymeric Heterojunctions in Ternary Organic Solar Cells*. DOI: 10.1021/acsaem.8b00828.
- C. Rodríguez Seco, M. Privado, P. de la Cruz, F. Langa, G. D. Sharma, E. Palomares. *Reduced Energy Offsets and Low Energy Losses Lead to Efficient (10% at 1sun) Triple Heterojunction Organic Solar Cells*. ACS Energy Lett. 2018, 2, 10, 2418-2424.

List of publications not included in this Thesis.

- L. Xu, C. Aumaitre, Y. Kervella, G. Lapertot, C. Rodríguez-Seco, E. Palomares, R. Demadrille, and P. Reiss. *Solar Cells: Increasing the Efficiency of Organic Dye-Sensitized Solar Cells over 10.3% Using Locally Ordered Inverse Opal Nanostructures in the Photoelectrode*. Adv. Funct. Mater. 2018, 1706291.
- R. Pudi, C. Rodríguez-Seco, A. Vidal-Ferran, P. Ballester, E. Palomares. *o,p-Dimethoxybiphenyl Arylamine Substituted Porphyrins as Hole-Transport Materials: Electrochemical, Photophysical, and Carrier Mobility Characterization*. Journal of Organic Chemistry 2018, 18, 2064-2070.
- C. Aumaitre, C. Rodriguez-Seco, J. Jover, O. Bardagot, F. Caffy, Y. Kervella, N. Lopez, E. Palomares, R. Demadrille. *Visible and near-infrared organic photosensitizers comprising isoindigo derivatives as chromophores: synthesis, optoelectronic properties and factors limiting their efficiency in dye solar cells*. J. Mater. Chem. A, 2018, 6, 10074.
- E. Yalcin, M. Can, C. Rodriguez-Seco, E. Aktas, R. Pudi, W. Cambarau, S. Demica, E. Palomares. *Semiconductor Self-Assembled Monolayers as Selective Contact for Efficient PiN Perovskite Solar Cells*. Energy Enviroment. Sci., 2019, 12, 230-237.

E. Aktas, J. Jiménez-López, C. Rodríguez-Seco, R. Pudi1, M. A. Ortuño, N. López, E. Palomares. *Supramolecular Coordination of Pb²⁺ Defects in Hybrid Lead Halide Perovskite Films Using Truxene Derivatives as Lewis Base Interlayers*. ChemPhysChem 2019, DOI: 10.1002/cphc.201900068.

Table of contents

Chapter 1. Introduction.....	1
Chapter 2. Aim of the Thesis.....	63
Chapter 3. Materials, Methods and Experimental Techniques.....	69
Chapter 4. Design, Synthesis and Characterization of Small Molecules for Optoelectronic Applications.....	93
Chapter 5. Organic Solar Cells.....	173
Chapter 6. Perovskite Solar Cells.....	243
Chapter 7. Concluding Remarks and Perspective.....	301

UNIVERSITAT ROVIRA I VIRGILI

LOW-MOLECULAR WEIGHT ORGANIC SEMICONDUCTORS FOR ORGANIC AND PEROVSKITE SOLAR CELLS

Cristina Rodríguez Seco

,



1. INTRODUCTION

Chapter 1

Table of contents

1.1. An overview: From silicon to perovskite solar cells.....	5
1.2. Organic Solar Cells.....	7
1.2.1. Device architecture and components.....	7
1.2.1.1. Transparent and back electrodes.....	8
1.2.1.2. Active layer architectures.....	9
1.2.2. Device operating principles.....	13
1.3. Organic Donor Materials for Organic Solar Cells.....	14
1.3.1. Polymer Donor Materials for Organic Solar Cells.....	15
1.3.2. Small Molecule Donor Materials for Organic Solar Cells.....	16
1.3.2.1. Porphyrin-based small molecules.....	17
1.3.2.2. Diketopyrrolopyrrole-based (DPP) small molecules.....	18
1.3.2.3. Push-and-pull small molecules: oligothiophenes and its derivatives.....	18
1.3.2.4. Other small molecules.....	18
1.4. Perovskite Solar Cells.....	19
1.4.1. Perovskite.....	19
1.4.2. Perovskite device architecture and components.....	23
1.4.2.1. Device architecture.....	24
1.4.2.2. Components.....	26
1.4.3. Device operating principles.....	30
1.5. Hole Transporting Materials for Perovskite Solar Cells.....	31
1.5.1. Inorganic HTMs.....	33
1.5.2. Organic Polymers HTMs.....	33
1.5.3. Organic Small Molecules as HTMs.....	34
1.5.3.1. State-of-the-art: Spiro-OMeTAD.....	35
1.5.3.2. Aryl amine HTMs.....	36
1.5.3.3. Small organic molecules as HTMs without arylamine substituents.....	39
1.5.3.4. Porphyrins and Phthalocyanines as HTM.....	42
1.6. References.....	44

Chapter 1

1.1. An overview: From silicon to perovskite solar cells.

The first inorganic solar cell has its roots in the process called photoelectrochemistry. In 1839, Becquerel observed current flow resulted from two silver electrodes in an electrolyte media when they were exposed to a light source¹. Afterwards, W. G. Adams and R. E. Day observed the influence of sunlight on the performance of selenium wires, used in telecommunications, probing that a solid material could generate electricity when it is exposed to illumination². However, they were not efficient enough to convert more than 0.5 % of the sun's energy into electricity. Accidentally, in 1953 researchers at Bell Laboratories (USA) discovered the first silicon p-n junction solar cell. After device optimization, silicon solar cells were able to convert light into electricity with an efficiency of 6 %, allowing to start with their commercialization². At first, this new technology equipped the USA satellites. Inorganic solar cells have been widely developed and have many military, space and consumer applications. They are formed by a p-n junction of inorganic materials. Different approaches have been evolved, such as doped monocrystalline, polycrystalline or amorphous silicon with efficiencies of 25 %, 20 % and 13 %, respectively. Furthermore, doped silicon with elements from the group III and IV of the periodic table, as gallium arsenide (GaAs) showed better stability. However, silicon-based solar cells require high cost purification and fabrication processes³. Additionally, this technology has not been able to produce flexible substrates, which limited their used to rigid flat surfaces and large-scale applications.

Over the last 30 years, many attempts have been carried out in order to provide low-cost and highly efficient solar cells. For example, in 1991, M. Grätzel and B. O'Regan, developed the Dye-Sensitized Solar Cells (DSSCs) that consists in a mesoporous semiconductor that increased the surface area up to 1000 times, allowing higher concentration of the dye to anchor. This resulted in more efficient light harvesting, increasing the photocurrent and the device

Chapter 1

efficiency⁴. Other alternatives to replace silicon solar cells have been emerged, such as organic photovoltaic (OPV) and perovskite solar cells (PSCs), that has attracted a lot of attention in the recent years.

A detailed description of organic solar cells (OSCs) and PSCs is explained in section 1.2 and 1.4 of this chapter.

As it can be seen in Figure 1.1, many attempts have been done in the last decades to improve the efficiencies of the different photovoltaic technologies. OPV and PSCs have had a rapid development in the last ten years, improving their efficiencies up to 15.6 % for OPV and 24.2 % for PSCs, receiving much attention into scientific community.

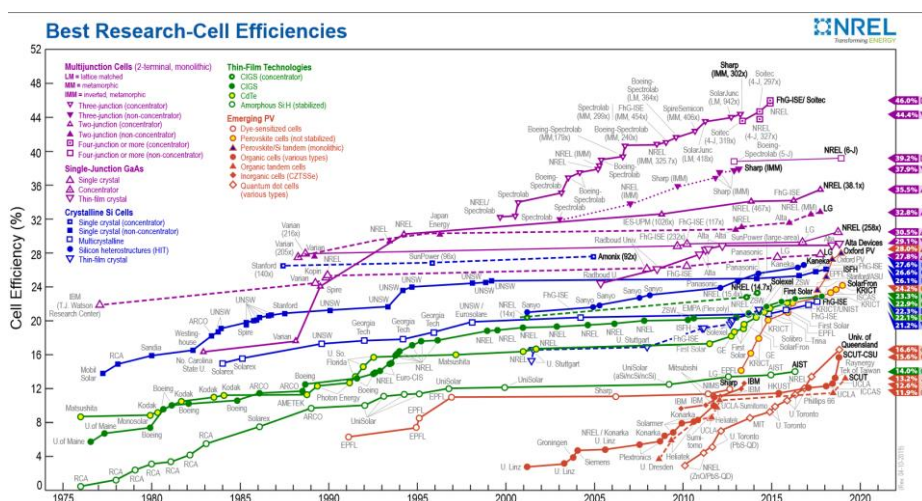


Figure 1.1: Progress on solar cells devices. Copyright NREL.

Due to the need of replacing silicon-based solar cells, this thesis has focused in the study of novel organic materials that could be utilized in the third generation of solar cells.

1.2. Organic Solar Cells.

Solution-processed organic photovoltaic cells (OPVs) have attracted considerable attention recently because of their potential as a promising next-generation environmentally-friendly technology with the advantages of solution processability, low cost, lightweight, flexibility and components with low toxicity, compared to the silicon and heavy metal based semiconductors⁵⁻⁷. Thus, it can be considered the most promising cost-effective alternative to silicon-based solar cells.

The first OSC was fabricated as a single-layer showing a very poor efficiency of 0.5 %⁸. Afterwards, conjugated polymers were widely investigated, being reported in 1984 by Garnier et al.⁹ the first example of solar cell based on poly(thiophene) (P3HT). The discovery of the photo-induced electron transfer between the conjugated polymers and the fullerene C₆₀ by Sariciftci et al.¹⁰ and the invention of the concept of bulk heterojunction (BHJ) solar cells and the research focused on the design and synthesis of novel donors and acceptor molecules, opened the pathway towards high efficient OSCs. Recently, more complex systems have been developed, such as the incorporation of a third component in the active layer (ternary BHJ-OSC)¹¹ or tandem⁸ OSCs.

1.2.1. Device architecture and components.

This section will address the components used in the organic solar cells fabrication and the different device architectures. To that end, it will be divided in two sections describing the most important characteristics of, first, the electrodes with their corresponding interlayers and finally the active layer, what is certainly the key component of the device to obtain high efficiencies.

Chapter 1

1.2.1.1. *Transparent and back electrodes.*

OSCs are fabricated over a transparent substrate, commonly glass, allowing the light strikes to the active layer avoiding shadows as much as possible. On top of the substrate is deposited a transparent conducting electrode (TCO). The best candidate over the last decades has been indium tin oxide (ITO) due to its wide band-gap (4.1 eV – 5.2 eV), its transparency in the visible range of the solar spectrum and the possibility to tune its work function by applying a UV ozone treatment¹². There has been tried other TCO with the aim of reducing the high price of ITO by using fluorine-doped tin oxide (FTO) or aluminium-doped zinc oxide (AZO). However, ITO continues being the most used metal oxide¹³.

On top of the electrode is deposited an electron blocking layer. The most common material in use is Poly(3,4-ethylenedioxythiophene)-poly(styrenesulfonate) (**PEDOT:PSS**). **PEDOT:PSS** is a mixture of two π -conjugated polymers, **PEDOT** and **PSS**, with a high conductivity and relatively good stability. The energy level perfectly fits with the work function of ITO, allowing an optimal hole injection¹⁴. Lately, there were some alternates to **PEDOT:PSS** due to its stability issues in the device when exposed to air because of its acidic and hygroscopic nature. Some of the alternatives are the followings: solvent-doped **PEDOT:PSS**¹⁵⁻¹⁶, doped graphene¹⁷ or a **MAM** (MoO₃/Au nanoparticles/MoO₃) layer¹⁸, although PEDOT:PSS is still the most used alternative.

The back electrode corresponds to the cathode. It is deposited by vacuum-deposition techniques. The work function has to be lower than that of the ITO and higher than the lowest unoccupied molecular orbital (LUMO) level of the electron acceptor¹³. The back electrode chosen in this work was Al, accomplishing all the requirements exposed below. Additionally, an interfacial layer was used. In our case, a very thin layer (around 10 nm) of the polymer poly [(9,9-bis(3'-(N,N-dimethylamino)propyl)-2,7-fluorene)-alt-2,7-(9,9-

diocetylfluorene)] (**PFN**) was deposited. The use of an interlayer enhances the electron injection from the fullerene to the cathode and protects the active layer from the Al evaporation process. It has been widely demonstrated that these few nanometers of PFN improves the open-circuit voltage (V_{oc}), short-circuit current (J_{sc}) and fill factor (FF) of the devices¹⁹.

1.2.1.2. Active layer architectures.

The active layer configuration is the key parameter in organic solar cells. It has to be optimized in order to improve the donor/acceptor interaction, physically and energetically, to obtain an efficient separation of the photogenerated excitons.

The simplest device structure is a layer of organic material sandwiched between two different conducting contacts. However, historically, extremely low efficiencies (below 1 %) were obtained with this configuration²⁰.

The progress that launched the improvement of the performance of organic photovoltaic devices was the used of the donor-acceptor heterojunctions. The electron-donor (D) material is the component that mainly absorbs the light and generates the charges that will be transferred to the electron-acceptor material before being collected by the cathode. An important breakthrough took place when in 1986, Tang fabricated the first donor-acceptor heterojunction organic solar cells²¹. The active layer consisted of two films deposited one on top of the other as it is shown in Figure 1.2b. The donor material is coated by the electron acceptor. It was commonly known as bilayer or planar heterojunction device. This architecture took advance over the monolayer because at the interface between both materials a favourable local electric field is created that can break up the photogenerated excitons if the differences in the potential energy are larger than the exciton binding energy and the electron can be transfer to the acceptor network²⁰.

Chapter 1

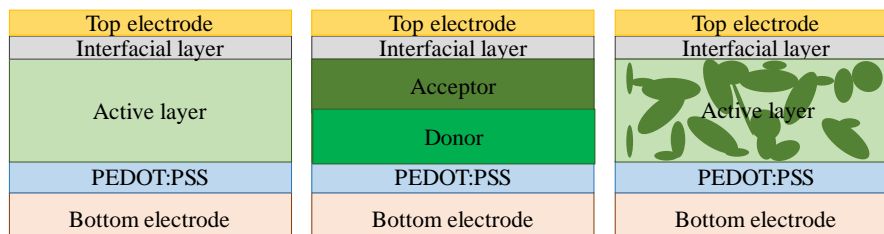


Figure 1.2: Device architecture of a generic left) mono layer, middle) bilayer and right) bulk heterojunction organic solar cell.

Even all the obvious advantage over the monolayer, bilayer structure presents also some drawbacks, for example the difficulties that the charges generated at the first nanometers of the donor (closer to the bottom electrode) find to reach the interface with the acceptor and many of them recombine within the same material.

In order to solve that and improve the charge transfer, in the mid-1990s, the bulk heterojunctions (BHJs) appeared. This concept is based on blending the electron donating and the electron accepting materials. With this configuration, the geminate recombination noticeably decreased as the excitons can reach easily the donor/acceptor interface because of the similar length scale of the blend and the exciton diffusion. This strategy considerable enlarge the interfacial area and reduce the donor and acceptor domains in order to avoid surpass the exciton diffusion length²². It results in a general enhancement of the working device.

Another approach has been developed in the recent years with the incorporation of a third component to the active layer: ternary bulk heterojunction organic solar cells²³. It can be either an electron donating or accepting material, so the configuration can be written as D¹-D²-A or A¹-A²-D. Usually, there is an increase in the current density because of the photogenerated electrons of the third component and helps the charge transfer due to the smaller energy offset

between the LUMO level of all the materials that take part of the active layer, which leads also in an increase of the overall PCE.

Nevertheless, in BHJ OSCs, the increase of the charge trapping caused by possible defects formed in the blend is one issue that needs to be taken into account. The way to improve the morphology of the film is by performing an annealing treatment, thermally or with solvent vapours, or by the use of additives²⁴.

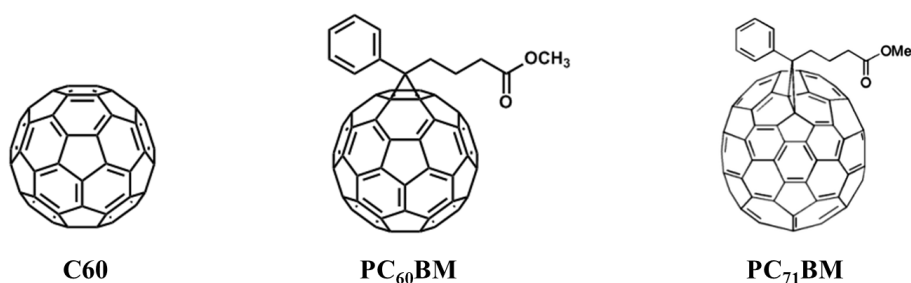


Figure 1.3: Molecular structure of two of the most used electron-accepting materials in BHJ OSCs.

The most common electron acceptor unit used in BHJ solar cells are the well-known fullerenes, such as **C₆₀**, **PC₆₀BM** or **PC₇₁BM** (Figure 1.3) because of their high electron mobility ($\sim 10^{-2} - 10^{-1} \text{ cm}^2 \text{ V}^{-1} \text{ s}^{-1}$)¹³ and their good alignment with the energy levels of the other materials that helps an efficient electron transfer to the electrode¹³. The spherical shape makes them an excellent acceptor in any direction. Another important advantage is the possibility of depositing them by solution processing techniques.

However, polymer acceptors are attracting research attention for their strong light absorption and the possibility of tuning their energy level²⁵ and because of the high production cost associated to the difficult synthesis of fullerenes. Additionally, in the last years, new small-molecule non-fullerene electron

Chapter 1

acceptors for OSCs have been developed successfully, leading to PCEs up to 14 % in 2018²⁶.

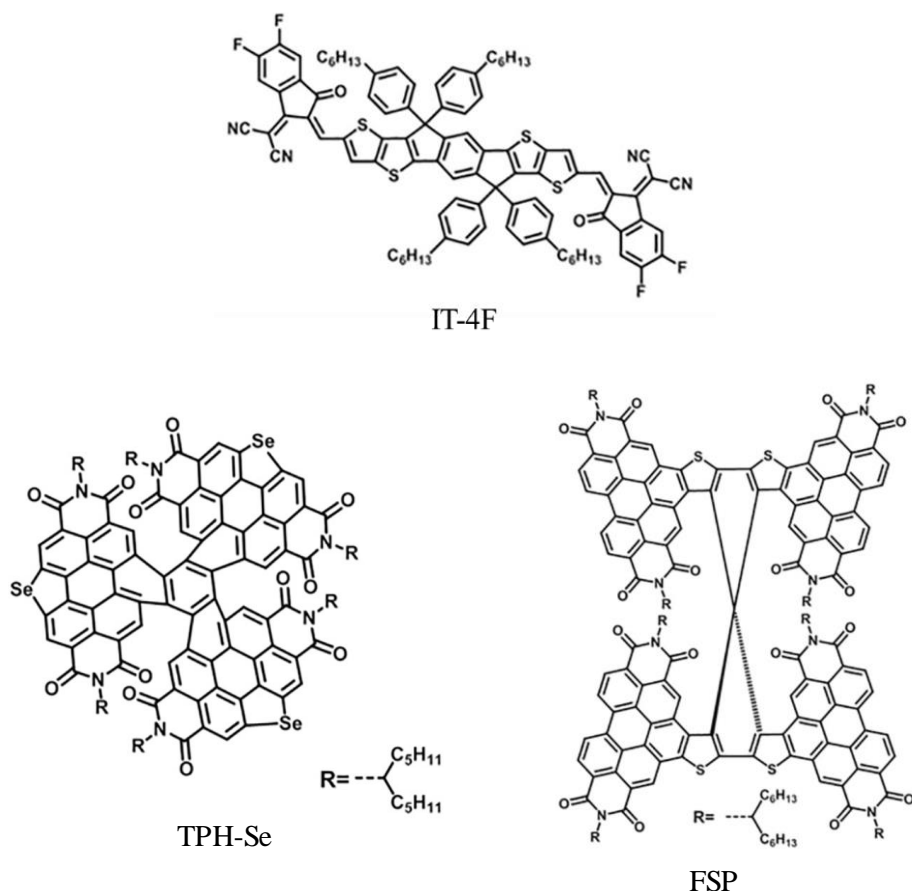


Figure 1.4: Molecular structure of four non-fullerene electron accepting materials for OSCs.

Figure 1.4 shows three of the most used non-fullerene electron acceptors. **IT-4F** has high absorption coefficient ($1.16 \times 10^5 \text{ cm}^{-1}$ in chloroform solution) and its maximum lies in the infrared region of the spectrum. It presented a certified PCE of 13 % when used it blended with the electron donor **PBDB-T-SF**²⁷. **TPH-Se** and **FSP** are based in a well-known group perylene diimide (PDI) with electron accepting properties. **TPH-Se** exhibits the best photovoltaic

performance (9.28 %) due to its high electron mobility and favourable aggregation²⁸.

In the following section 1.2.3. the role and the different types of electron-donor materials utilized in OSCs will be described in detail, as it is one of the main topics of this work.

1.2.2. Device operating principles.

The mechanism of the charge transfer processes of a typical OSC is shown in Figure 1.5. When the light reaches the active layer the excitons that are formed (1) travel to the interface of the D-A nanodomains and dissociate, leaving the corresponding hole in the donor material. Charge transfer (2) should occur in order to have an efficient photocurrent generation. Geminate recombination (3) happens as a detrimental process opposite to the charge dissociation and diffusion within the same material, as well as interfacial recombination (4) at the interface between the donor and the acceptor materials²⁰.

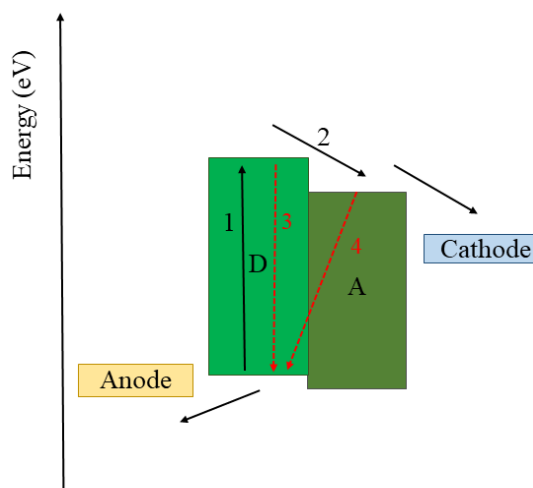


Figure 1.5. Schematic energy-band diagram of the active layer for OSCs.

Chapter 1

The process where a free charge meets an opposite charge carrier and recombine is called non-geminate recombination since the electron and hole that recombine were not originated from the same initial exciton. This last, is considered the largest source of energy loss in OSCs and it strongly contributes to a reduction of the open-circuit voltage²⁹ (V_{oc}) and the fill factor (FF)³⁰⁻³¹. Non-geminate recombination can be classified in three types: trap-assisted (when one of the two charge carriers is stuck in a trap state)³², surface recombination (takes place when a charge is collected at the wrong electrode)³³ and bimolecular recombination (it is the dominant recombination process and occurs whenever photogenerated electrons and holes recombine in the active layer)³⁴.

1.3. Organic Donor Materials for Organic Solar Cells.

Organic donor materials for OSCs are divided in two main groups: polymer and small molecules. While small molecules are formed by a discrete number of atoms, polymers consist in a variable number of monomers, being frequently difficult to control their molecular weight.

However, all of them must have in common the following properties: broad and strong absorption band in the visible and NIR (near-infrared) spectra, suitable energy levels that match with the electron acceptor and maximize the value of V_{oc} and high carrier mobility to enhance the charge transport from the active layer to the electrodes. It is desirable that they have high solubility for solution process fabrication and the capability to have an optimal nano-scale morphology to maximize the charge separation³⁵.

1.3.1. Polymer Donor Materials for Organic Solar Cells.

Although it is not the main topic of this thesis, this section will describe briefly the most representative donor polymers used in OSCs: poly(3-hexylthiophene-2,5-diyl) (**P3HT**) and poly({4,8-bis[(2-ethylhexyl)oxy]benzo[1,2-b:4,5-b']dithiophene-2,6-diyl}{3-fluoro-2-[(2-ethylhexyl)carbonyl]thieno[3,4-b]thiophenediyl}) (**PTB7**). Figure 1.6 shows their molecular structures.

P3HT has an excellent absorption and transport charges efficiently. It was one of the first conjugated systems studied for OSCs. Initially, the results obtained were not the desirable ones but within years, it achieved 3.5 %³⁶ and, 4.4 %³⁷ later when thermal annealing treatments or crystal growing techniques were developed. Its main limitation is the low V_{oc} (around 0.66 V) obtained in **P3HT**-based devices due to its high highest occupied molecular orbital (HOMO) level.

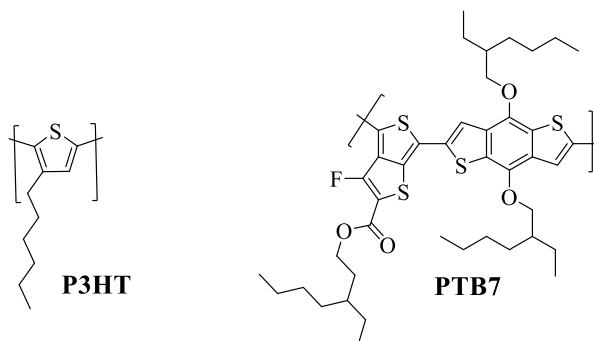


Figure 1.6. Molecular structure of the polymers **P3HT** and **PTB7**.

PTB7 has a wide absorption spectrum close to 700 nm. Besides, because of its rigid molecular structure, it is soluble to deposit it with solution process techniques and it presents high hole mobility. Its HOMO level is lower than that of **P3HT** so the theoretical value of V_{oc} is superior³⁸. For this reason, **PTB7** derivatives have been widely used as donor materials in non-fullerene-based devices or D-A-A ternary architectures³⁹.

1.3.2. Small Molecule Donor Materials for Organic Solar Cells.

Despite receiving less attention than polymer OSCs, solar cells made with solution-processed small molecule (SM) donor materials have achieved rapid progress in recent years. They offer some advantages over polymer donors. For example, whereas polymers usually contain a broad distribution of molecular weights, SMs are well-defined, allowing easier purification and reproducibility from batch to batch. SMs usually require fewer synthetic steps that able us to tune their optical and electrochemical properties⁴⁰. Recent results show efficiencies around 9 %⁴¹ with some examples up to 11 %⁴².

In the early stages, many small molecules have been defined as electron donor materials as they are used as the main light-harvesting moiety in OSCs. This is the main reason why SMs have been initially based on dyes and pigments, such as porphyrins, squarines or merocyanines initially utilized for other applications, like xerography or DSSCs. From 2005⁴³, there has been a rapid development of solution-processed SMs for OSCs, leading to the synthesis of many types of chromophores: oligothiophenes, triphenylamines, diketopyrrolopyrroles or porphyrin-based SMs; most of them based on push-and-pull structures (see Figure 1.9). The mentioned push-pull molecules consist in molecules with electron-donor and acceptor moieties bounded one next to the other to enhance the charge transfer within the molecule.

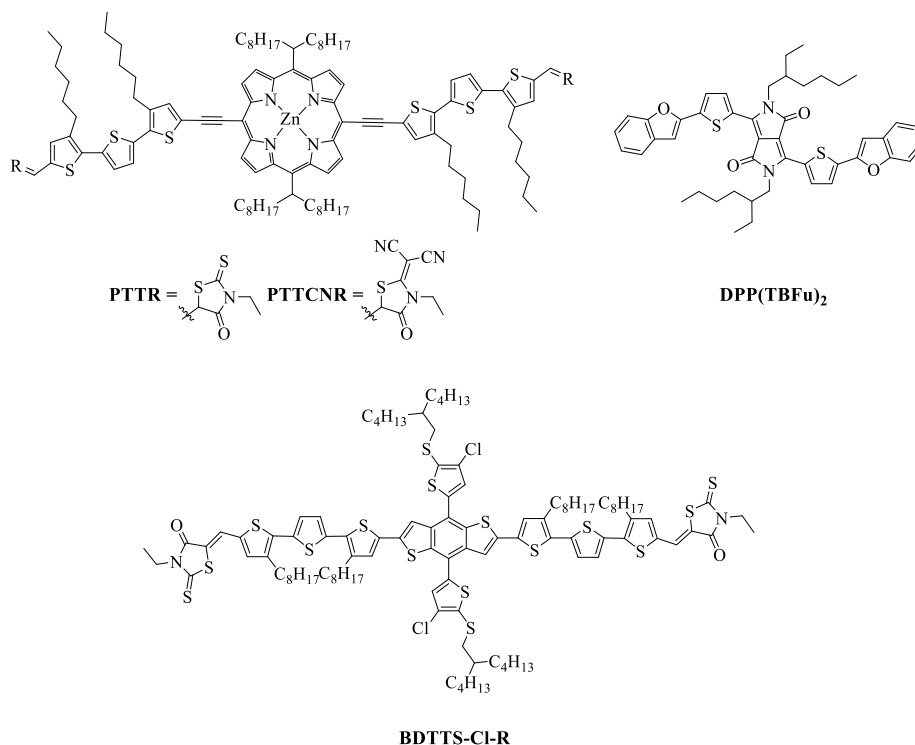


Figure 1.7: Molecular structure of common small molecules used as electron donor in OSCs: a) PTTTR and PTTTCNR are porphyrins, b) DPP(TBFu)₂ is a DPP-based molecule and c) BCTTS-Cl-R is an oligothiophene derivative.

1.3.2.1. Porphyrin-based small molecules.

Porphyrins have been widely studied and used not only in OSCs, but also in DSSCs due to their high molar extinction coefficient, their thermal stability and the possibility to tune their energy levels by modifying the molecular structure or the metal⁴⁴. Lately, researchers have focus their attention in the synthesis of A- π -D- π -A structures. Two of the most efficient porphyrins were designed and synthesized by Xiao et al.: **PTRR** and **PTTCNR** (Figure 1.7a), which have excellent performance with PCE values of 7.66 % and 8.21 % respectively⁴⁵. The main disadvantage of the porphyrins is their arduous synthetic steps.

Chapter 1

1.3.2.2. Diketopyrrolopyrrole-based (DPP) small molecules.

DPP-based SMs have the same advantages than porphyrins: the energy levels can be easily tuned and they have a broad absorption in the UV-Vis region of the spectrum. On the contrary, they are easy to synthesize. One example using a DPP in a donor-acceptor-donor (D-A-D) structure is **DPP(TBFu)₂** (see Figure 1.7b). It showed an efficiency of 4.4 % (the best PCE for a small molecule: fullerene OSC at that time). This was the first molecular BHJ to have good nanoscale, phase separation, moderate hole mobility in a blend film and a relatively high V_{oc} due to its deeper HOMO level⁴⁶.

1.3.2.3. Push-and-pull small molecules: oligothiophenes and its derivatives.

Thiophene is the most common and widely used moiety in OSCs donor materials. It plays an important role in π -conjugated bridges participating in the intramolecular charge transfer. Many attempts have been done trying to adjust the end acceptor moieties to avoid the aggregation, such as the introduction of alkyl chains, rhodanine and cyano and their derivatives⁴⁷⁻⁴⁸, to study the influence of the molecular structure or trap states. In the last years, the most common strategy to synthesize novel SMs have been the combination of electron-deficient ending groups and electron-rich central unit with high efficiencies around 8 %⁴⁹ and 9 %⁵⁰. Ji and co-workers designed three oligothiophenes changing the halogen atoms (F, Cl and Br) obtaining for the chlorine derivative (**BDTTS-Cl-R**) the highest PCE of 10.78 %³⁵. Figure 1.7 shows its molecular structure.

1.3.2.4. Other small molecules.

There are two specific small groups of electron donor SMs that can be solution-processed but due to their low solubility in common solvents, they are also deposited by thermal evaporation techniques. Squaraines are characterized by their aromatic four membered ring system derived from squaric acid. The

present good absorption in the red and near infrared region of the spectrum. In 2005 Yang et al. synthesized an asymmetrical squaraine derivative (**ASQ-5-CN**)⁵¹ with a D-A-D' structure. The cyano substitution contributed to a lower HOMO energy level, increasing the V_{oc} up to 0.83 V and obtaining a PCE of 5.00 %. Polyacenes consist on a chain of fused benzene rings. They exhibit a high hole mobility, strong π - π interactions but they have to be deposited via thermal evaporation. Their efficiencies have not reached 3 %⁵². Figure 1.8 shows the molecular structure of two representative squaraine and polyacene.

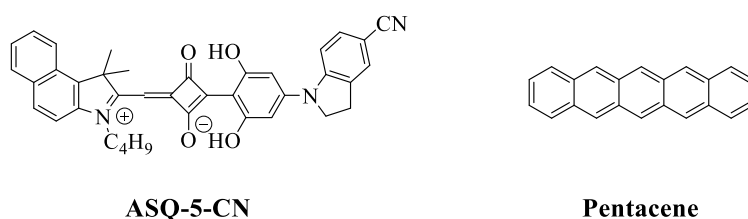


Figure 1.8: Molecular structure of ASQ-5CN and Pentacene.

1.4. Perovskite Solar Cells.

This section will address the state-of-the-art of hole transporting materials (HTMs) in PSCs. It will start with a description of the perovskite itself and a description of the components and functioning of perovskite-based devices.

1.4.1. Perovskite.

The term "perovskite" was first attributed to the crystal structure of calcium titanium oxide mineral composed of calcium titanate (CaTiO_3). The mineral was discovered by Gustav Rose (1798 – 1873) in 1839 in the Ural Mountains. He named it after the Russian mineralogist L. A. von Perovski (1792 – 1856). It lends its name to the class of compounds that have the same type of crystal structure as CaTiO_3 (ABX_3)⁵³. As it can be seen in Figure 1.9, B corresponds to the metal cation and X an oxide or halide anion. They form a BX_6 octahedral arrangement where B is in the centre of an octahedron enclosed by X anions

Chapter 1

located at the corners. A represents a cation which fills the hole formed by the eight adjacent octahedral in the three-dimensional structure and balances the charge of the whole network⁵⁴. Any sort of distortion will affect physical properties of perovskite materials, such as electronic, optical, magnetic and dielectric properties.

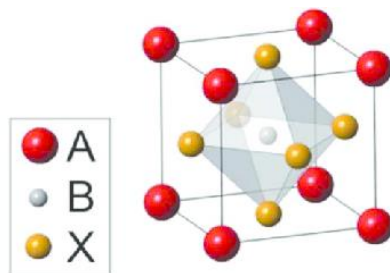


Figure 1.9: Perovskite general structure.

The organic-inorganic hybrid halide perovskites, also called organometallic perovskites, were widely studied in the 1990s for its application in transistor technology and light emitting diodes⁵⁵⁻⁵⁶. In those perovskites, A is an organic cation surrounded by twelve nearest X anions. The size of the cations and anions is an important parameter to modulate the optical and electronic properties of the perovskite material⁵⁷. To have a closed-packed structure, it is needed that the organic cation fits well in the hole formed by the eight adjacent octahedral connected through the corners where the X anions are located. The size of the A cation suitable is experimentally defined by the Goldschmidt tolerance factor:

$$t = \frac{R_A + R_X}{\sqrt{2}(R_B + R_X)} \quad \text{Equation 1.1}$$

Where R_A , R_B and R_X are the ionic radius for each component. A perfect packed structure would correspond to $t = 1.0$ and only A tolerance factor in the range $0.8 < t < 1.0$ perovskites generally do form, although in the lower part of this range they may be distorted due to tilting of the BX_6 octahedral and lowering of

the symmetry. If $t > 1$, the A site cation is too large, preventing from forming the perovskite and if $t < 0.8$, the cation is too small, again often leading to alternative structures⁵⁸. The three A cations known to date that better stabilize the perovskite structure in heavy halides are Cs^+ , CH_3NH_3^+ (MA^+) and $\text{HC}(\text{NH}_2)_2^+$ (FA^+). Cs^+ is the only elemental cation that is large enough to sustain the perovskite. For organic cations, it seems it is important the size, but also the distribution of the net positive charge⁵⁹.

Although organolead halide perovskites have been known to have good hole and electron transporting properties for over a decade⁶⁰, the first work published using the perovskite as an absorbing material was in DSSCs in 2009 by Miyasaka and co-workers, where methylammonium lead triiodide (MAPbI_3) and methylammonium lead tribromide (MAPbBr_3) were used as sensitizers instead of the organic dyes, obtaining 3.8 % and 3.1 % of efficiency, respectively⁶¹. Particularly, MAPbI_3 exhibits excellent optoelectronic properties, covering almost the whole visible region with a direct bandgap of 1.55 eV and a light absorption spectrum up to 800 nm⁶². More attempts were done, for example, by using 2 – 3 nm size MAPbI_3 perovskite nanocrystals⁶³ or the composition of the perovskite (replacing MA^+ by ethylammonium, EA^+)⁶⁴, but it was not until 2012, when a major breakthrough in the PSCs was achieved by replacing the liquid electrolyte with a solid-state hole transport material (HTM), obtaining 9.7 %⁶⁵. Since then, many approaches have been done to increase the power conversion efficiency (PCE) until 23.2 % for a small area ($\sim 0.094 \text{ cm}^2$)⁶⁶, the record reported to date.

Modifications on the halide substitution were the first strategy to design novel materials with optimized optoelectronic properties. By varying the halide composition between iodide and bromide in the perovskite ($\text{MAPb}(\text{I}_{1-x}\text{Br}_x)_3$) the bandgap can be tuned from 1.55 to 2.3 eV, making possible to modify the colour and optimize it for, as instance, multi-junction solar cells or application as smart windows in roofs⁵⁷. The optical absorption caused by tuning the

Chapter 1

bandgap, can be controlled to ensure that almost the whole range of the visible spectrum is covered, as it is depicted in Figure 1.10. By adding a low ionic radius of Br^- in a concentration between 10 – 20 % to the mixed halides, the efficiency and stability of the device increased significantly due to the tetragonal to pseudo-cubic structural transition of perovskites formed⁶⁷. The incorporation of chloride instead of iodide forming MAPbCl_3 increased even more the bandgap up to 2.97 eV⁶⁸. Motivated by this, Snaith and co-workers study the bandgap tunability of the $\text{FAPbI}_x\text{Br}_{3-x}$ perovskite⁶⁹. Besides, they compared the optical and electronic properties when the MA^+ was replaced by FA^+ and Cs^+ , showing that as the cation increases its ionic radius, the lattice would expand, so the bandgap decreases.

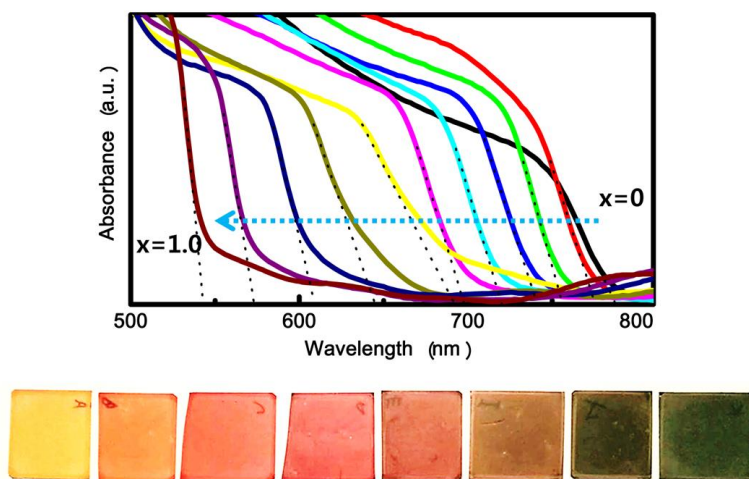


Figure 1.10. UV-Vis absorption spectra of $\text{MAPb}(\text{I}_{1-x}\text{Br}_x)_3$ based cells and a picture of $\text{FAPb}(\text{I}_{1-x}\text{Br}_x)_3$ films. Reprinted with permission from Nano Lett. 2013, 13, 4, 1764-1769. Copyright (2013) American Chemical Society.

It has also been studied the replacement of the lead cation because of its high toxicity, which may cause important legal restrictions to the commercialization of solar devices⁷⁰⁻⁷¹. It was demonstrated that the desirable photovoltaic properties of a lead-base perovskite were attributed to the high symmetry of the structure and the strong $\text{Pb } 6s\text{-}I 5p$ anti-bonding coupling⁷². As a consequence,

the metal cations with ns^2 lone pairs electrons that can form octahedral structure with halogen anions are good candidates to replace lead. Several metals have been tested, such as Bi^{3+} , Sb^{3+} , Ge^{2+} or Sn^{2+} , with PCEs for this last one no higher than 6 % and poor stability of the devices due to the rapid oxidation of Sn^{2+} to Sn^{4+} ⁷³⁻⁷⁴.

Among all the monovalent organic/inorganic cations, only FA^+ and Cs^+ besides MA^+ have been incorporated into perovskites for photovoltaics. They are the only ones that possess Goldschmidt tolerance factors (see Equation 1.1) between 0.8 and 1.0 to ensure the formation of the 3D phases with optimal optoelectronic properties. The perovskites with the composition of CsPbI_3 and FAPbI_3 are only stable at high temperature but they can be stabilized at ambient temperature by partially mixing them with the MA^+ in different combinations, in the so-called multiple cation approach ⁷⁵⁻⁷⁷. At first, different proportions of FA^+ and MA^+ were mix in the same perovskite composition. By adding FA^+ to the mixture, the transformation into the yellow unstable perovskite polymorph was avoided ⁷⁸. In 2016, Saliba et al. first introduced Cs^+ into the MA^+/FA^+ perovskite composition ⁷⁶ and they observed high-uniform perovskite grains growing from the electron transport layer (ETL) to the hole collecting layer without traces of any yellow phase impurities. To date, the best results in efficiency and stability have been achieved with this triple-mix perovskite $\text{Cs}_{0.1}(\text{MA}_{0.15}\text{FA}_{0.85})\text{Pb}(\text{I}_{0.85}\text{Br})_3$ with mix cations as well as mix halides and that is the one chosen to fabricate devices for this work.

1.4.2. Perovskite device architecture and components.

This section will describe the main components of PSCs devices and the most utilized device architectures.

Chapter 1

1.4.2.1. Device architecture.

The ambipolar charge transport property of the perovskite makes the device architecture highly versatile. It can act as a light absorber with n- and p-type semiconductors⁷⁹. The architecture of PSCs consists in a multilayer device, typically composed of a transparent electrode, an electron transport layer (ETL), perovskite layer, hole transport layer (HTL) and a metal electrode. The perovskite acts as the active layer absorbing the sunlight and generating free charges. The ETL and HTL are deposited to prevent the charge recombination and they extract electrons and holes, respectively, from the perovskite⁸⁰. Those charges are transported to the electrodes, cathode or anode. It is crucial that the energy levels of all the materials that form the device are aligned to assure the charge transfer.

1.4.2.1.1. Conventional structure: n-i-p.

This configuration consists in a transparent electrode covered with an ETL. The perovskite is sandwiched between the ETL and the HTL, usually an organic semiconductor. To complete the device, a metal electrode is deposited. Depending on the structure of the ETL layer, there are two types of n-i-p PSCs: mesoscopic and planar (Figure 1.11 left). In the mesoscopic PSCs a mesoporous TiO₂ layer is deposited on top of the ETL layer, which is usually composed by 20 – 50 nm of compact TiO₂⁸⁰. The perovskite material fills the porous TiO₂ layer followed by the deposition of the HTM, typically N2,N2,N2',N2',N7,N7,N7',N7'-octakis(4-methoxyphenyl)-9,9'-spirobi[9H-fluorene]-2,2',7,7'-tetramine (spiro-OMeTAD), and finally a metal anode (50 - 100 nm of Au or Ag). In the planar architecture the mesoporous TiO₂ layer is suppressed and the perovskite is deposited directly over the compact TiO₂. This makes the fabrication process much simpler when compared to the mesoporous PSCs since no high temperature treatments are involved and it allows the use of flexible substrates.

The charge extraction of the photoinduced electrons from the perovskite is more efficient with the mesoporous architecture because it shortens the electron transport length and it does not require high crystal quality for an efficient light harvest⁸¹.

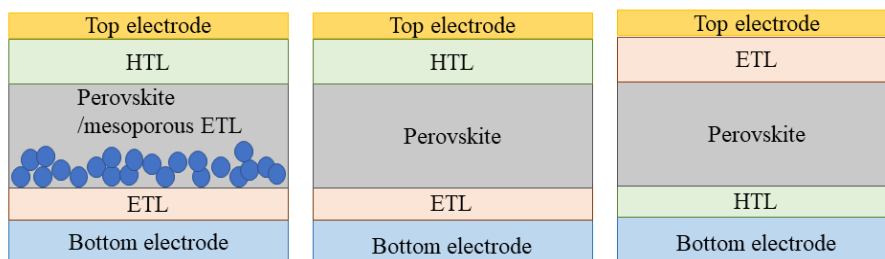


Figure 1.11. Most common device architecture for PSCs. Left: mesoporous n-i-p, center; planar n-i-p and right: inverted p-i-n structures.

1.4.2.1.2. Inverted structure: p-i-n.

In an inverted structure, (see Figure 1.11 right) the perovskite film is deposited on top of a HTL, which can be an oxide (like NiOx), an organic small molecule or a polymer (for instance, PEDOT:PSS). The small molecules ETMs can be classified in fullerene-based molecules, such as **C₆₀** or **PC₇₁BM**, and non-fullerene based molecules, as bathocuproine (**BCP**)⁸². The cathode is deposited on top of the ETL and it is usually a metal (Al, Cu or Ag)⁸⁰. The efficiency of inverted PSCs has increased by various approaches achieving up to 20 %⁸³.

Moreover, since perovskites are ambipolar semiconductors, there are devices employing only one of the selective contacts, as HTM-free or ETM-free⁸⁴⁻⁸⁵. However, the efficiencies are considerably lower, therefore the use of both electron and hole selective contact materials seems to be vital to reach high performance in PSCs.

Chapter 1

1.4.2.2. Components.

The main components of PSCs are listed in this section.

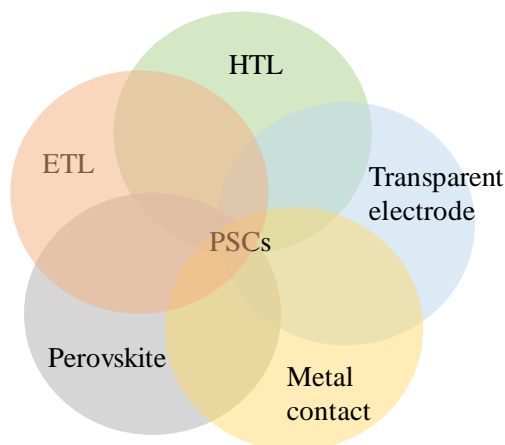


Figure 1.12. General components of PSCs devices.

Transparent conductive electrode.

The transparent electrode acts as a working electrode and generally consists on a transparent conducting oxide (TCO). The more used electrodes that are coated on the glass substrate are fluorine-doped tin oxide (FTO) and tin-doped indium oxide (ITO). The use of FTO has many advantages: it is stable under the operating conditions, chemically inert, high-temperature resistant and low sheet resistance. On top of that, it has low reflection and absorption and is less expensive than ITO. In this work FTO glass from Nippon Sheet Glass with a sheet resistance of $10 \Omega/\text{sq}$ were used for PSCs fabrication. ITO substrates were used for hole mobility devices.

Electron transport layer.

The energy levels of the electron transport material (ETM) have to be aligned with the perovskite's. It helps to inject the photogenerated electrons in the

contact, preventing the recombination with the holes. It must have high transmittance in the UV-Vis region of the spectrum and higher LUMO than that of the perovskite. Several metal oxides have been tested successfully as ETMs for planar and mesoscopic PSCs, such as TiO_2 , ZnO or SnO_2 ⁸⁶⁻⁸⁸. Among them, TiO_2 is the most used ETM in mesoscopic PSCs, due to its low cost, non-toxicity, its thermal and photostability and the high efficiencies obtained. However, its high-temperature process requires removing any organic material in the fabrication of the device before its deposition⁸⁹. For this reason, organic ETMs are being developed, as for instance fullerene and its derivatives, as C_{60} , C_{70} , **PC₇₁BM** or **ICBA** (Figure 1.13) that are used in OSCs as electron acceptor and are also the most widely used n-type materials for inverted PSCs because of their high electron mobility and the suitable energy level alignment^{87, 90}. Nevertheless, fullerenes are not stable under ambient conditions and it is difficult to make structural modifications. Nowadays, seeking for new non-fullerene organic ETMs is vital for further development of inverted PSCs⁹¹⁻⁹². For the organic ETMs used in inverted PSCs, on the contrary, LUMO level has to be lower than that of the perovskite⁹³.

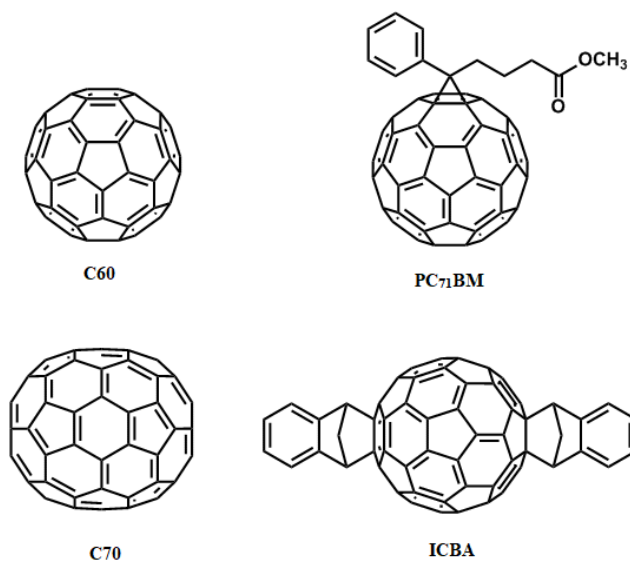


Figure 1.13: Molecular structure of the most common fullerene derivatives used in inverted PSCs.

Chapter 1

In this work, TiO₂ blocking layer was deposited by spray pyrolysis technique followed by mesoporous TiO₂, deposited by spin coating. This mesoporous layer facilitates the crystallization of the perovskite and enlarges the contact area between the perovskite and the ETM to collect the photogenerated electrons efficiently.

Perovskite.

Organolead halide perovskite layer is the key component in all devices configurations used to date because it is responsible for the light absorption and the generation of free carriers. Its optoelectronic properties (high absorption coefficient, long carrier diffusion length, moderate carrier mobility, high defect tolerance, tunable band gap, among others), the simple fabrication methods and the low-cost precursors (as PbI₂ or CH₃NH₃) and solvents (DMF and DMSO) have made it attract a huge attention for solar cell application. The perovskite can infiltrate into the pores of the TiO₂ mesoporous layer.

The phase, temperature and humidity instability of single-cation perovskites leded in a lack of reproducibility and the necessity of using double-cation, double-anion perovskite (like MA⁺ and FA⁺ and I⁻ and Br⁻), which has a stable black phase at room temperature. The introduction of a third cation, cesium⁷⁶, to that composition suppressed the detrimental yellow phase impurities in the double-cation perovskite, increasing the stability, the film quality the reproducibility. Due to these advantages, it has been adopted for several groups since.

Different deposition protocols have been studied such as solution deposition, thermal evaporation or spin coating.

Hole transport layer (HTL).

The hole transport material is responsible for the efficient hole extraction from the perovskite and prevents the undesirable recombination between electrons and holes, leading to improvement in the device performance. The energy levels of the HTM have to be well-aligned with the perovskite. HOMO level must be slightly higher than the valence band edge of the perovskite to allow the hole injection, while LUMO level has to be as high as possible, acting as an electron blocking⁹⁴⁻⁹⁵. Furthermore, it should have high hole mobility to avoid the use of additives that degrade devices faster because of their hygroscopic properties⁹⁶⁻⁹⁷. HTMs have to be soluble in not strong polar solvents that may dissolve the perovskite layer. In addition, an ideal HTM should protect the perovskite from the air and moisture so high hydrophobicity is desirable. Thermal and photochemical stability are also two important properties to resist from degradation to ensure long-term durable devices. A reduced tendency to crystallize (glass transition temperature above 100 °C) is required to avoid phase transitions during device operation⁹⁸. The most common HTM used is the well-known spiro-OMeTAD. Its synthesis and purification make it an expensive compound thus the seeking of new HTMs that reduce the production cost of the overall device is a topic of interest.

The classification of the HTMs used in PSCs will be described later in this chapter.

Metal contact.

Counter-electrode is required to complete the internal circuit. Commonly, the back electrode is deposited by thermal evaporation of a noble metal with a high work function, such as gold or silver. However, both present limitations: gold is expensive and it can migrate through the HTM at high temperatures and silver oxidases when expose to air. Carbon composites have been tested successfully

Chapter 1

in HTM-free PSCs, allowing the use of simpler deposition methods as screen printing or drop-casting⁹⁹⁻¹⁰⁰.

1.4.3. Device operating principles.

The simplified mechanism of the charge transfer processes of a typical PSC is shown in Figure 1.14. The perovskite layer is excited by the photons through the transparent electrode, leading to the photogeneration of the electron-hole pairs. The electrons and the hole are separated (1) and are injected into the conduction band of the ETL (2) and the HOMO level of the HML (3), respectively, before travelling to the electrodes. Nevertheless, there are undesirable photovoltage losses due to the recombination processes that can take place between the ETL, the perovskite layer and the HTL (5, 6 and 7). Non-radiative recombination (4) also occurs, although it is not the main factor for the mentioned photovoltage loss⁸².

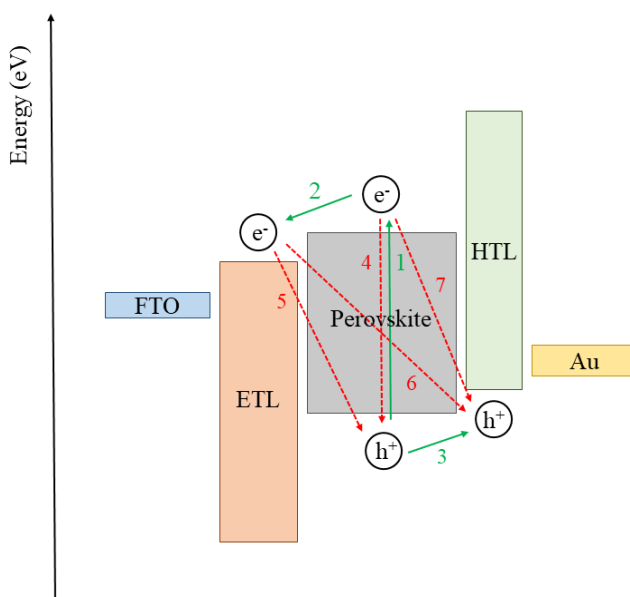


Figure 1.14. Energy diagram representing the energy levels and the charge transfer processes in PSCs. 1 represents the charge generation (electron and hole), 2 and 3, the transfer of the electrons and holes to the ETL and

HTL, respectively. 4, d, 6 and 7 depict the different recombination processes that can occur in an operating device.

In order to obtain high efficiencies, the charge recombination processes (4 – 7) should occur at a higher time scale than the charge generation, separation and extraction processes (1 – 3).

1.5. Hole Transporting Materials for Perovskite Solar Cells.

This section will describe the main properties that HTMs must exhibit for an optimal performance of PSCs. In addition, there will be explained in detail the different categories of HTMs to date.

HTMs have an important role in the regeneration of the oxidized state of the light absorber and transportation of the holes from the perovskite to the counter electrode. In PSCs, an HTM needs to fulfil several requirements^{80, 101}.

1. It must have a HOMO energy level slightly higher than the valence band of the perovskite, ideally no more than 0.3 eV higher, in order to have an efficient hole transfer. A lower HOMO should result in higher V_{oc} (open circuit voltage) as it depends on the energy difference between the Fermi level of the electron accepting material and the HOMO of the HTM. High LUMO level will ensure low charge recombination.
2. A reasonable charge carrier mobility (ideally higher than $10^{-3} \text{ cm}^2 \text{ V}^{-1} \text{ s}^{-1}$) is needed to produce rapid hole transfer from the perovskite to the metal electrode. The additions of dopants can help to HTMs with low hole mobility values. The most common dopants are lithium or cobalt salts combined with a pyridine derivative. Nevertheless, they are usually hygroscopic and cause a faster device degradation.
3. HTMs should be solution processable from solvents (nonpolar and aprotic solvents) that do not attack the perovskite layer. High solubility

Chapter 1

in organic solvents is desirable for low cost production processes such as inkjet printing or spin coating.

4. It is needed they have high thermal and photochemical stability. High hydrophobicity is also important in order to protect the perovskite from water and retard the degradation in long-term durable photovoltaic devices.
5. HTMs should have a low tendency to crystallize so they can form smooth thin layer at the interface that can help with the charge transfer. An amorphous phase with a glass transition temperature (T_g) above 100 °C would be desirable since phase transitions during device operation (80 °C – 100 °C) may reduce the efficiency and lead to a device breakdown. It should fill the pores of the perovskite layer. It is needed to find a balance regarding this property because while the T_g gets higher, the charge carrier mobility gets smaller in amorphous or non-crystalline solids.
6. Finally, HTMs should be environmental-friendly and have low-cost. An easy and palladium-free synthesis is beneficial.
7. It can help if the absorption spectrum of the HTM is complementary to that of the perovskite so it can contribute to the generated photocurrent. As the perovskite is a strong absorber in the visible range, a strong absorption in the visible region is not a must for a good HTM. It can also help preventing the perovskite degradation originated from the metal electrode and humidity¹⁰².

A huge research is being done to find a better understanding of the relation between the HTM and PSCs performance. A large number of HTMs have been reported to date. They can be classified in organic small-molecules (SMs), organic polymers and inorganic HTMs.

Organic semiconductors have different electrical properties when compared to traditional inorganic semiconductors. In inorganic semiconductors, the

interaction between atoms are strong covalent or ionic bonds forming crystalline solids. Nevertheless, organic semiconductors are formed by individual molecules weakly bound together by van der Waals forces, hydrogen bonding and π - π interactions, increasing the amorphous nature of them. In organic semiconductors (small molecules and polymers), holes and electrons in π -orbitals are the responsible of the charge carriers to move from one molecule to another. Change the degree of conjugation or the conjugation length of the organic semiconductors will cause a change in the electrical properties, the morphology of the layer and the charge carrier mobilities.

1.5.1. Inorganic HTMs.

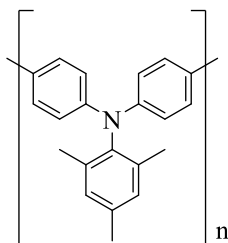
The number of inorganic HTMs tested in PSCs is low compared to the organic HTMs due to their slow development. The most used have been CuI¹⁰³, CuO₂¹⁰⁴, CuSCN, NiO¹⁰⁵ and NiO doped with magnesium and lithium oxides¹⁰⁶. NiO with and without dopants have been tested in inverted PSCs, achieving a PCE of 16.40 % with V_{oc} values of 1.04 V. CuSCN can be processed from organic solution and shows similar efficiencies (18.0 % with the mixture perovskite with a conventional device architecture)¹⁰⁷ and better device stability than the devices using organic HTMs. It is currently the most promising inorganic HTM. The main disadvantages compared to organic HTM are the high-temperature processes they need and the high level of toxicity and carcinogenicity associated with them¹⁰¹.

1.5.2. Organic Polymers HTMs.

Conjugated polymers have been extensively used for electronic devices, such as organic light emitting devices (OLEDs)¹⁰⁸, organic solar cells (OSCs)¹⁰⁹ and field-effect transistors (FETs)¹¹⁰. Polymers are known to have high hole mobilities compared to small-molecules HTMs, good solubility and good film forming abilities, which are properties that make them good candidates for

Chapter 1

PSCs. However, they have the noticeable disadvantage of having a poor batch to batch reproducibility since different samples of the same polymer can show different average molar masses, which may affect their optical and electronic properties. Poly(triaryl amine), Poly[bis(4-phenyl)(2,4,6-trimethylphenyl)amine] (**PTAA**) (see Figure 1.14) was the first polymer reported and the most efficient to date with a PCE of 22.1 %¹¹¹.



PTAA

Figure 1.14. Molecular structure of the polymer PTAA.

1.5.3. Organic Small Molecules as HTMs.

Organic SMs HTMs are widely developed in PSCs due to their synthetic variety, tunable properties, high purity and simple solution processing. In order to ensure low-cost devices and cost-effective upscale, an ideal HTM has to be easy to synthesize by minimizing the number of steps, easy workup and purification procedures.

The main characteristics for an efficient HTM have been already explained previously in this chapter. It is important not only the molecular structure of HTM, but also the thickness of the organic HTL. It should not be too thin to avoid short circuits but neither too thick, because that would lead to high series resistance and low conductivity if the hole mobility is not high enough.

This section will describe first, the most used HTM to date, spiro-OMeTAD, followed by the more efficient molecules divided in categories depending on

their molecular structure. There are hundreds of organic HTMs due to the possibility that organic chemistry offers regarding to the infinite number of imaginable structures that can be synthesized.

1.5.3.1. State-of-the-art: Spiro-OMeTAD.

On the one hand, as it has been explained before, the most used contact for the electrons is a thin layer of mesoporous TiO₂ or a thin layer of fullerene derivatives¹¹². On the other hand, different organic molecules have been used as contact for holes. To date, **spiro-OMeTAD** has been so far the best molecule to achieve reproducible and highly efficient perovskite solar cells. The chemical structure (Figure 1.15) is based on a bifluorene central core surrounded by four diphenylamine derivatives.

Initially, it was utilized in ss-DSSCs with efficiencies up to 7.2 % when using additives¹¹³. In 2012, Grätzel and Snaith, simultaneously published the first hybrid solar cell.

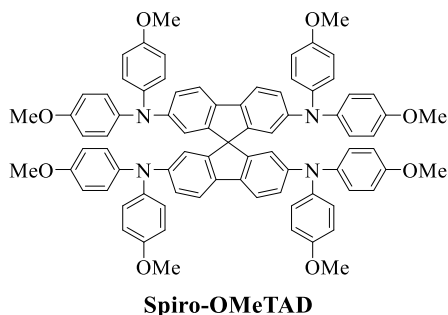


Figure 1.15: Molecular structure of the **spiro-OMeTAD**.

However, its complicated five synthetic steps and the high purity required increase the product cost and hamper the scaling-up of perovskite photovoltaics. Additionally, the use of additives decrease the long-term stability of devices containing it. Therefore, numerous research approaches

Chapter 1

have been made in the molecular design and synthesis route selection to pursue both high efficiency and low cost.

1.5.3.2. *Aryl amine HTMs.*

The choice of known HTMs in organic semiconductors is endless. For example, Xiao, Li and coworkers,¹¹⁴ reported a series of linear π -conjugated HTMs having diaryl and triaryl amino groups and found that, increasing the π -conjugated bridge of these structures led to lower hole mobility (measured using spacecharge-limited current method (SCLC)) and poorer performance, and although they have similar oxidation potentials as **spiro-OMeTAD**, only the HTM **2TPA-2DP** (Figure 1.16) had an efficiency close to that of the **spiro-OMeTAD**-based device used for comparison.

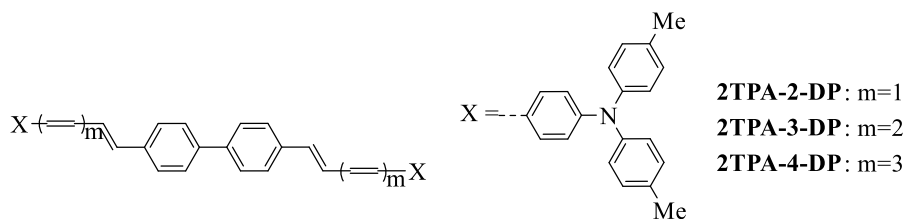


Figure 1.16. Linear π -conjugated HTMs developed by Li and co-workers.

The HTM **EDOT-OMeTPA** (Figure 1.17) can be efficiently synthesized by formation of two C=N bonds through condensation of the corresponding bisaldehyde with *N*¹,*N*¹-bis(4-methoxyphenyl)benzene-1,4-diamine¹¹⁵. **EDOT-OMeTPA** was designed to increase the glass transition temperature (T_g) thus increasing the device stability, and lower the LUMO energy level in order to, a priori, improve the energy band alignment compared to the HTM **H101** reported beforehand by Mhaisalkar, Grimsdale and co-workers¹¹⁶. **H101** (Figure 1.17), was among the very first “linear” HTMs that could match **spiro-OMeTAD**. Solar cell efficiencies as high as 13% at 1 sun were reported. However, both **H101** and **spiro-OMeTAD** were doped. Later, the(2,3-

dihydrothieno[3,4-*b*][1,4]dioxine-5,7-diyl)dimethanimine (EDOT) central core in **EDOT-OMeTPA** was substituted by a furan (**F101**)¹¹⁷, thiophene (**H111**)¹¹⁸, and 2,2'-bithiophene (**H112**) cores¹¹⁸, with almost identical result regarding solar cell performance.

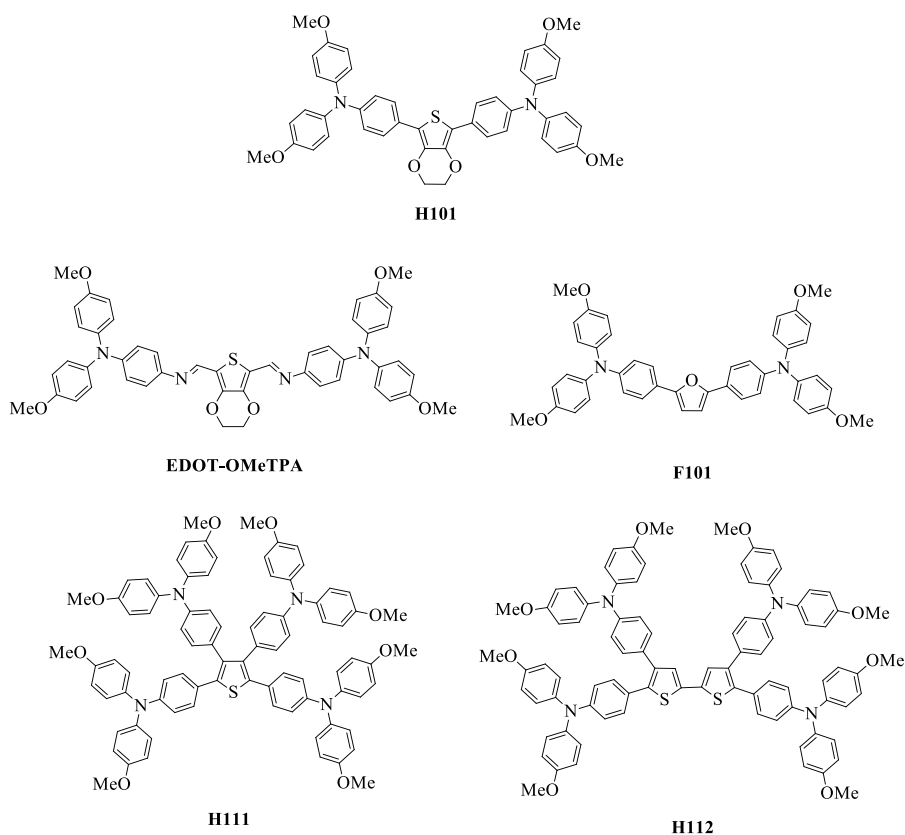


Figure 1.17. The **H101** hole transport material and analogues.

Other authors focused their studies in the use of “linear” HTMs bearing 4-(bis(4-substituted-aryl)amino)phenyl groups, on the effect of the redox potential differences, having in mind the possible differences in the HOMO energy alignment with the perovskite-like material’s VB (valence band). For instance, using HTMs that contain a buta-1,3-diyne core (see **MeO-DATPA** and **Me₂N-DATPA** in Figure 1.18), Snaith, Robertson and coworkers¹¹⁹ could control a wide range of oxidation potentials above and below the redox value

Chapter 1

measured for **spiro-OMeTAD**. The devices show differences in open circuit voltage (V_{oc}) but because of the lower hole mobility values (measured using SCLC) compared to **spiro-OMeTAD**, it is still difficult to draw a conclusion. Seok and co-workers¹²⁰ prepared HTM materials having pyrene diarylamine motifs (see structures **Py-A**, **Py-B** and **Py-C** in Figure 1.18). Again, no trend between the redox potentials for the HTMs and the V_{oc} of the solar cells was observed. 12.4 % of efficiency was obtained for the derivative **Py-C**.

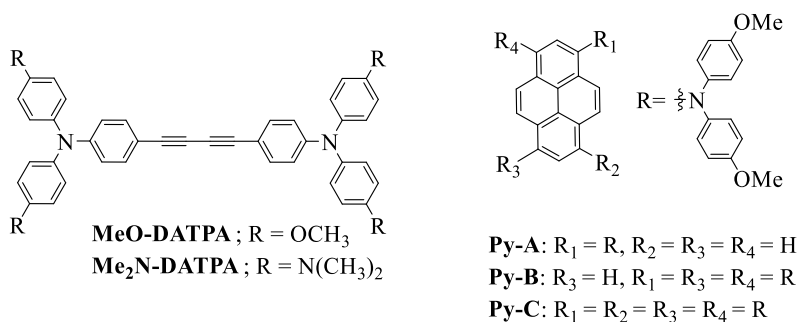


Figure 1.18. Different families of HTMs with bearing diaryl- and triarylamine moieties.

Synthetic strategies to “mimic” the spiro motif have also been studied. Grimsdale, Mhaisalkar, and co-workers used a decorated triptycene core to synthesize HTMs with good thermal stability and appropriated redox properties (structures **T101**, **T102** and **T103** in Figure 1.19)¹²¹. Nevertheless, despite that the fact that the V_{oc} matched the values measured for **spiro-OMeTAD** devices, the overall efficiencies (8.42 %, 12.24 % and 12.38 % respectively) were lower, mainly due to the lower photocurrent¹²¹. Other examples also show lower performances than **spiro-OMeTAD**¹²²⁻¹²³, with the exception of the HTMs developed by Chi, Chen, and co-workers¹²⁴ (structures **CW3**, **CW4** and **CW5** in Figure 1.19), which show a champion efficiency of 16.56 % for **CW4**. The use of triphenylamine-based HTMs without the use of dopants has also been explored by Yi et al.¹²⁵ (structure **Z1011** in Figure 1.19). Interestingly, the use

of chemical dopants had a negative effect on the performance of **Z1011** in perovskite solar cells, decreasing the long-term stability of these cells.

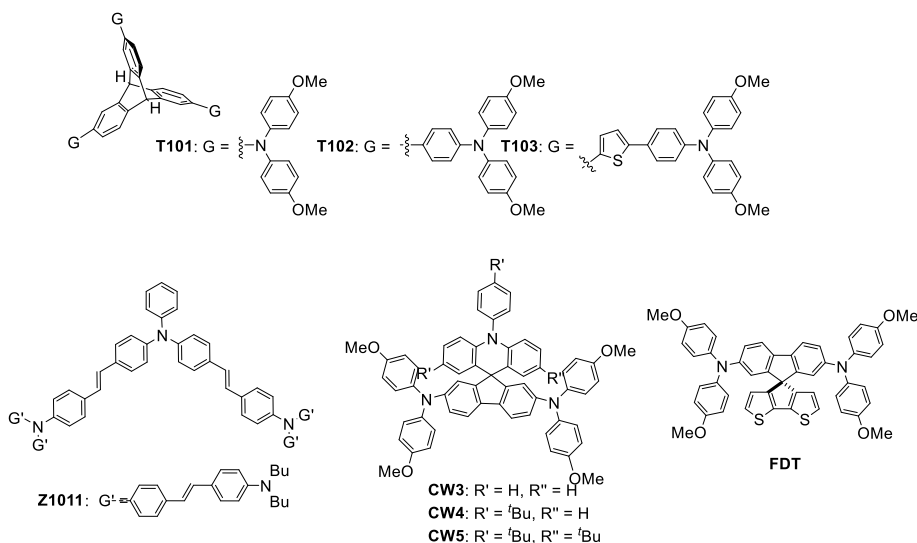


Figure 1.19. Some examples of HTMs bearing triarylamine moieties and different central cores.

Last but not least, the best efficiencies reported with arylamine containing HTM has been reported with the **FDT** molecule (Figure 1.19). The molecule design consists in the introduction of a [2,2'-bithiophene]-3,3'-diyl fragment/motif in the central spiro core with the rationale that the sulfur atoms of the bithiophene group will interact with the iodine present in the perovskite material and favor the hole transfer process. Moreover, the aforementioned fragment does not changes the HOMO energy level (-5.16 eV) with respect to the reference **spiro-OMeTAD** (-5.14 eV) noticeably. Using chemical dopants the efficiency reported Nazeeruddin et al.¹²⁶, is as high as 20.2 % for materials processed from toluene instead of chlorobenzene.

1.5.3.3. Small organic molecules as HTMs without arylamine substituents.

It was also of interest to use carbazole units as HTMs. For instance, Wang, Wu and collaborators demonstrated an easy and straightforward synthesis of **R01**

Chapter 1

(Figure 1.20)²⁸. This molecule displayed excellent hole mobility ($2.05 \times 10^{-4} \text{ cm}^2 \text{ V}^{-1} \text{ s}^{-1}$) and an oxidation potential similar to that of **spiro-OMeTAD**. The solar cells efficiencies were quite similar (about 12% at 1 sun) but, as an advantage, less dopant was needed per mol of **R01**¹²⁷.

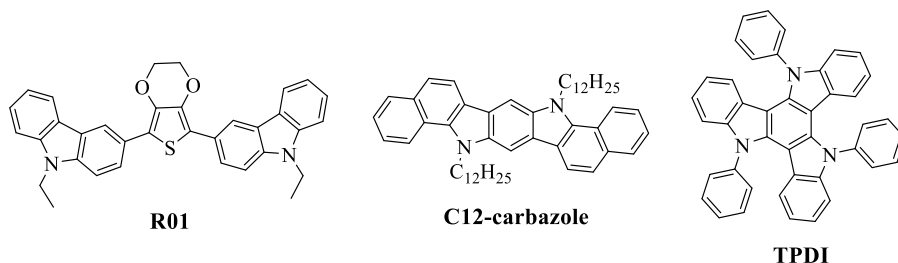


Figure 1.20. Carbazole-based and **TPDI** HTMs for efficient perovskite solar cells.

Fused carbazoles such as the **C12-carbazole** have also been tested¹²⁸. Devices using this HTM also displayed better efficiencies than those from **spiro-OMeTAD** due to better fill factor parameter. The V_{oc} was lower despite having lower lying energy for the HOMO orbital and it had good thermal stability. The conjugated compound **TPDI** (Figure 1.20) led to higher device efficiencies than those for **spiro-OMeTAD** although, when doped, both HTMs had alike efficiency at 1 sun conditions¹²⁹. Undoped **TPDI** showed good stability for days under ambient conditions. The cathode used was a carbon electrode, which does not need of high vacuum deposition and further reduces the cost of the solar cell.

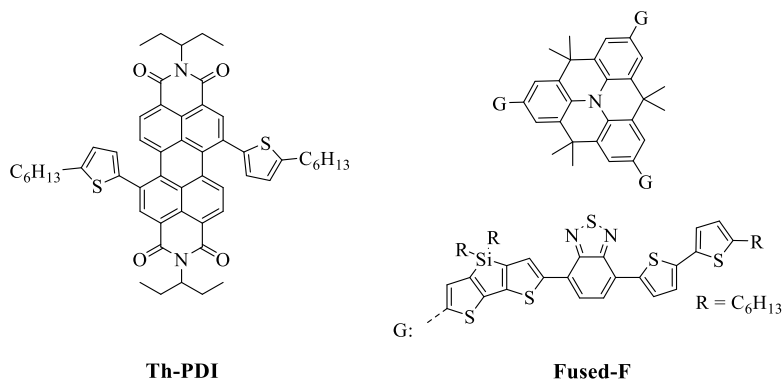


Figure 1.21. Examples of thiophene containing small semiconductor organic molecules.

More complex molecular architectures as HTMs have been synthesized. For example, the perylenediimide-based HTM **Th-PDI** (Figure 1.21) reached a V_{oc} of 1.23 V with a perovskite with larger band-gap as the MAPbBr_3 (bandgap of 2.3 eV) with almost no hysteresis on their J-V curve¹³⁰. Furthermore, a fused hexacyclic heterocyclic core (structure **Fused-F** in Figure 1.20) achieved also very high V_{oc} , (> 1 V) with a similar efficiency compared to **spiro-OMeTAD** (12.8 % and 11.7 % respectively) and using a perovskite, FAPbI_3 , with a narrower bandgap (1.6 eV) than the above mentioned¹³¹.

Nazeeruddin, Ahmad and co-workers¹³²⁻¹³³ developed interesting HTMs with heptacyclic heteroaromatic cores, (**KR122**, **KR131**, **KR145**, **KR133** and **HPDI** in Figure 1.22) and demonstrated that in the case of **KR131** that the efficiencies matched the values reported for **spiro-OMeTAD** (18.3 % and 17.9 % respectively). The key novelties in the use of a heptacyclic heteroaromatic core were the introduction of electron-rich methoxy substituents and the development of an efficient four-step synthesis.

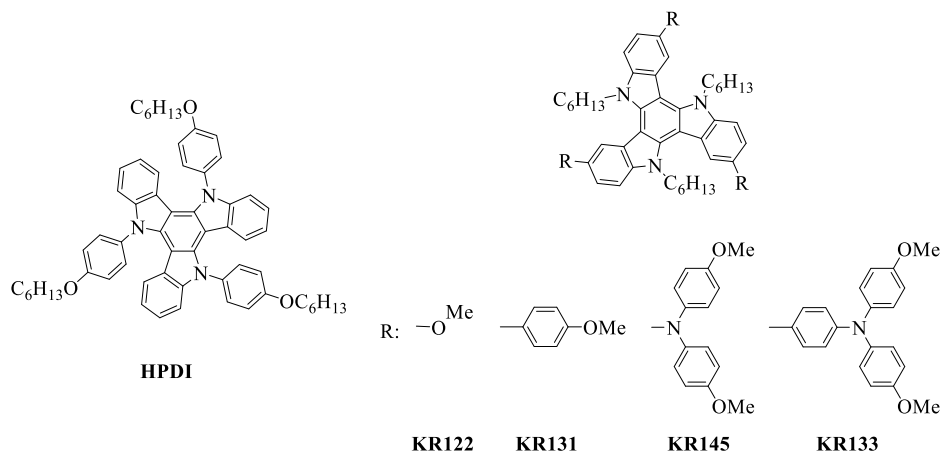


Figure 1.22. Examples of HTMs with conjugated (hetero)aromatic cores.

1.5.3.4. Porphyrins and Phthalocyanines as HTM.

Porphyrins and phthalocyanines have also been designed, synthesized and processed from solution as HTMs. Recently, porphyrins have played a major role in organic photovoltaics (OPV) as HTMs with very low energy losses that can be compared to the best perovskite solar cell¹³⁴.

Chen, Yeh and co-workers reported efficiencies of 16.6 % when using porphyrins with two 2-(4-(*N,N*-dialkylamino)phenyl)ethynyl substituents at two *meso* positions (structure **Y2** in Figure 1.23)¹³⁵.

More recently symmetrically substituted zinc porphyrin **ZnP** (Figure 1.23) with four diarylamino phenyl groups at the *meso* positions achieved values close to 18 % at 1sun¹³⁶. Interestingly its copper(II) analogue (**CuP**; Figure 1.23) also performed very well as HTM. As pointed in their work, Hua, Wong, Zhu et al. assigned the lower V_{oc} observed for **CuP** to an increase of the carrier recombination¹³⁶.

In the case of phthalocyanines, more research has been carried out when compared to their porphyrin counterparts. We will focus herein only on those

examples that use solution processed phthalocyanines. Nonetheless, we acknowledge the fact that high vacuum assisted deposition for phthalocyanines has been also reported¹³⁷⁻¹⁴⁰.

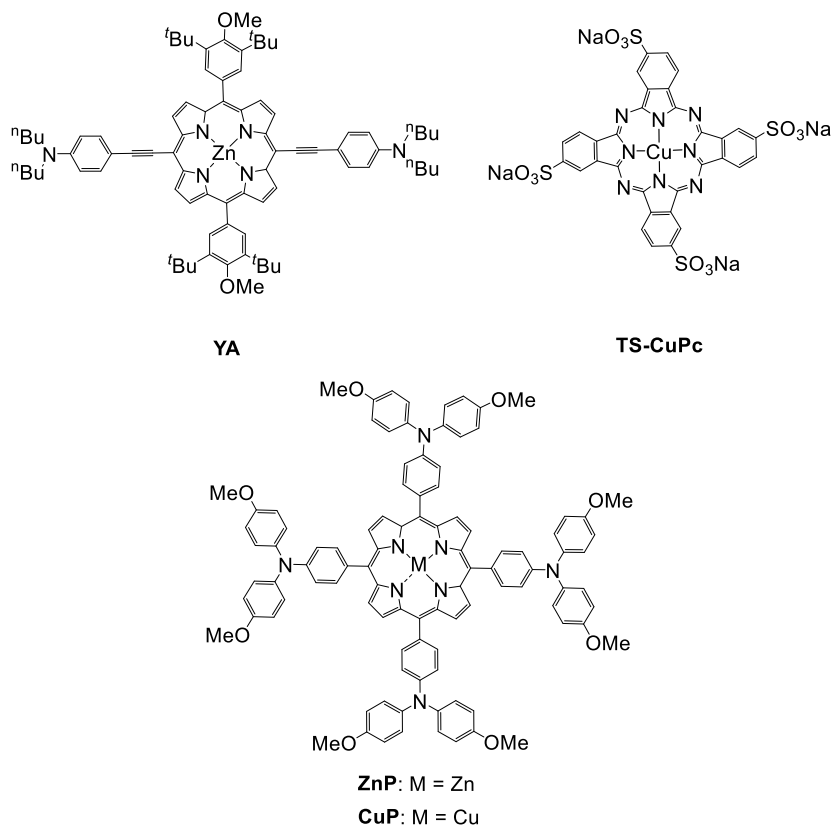


Figure 1.23. Porphyrins employed as HTMs in PSCs.

Phthalocyanines containing Cu, Ni and Fe as metal centers have been recently developed¹⁴¹. Copper phthalocyanine **TS-CuPc** (Figure 1.23) has been used as a co-HTM with PEDOT:PSS¹⁴². The efficiency achieved was 17.29 % at 1sun. According to the authors, the co-HTM leads to better perovskite crystal growth onto the HTM and faster carrier mobility. Moreover, the use of this phthalocyanine leads to lower acidity on the PEDOT:PSS and, thus, increases the device stability¹⁴².

1.6. References.

1. Becquerél, A. E., Memoire sur les Effects d'Electriques Produits Sous l'Influence des Rayons Solarires. *Comptes Rendus de l'Academie des Sciences* **1839**, *9*, 561 - 567.
2. Perlin, J., *Optical Science Engineering* **2005**, *99*, 3.
3. Green, M. A., Third generation photovoltaics: solar cells for 2020 and beyond. *Physica E: Low-dimensional Systems and Nanostructures* **2002**, *14* (1), 65-70.
4. O'Regan, B.; Grätzel, M., A low-cost, high-efficiency solar cell based on dye-sensitized colloidal TiO₂ films. *Nature* **1991**, *353* (6346), 737-740.
5. Clarke, T. M.; Durrant, J. R., Charge Photogeneration in Organic Solar Cells. *Chemical Reviews* **2010**, *110* (11), 6736-6767.
6. Ameri, T.; Dennler, G.; Lungenschmied, C.; Brabec, C. J., Organic tandem solar cells: A review. *Energy & Environmental Science* **2009**, *2* (4), 347-363.
7. Ratcliff, E. L.; Zacher, B.; Armstrong, N. R., Selective Interlayers and Contacts in Organic Photovoltaic Cells. *The Journal of Physical Chemistry Letters* **2011**, *2* (11), 1337-1350.
8. Yuan, J.; Gu, J.; Shi, G.; Sun, J.; Wang, H.-Q.; Ma, W., High efficiency all-polymer tandem solar cells. *Scientific Reports* **2016**, *6*, 26459.
9. Glenis, S.; Horowitz, G.; Tourillon, G.; Garnier, F., Electrochemically grown polythiophene and poly(3-methylthiophene) organic photovoltaic cells. *Thin Solid Films* **1984**, *111* (2), 93-103.
10. Sariciftci, N. S.; Smilowitz, L.; Heeger, A. J.; Wudl, F., Photoinduced Electron Transfer from a Conducting Polymer to Buckminsterfullerene. *Science* **1992**, *258* (5087), 1474.
11. Huang, H.; Yang, L.; Sharma, B., Recent advances in organic ternary solar cells. *Journal of Materials Chemistry A* **2017**, *5* (23), 11501-11517.
12. Destruel, P.; Bock, H.; Séguy, I.; Jolinat, P.; Oukachmih, M.; Bedel-Pereira, E., Influence of indium tin oxide treatment using UV–ozone and argon

plasma on the photovoltaic parameters of devices based on organic discotic materials. *Polymer International* **2006**, *55* (6), 601-607.

13. Hains, A. W.; Liang, Z.; Woodhouse, M. A.; Gregg, B. A., Molecular Semiconductors in Organic Photovoltaic Cells. *Chemical Reviews* **2010**, *110* (11), 6689-6735.

14. Huang, J.; Miller, P. F.; Wilson, J. S.; de Mello, A. J.; de Mello, J. C.; Bradley, D. D. C., Investigation of the Effects of Doping and Post-Deposition Treatments on the Conductivity, Morphology, and Work Function of Poly(3,4-ethylenedioxythiophene)/Poly(styrene sulfonate) Films. *Advanced Functional Materials* **2005**, *15* (2), 290-296.

15. Hu, Z.; Zhang, J.; Zhu, Y., Effects of solvent-treated PEDOT:PSS on organic photovoltaic devices. *Renewable Energy* **2014**, *62*, 100-105.

16. Huang, C.-J.; Chen, K.-L.; Tsao, Y.-J.; Chou, D.-W.; Chen, W.-R.; Meen, T.-H., Study of solvent-doped PEDOT: PSS layer on small molecule organic solar cells. *Synthetic Metals* **2013**, *164*, 38-41.

17. Lee, J. H.; Yoon, S.; Ko, M. S.; Lee, N.; Hwang, I.; Lee, M. J., Improved performance of organic photovoltaic devices by doping F4TCNQ onto solution-processed graphene as a hole transport layer. *Organic Electronics* **2016**, *30*, 302-311.

18. Zhang, W.; Lan, W.; Lee, M. H.; Singh, J.; Zhu, F., A versatile solution-processed MoO₃/Au nanoparticles/MoO₃ hole contact for high performing PEDOT:PSS-free organic solar cells. *Organic Electronics* **2018**, *52*, 1-6.

19. He, Z.; Zhong, C.; Huang, X.; Wong, W.-Y.; Wu, H.; Chen, L.; Su, S.; Cao, Y., Simultaneous Enhancement of Open-Circuit Voltage, Short-Circuit Current Density, and Fill Factor in Polymer Solar Cells. *Advanced Materials* **2011**, *23* (40), 4636-4643.

20. Nelson, J., Organic photovoltaic films. *Current Opinion in Solid State and Materials Science* **2002**, *6* (1), 87-95.

21. Tang, C. W., Two-layer organic photovoltaic cell. *Applied Physics Letters* **1986**, *48* (2), 183-185.

Chapter 1

22. Yoshino, K.; Tada, K.; Fujii, A.; Conwell, E. M.; Zakhidov, A. A., Novel photovoltaic devices based on donor-acceptor molecular and conducting polymer systems. *IEEE Transactions on Electron Devices* **1997**, *44* (8), 1315-1324.
23. Gasparini, N.; Salleo, A.; McCulloch, I.; Baran, D., The role of the third component in ternary organic solar cells. *Nature Reviews Materials* **2019**, *4* (4), 229-242.
24. Mishra, A.; Bäuerle, P., Small Molecule Organic Semiconductors on the Move: Promises for Future Solar Energy Technology. *Angewandte Chemie International Edition* **2012**, *51* (9), 2020-2067.
25. Sun, H.; Chen, F.; Chen, Z.-K., Recent progress on non-fullerene acceptors for organic photovoltaics. *Materials Today* **2019**, *24*, 94-118.
26. Gasparini, N.; Wadsworth, A.; Moser, M.; Baran, D.; McCulloch, I.; Brabec, C. J., The Physics of Small Molecule Acceptors for Efficient and Stable Bulk Heterojunction Solar Cells. *Advanced Energy Materials* **2018**, *8* (12), 1703298.
27. Zhao, W.; Li, S.; Yao, H.; Zhang, S.; Zhang, Y.; Yang, B.; Hou, J., Molecular Optimization Enables over 13% Efficiency in Organic Solar Cells. *Journal of the American Chemical Society* **2017**, *139* (21), 7148-7151.
28. Meng, D.; Fu, H.; Xiao, C.; Meng, X.; Winands, T.; Ma, W.; Wei, W.; Fan, B.; Huo, L.; Doltsinis, N. L.; Li, Y.; Sun, Y.; Wang, Z., Three-Bladed Rylene Propellers with Three-Dimensional Network Assembly for Organic Electronics. *Journal of the American Chemical Society* **2016**, *138* (32), 10184-10190.
29. Collins, S. D.; Proctor, C. M.; Ran, N. A.; Nguyen, T.-Q., Understanding Open-Circuit Voltage Loss through the Density of States in Organic Bulk Heterojunction Solar Cells. *Advanced Energy Materials* **2016**, *6* (4), 1501721.
30. Dibb, G. F. A.; Jamieson, F. C.; Maurano, A.; Nelson, J.; Durrant, J. R., Limits on the Fill Factor in Organic Photovoltaics: Distinguishing

Nongeminate and Geminate Recombination Mechanisms. *The Journal of Physical Chemistry Letters* **2013**, *4* (5), 803-808.

31. Bartesaghi, D.; Pérez, I. d. C.; Kniepert, J.; Roland, S.; Turbiez, M.; Neher, D.; Koster, L. J. A., Competition between recombination and extraction of free charges determines the fill factor of organic solar cells. *Nature Communications* **2015**, *6*, 7083.

32. Kyaw, A. K. K.; Wang, D. H.; Gupta, V.; Leong, W. L.; Ke, L.; Bazan, G. C.; Heeger, A. J., Intensity Dependence of Current–Voltage Characteristics and Recombination in High-Efficiency Solution-Processed Small-Molecule Solar Cells. *ACS Nano* **2013**, *7* (5), 4569-4577.

33. Kniepert, J.; Lange, I.; van der Kaap, N. J.; Koster, L. J. A.; Neher, D., A Conclusive View on Charge Generation, Recombination, and Extraction in As-Prepared and Annealed P3HT:PCBM Blends: Combined Experimental and Simulation Work. *Advanced Energy Materials* **2014**, *4* (7), 1301401.

34. Cowan, S. R.; Banerji, N.; Leong, W. L.; Heeger, A. J., Charge Formation, Recombination, and Sweep-Out Dynamics in Organic Solar Cells. *Advanced Functional Materials* **2012**, *22* (6), 1116-1128.

35. Ji, Z.; Xu, X.; Zhang, G.; Li, Y.; Peng, Q., Synergistic effect of halogenation on molecular energy level and photovoltaic performance modulations of highly efficient small molecular materials. *Nano Energy* **2017**, *40*, 214-223.

36. Padinger, F.; Rittberger, R. S.; Sariciftci, N. S., Effects of Postproduction Treatment on Plastic Solar Cells. *Advanced Functional Materials* **2003**, *13* (1), 85-88.

37. Li, G.; Shrotriya, V.; Huang, J.; Yao, Y.; Moriarty, T.; Emery, K.; Yang, Y., High-efficiency solution processable polymer photovoltaic cells by self-organization of polymer blends. *Nature Materials* **2005**, *4* (11), 864-868.

38. Liang, Y.; Xu, Z.; Xia, J.; Tsai, S.-T.; Wu, Y.; Li, G.; Ray, C.; Yu, L., For the Bright Future—Bulk Heterojunction Polymer Solar Cells with Power Conversion Efficiency of 7.4%. *Advanced Materials* **2010**, *22* (20), E135-E138.

Chapter 1

39. Dai, S.; Chandrabose, S.; Xin, J.; Li, T.; Chen, K.; Xue, P.; Liu, K.; Zhou, K.; Ma, W.; Hodgkiss, J. M.; Zhan, X., High-performance organic solar cells based on polymer donor/small molecule donor/nonfullerene acceptor ternary blends. *Journal of Materials Chemistry A* **2019**, *7* (5), 2268-2274.
40. Collins, S. D.; Ran, N. A.; Heiber, M. C.; Nguyen, T.-Q., Small is Powerful: Recent Progress in Solution-Processed Small Molecule Solar Cells. *Advanced Energy Materials* **2017**, *7* (10), 1602242.
41. Yang, L.; Zhang, S.; He, C.; Zhang, J.; Yao, H.; Yang, Y.; Zhang, Y.; Zhao, W.; Hou, J., New Wide Band Gap Donor for Efficient Fullerene-Free All-Small-Molecule Organic Solar Cells. *Journal of the American Chemical Society* **2017**, *139* (5), 1958-1966.
42. Deng, D.; Zhang, Y.; Zhang, J.; Wang, Z.; Zhu, L.; Fang, J.; Xia, B.; Wang, Z.; Lu, K.; Ma, W.; Wei, Z., Fluorination-enabled optimal morphology leads to over 11% efficiency for inverted small-molecule organic solar cells. *Nature Communications* **2016**, *7*, 13740.
43. Roncali, J.; Frère, P.; Blanchard, P.; de Bettignies, R.; Turbiez, M.; Roquet, S.; Leriche, P.; Nicolas, Y., Molecular and supramolecular engineering of π -conjugated systems for photovoltaic conversion. *Thin Solid Films* **2006**, *511-512*, 567-575.
44. Kesters, J.; Verstappen, P.; Kelchtermans, M.; Lutsen, L.; Vanderzande, D.; Maes, W., Porphyrin-Based Bulk Heterojunction Organic Photovoltaics: The Rise of the Colors of Life. *Advanced Energy Materials* **2015**, *5* (13), 1500218.
45. Xiao, L.; Chen, S.; Gao, K.; Peng, X.; Liu, F.; Cao, Y.; Wong, W.-Y.; Wong, W.-K.; Zhu, X., New Terthiophene-Conjugated Porphyrin Donors for Highly Efficient Organic Solar Cells. *ACS Applied Materials & Interfaces* **2016**, *8* (44), 30176-30183.
46. Walker, B.; Tamayo, A. B.; Dang, X.-D.; Zalar, P.; Seo, J. H.; Garcia, A.; Tantiwiwat, M.; Nguyen, T.-Q., Nanoscale Phase Separation and High Photovoltaic Efficiency in Solution-Processed, Small-Molecule Bulk

Heterojunction Solar Cells. *Advanced Functional Materials* **2009**, *19* (19), 3063-3069.

47. Zhang, Q.; Kan, B.; Liu, F.; Long, G.; Wan, X.; Chen, X.; Zuo, Y.; Ni, W.; Zhang, H.; Li, M.; Hu, Z.; Huang, F.; Cao, Y.; Liang, Z.; Zhang, M.; Russell, T. P.; Chen, Y., Small-molecule solar cells with efficiency over 9%. *Nature Photonics* **2014**, *9*, 35.

48. Peng, J.; Chen, Y.; Wu, X.; Zhang, Q.; Kan, B.; Chen, X.; Chen, Y.; Huang, J.; Liang, Z., Correlating Molecular Structures with Transport Dynamics in High-Efficiency Small-Molecule Organic Photovoltaics. *ACS Applied Materials & Interfaces* **2015**, *7* (24), 13137-13141.

49. Wang, J.-L.; Yin, Q.-R.; Miao, J.-S.; Wu, Z.; Chang, Z.-F.; Cao, Y.; Zhang, R.-B.; Wang, J.-Y.; Wu, H.-B.; Cao, Y., Rational Design of Small Molecular Donor for Solution-Processed Organic Photovoltaics with 8.1% Efficiency and High Fill Factor via Multiple Fluorine Substituents and Thiophene Bridge. *Advanced Functional Materials* **2015**, *25* (23), 3514-3523.

50. Cui, C.; Guo, X.; Min, J.; Guo, B.; Cheng, X.; Zhang, M.; Brabec, C. J.; Li, Y., High-Performance Organic Solar Cells Based on a Small Molecule with Alkylthio-Thienyl-Conjugated Side Chains without Extra Treatments. *Advanced Materials* **2015**, *27* (45), 7469-7475.

51. Yang, D.; Jiao, Y.; Yang, L.; Chen, Y.; Mizoi, S.; Huang, Y.; Pu, X.; Lu, Z.; Sasabe, H.; Kido, J., Cyano-substitution on the end-capping group: facile access toward asymmetrical squaraine showing strong dipole-dipole interactions as a high performance small molecular organic solar cells material. *Journal of Materials Chemistry A* **2015**, *3* (34), 17704-17712.

52. Yoo, S.; Domercq, B.; Kippelen, B., Efficient thin-film organic solar cells based on pentacene/C60 heterojunctions. *Applied Physics Letters* **2004**, *85* (22), 5427-5429.

53. Sebastian, M. T., CHAPTER SIX - ABO₃ TYPE PEROVSKITES. In *Dielectric Materials for Wireless Communication*, Sebastian, M. T., Ed. Elsevier: Amsterdam, 2008; pp 161-203.

Chapter 1

54. Kazim, S.; Nazeeruddin, M. K.; Grätzel, M.; Ahmad, S., Perovskite as Light Harvester: A Game Changer in Photovoltaics. *Angewandte Chemie International Edition* **2014**, *53* (11), 2812-2824.
55. Kagan, C. R.; Mitzi, D. B.; Dimitrakopoulos, C. D., Organic-Inorganic Hybrid Materials as Semiconducting Channels in Thin-Film Field-Effect Transistors. *Science* **1999**, *286* (5441), 945.
56. Chondroudis, K.; Mitzi, D. B., Electroluminescence from an Organic-Inorganic Perovskite Incorporating a Quaterthiophene Dye within Lead Halide Perovskite Layers. *Chemistry of Materials* **1999**, *11* (11), 3028-3030.
57. Noh, J. H.; Im, S. H.; Heo, J. H.; Mandal, T. N.; Seok, S. I., Chemical Management for Colorful, Efficient, and Stable Inorganic-Organic Hybrid Nanostructured Solar Cells. *Nano Letters* **2013**, *13* (4), 1764-1769.
58. Travis, W.; Glover, E. N. K.; Bronstein, H.; Scanlon, D. O.; Palgrave, R. G., On the application of the tolerance factor to inorganic and hybrid halide perovskites: a revised system. *Chemical Science* **2016**, *7* (7), 4548-4556.
59. Stoumpos, C. C.; Kanatzidis, M. G., The Renaissance of Halide Perovskites and Their Evolution as Emerging Semiconductors. *Accounts of Chemical Research* **2015**, *48* (10), 2791-2802.
60. Mitzi, D. B.
61. Kojima, A.; Teshima, K.; Shirai, Y.; Miyasaka, T., Organometal Halide Perovskites as Visible-Light Sensitizers for Photovoltaic Cells. *Journal of the American Chemical Society* **2009**, *131* (17), 6050-6051.
62. Baikie, T.; Fang, Y.; Kadro, J. M.; Schreyer, M.; Wei, F.; Mhaisalkar, S. G.; Graetzel, M.; White, T. J., Synthesis and crystal chemistry of the hybrid perovskite (CH₃NH₃)PbI₃ for solid-state sensitised solar cell applications. *Journal of Materials Chemistry A* **2013**, *1* (18), 5628-5641.
63. Im, J.-H.; Lee, C.-R.; Lee, J.-W.; Park, S.-W.; Park, N.-G., 6.5% efficient perovskite quantum-dot-sensitized solar cell. *Nanoscale* **2011**, *3* (10), 4088-4093.

64. Im, J.-H.; Chung, J.; Kim, S.-J.; Park, N.-G., Synthesis, structure, and photovoltaic property of a nanocrystalline 2H perovskite-type novel sensitizer (CH₃CH₂NH₃)PbI₃. *Nanoscale Research Letters* **2012**, 7 (1), 353.
65. Kim, H.-S.; Lee, C.-R.; Im, J.-H.; Lee, K.-B.; Moehl, T.; Marchioro, A.; Moon, S.-J.; Humphry-Baker, R.; Yum, J.-H.; Moser, J. E.; Grätzel, M.; Park, N.-G., Lead Iodide Perovskite Sensitized All-Solid-State Submicron Thin Film Mesoscopic Solar Cell with Efficiency Exceeding 9%. *Scientific Reports* **2012**, 2, 591.
66. Jeon, N. J.; Na, H.; Jung, E. H.; Yang, T.-Y.; Lee, Y. G.; Kim, G.; Shin, H.-W.; Il Seok, S.; Lee, J.; Seo, J., A fluorene-terminated hole-transporting material for highly efficient and stable perovskite solar cells. *Nature Energy* **2018**, 3 (8), 682-689.
67. Assadi, M. K.; Bakhoda, S.; Saidur, R.; Hanaei, H., Recent progress in perovskite solar cells. *Renewable and Sustainable Energy Reviews* **2018**, 81, 2812-2822.
68. Liu, Y.; Yang, Z.; Cui, D.; Ren, X.; Sun, J.; Liu, X.; Zhang, J.; Wei, Q.; Fan, H.; Yu, F.; Zhang, X.; Zhao, C.; Liu, S., Two-Inch-Sized Perovskite CH₃NH₃PbX₃ (X = Cl, Br, I) Crystals: Growth and Characterization. *Advanced Materials* **2015**, 27 (35), 5176-5183.
69. Eperon, G. E.; Stranks, S. D.; Menelaou, C.; Johnston, M. B.; Herz, L. M.; Snaith, H. J., Formamidinium lead trihalide: a broadly tunable perovskite for efficient planar heterojunction solar cells. *Energy & Environmental Science* **2014**, 7 (3), 982-988.
70. Jacobsson, T. J.; Pazoki, M.; Hagfeldt, A.; Edvinsson, T., Goldschmidt's Rules and Strontium Replacement in Lead Halogen Perovskite Solar Cells: Theory and Preliminary Experiments on CH₃NH₃SrI₃. *The Journal of Physical Chemistry C* **2015**, 119 (46), 25673-25683.
71. Giustino, F.; Snaith, H. J., Toward Lead-Free Perovskite Solar Cells. *ACS Energy Letters* **2016**, 1 (6), 1233-1240.

Chapter 1

72. Yin, W.-J.; Shi, T.; Yan, Y., Unique Properties of Halide Perovskites as Possible Origins of the Superior Solar Cell Performance. *Advanced Materials* **2014**, *26* (27), 4653-4658.
73. Noel, N. K.; Stranks, S. D.; Abate, A.; Wehrenfennig, C.; Guarnera, S.; Haghighirad, A.-A.; Sadhanala, A.; Eperon, G. E.; Pathak, S. K.; Johnston, M. B.; Petrozza, A.; Herz, L. M.; Snaith, H. J., Lead-free organic–inorganic tin halide perovskites for photovoltaic applications. *Energy & Environmental Science* **2014**, *7* (9), 3061-3068.
74. Hao, F.; Stoumpos, C. C.; Cao, D. H.; Chang, R. P. H.; Kanatzidis, M. G., Lead-free solid-state organic–inorganic halide perovskite solar cells. *Nature Photonics* **2014**, *8*, 489.
75. Lee, J.-W.; Kim, D.-H.; Kim, H.-S.; Seo, S.-W.; Cho, S. M.; Park, N.-G., Formamidinium and Cesium Hybridization for Photo- and Moisture-Stable Perovskite Solar Cell. *Advanced Energy Materials* **2015**, *5* (20), 1501310.
76. Saliba, M.; Matsui, T.; Seo, J.-Y.; Domanski, K.; Correa-Baena, J.-P.; Nazeeruddin, M. K.; Zakeeruddin, S. M.; Tress, W.; Abate, A.; Hagfeldt, A.; Grätzel, M., Cesium-containing triple cation perovskite solar cells: improved stability, reproducibility and high efficiency. *Energy & Environmental Science* **2016**, *9* (6), 1989-1997.
77. Jesper Jacobsson, T.; Correa-Baena, J.-P.; Pazoki, M.; Saliba, M.; Schenk, K.; Grätzel, M.; Hagfeldt, A., Exploration of the compositional space for mixed lead halogen perovskites for high efficiency solar cells. *Energy & Environmental Science* **2016**, *9* (5), 1706-1724.
78. Correa Baena, J. P.; Steier, L.; Tress, W.; Saliba, M.; Neutzner, S.; Matsui, T.; Giordano, F.; Jacobsson, T. J.; Srimath Kandada, A. R.; Zakeeruddin, S. M.; Petrozza, A.; Abate, A.; Nazeeruddin, M. K.; Grätzel, M.; Hagfeldt, A., Highly efficient planar perovskite solar cells through band alignment engineering. *Energy & Environmental Science* **2015**, *8* (10), 2928-2934.
79. Etgar, L.; Gao, P.; Xue, Z.; Peng, Q.; Chandiran, A. K.; Liu, B.; Nazeeruddin, M. K.; Grätzel, M., Mesoscopic CH₃NH₃PbI₃/TiO₂

Heterojunction Solar Cells. *Journal of the American Chemical Society* **2012**, *134* (42), 17396-17399.

80. Wang, F.; Cao, Y.; Chen, C.; Chen, Q.; Wu, X.; Li, X.; Qin, T.; Huang, W., Materials toward the Upscaling of Perovskite Solar Cells: Progress, Challenges, and Strategies. *Advanced Functional Materials* **2018**, *28* (52), 1803753.

81. Xiao, J.; Shi, J.; Li, D.; Meng, Q., Perovskite thin-film solar cell: excitation in photovoltaic science. *Science China Chemistry* **2015**, *58* (2), 221-238.

82. Schulz, P.; Cahen, D.; Kahn, A., Halide Perovskites: Is It All about the Interfaces? *Chemical Reviews* **2019**, *119* (5), 3349-3417.

83. Chiang, C.-H.; Nazeeruddin, M. K.; Grätzel, M.; Wu, C.-G., The synergistic effect of H₂O and DMF towards stable and 20% efficiency inverted perovskite solar cells. *Energy & Environmental Science* **2017**, *10* (3), 808-817.

84. Zhou, X.; Bao, C.; Li, F.; Gao, H.; Yu, T.; Yang, J.; Zhu, W.; Zou, Z., Hole-transport-material-free perovskite solar cells based on nanoporous gold back electrode. *RSC Advances* **2015**, *5* (72), 58543-58548.

85. Liu, D.; Yang, J.; Kelly, T. L., Compact Layer Free Perovskite Solar Cells with 13.5% Efficiency. *Journal of the American Chemical Society* **2014**, *136* (49), 17116-17122.

86. Mahmood, K.; Sarwar, S.; Mehran, M. T., Current status of electron transport layers in perovskite solar cells: materials and properties. *RSC Advances* **2017**, *7* (28), 17044-17062.

87. Yang, G.; Tao, H.; Qin, P.; Ke, W.; Fang, G., Recent progress in electron transport layers for efficient perovskite solar cells. *Journal of Materials Chemistry A* **2016**, *4* (11), 3970-3990.

88. Liu, H.; Huang, Z.; Wei, S.; Zheng, L.; Xiao, L.; Gong, Q., Nano-structured electron transporting materials for perovskite solar cells. *Nanoscale* **2016**, *8* (12), 6209-6221.

Chapter 1

89. Xiong, L.; Guo, Y.; Wen, J.; Liu, H.; Yang, G.; Qin, P.; Fang, G., Review on the Application of SnO₂ in Perovskite Solar Cells. *Advanced Functional Materials* **2018**, 28 (35), 1802757.
90. Malinkiewicz, O.; Yella, A.; Lee, Y. H.; Espallargas, G. M.; Graetzel, M.; Nazeeruddin, M. K.; Bolink, H. J., Perovskite solar cells employing organic charge-transport layers. *Nature Photonics* **2013**, 8, 128.
91. Liu, X.; Li, X.; Zou, Y.; Liu, H.; Wang, L.; Fang, J.; Yang, C., Energy level-modulated non-fullerene small molecule acceptors for improved VOC and efficiency of inverted perovskite solar cells. *Journal of Materials Chemistry A* **2019**, 7 (7), 3336-3343.
92. Gao, W.; Wu, F.; Liu, T.; Zhang, G.; Chen, Z.; Zhong, C.; Zhu, L.; Liu, F.; Yan, H.; Yang, C., Multifunctional asymmetrical molecules for high-performance perovskite and organic solar cells. *Journal of Materials Chemistry A* **2019**, 7 (5), 2412-2420.
93. Chiang, C.-H.; Tseng, Z.-L.; Wu, C.-G., Planar heterojunction perovskite/PC71BM solar cells with enhanced open-circuit voltage via a (2/1)-step spin-coating process. *Journal of Materials Chemistry A* **2014**, 2 (38), 15897-15903.
94. Swetha, T.; Singh, S. P., Perovskite solar cells based on small molecule hole transporting materials. *Journal of Materials Chemistry A* **2015**, 3 (36), 18329-18344.
95. Zhang, J.; Xu, B.; Yang, L.; Ruan, C.; Wang, L.; Liu, P.; Zhang, W.; Vlachopoulos, N.; Kloo, L.; Boschloo, G.; Sun, L.; Hagfeldt, A.; Johansson, E. M. J., The Importance of Pendant Groups on Triphenylamine-Based Hole Transport Materials for Obtaining Perovskite Solar Cells with over 20% Efficiency. *Advanced Energy Materials* **2018**, 8 (2), 1701209.
96. Juarez-Perez, E. J.; Leyden, M. R.; Wang, S.; Ono, L. K.; Hawash, Z.; Qi, Y., Role of the Dopants on the Morphological and Transport Properties of Spiro-MeOTAD Hole Transport Layer. *Chemistry of Materials* **2016**, 28 (16), 5702-5709.

97. Shao, Y.; Yuan, Y.; Huang, J., Correlation of energy disorder and open-circuit voltage in hybrid perovskite solar cells. *Nature Energy* **2016**, *1*, 15001.
98. Urieta-Mora, J.; García-Benito, I.; Molina-Ontoria, A.; Martín, N., Hole transporting materials for perovskite solar cells: a chemical approach. *Chemical Society Reviews* **2018**, *47* (23), 8541-8571.
99. Hashmi, S. G.; Martineau, D.; Dar, M. I.; Myllymäki, T. T. T.; Sarikka, T.; Ulla, V.; Zakeeruddin, S. M.; Grätzel, M., High performance carbon-based printed perovskite solar cells with humidity assisted thermal treatment. *Journal of Materials Chemistry A* **2017**, *5* (24), 12060-12067.
100. Behrouznejad, F.; Tsai, C.-M.; Narra, S.; Diao, E. W. G.; Taghavinia, N., Interfacial Investigation on Printable Carbon-Based Mesoscopic Perovskite Solar Cells with NiO_x/C Back Electrode. *ACS Applied Materials & Interfaces* **2017**, *9* (30), 25204-25215.
101. Krishna, A.; Grimsdale, A. C., Hole transporting materials for mesoscopic perovskite solar cells – towards a rational design? *Journal of Materials Chemistry A* **2017**, *5* (32), 16446-16466.
102. Liu, D.; Wang, Y.; Zheng, H.; Wu, J.; Ji, L.; Zhang, P.; Ahmad, W.; Chen, H.; Chen, Z.; Li, S., Improved stability of perovskite solar cells with enhanced moisture-resistant hole transport layers. *Electrochimica Acta* **2019**, *296*, 508-516.
103. Christians, J. A.; Fung, R. C. M.; Kamat, P. V., An Inorganic Hole Conductor for Organo-Lead Halide Perovskite Solar Cells. Improved Hole Conductivity with Copper Iodide. *Journal of the American Chemical Society* **2014**, *136* (2), 758-764.
104. Nejand, B. A.; Ahmadi, V.; Gharibzadeh, S.; Shahverdi, H. R., Cuprous Oxide as a Potential Low-Cost Hole-Transport Material for Stable Perovskite Solar Cells. *ChemSusChem* **2016**, *9* (3), 302-313.
105. Wang, K.-C.; Shen, P.-S.; Li, M.-H.; Chen, S.; Lin, M.-W.; Chen, P.; Guo, T.-F., Low-Temperature Sputtered Nickel Oxide Compact Thin Film as Effective Electron Blocking Layer for Mesoscopic NiO/CH₃NH₃PbI₃

Chapter 1

Perovskite Heterojunction Solar Cells. *ACS Applied Materials & Interfaces* **2014**, *6* (15), 11851-11858.

106. Chen, W.; Wu, Y.; Yue, Y.; Liu, J.; Zhang, W.; Yang, X.; Chen, H.; Bi, E.; Ashraful, I.; Grätzel, M.; Han, L., Efficient and stable large-area perovskite solar cells with inorganic charge extraction layers. *Science* **2015**, *350* (6263), 944.

107. Jung, M.; Kim, Y. C.; Jeon, N. J.; Yang, W. S.; Seo, J.; Noh, J. H.; Il Seok, S., Thermal Stability of CuSCN Hole Conductor-Based Perovskite Solar Cells. *ChemSusChem* **2016**, *9* (18), 2592-2596.

108. Grimsdale, A. C.; Leok Chan, K.; Martin, R. E.; Jokisz, P. G.; Holmes, A. B., Synthesis of Light-Emitting Conjugated Polymers for Applications in Electroluminescent Devices. *Chemical Reviews* **2009**, *109* (3), 897-1091.

109. Cheng, Y.-J.; Yang, S.-H.; Hsu, C.-S., Synthesis of Conjugated Polymers for Organic Solar Cell Applications. *Chemical Reviews* **2009**, *109* (11), 5868-5923.

110. Arias, A. C.; MacKenzie, J. D.; McCulloch, I.; Rivnay, J.; Salleo, A., Materials and Applications for Large Area Electronics: Solution-Based Approaches. *Chemical Reviews* **2010**, *110* (1), 3-24.

111. Yang, W. S.; Park, B.-W.; Jung, E. H.; Jeon, N. J.; Kim, Y. C.; Lee, D. U.; Shin, S. S.; Seo, J.; Kim, E. K.; Noh, J. H.; Seok, S. I., Iodide management in formamidinium-lead-halide-based perovskite layers for efficient solar cells. *Science* **2017**, *356* (6345), 1376.

112. Tao, C.; Van Der Velden, J.; Cabau, L.; Montcada, N. F.; Neutzner, S.; Srimath Kandada, A. R.; Marras, S.; Brambilla, L.; Tommasini, M.; Xu, W.; Sorrentino, R.; Perinot, A.; Caironi, M.; Bertarelli, C.; Palomares, E.; Petrozza, A., Fully Solution-Processed n-i-p-Like Perovskite Solar Cells with Planar Junction: How the Charge Extracting Layer Determines the Open-Circuit Voltage. *Advanced Materials* **2017**, *29* (15), 1604493-n/a.

113. Burschka, J.; Dualeh, A.; Kessler, F.; Baranoff, E.; Cevey-Ha, N.-L.; Yi, C.; Nazeeruddin, M. K.; Grätzel, M., Tris(2-(1H-pyrazol-1-yl)pyridine)cobalt(III) as p-Type Dopant for Organic Semiconductors and Its

Application in Highly Efficient Solid-State Dye-Sensitized Solar Cells. *Journal of the American Chemical Society* **2011**, *133* (45), 18042-18045.

114. Wang, J.; Wang, S.; Li, X.; Zhu, L.; Meng, Q.; Xiao, Y.; Li, D., Novel hole transporting materials with a linear [small pi]-conjugated structure for highly efficient perovskite solar cells. *Chemical Communications* **2014**, *50* (44), 5829-5832.

115. Petrus, M. L.; Bein, T.; Dingemans, T. J.; Docampo, P., A low cost azomethine-based hole transporting material for perovskite photovoltaics. *Journal of Materials Chemistry A* **2015**, *3* (23), 12159-12162.

116. Li, H.; Fu, K.; Hagfeldt, A.; Grätzel, M.; Mhaisalkar, S. G.; Grimsdale, A. C., A Simple 3,4-Ethylenedioxythiophene Based Hole-Transporting Material for Perovskite Solar Cells. *Angewandte Chemie International Edition* **2014**, *53* (16), 4085-4088.

117. Krishna, A.; Sabba, D.; Yin, J.; Bruno, A.; Boix, P. P.; Gao, Y.; Dewi, H. A.; Gurzadyan, G. G.; Soci, C.; Mhaisalkar, S. G.; Grimsdale, A. C., Facile Synthesis of a Furan–Arylamine Hole-Transporting Material for High-Efficiency, Mesoscopic Perovskite Solar Cells. *Chemistry – A European Journal* **2015**, *21* (43), 15113-15117.

118. Li, H.; Fu, K.; Boix, P. P.; Wong, L. H.; Hagfeldt, A.; Grätzel, M.; Mhaisalkar, S. G.; Grimsdale, A. C., Hole-Transporting Small Molecules Based on Thiophene Cores for High Efficiency Perovskite Solar Cells. *ChemSusChem* **2014**, *7* (12), 3420-3425.

119. Abate, A.; Planells, M.; Hollman, D. J.; Barthi, V.; Chand, S.; Snaith, H. J.; Robertson, N., Hole-transport materials with greatly-differing redox potentials give efficient TiO₂-[CH₃NH₃][PbX₃] perovskite solar cells. *Physical Chemistry Chemical Physics* **2015**, *17* (4), 2335-2338.

120. Jeon, N. J.; Lee, J.; Noh, J. H.; Nazeeruddin, M. K.; Grätzel, M.; Seok, S. I., Efficient Inorganic–Organic Hybrid Perovskite Solar Cells Based on Pyrene Arylamine Derivatives as Hole-Transporting Materials. *Journal of the American Chemical Society* **2013**, *135* (51), 19087-19090.

Chapter 1

121. Krishna, A.; Sabba, D.; Li, H.; Yin, J.; Boix, P. P.; Soci, C.; Mhaisalkar, S. G.; Grimsdale, A. C., Novel hole transporting materials based on triptycene core for high efficiency mesoscopic perovskite solar cells. *Chemical Science* **2014**, *5* (7), 2702-2709.
122. Ganesan, P.; Fu, K.; Gao, P.; Raabe, I.; Schenk, K.; Scopelliti, R.; Luo, J.; Wong, L. H.; Gratzel, M.; Nazeeruddin, M. K., A simple spiro-type hole transporting material for efficient perovskite solar cells. *Energy & Environmental Science* **2015**, *8* (7), 1986-1991.
123. Krishnamoorthy, T.; Kunwu, F.; Boix, P. P.; Li, H.; Koh, T. M.; Leong, W. L.; Powar, S.; Grimsdale, A.; Gratzel, M.; Mathews, N.; Mhaisalkar, S. G., A swivel-cruciform thiophene based hole-transporting material for efficient perovskite solar cells. *Journal of Materials Chemistry A* **2014**, *2* (18), 6305-6309.
124. Li, M.-H.; Hsu, C.-W.; Shen, P.-S.; Cheng, H.-M.; Chi, Y.; Chen, P.; Guo, T.-F., Novel spiro-based hole transporting materials for efficient perovskite solar cells. *Chemical Communications* **2015**, *51* (85), 15518-15521.
125. Zhang, F.; Yi, C.; Wei, P.; Bi, X.; Luo, J.; Jacopin, G.; Wang, S.; Li, X.; Xiao, Y.; Zakeeruddin, S. M.; Grätzel, M., A Novel Dopant-Free Triphenylamine Based Molecular “Butterfly” Hole-Transport Material for Highly Efficient and Stable Perovskite Solar Cells. *Advanced Energy Materials* **2016**, *6* (14), 1600401-n/a.
126. Saliba, M.; Orlandi, S.; Matsui, T.; Aghazada, S.; Cavazzini, M.; Correa-Baena, J.-P.; Gao, P.; Scopelliti, R.; Mosconi, E.; Dahmen, K.-H.; De Angelis, F.; Abate, A.; Hagfeldt, A.; Pozzi, G.; Graetzel, M.; Nazeeruddin, M. K., A molecularly engineered hole-transporting material for efficient perovskite solar cells. *Nature Energy* **2016**, *1*, 15017.
127. Wang, H.; Sheikh, A. D.; Feng, Q.; Li, F.; Chen, Y.; Yu, W.; Alarousu, E.; Ma, C.; Haque, M. A.; Shi, D.; Wang, Z.-S.; Mohammed, O. F.; Bakr, O. M.; Wu, T., Facile Synthesis and High Performance of a New Carbazole-Based Hole-Transporting Material for Hybrid Perovskite Solar Cells. *ACS Photonics* **2015**, *2* (7), 849-855.

128. Lim, I.; Kim, E.-K.; Patil, S. A.; Ahn, D. Y.; Lee, W.; Shrestha, N. K.; Lee, J. K.; Seok, W. K.; Cho, C.-G.; Han, S.-H., Indolocarbazole based small molecules: an efficient hole transporting material for perovskite solar cells. *RSC Advances* **2015**, *5* (68), 55321-55327.
129. Zhang, F.; Yang, X.; Cheng, M.; Li, J.; Wang, W.; Wang, H.; Sun, L., Engineering of hole-selective contact for low temperature-processed carbon counter electrode-based perovskite solar cells. *Journal of Materials Chemistry A* **2015**, *3* (48), 24272-24280.
130. Das, J.; Bhaskar Kanth Siram, R.; Cahen, D.; Rybtchinski, B.; Hodes, G., Thiophene-modified perylenediimide as hole transporting material in hybrid lead bromide perovskite solar cells. *Journal of Materials Chemistry A* **2015**, *3* (40), 20305-20312.
131. Qin, P.; Paek, S.; Dar, M. I.; Pellet, N.; Ko, J.; Grätzel, M.; Nazeeruddin, M. K., Perovskite Solar Cells with 12.8% Efficiency by Using Conjugated Quinolizino Acridine Based Hole Transporting Material. *Journal of the American Chemical Society* **2014**, *136* (24), 8516-8519.
132. Rakstys, K.; Abate, A.; Dar, M. I.; Gao, P.; Jankauskas, V.; Jacopin, G. n.; Kamarauskas, E.; Kazim, S.; Ahmad, S.; Grätzel, M.; Nazeeruddin, M. K., Triazatruxene-Based Hole Transporting Materials for Highly Efficient Perovskite Solar Cells. *Journal of the American Chemical Society* **2015**, *137* (51), 16172-16178.
133. Ramos, F. J.; Rakstys, K.; Kazim, S.; Gratzel, M.; Nazeeruddin, M. K.; Ahmad, S., Rational design of triazatruxene-based hole conductors for perovskite solar cells. *RSC Advances* **2015**, *5* (66), 53426-53432.
134. Gao, K.; Xiao, L.; Kan, Y.; Yang, B.; Peng, J.; Cao, Y.; Liu, F.; Russell, T. P.; Peng, X., Solution-processed bulk heterojunction solar cells based on porphyrin small molecules with very low energy losses comparable to perovskite solar cells and high quantum efficiencies. *J. Mater. Chem. C* **2016**, *4* (Copyright (C) 2017 American Chemical Society (ACS). All Rights Reserved.), 3843-3850.
-

Chapter 1

135. Chou, H.-H.; Chiang, Y.-H.; Li, M.-H.; Shen, P.-S.; Wei, H.-J.; Mai, C.-L.; Chen, P.; Yeh, C.-Y., Zinc Porphyrin-Ethynylaniline Conjugates as Novel Hole-Transporting Materials for Perovskite Solar Cells with Power Conversion Efficiency of 16.6%. *ACS Energy Lett.* **2016**, *1* (Copyright (C) 2017 American Chemical Society (ACS). All Rights Reserved.), 956-962.
136. Chen, S.; Liu, P.; Hua, Y.; Li, Y.; Kloo, L.; Wang, X.; Ong, B.; Wong, W.-K.; Zhu, X., Study of Arylamine-Substituted Porphyrins as Hole-Transporting Materials in High-Performance Perovskite Solar Cells. *ACS Appl. Mater. Interfaces* **2017**, *9* (Copyright (C) 2017 American Chemical Society (ACS). All Rights Reserved.), 13231-13239.
137. Kumar, C. V.; Sfyri, G.; Raptis, D.; Stathatos, E.; Lianos, P., Perovskite solar cell with low cost Cu-phthalocyanine as hole transporting material. *RSC Adv.* **2015**, *5* (Copyright (C) 2017 American Chemical Society (ACS). All Rights Reserved.), 3786-3791.
138. Wang, Q.-K.; Wang, R.-B.; Shen, P.-F.; Li, C.; Li, Y.-Q.; Liu, L.-J.; Duhm, S.; Tang, J.-X., Energy Level Offsets at Lead Halide Perovskite/Organic Hybrid Interfaces and Their Impacts on Charge Separation. *Adv. Mater. Interfaces* **2015**, *2* (Copyright (C) 2017 American Chemical Society (ACS). All Rights Reserved.), 1400528/1-1400528/7.
139. Ke, W.; Zhao, D.; Grice, C. R.; Cimaroli, A. J.; Fang, G.; Yan, Y., Efficient fully-vacuum-processed perovskite solar cells using copper phthalocyanine as hole selective layers. *J. Mater. Chem. A* **2015**, *3* (Copyright (C) 2017 American Chemical Society (ACS). All Rights Reserved.), 23888-23894.
140. Jiang, X.; Yu, Z.; Lai, J.; Zhang, Y.; Hu, M.; Lei, N.; Wang, D.; Yang, X.; Sun, L., Interfacial Engineering of Perovskite Solar Cells by Employing a Hydrophobic Copper Phthalocyanine Derivative as Hole-Transporting Material with Improved Performance and Stability. *ChemSusChem* **2017**, *10* (Copyright (C) 2017 American Chemical Society (ACS). All Rights Reserved.), 1838-1845.

141. Qi, P.; Zhang, F.; Li, X.; Xiao, Y.; Guo, J.; Wang, S., 2,9,16,23-Tetrakis(7-coumarinoxy-4-methyl)- metallophthalocyanines -based hole transporting material for mixed-perovskite solar cells. *Synthetic Metals* **2017**, *226*, 1-6.

142. Wang, J.-M.; Wang, Z.-K.; Li, M.; Hu, K.-H.; Yang, Y.-G.; Hu, Y.; Gao, X.-Y.; Liao, L.-S., Small Molecule-Polymer Composite Hole-Transporting Layer for Highly Efficient and Stable Perovskite Solar Cells. *ACS Appl. Mater. Interfaces* **2017**, *9* (Copyright (C) 2017 American Chemical Society (ACS). All Rights Reserved.), 13240-13246.



2. MOTIVATION AND AIM OF THE THESIS

Chapter 2

The fast increasing energy demand in the world together with the higher global climate change consciousness has made researches to pay attention on renewable energy sources. Since the sun provides in one hour more energy than humans consume in a year, photovoltaic devices are considered one of the most promising technologies, especially, in terms of efficiency since perovskite solar cells (PSCs) is exceeding the 24 %. However, although perovskite solar cells have reached high power conversion efficiencies, there are still several challenges limiting the industrial fabrication, such as the instability due to the doping, moisture degradation and fabrication cost. In addition, some of the materials used in organic and perovskite solar cells are not low-cost nor easy to prepare. Spiro-OMeTAD is the most widely hole transport material (HTM) employed in PSCs and it contributes to more than 30 % of the overall cost because of its complicated synthetic procedure.

On the one hand, even PSCs seemed to eclipse all the other third generation photovoltaics, organic solar cells (OSCs) have been in constant development since 1986, as it is the least expensive solar devices and the cleanest. Traditionally, the use of polymers in organic solar cells have many advantages, like providing high conductive layers, can be deposited by many solution processing techniques and they bring the possibility, due to the extremely low cost, to scale-up to large area devices. Nevertheless, regarding polymers, it is difficult to control their molecular weight due to batch-to-batch variations which may change their optical and electrochemical properties. In order to solve these problems, the design and the synthesis of the commonly known small molecules (SMs) have been driven the progress of OSCs. SMs present the advantage, over polymers, of being extremely reproducible and tuneable in terms of optical and electrochemical properties and morphology (crystallinity, aggregation capability, etc) after its depositing forming the active layer.

To contribute in these two fields, this PhD thesis involved the design, synthesis and characterization of two novel families of organic small molecules (SMs)

Chapter 2

with two different applications in photovoltaics: as electron donors for OSCs and as a hole transporting materials (HTMs) for PSCs.

The objective of this work is to understand the underlying requirements for an efficient design of donors and HTMs for OSCs and PSCs respectively. For this purpose, eight new organic semiconductors were designed so that they were low-cost synthesis, easy to prepare and purify with the idea of fabricating reproducible devices reaching considerably high efficiencies.

This section will be briefly described the contents and motivation of each chapter of this thesis.

Chapter 1 introduces the general concepts of two different types of photovoltaic devices. It includes a brief summary of photovoltaic devices, follow by the description of the two type of devices that were fabricated in this work. The required properties for SMs with electron donor properties are also described for their application as absorbers in OSCs and as HTMs in PSCs.

Chapter 3 describes the methods and techniques utilized in the synthesis and characterization of the new small molecules and in the fabrication and characterization of the devices fabricated using those molecules.

Chapter 4 details the synthesis and characterization of the two novel series of small molecules with electron donor properties: the benzothiadiazole family formed by the named **CS01**, **CS03**, **EP02** and **LCS01** (Figure 2.1); and the triphenylamine and carbazole-based family that contains **CS01**, **CS04**, **CS05** and **CS06** (Figure 2.2). Based on their optical and electrochemical properties, they were thought to be used in OSCs and PSCs.

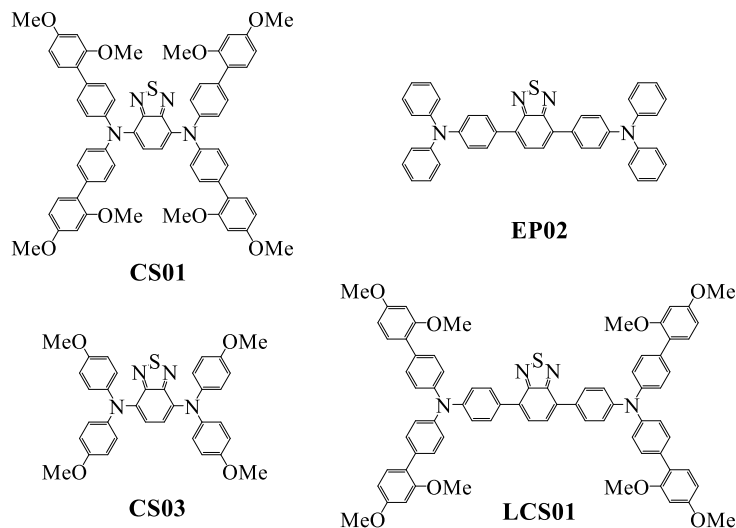


Figure 2.1. Molecular structure of the benzothiadiazole family of SMs synthesized in this work.

Chapter 5 studies the fabrication and photovoltaic characterization of binary and ternary bulk heterojunction organic solar cells using the benzothiadiazole family as electron donors blended with one (binary) or two fullerene and non-fullerene electron acceptors (ternary) as components of the active layer.

Chapter 6 delves into the optimization process of the perovskite-based device fabrication using the HTMs described in Chapter 4, as well as their photovoltaic properties: current density, voltage, fill factor, efficiency and incident-photon to current efficiency. It is explained as well the links between their molecular structure and optoelectronic properties with the device performance.

Chapter 2

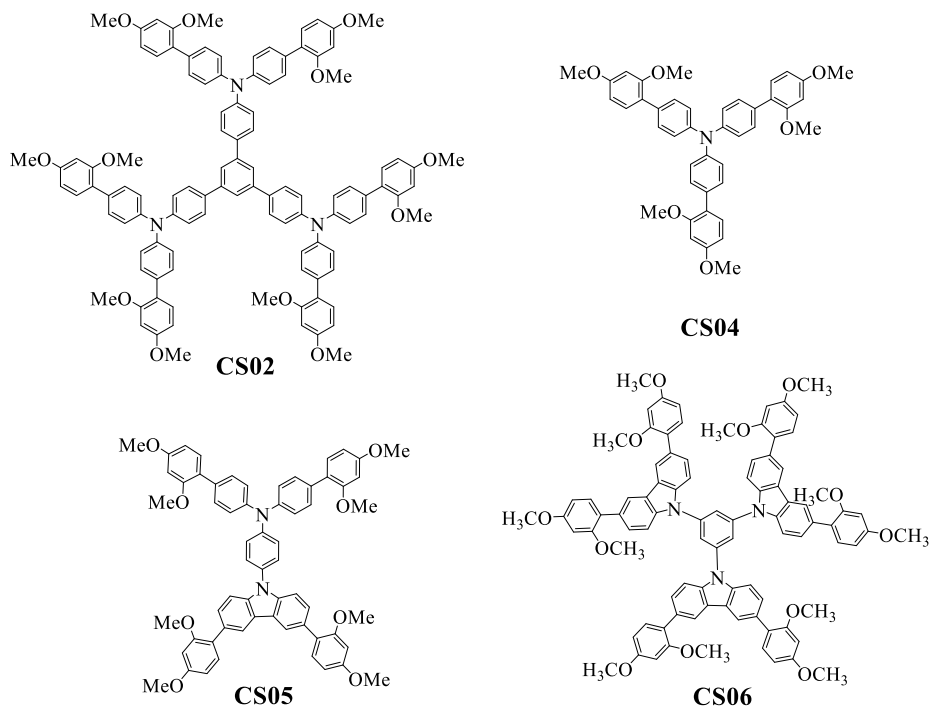


Figure 2.2. Molecular structure of the SMs used as HTMs for PSCs.

Chapter 7 shows the relevant conclusions of each chapter to summarize the results obtained in this work and the perspectives.



3. MATERIALS, METHODS AND EXPERIMENTAL TECHNIQUES

Table of contents

3.1. Introduction.....	71
3.2. Organic synthesis.....	71
3.2.1. General reagents and solvents.....	71
3.2.2. General instrumentation and characterization.....	72
3.2.2.1. Optical measurements.....	72
3.2.2.2. Electrochemical measurements.....	73
3.2.2.3. Thermal measurements.....	74
3.3. Layer deposition techniques.....	76
3.3.1. Spray pyrolysis.....	76
3.3.1. Spin coating.....	77
3.3.2. Solvent vapour annealing.....	78
3.3.3 Thermal evaporation.....	79
3.4. Device fabrication.....	80
3.4.1. Organic Solar Cells fabrication.....	80
3.4.2. Perovskite Solar Cells fabrication.....	81
3.4.2.1. Triple-cation mix-perovskite solar cells. $\text{Cs}_{0.1}(\text{MA}_{0.15}\text{FA}_{0.85})\text{Pb}(\text{I}_{0.85}\text{Br})_3$	81
3.4.2.2. MAPBr ₃ perovskite solar cells.....	83
3.4. Hole mobility devices.....	84
3.4.1. Device fabrication.....	86
3.5. Device performance techniques.....	86
3.5.1. Power conversion efficiency and J-V curve.....	86
3.5.2. Incident photon-to-current conversion efficiency (IPCE).....	88
3.5.3. Scanning electron microscopy (SEM).....	89
3.6. References.....	90

3.1. Introduction.

In this chapter the general methodology used in the synthesis and characterization of new organic semiconductors as well as the fabrication steps and the techniques used in organic solar cells (OSCs) and perovskite solar cells (PSCs) device preparation will be explained.

The first section illustrates not only the materials and the instruments used in the characterization of the molecules, but also the methodology applied (optical, electrochemical and hole mobility measurements) in order to obtain sufficient parameters to evaluate if the novel molecules are good candidates for testing them in devices.

The second section is focused in the analysis of the device fabrication and characterization. In there, in detail the different processes involved in the preparation of both OSCs and PSCs will be described. To conclude with this part, there will be explained the measurements required to characterize both of devices will be explained.

3.2. Organic synthesis.

3.2.1. General reagents and solvents.

All reagents were purchased from Sigma-Aldrich, TCI Europe, Lumtec or Alfa Aesar and they were used as received without further purification unless otherwise stated.

Common solvents were purchased from SdS. THF was always distilled prior use. For sensitive reactions, anhydrous solvents which contained less than 0.005 % of H₂O were purchased from Fluka.

3.2.2. General instrumentation and characterization.

^1H and ^{13}C NMR spectra were recorded on a Bruker Avance 500 (500 MHz for ^1H and 125 MHz for ^{13}C) and 400 (400 MHz for ^1H and 100 MHz for ^{13}C). The deuterated solvents used are indicated; chemical shifts, δ , are given in ppm, referenced to the solvent residual signal (^1H , ^{13}C). Coupling constants, J , are given in Hz.

High Resolution Mass Spectra (HR-MS) were recorded on a Waters LCT Premier liquid chromatograph couple time-of-flight mass spectrometer (HPLC/MS-TOF), using electrospray ionization (ESI) as ionization mode. Matrix assisted laser desorption ionization (MALDI) were recorded on a BRUKER Autoflex time-of-flight mass spectrometer.

3.2.2.1. Optical measurements.

Absorption spectra were measured using 1 cm path length quartz cells in a Shimadzu UV spectrophotometer 1700 with optical range from 190 to 1100 nm. All the measurements were carried out using dichloromethane as solvent.

The fluorescence spectra in solution were also recorded using 1 cm path length quartz cuvettes in Spectrofluorimeter Fruorolog from Horiba Jobin Yvon Lrd with a PMT(UV-vis) and InGaAs (NIR) detectors that allow fluorescence measurements in the wavelengths range from 250 to 1600 nm.

For organic molecules, the energy of the bandgap (E_{0-0}) can be calculated according to the Equation 3.1¹:

$$E_{0-0} = \frac{1242}{\lambda_{0-0}} \quad \text{Equation 3.1}$$

λ_{0-0} is the wavelength onset and its value is taken from the intersection of the normalized absorption and emission spectra recorded in diluted solutions.

3.2.2.2. Electrochemical measurements.

The electrochemical measurements were carried out employing a conventional three-electrode cell connected to a CH Instruments© 660c potentiostat-galvanostat. The working electrode consisted of carbon while the auxiliary electrode was platinum. The reference electrode was Ag/AgCl electrode (saturated KCl). The solvents were purged under argon before use. Cyclic voltammeteries (CV) were obtained in the presence of 0.1 M TBAPF₆ (Tetrabutylammonium hexafluorophosphate) supporting electrolyte, using ferrocene as an internal reference. An example of a CV measured in this work is shown in Figure 3.1.

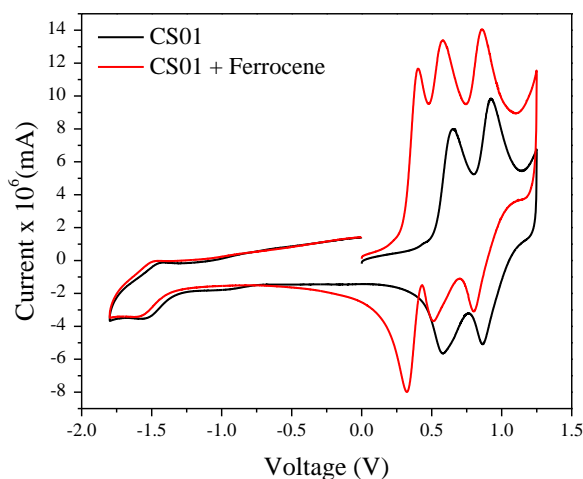


Figure 3.1: CV of **CS01** solved in DCM recorded in 0.1 M tetrabutylammonium hexafluorophosphate at a scan rate of 10 mV s⁻¹ at room temperature with ferrocene as an internal standard.

Cyclic voltammetry is a very suitable method for a wide range of applications. In our research area, the main purpose of performing a CV is to estimate the

Chapter 3

energy levels, HOMO and LUMO (highest occupied molecular orbital and lowest unoccupied, respectively) of organic semiconductors or the valence and the conduction band (VB and CB) of inorganic semiconductors by measuring the redox potentials. With the estimation of HOMO and LUMO levels it is possible to know if mentioned energy levels will fit well with the other components of the device and so making the charge transfer effective².

In order to calculate HOMO and LUMO, we will base our calculations in empirical equations^{1,3} that depend on the conditions used, such as the solvent or the electrodes used.

$$E_{\text{HOMO}} = -(E_{\text{OX}} + E_{\text{ferr}}) \quad \text{Equation 3.2}$$

$$E_{\text{LUMO}} = E_{\text{HOMO}} + E_{0-0} \quad \text{Equation 3.3}$$

E_{ox} is the oxidation potential, E_{0-0} is the energy of the bandgap, λ is intersection wavelength of the normalized absorption and the emission spectra, c is the value of the light speed in vacuum and h is the Planck constant.

3.2.2.3. Thermal measurements.

Thermogravimetric analysis (TGA) determines the rate and the weight loss of a phase as a function of temperature or time under a controlled atmosphere⁴. The measurements were carried out in a TGA/SDTA851 Mettler Toledo equipment, reporting the decomposition temperature when the sample loses a significant amount of weight.

In this work, an important parameter to consider is the decomposition temperature (T_{des}) which is defined as the temperature when the sample losses up to 5 % of its initial weight. The working temperature went from 30 °C to 600 °C or 1100 °C depending on the sample, at a scan rate of 10 °C/min.

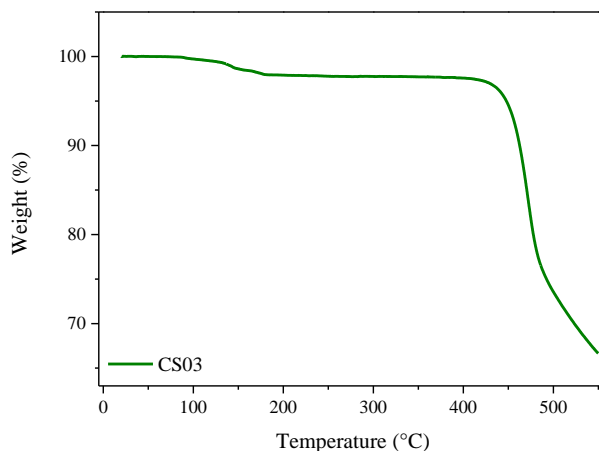


Figure 3.2: TGA of CS03 recorded under N₂ atmosphere from 30 to 550 °C.

Differential Scanning Calorimetry (DSC) analysis provides information about physical and chemical changes that involve endothermic and exothermic processes, or changes in the heat capacity. DSC analysis were measured in DSC822e Mettler Toledo calorimeter. The working temperatures went from 30°C to 450 °C performing three continuous cycles.

From a DSC analysis, it is possible to obtain several parameters. The melting temperature (T_m) is the temperature when the sample goes from a solid state to a liquid state (endothermic process) and the crystal temperature (T_c), when the sample recrystallizes (exothermic process); both determined from the first cycle of DSC analysis. None of them are not observed after the first cycle. Glass transition temperature (T_g) is the temperature where the sample goes from an amorphous solid state to a glass face (endothermic process). It is usually reversible, and it is determined from the seconds and third cycle of the DSC⁵.

Chapter 3

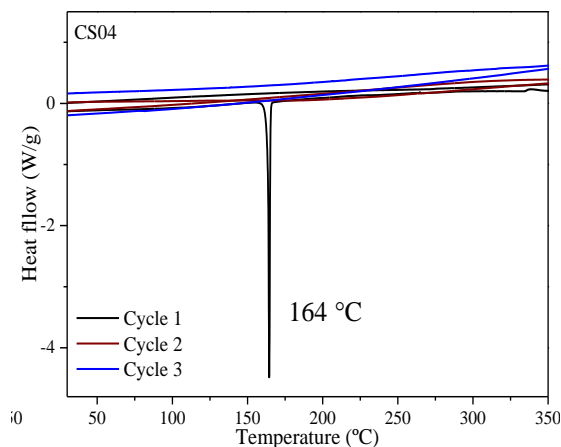


Figure 3.3: DSC of CS04 performed under N₂ atmosphere from 30 to 400 °C.

3.3. Layer deposition techniques.

This section will describe the different techniques used in the fabrication of both organic and perovskite solar cells studied in this work.

3.3.1. Spray pyrolysis.

Spray pyrolysis is a deposition technique where a precursor solution is pulverised by means of a gas so that it deposits on the substrate as very fine droplets. The solvent or other components of the precursor solution that are not desirable to take part in the deposited system are selected such that they evaporate easily⁶. Some of the advantages are the followings: is possible to use a large choice of precursors including solvents such as water or alcohols, it operates at moderate temperatures (up to 500 °C approximately) so it is possible to produce films on less robust materials, it is suitable for low-cost scale-up production and the composition or concentration of the precursor during the spray process can be changed in any moment⁷. The system consists of a spray nozzle, precursor solution, substrate heating, temperature controller and air compressor or gas propellant. One of its most famous applications is in

optoelectronic devices, but also in the formation of superconducting oxide films⁶.



Figure 3.4: Spray pyrolysis gun used in the fabrication of the compact TiO₂ layer for PSCs.

In this work, the compact TiO₂ was deposited by spray pyrolysis by diluting titanium diisopropoxide bis(acetylacetonate) (TAA) in ethanol (6.00 % v/v) while the FTO substrates were on top of a hotplate at 450 °C. The thickness of the layer was 40 nm, approximately.

3.3.1. Spin coating.

Spin-coating is the technique used in the deposition of most of the layers that take part in the OSCs and PSCs. It consists in the deposition of a small amount of a fluid in the center of the substrate. Afterward, the substrate is spun and the coating solution is dispensed onto the surface. The spinning causes the solution to spread and a very uniform film of the selected material is formed on top of the substrate⁸. The advantages of using this technique are the high reproducibility of the devices, the homogeneous film formation and the relative simplicity of the set up.

The final thickness of the layer depends on several conditions, such as the solution concentration of the molecule, the viscosity of the solution, the spin-

Chapter 3

coating angular speed, the acceleration and the running time. It is also important to stress that the solvent used in the fabrication and the ambient conditions (atmosphere and temperature) play an important role in the film formation.



Figure 3.5: Picture of the spin coater used in the fabrication of the solar cells.

As it will be explained in Chapter 6, the optimization of the hole transport layer was done changing not only the concentration of the HMT in chlorobenzene, but also the spin speed. The high-speed spin step generally defines the final film thickness.

3.3.2. Solvent vapour annealing.

Solvent vapour annealing (SVA) is a technique in which the active layer, (generally in OSCs but it has been tested in PSCs⁹ as well) is exposed to vapours of one or more solvents with a high vapour pressure, in a closed vessel at temperatures below the glass transition temperature. The active layer has to be partially soluble in the chosen solvent¹⁰⁻¹¹.

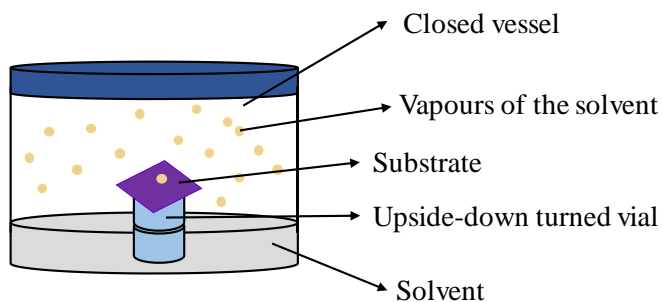


Figure 3.6: Graphical description of the SVA process.

It is a versatile and low-cost alternative method to thermal annealing when it is needed to control the film morphology. However it is necessary to improve its reproducibility. The vapours diffuse into to the film and partially reorganize the components of the bulk heterojunction (BHJ) system, increasing the crystallinity of the active layers, and consequently increasing the hole transport mobility of the donor material. The degree of reorganization will depend on the exposure time. It can be observed by eye a change in the color of the layer or by measuring the absorption of the film.

3.3.3 Thermal evaporation.

The metal contact is deposited by vacuum-deposition techniques. The complete devices are placed in a mask with a concrete shape that will determine the area of the device. The mask is introduced in a thermal evaporator, which is inside a nitrogen atmosphere glovebox. The metal is deposited in ultra-high vacuum conditions while a high voltage is passing through a metallic container (boat) which hold the metal that will be deposited.

Chapter 3



Figure 3.7: Picture of the outside of thermal evaporators (left) and the devices in the mask used for preparing PSCs devices at EPFL.

Aluminium was evaporated as cathode in the OSCs fabricated in this work, while gold was utilized as anode for PSCs.

3.4. Device fabrication.

In this section, the device fabrication process of all types of solar cells studied in this work will be described. More specifications will be given in Chapter 5 and 6 when needed or differed from the general procedure here described.

3.4.1. Organic Solar Cells fabrication.

The OSCs were fabricated with a conventional structure of glass/ITO/PEDOT:PSS/active layer/PFN/Al, as it can be seen in Figure 8. The alcohol-soluble conjugated polymer, poly [(9,9-bis(32-(*N,N*-dimethylamino)propyl)-2,7-fluorene)-alt-2,7-(9,9-dioctylfluorene)] (PFN) was used as an cathode interfacial layer. The ITO (indium tin oxide) coated glass substrates were cleaned by ultrasonic treatment in detergent, deionized water, acetone and isopropanol for 15 min each and subsequently dried in vacuum oven for 15 min at a temperature of 40° C. Then a thin layer of poly (3,4-ethylenedioxythiophene):(polystyrene sulfonate) (PEDOT:PSS) was spin-coated onto the pre-cleaned ITO coated glass substrate at 3500 rpm for 40 s and subsequently baked at 110° C for 20 min and allowed to cool to room

temperature. In order to deposit the thin film of the active layer, a mixture of a SM as an absorber (electron donor) with one or two electron acceptors (PC₇₁BM and/or a non-fullerene small molecule) with different weight ratios in chloroform was spin coated at 2000 rpm for 20 s on the top of the PEDOT:PSS substrate and then dried at room temperature. After the active layer deposition, solvent vapour annealing (SVA) was used to tune the morphology of the blend film. The thin PFN layer was spin coated from a 1.5mg/mL solution in methanol at 3000 rpm for 30 s and dried in a vacuum oven at room temperature for 90 s. Finally, an aluminium (Al) layer was deposited by thermal evaporation under vacuum (ca. 10⁻⁵ Pa).

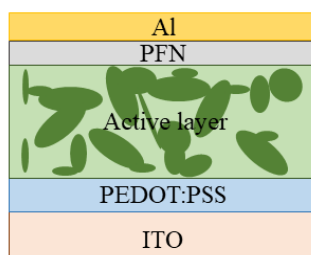


Figure 3.8: General architecture of the organic solar cells fabricated in this work.

3.4.2. Perovskite Solar Cells fabrication.

This section will address the two procedures used in the fabrication of PSCs. More details regarding the deposition of HTMs will be given in Chapter 6.

3.4.2.1. Triple-cation mix-perovskite solar cells. $Cs_{0.1}(MA_{0.15}FA_{0.85})Pb(I_{0.85}Br)_3$

Solar cell devices were fabricated onto conductive FTO (fluorine-doped tin oxide) coated glass Nippon Sheet Glass 10 Ω /square substrates. The substrates were cut and cleaned by sequential treatment with 2 % aqueous Hellmanex solution, acetone and isopropanol in an ultrasonic bath for 10 minutes respectively, followed by a 15 - 30 minutes UV-ozone exposure. The titania

Chapter 3

blocking layer was applied by spray pyrolysis from a precursor solution of titanium diisopropoxide bis(acetylacetonate) (TAA) in ethanol (6.00 % v/v) at 450°C in ambient atmosphere. Mesoporous TiO₂ layer was deposited by spin coating a 30 nm titanium dioxide particle (30 NR-D) paste from Dyesol diluted in ethanol (125 mg/mL) at 3000 rpm for 30 s. The substrates were gradually heated under a flow at 125°C for 20 minutes, 250°C for 10 minutes, 350°C for 10 minutes, 450°C for 10 minutes and 500° for 30 minutes. After cooling down the substrates, SnO₂ layer was deposit by spin coating a solution of SnCl₄ anhydrous in deionized water (1.2 % v/v) at 5000 rpm for 20 s, followed by a sintering step at 390°C for one hour. The perovskite layer was applied by one step spin coating procedure, reported by M. Saliba et al¹², from a precursor solution of Cs_{0.1}(MA_{0.15}FA_{0.85})Pb(I_{0.85}Br)₃ by mixing CsI (0.11 M), FAI (1.07 M), PbI₂ (1.23 M), MABr (0.19 M) and PbBr₂ (0.19 M) in a mix blend of DMF:DMSO = 4:1 vol% solvents. The spin coating sequence includes two steps: 2000 rpm for 12 s with an acceleration of 200 rpm s⁻¹ and 5000 rpm for 25 s with an acceleration of 2000 rpm s⁻¹. Prior to the end of the second step 100 µL of chlorobenzene are poured onto the spinning substrate. At the end of the spin program the substrate is immediately transferred onto a hotplate set at 100°C and is kept at that temperature for one hour under nitrogen atmosphere. The HTMs are deposited from solutions in chlorobenzene by spin coating. The thickness of the layer was optimized to obtain the best device performance for each molecule, as well as the concentration of additives that were added to the solutions. For this reason, the spin coated conditions and the concentration of the HTM in the solutions were optimized for each one. *t*BP, LiTFSI and cobalt complex FK209 were added as additives to all the HTMs: 330 mol% *t*BP, 50 mol% Li-TFSI from a 1.8 M stock solution in acetonitrile and 10 mol% FK209 from a 0.25 M stock solution in acetonitrile. Finally, the gold electrode was deposited by thermal evaporation of 70 nm layer of gold using a shadow mask under high-vacuum conditions.

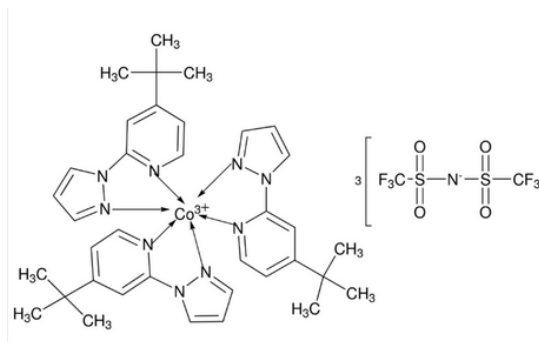


Figure 3.9: Molecular structure of FK209.

3.4.2.2. MAPBr₃ perovskite solar cells.

Solar cell devices were fabricated onto conductive FTO coated glass substrates. The substrates were cut and cleaned by sequential treatment with 2 % aqueous Helmanex solution, acetone and isopropanol in an ultrasonic bath for 10 minutes respectively, followed by a 15 minutes UV-ozone exposure. The titania blocking layer was applied by spray pyrolysis from a precursor solution of titanium diisopropoxide bis(acetylacetonate) in ethanol (6.00 % v/v) at 500°C in ambient atmosphere. Mesoporous TiO₂ layer was deposited by spin coating a 30 nm titanium dioxide particle (30 NR-D) paste from Dyesol diluted in ethanol (125 mg/mL). The substrates were heated at 500 °C for 30 minutes. After cooling down the substrates and applying UV-ozone treatment for 15 minutes, SnO₂ layer was deposited by spin coating a solution of anhydrous SnCl₄ 0.1 M in deionized water at 3000 rpm for 30 s, followed by a sintering step at 390°C for one hour. Right after another UV-ozone treatment of 15 minutes, the perovskite layer was applied by spin coating a precursor solution of MAPbBr₃, 1.3 M, by mixing methylammonium bromide (MABr) and lead (II) bromide (PbBr₂) (mol ratio 1:1) in DMF:DMSO 4:1 (volume ratio). The spin coating sequence includes two steps. Prior to the end of the second step 100 μL of chlorobenzene are poured onto the spinning substrate. At the end of the spin program the substrate is immediately transferred onto a hotplate set at 100°C and is kept at that temperature for one hour under nitrogen atmosphere.

Chapter 3

Spiro-OMeTAD and PTAA were deposited on top of the perovskite layer by spin coating at 4000 rpm for 30 s. **CS05** and **CS06** were deposited at 2000 rpm for 30 s. tBP, LiTFSI and cobalt complex FK209 were added as additives to all HTMs: 330 mol% tBP, 50 mol% Li-TFSI from a 1.8 M stock solution in acetonitrile and 10 mol% FK209 from a 0.25 M stock solution in acetonitrile. Finally, the gold electrode was deposited by thermal evaporation of 70 nm layer of gold using a mask under high-vacuum conditions (10^{-5} mbar).

3.4. Hole mobility devices.

The Space-Charge Limited Current (SCLC) is widely used to estimate the hole mobility of an organic semiconductor, according to the modified Mott-Gurney's law. The current-voltage curve is determined by mobility and concentration of carriers and the electric field in the device and not by the recombination of the holes¹³.

$$J_{\text{SCLC}} = \frac{9}{8} \epsilon_0 \epsilon_r \mu \frac{V_{\text{eff}}}{d^3} \quad \text{Equation 3.4}$$

The devices for hole mobility measurement were fabricated all under the same conditions with an architecture of ITO/PEDOT:PSS/layer to study/Au, as it can be seen in Figure 3.10. What it was called layer to study consists in the same layer of HTM that was used for PSCs or the mixture of the absorber with the electron acceptor/s (PC₇₁BM and/or non-fullerene small molecule), the so called active layer in OSCs.

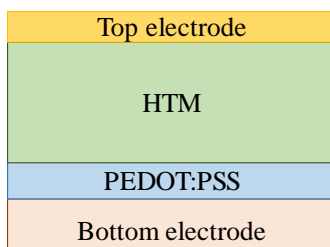


Figure 3.10: General architecture of the only hole devices fabricated in this work.

The devices are forced to work at very large voltages where it is possible to apply the SCLC conditions and the curves in dark and under light are superimposed or parallels, as Figure 3.11 shows. Curves are fitted to the Equation 3.4 where μ is the mobility, d is the film thickness, V_{eff} is the applied voltage and $\epsilon_0\epsilon_r \approx 3$ is the media permittivity for organic semiconductors¹⁴.

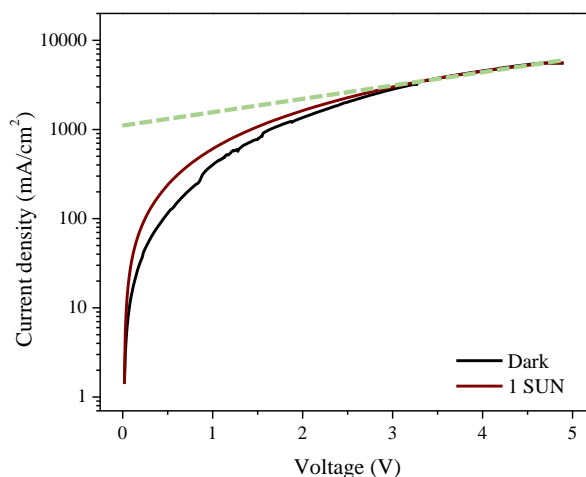


Figure 3.11: J-V curve for a hole-only device of CS02 under light illumination and in the dark. The fitting to the Equation 3.4 is shown as a dash green line.

Chapter 3

3.4.1. Device fabrication.

ITO coated glass substrates were cleaned by sequential treatment with 2 % aqueous solution and isopropanol twice in an ultrasonic bath for 15 minutes respectively, dried with an air flow, followed by 15 minutes of UV-ozone exposure. Then, a thin layer of poly (3,4-ethylenedioxythiophene):(polystyrene sulfonate) (PEDOT:PSS) was spin-coated onto the pre-cleaned ITO coated glass substrate in a two-step deposition at 4500 rpm for 30 s and 3500 rpm for 30 seconds. Subsequently, the substrates were heated at 125° C for 20 min and allowed to cool to room temperature. In order to deposit the thin film of the layer to study, 45 µL of a solution of the corresponding HTMs in CB, with and without additives was deposited at 2000 rpm for 30 seconds on top of the PEDOT:PSS layer for the hole mobility measurements for PSCs application. For OSCs devices, a mixture of **CS01**, **CS03**, **EP02** or **LCS01** with PC₇₁BM and/or the SM non-fullerene acceptor (**DPP8** or **MPU3**) in chloroform was spin coated at 2000 rpm for 20 s. Then, they were dried at room temperature. After the spin coating of the active layer for the OSCs measurements SVA was performed. Finally, 120 nm of gold were deposited by thermal evaporation under vacuum (10⁻⁵ Pa) through a mask.

3.5. Device performance techniques.

3.5.1. Power conversion efficiency and J-V curve.

The power conversion efficiency (PCE) is calculated by the following equation:

$$\text{PCE} = \text{FF} \frac{J_{\text{SC}} V_{\text{OC}}}{P_{\text{in}}} = \frac{P_{\text{out}}}{P_{\text{in}}} \quad \text{Equation 3.5}$$

where J_{SC} is the short-circuit current density, V_{OC} is the open-circuit voltage and FF is the filling factor. PCE is defined also simplistically as the ratio of power out (P_{out}) to power in (P_{in}). FF depends on the thickness of the active layer and

it is defined as the square-shaped part of the curve and can be calculated by the following equation:

$$FF = \frac{J_m \cdot V_m}{J_{sc} \cdot V_{oc}} \quad \text{Equation 3.6}$$

where J_m and V_m are the current and voltage at the maximum power. Figure 3.11 shows the typical current-voltage characteristics for dark and light current in a solar cell.

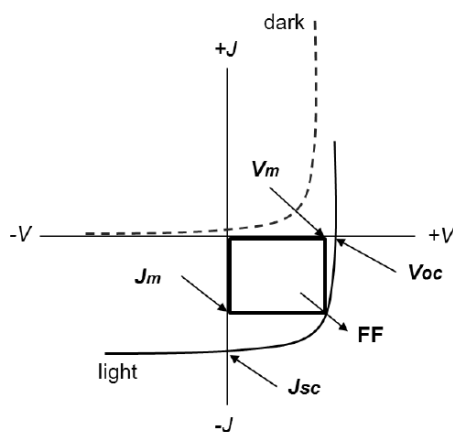


Figure 3.12: Current-voltage characteristics for dark and illuminated solar cell.

The photovoltaic measurements were carried out with a 150 W solar simulator from ABET© Technologies with the appropriate set of filters for the correct simulation of the 1.5 AM G solar spectrum. The incident light power was measured at 100 mW cm^{-2} with a calibrated Silicon photodiode, in which the spectral sensitivity was close to the devices under test. On a clear sunny day in Florida the power of the Sun is 100 mW cm^{-2} . This has become the standard which the efficiencies of solar cells are reported and is often referred to as 1 Sun conditions. The applied potential and cell current were measured with a

Chapter 3

Keithley model 2400 digital source meter at the ICIQ laboratories for hole mobility measurements.

At EPFL laboratory, the solar cells were measured using 450 W xenon light source (Oriel). The spectral mismatch between AM1.5G and the simulated illumination was reductive by the use of a Schott 113 Tempax filter (Präzisions Glas & Optik GmbH). The light intensity was calibrated with that Si photodiode equipped with an IR cutoff filter (KG3, Chott) and it was recorded during each measurement. Current-voltage characteristics of the cells were obtained by applying an external voltage bias while measuring the current response with a digital source meter (Keithley 2400). The voltage scan rate was 10 mV s^{-1} and a light soaking was applied before starting the measurement. The starting voltage was that in mind as the potential at which the cells furnishes 1 mA in forward bias. The cells were masked with a black metal mask (0.16 cm^2) to estimate the active area and reduce the influence of the scattered light.

3.5.2. Incident photon-to-current conversion efficiency (IPCE).

The incident photon-to-current conversion efficiency (IPCE) or external quantum efficiency (EQE) measures the spectral response of the photoelectric conversion device. Its spectrum is a plot of the ratio between the number of output electrons (current) and the input photons (irradiance) against wavelengths. IPCE is calculated as shown in Equation 3.7.

$$\text{IPCE} = \frac{h\nu J_{SC}}{e \cdot P_{\text{light}}} = \frac{1240 J_{SC}}{\lambda \cdot P_{\text{light}}} \quad \text{Equation 3.7}$$

where J_{SC} is the short circuit current density, P_{light} is the number of incident photons, λ is the measured wavelength, and 1240 is a conversion factor. This measurement includes the losses due to experiment factors like the substrate absorption and reflection. The shape of the curve usually follows the absorbance a spectrum of the molecules implied in the photovoltaic process.

These measurements were carried out at EPFL (Sion, Switzerland). IPCE measurements were made using 300 W xenon light source (ILC Technology, USA). A double-monochromator spectrometer (Gemini-180, JobinYvon Ltd. UK) was used to select an increment the wavelength of the radiation impinging on the cells. The monochromatic incident light was passed through a chopper running at 1 Hz and the on/off ratio was measured by an operational amplifier. This was superimposed on a white light bias corresponding to an intensity of 10 nW/cm².

3.5.3. Scanning electron microscopy (SEM).

A field-emission scanning electron microscope (FESEM, Merlin) was employed to analyse the morphology of the samples. An electron beam accelerated to 3 kV was used with an in-lens detector. The cross-sectional topography was visualized by SEM images to qualitatively study the pore filling of the HTMs. The thickness of the layer of the HTMs on top of the perovskite was estimated by zooming into the top-most region of the films.

3.6. References.

1. Leonat, L.; Beatrice Gabriela, S.; Brañzoi, I. V., Cyclic voltammetry for energy levels estimation of organic materials. 2013; Vol. 75, p 111-118.
2. D'Andrade, B. W.; Datta, S.; Forrest, S. R.; Djurovich, P.; Polikarpov, E.; Thompson, M. E., Relationship between the ionization and oxidation potentials of molecular organic semiconductors. *Organic Electronics* **2005**, *6* (1), 11-20.
3. Leonat Lucia; Sbarcea Gabriela; Viorel Brânzo, I. cyclic voltammetry for energy levels estimation of organic materials. *Scientific Bulletin, Series B* [Online], **2013**, p. 111-118. https://www.scientificbulletin.upb.ro/rev_docs_arhiva/full982_152789.pdf.
4. Sichina, W. J. Characterization of polymers using TGA.
5. Kodre KV; Attarde SR; Yendhe PR; Patil RY; VU, B., Differential Scanning Calorimetry: A Review. *Research & Reviews: Journal of Pharmaceutical Analysis* **2014**.
6. Patil, P. S., Versatility of chemical spray pyrolysis technique. *Materials Chemistry and Physics* **1999**, *59* (3), 185-198.
7. Sankir, N. D.; Aydin, E.; Ugur, E.; Sankir, M.
8. D.P., B., *Spin Coating Technique*. Springer, Boston, MA: Boston, **2004**.
9. Liu, G.; Xie, X.; Zeng, F.; Liu, Z., Improving the Performance of Perovskite Solar Cells Through Solvent Vapor Annealing-based Morphology Control of the Hole-Transport Layer. *Energy Technology* **2018**, *6* (7), 1283-1289.
10. Sinturel, C.; Vayer, M.; Morris, M.; Hillmyer, M. A., Solvent Vapor Annealing of Block Polymer Thin Films. *Macromolecules* **2013**, *46* (14), 5399-5415.
11. Hegde, R.; Henry, N.; Whittle, B.; Zang, H.; Hu, B.; Chen, J.; Xiao, K.; Dadmun, M., The impact of controlled solvent exposure on the morphology,


structure and function of bulk heterojunction solar cells. *Solar Energy Materials and Solar Cells* **2012**, *107*, 112-124.

12. Saliba, M.; Matsui, T.; Seo, J.-Y.; Domanski, K.; Correa-Baena, J.-P.; Nazeeruddin, M. K.; Zakeeruddin, S. M.; Tress, W.; Abate, A.; Hagfeldt, A.; Grätzel, M., Cesium-containing triple cation perovskite solar cells: improved stability, reproducibility and high efficiency. *Energy & Environmental Science* **2016**, *9* (6), 1989-1997.

13. Kirchartz, T., Influence of diffusion on space-charge-limited current measurements in organic semiconductors. *Beilstein Journal of Nanotechnology* **2013**, *4*, 180-188.

14. Montcada, N. F.; Cabau, L.; Kumar, C. V.; Cambarau, W.; Palomares, E., Indoline as electron donor unit in “Push–Pull” organic small molecules for solution processed organic solar cells: Effect of the molecular π -bridge on device efficiency. *Organic Electronics* **2015**, *20*, 15-23.

Chapter 3



4. DESIGN, SYNTHESIS AND CHARACTERIZATION OF SMALL MOLECULES FOR OPTOELECTRONIC APPLICATIONS

Chapter 4

Design, synthesis and characterization of SMs for optoelectronic applications

Table of contents

4.1. Introduction.....	97
4.1.1 Electron donor groups.....	99
4.2. Benzothiadiazole-based organic semiconductors.....	100
4.2.2. Design and synthesis of BT-based organic semiconductors.....	102
4.2.3. Thermal, optical, electrochemical and hole mobility properties.....	104
4.2.3.1. Thermal properties.....	105
4.2.3.2. Optical and electrochemical characterization.....	108
4.2.3.3. Hole mobility measurements.....	111
4.3. Triphenylamine and carbazole-based organic semiconductors.....	116
4.3.1. Donor units based on TPA and carbazole.....	116
4.3.2. Design and synthesis of triphenylamine and carbazole-based small molecules.....	117
4.3.3. Thermal, optical, electrochemical and hole mobility properties.....	119
4.3.3.1. Thermal properties.....	119
4.3.3.2. Optical and electrochemical properties.....	122
4.3.3.3. Hole mobility measurements.....	126
4.4. Conclusions.....	128
4.5. Experimental procedures.....	130
4.5.1 Benzothiadiazole-based small molecules.....	130
4.5.1.1. Synthesis of CS01	130
4.5.1.2. Synthesis of CS03	132
4.5.1.3. Synthesis of EP02.....	133
4.5.1.4. Synthesis of LCS01	134
4.5.2. Triphenylamine and carbazole-based Organic Semiconductors as Hole Transporting Materials.....	136
4.5.2.1. Synthesis and characterization of CS02	136
4.5.2.2. Synthesis and characterization of CS04	138

Chapter 4

4.5.2.3. Synthesis and characterization of CS05	140
4.5.2.4. Synthesis and characterization of CS06	142
4.6. Annex.....	143
4.6.1. NMRs.....	143
4.6.2. MS spectra.....	156
4.7. References.....	168

Design, synthesis and characterization of SMs for optoelectronic applications

4.1. Introduction.

Nowadays, the reduction of the CO₂ emissions that are causing the global warming has become an urgency, thus, renewable energy sources are attracting a lot of attention, especially solar cells, that convert solar energy into electricity. Conventional silicon-based solar cells require high cost purification and fabrication processes due to the need of obtaining a very pure material in order to achieve its highest efficiencies (around 23 %¹). Moreover, this type of devices are rigid, fragile and bulky, and thus its applications are limited²⁻³. Therefore, during the last three decades, many alternatives of PV technologies have been developed and attract notable attention, specially, the ones that incorporate organic materials into the configuration; because their fabrication costs are lower. The main advantages of the organic photovoltaics (OPV) are the possibility of fabricating flexible and transparent devices, that can be portable or implemented in the roof or windows of our buildings, among other applications³.

Depending on the final device fabrication, a precise molecular structure will need to fulfil the requirements of its purpose. For instance, in organic solar cells (OSCs), the electron donor or absorber, usually combines electron-rich and electron-poor moieties, to create donor-acceptor (D-A) structures or any other combination of them, for instance, A-D-A, A-D¹-D²-D¹-A or A- π -D- π -A. The conjugation length, the intramolecular charge transfer between the electron-donor and electron-acceptor units, the side of the alkyl chains or the solubility in the casting solvent, will affect the energy levels of the small molecule, the phase separation or the hole and electron mobility of the film⁴.

However, in perovskite solar cells (PSCs), the research of organic semiconductors is focused on the design and synthesis of new electron transport materials (ETMs) and hole transport materials (HTMs), which are the ones that

Chapter 4

will be analysed in this Chapter. Since spiro-OMeTAD is the most expensive component of the device due to its complicated synthesis and purification, the research of new HTMs in order to replace it, has been an important theme over the last years. In the design of HTMs, it is desirable to have strong electron-donating units, like diphenylamines (DPA), triphenylamines (TPA) and carbazoles, already studied in DSSCs⁵⁻⁸. They should have excellent film forming ability and be able to fill the pores of the perovskite layer to enhance the charge transfer. A high hole mobility is also a desired parameter. Additionally, it is desirable that the HTM has a low tendency to crystallize, therefore the glass transition temperature (T_g) should be as high as possible. A T_g above 100 °C is considered optimal since a phase transition during the device operation might reduce the efficiency. Suppressing crystallization, the hole mobility can be compromised thus it is needed to balance both parameters (hole mobility and T_g) to obtain an optimal performance of the device⁹.

The research for new materials has always been a challenge, and sometimes it follows a pattern of trial and error. It is, as well, often difficult to draw conclusions when we compare the performance of different HTMs. The preparation of the solar cells may differ from one laboratory to another, as well as the device structure, perovskite composition and the use of the same dopants or the lack of them. It is needed to understand how the molecular structure can influence the device performance in order to synthesize new efficient organic semiconductors that also lower the cost of the overall device in PSCs and to achieve higher efficiencies in OSCs.

In this chapter, the design, synthesis and characterization of two families of small molecules will be studied. The first family composed by **CS01**, **CS03**, **EP02** and **LCS01** was designed to take part into OSCs as absorbers and into PSCs as HTMs. The second family is also composed by four molecules (**CS02**,

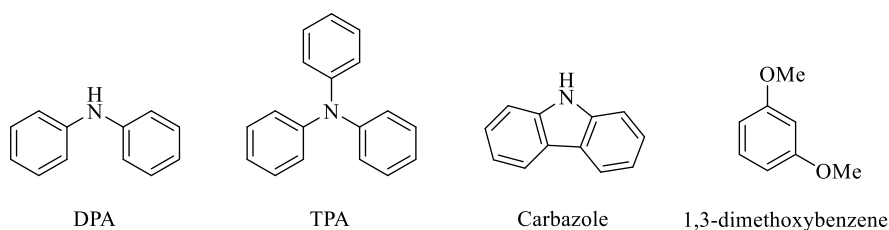
Design, synthesis and characterization of SMs for optoelectronic applications

CS04, **CS05** and **CS06**) based on electron donor groups for their use as HTMs in PSCs will be described.

4.1.1 Electron donor groups.

Typically, electron donors (D) are obtained by substituting functional groups like -NH₂, -OH or -SH. Hence, by attaching two electron donor moieties it is possible to tune the HOMO (Highest Occupied Molecular Orbital) level of the molecule by lowering its value. Moreover, the addition of extra π -bridge conjugation between two donors or a donor and an acceptor, can also change the electronic properties and the steric geometry.

In this work, different donor groups have been employed such as diphenylamine (DPA), triphenylamines (TPA) and carbazole (CBZ) derivatives (Scheme 4.1).



Scheme 4.1: Chemical structures of the electron donor moieties and substituents used in this work to synthesize SMs for OSCs and HTMs for PSCs.

The logical trend in donor strength moieties is the following: carbazole < TPA < DPA due to the possibility of compensating the photogenerated charge with the phenyl rings that surround the nitrogen atom. They are usually substituted in order to tune their electron donor ability by adding electron-rich groups to an adjacent phenyl ring, typically a methoxy unit. By incorporating methoxy

Chapter 4

groups to the structure, it will not only increase the solubility in organic solvents but also the possibility to enhance the electron-donating behaviour of the molecule under resonance stabilization. However, it depends on the substitution position in the aromatic ring of the DPA, TPA or carbazole moieties. If the methoxy group is located in the *ortho* and *para*-positions it will have an electron-donating effect and it will have an electron-withdrawing effect at the *meta*-position¹⁰. The introduction of a methoxy group in the *ortho*-position can have a marked steric effect, as the phenyl ring has to twist out of plane⁹. For this reason, the group 1,3-dimethoxybenzene (see Scheme 4.1) was chosen to be the substituent in all the subunits. Moreover, if mentioned group conjugates well with the TPA, DPA, carbazole and the core of the molecules, it will result in an increase on the molar extinction coefficient (ϵ) and consequently in an increase of the J_{sc} of the final device¹¹. The 1,3-dimethoxybenzene is bounded to the DPA and TPA in *para*-position and to the carbazole in 3.6 positions. The amine nitrogen atom of the DPA, TPA and carbazole easy oxidized, what enhances their ability to transport positive charge efficiently. Many HTMs are composed by aromatic amines, where the nitrogen atom is responsible for the hole transporting behaviour. The functionalization of mentioned groups generally leads to electron-rich star-shaped molecular structures¹².

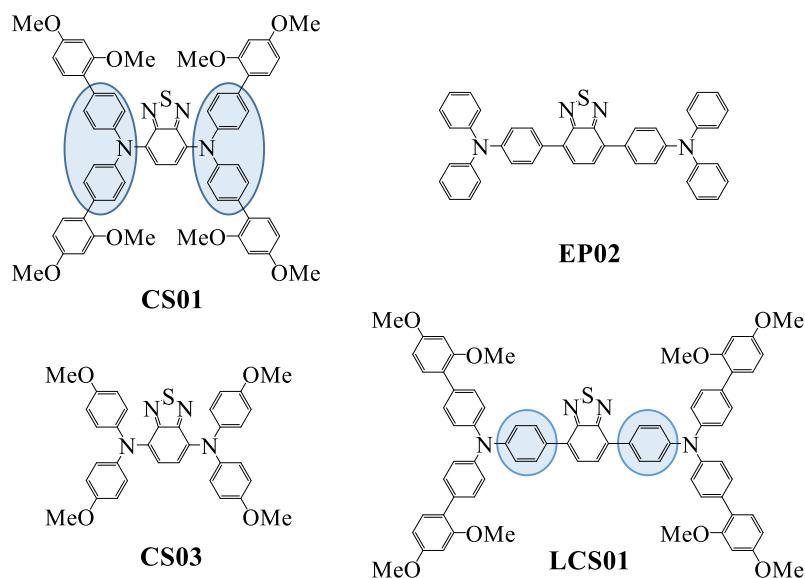
4.2. Benzothiadiazole-based organic semiconductors.

This section will address the preparation and properties of four new small molecules to be used in OSCs and PSCs. The structure is based on 2,1,3-benzothiadiazole (BT), an electron-rich unit, surrounded by di- and triphenylamines with different number of substituted phenyl rings.

The introduction of a phenyl ring in different positions (in blue in the Scheme 4.2) in relation to the DPA, TPA and the benzothiadiazole groups was studied in order to know the effect on the energy levels, the hole mobility and the layer

Design, synthesis and characterization of SMs for optoelectronic applications

deposition in the final device. As four of these molecules were designed to be used as absorbers in OSCs and as HTMs for PSCs, the introduction of an electron-acceptor moiety in the molecular structure was necessary.



Scheme 4.2: Molecular structure of the four molecules that form the BT-family.

Compounds bearing the BT ring have received much attention in the recent years, not only as part of organic semiconductors, but also for its potential use in herbicides¹³ or antibacterial¹⁴. BT derivatives have several characteristics that make them good alternatives for optoelectronic applications, as organic light-emitting diodes (OLEDs) or OSCs. The heterocyclic system has a strong electron-withdrawing nature, being this a favourable characteristic favourable for transporting electron carriers. They also act as fluorophores, and the compounds that contain BT units are expected to have a well-ordered crystal structure that lead to intermolecular interactions with the heteroatoms and π - π interactions¹⁵. It is reasonable to anticipate that BT unit can enhance the planarity and the conjugation in the structure of novel molecules. Scientists

Chapter 4

have recently reported many examples of polymers and small molecules based on this unit and used in DSSCs¹⁶⁻¹⁷, OSCs¹⁸⁻¹⁹ and PSCs²⁰⁻²².

4.2.2. Design and synthesis of BT-based organic semiconductors.

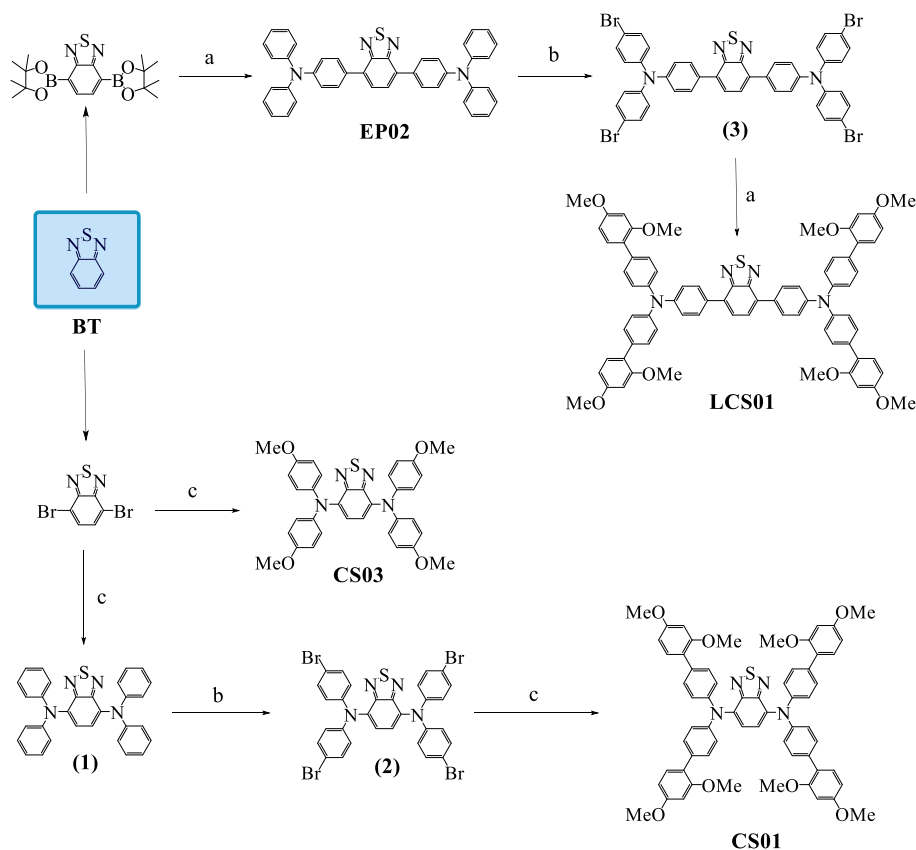
The aforementioned BT group was covalently surrounded to different electron-donor units through a simple synthetic route (Scheme 4.3), making these new molecules D-A-D semiconductors, also called push-pull systems. This kind of composition can improve the intramolecular charge transfer from the electron-donating to the electron-withdrawing moiety, generally leading to coloured chromophores. It is also known that electron-withdrawing groups, like BT, triazines or benzoxadiazoles^{12, 22-23}, are commonly used as electron acceptors for optoelectronic applications and may decrease the HOMO energy level to achieve higher V_{oc} ²⁴.

This section will address the preparation and properties of the benzothiadiazole derivatives. The structure is constituted by a 2,1,3-benzothiadiazole as a central moiety endowed with different electron donor groups, consisted in DPA and TPA, as it is illustrated in the Scheme 4.3. Therefore, it is possible to study the influence that can have the addition of phenyl groups to different positions in the molecules, to the electrochemical properties of the semiconductor and to the performance of the devices once they are tested.

One of the advantages of these molecules is the easy preparation. The synthetic route was carried out by stepwise synthesis as it is shown in the Scheme 4.3. N,N'-(benzo[c][1,2,5]thiadiazole-4,7-diylbis(4,1-phenylene))bis(N-(2',4'-dimethoxy-[1,1'-biphenyl]-4-yl)-2',4'-dimethoxy-[1,1'-biphenyl]-4-amine) (**LCS01**) was achieved following a two-steps procedure. Starting from commercially available 2,1,3-benzothiadiazole-4,7-bis(boronic acid pinacol ester), via a Suzuki-coupling reaction in presence of DMF and water leads to

Design, synthesis and characterization of SMs for optoelectronic applications

the intermediate compound 4,4'-(benzo[c][1,2,5]thiadiazole-4,7-diyl)bis(N,N-diphenylaniline) (**EP02**). **EP02** was subjected to a four-fold bromination with $(n\text{-C}_4\text{H}_9)_4\text{NBr}_3$ in DMF at room temperature and after that, another Suzuki cross-coupling reaction was performed with 2-(2,4-dimethoxyphenyl)-4,4,5,5-tetramethyl-1,3,2-dioxaborolane, to afford the desire compound **LCS01**.



Scheme 4.3: Synthetic pathways of the four new molecules based on the group benzothiadiazole (in blue). Reagents and conditions: a) 4-bromo-N,N-diphenylaniline, $\text{Pd}(\text{PPh}_3)_2\text{Cl}_2$, Cs_2CO_3 , DMF, H_2O , $120\text{ }^\circ\text{C}$. b) $(n\text{-C}_4\text{H}_9)_4\text{NBr}_3$, DCM, r.t. c) $\text{Pd}(\text{OAc})_2$, $[(t\text{-Bu})_3\text{PH}]\text{BF}_4$, $t\text{BuONa}$, toluene, $110\text{ }^\circ\text{C}$.

Chapter 4

Additionally, in the Scheme 4.3 it is shown the synthesis of N4,N4,N7,N7-tetrakis(2',4'-dimethoxy-[1,1'-biphenyl]-4-yl)benzo[c][1,2,5]thiadiazole-4,7-diamine (**CS01**) and N4,N4,N7,N7-tetrakis(4-methoxyphenyl)benzo[c][1,2,5]thiadiazole-4,7-diamine (**CS03**). Initially, a Buchwald-Hartwig amination was carried out using a Pd(II) catalyst and diphenylamine and bis(4-methoxyphenyl)amine, respectively for **CS01** and **CS03**, being this step the only one need to achieve **CS03**. In order to synthesize **CS01**, a four-fold bromination, using the same conditions as for the bromination used to obtain **LCS01**, lead to obtain compound **2** and finally, this compound was subjected to a four-fold Suzuki cross-coupling reaction with 2-(2,4-dimethoxyphenyl)-4,4,5,5-tetramethyl-1,3,2-dioxaborolane to yield **CS01**.

The formation of the mentioned new semiconductors was confirmed by common characterization techniques as ^1H , ^{13}C NMR and HRMS [MALDI-TOF] and [ESI⁺] techniques. Mass spectroscopy confirmed the presence of **CS01** with a molecular ion peak $[\text{M}+\text{Na}]^+$ at 1037.3507 (calcd. 1037.3555), **CS03** with the molecular ion peak $[\text{M} + \text{Na}]^+$ at 613.1883 (calcd. 613.1880), **EP02** with a molecular ion peak $[\text{M}]^+$ at 622.2223 (calcd. 622.2191) and **LCS01** with a molecular ion peak $[\text{M}]^+$ at 1166.4422 (calcd. 1166.4288).

4.2.3. Thermal, optical, electrochemical and hole mobility properties.

In this section the properties of the BT-based small molecules will be analysed to explore their potential as candidates to be used as absorbers in OSCs and as HTMs in PSCs, by studying their optical and electrochemical properties.

Design, synthesis and characterization of SMs for optoelectronic applications

4.2.3.1. Thermal properties.

To unveil the thermal properties of this novel family of semiconductors, TGA and DSC measurements were performed. The details of the thermal features are collected in Table 4.1.

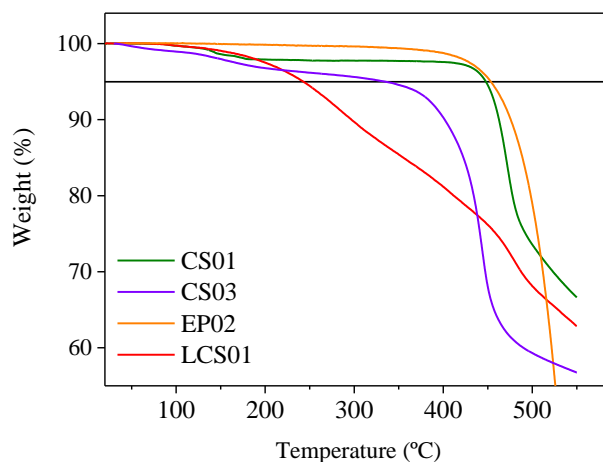


Figure 4.1: Thermogravimetry analysis of benzothiadiazole-based organic semiconductors at scan rate of 10 °C/min under N₂ atmosphere.

As Figure 4.1 shows, the new molecules exhibited good thermal stability, starting to decompose at temperatures above 350 °C, except for **LCS01**. Surprisingly, **LCS01** has a characteristic weigh loss curve and starts gradually to lose weight at 150 °C. The decomposition temperatures (5 % weight loss under N₂ atmosphere) are: **CS01**: 377 °C, **CS03**: 448 °C, **EP02**: 454 °C and **LCS01**: 243 °C. The first weight loss at 100 °C for **CS03** was attributed to the fact that the sample was not completely dry.

Chapter 4

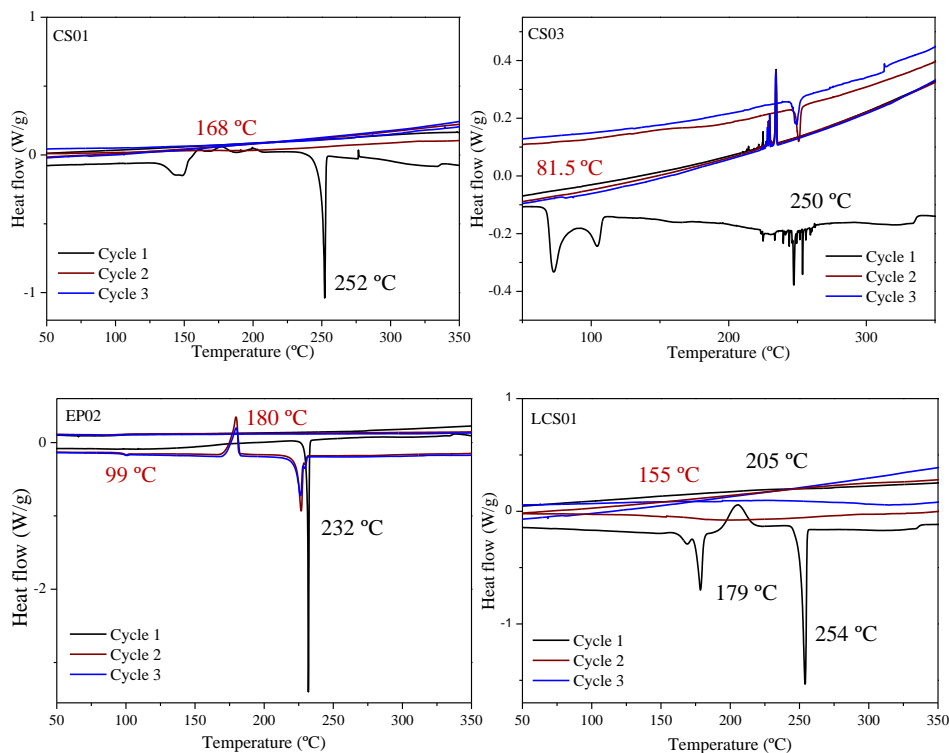


Figure 4.2: DSC curves of **CS01**, **CS03**, **EP02** and **LCS01** obtained at scan rate of 10 °C/min under N₂ atmosphere. Numbers in black correspond to the melting points from the first cycle and numbers in red correspond to the T_g and crystallization points from the second and third cycles.

Figure 4.2 illustrates the differential scanning calorimetry curves, which give as information about the thermal behaviour of each molecule. During the first DSC heating scan the melting points were detected as a sharp endothermic peak at 252 °C and 232 °C for **CS01** and **EP02**. **LCS01** shows two melting points, at 179 °C and 254 °C whereas **CS03** does not show any sharp peak. The second melting point of **LCS01** was above the decomposition temperature, indicating the appearance of secondary products from the decomposition of the mentioned molecule. However, a small amount of **EP02** and **CS03** melts during the second and third cycles. On the successive heating cycles transition temperature (T_g) of

Design, synthesis and characterization of SMs for optoelectronic applications

168 °C, 81.5 °C, 99 °C and 155 °C appeared for **CS01**, **CS03**, **EP02** and **LCS01**, respectively, which indicate they have crystalline and amorphous states. Only **EP02** and **LCS01** exhibit an exothermic crystallization temperature in the first cycle of the DSC at 180 °C and 205 °C respectively.

Table 4.1: Thermal properties of benzothiadiazole-based HTMs.

HTM	T _{des} (°C) ^[a]	T _m (°C) ^[b]	T _c (°C) ^[c]	T _g (°C) ^[d]
CS01	377	252	-	168
CS03	448	250	-	81.5
EP02	454	232	180	99
LCS01	243	179, 254	205	155
Spiro-OMeTAD	417	234	-	126

^[a] Decomposition temperature determined from TGA (5 % weight loss).

^[b] Melting temperature and ^[c] crystal temperature determined from the first cycle of DSC and ^[d] Glass transition temperature determine from the second cycle of DSC. All experiments were carried out under N₂ atmosphere at scan rate of 20 °C/min.

Based on the thermal data, it is possible to say that **CS01** and **LCS01** are good candidates as electron donor semiconductors in devices. Although **CS03** and **EP02** are not as thermally stable as their counterparts, they could also be used in devices.

Chapter 4

4.2.3.2. Optical and electrochemical characterization.

UV-Vis absorption and fluorescence measurements were carried out in order to know the optical properties of these new molecules. Figure 4.3 shows the normalized absorption and emission spectra of **CS01**, **CS03**, **EP02** and **LCS01** (10^{-5} M) in DCM. The recorded absorption and emission wavelength as well as the molar absorption coefficients (ϵ) and the band gap energy ($E_{0.0}$) are collated in Table 4.2.

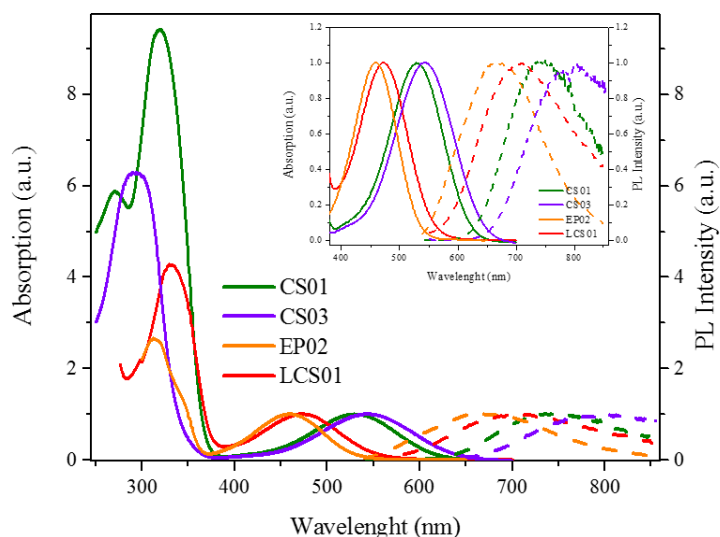


Figure 4.3: Absorption and emission spectra of benzothiadiazole-based organic semiconductors in DCM.

The UV-Vis absorption and fluorescence spectra of the four novel molecules show two absorption peaks. All of them have one broad absorption peak in the visible region, being the maximum absorption wavelength ($\lambda_{\max, \text{abs}}$) centred at 529 nm, 543 nm, 460 nm and 473 nm, for **CS01**, **CS03**, **EP02** and **LCS01**. This band corresponds to a weak intramolecular charge transfer process because of the presence of the BT unit into the molecules²¹. The stronger peak for all of

Design, synthesis and characterization of SMs for optoelectronic applications

them is located in the UV region of the spectra and it is due to π - π^* transitions. A red shift is observed when the π -conjugation system is extended²⁵. The emission spectra exhibit a maximum centred at 705 nm, 743 nm, 621 nm and 669 nm for **CS01**, **CS03**, **EP02** and **LCS01**, respectively, when the molecules dissolved in DCM are excited at the $\lambda_{\text{max, abs}}$ in the visible region.

Table 4.2: Optical properties of benzothiadiazole-based new organic small molecules.

	$\lambda_{\text{max, abs}}$ (nm) ^[a]	$\lambda_{\text{max, em}}$ (nm) ^[a]	ϵ ($\text{M}^{-1}\text{cm}^{-1}$) ^[b]	E_{0-0} (eV) ^[c]
CS01	529	705	7943.5	2.01
CS03	543	743	7655.1	1.93
EP02	460	621	27606	2.34
LCS01	473	669	38280	2.23

^[a] λ_{max} of absorption and emission for samples measured in DCM at room temperature. ^[b] ϵ was determined by measuring the absorption of two solutions with different concentrations was obtained by using the Equation 3.1 (in Chapter 3) with the value of λ_{0-0} at the intersection of the normalized absorption and emission spectra.

HOMO and LUMO were estimated using absorption, photoluminescence and CV measurements, so it will be possible to know if the energetic levels will fit with the materials that will sandwich the SMs.

Chapter 4

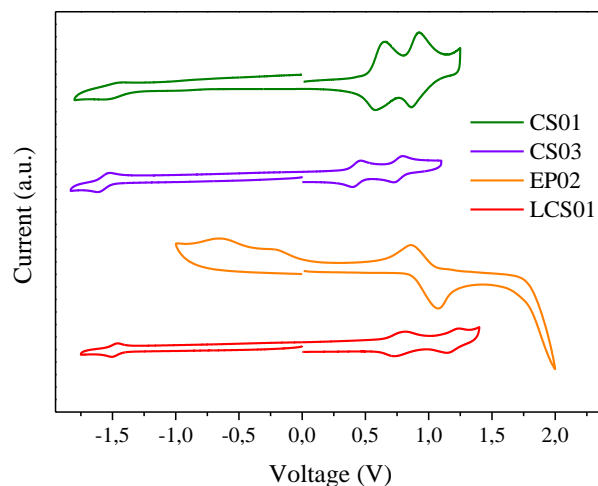


Figure 4.4: Cyclic voltammetry of **CS01**, **CS03**, **EP02** and **LCS01**, measured using ferrocene as an internal reference at room temperature with a scan rate of 10 mV/s.

As shown in Figure 4.4, the new family of molecules are active in the anodic and cathodic region. **CS01**, **CS03** and **LCS01** exhibit two reversible oxidation waves with the first $E^{\text{ox}}_{1/2}$ value of 0.21 V, 0.02 V and 0.37 V vs vacuum, respectively. The first two oxidation waves are assigned to a consecutive extraction, mainly, from the di and triphenylamine units corresponding to one- and one-electron processes. **EP02** has only one reversible oxidation wave, whose $E^{\text{ox}}_{1/2}$ value is 0.57 V, very close to the value of the most widely HTM used, spiro-OMeTAD. The reason why **EP02** only have one oxidation wave might be attributed to the fact that it does not have *o,p*-methoxy groups in its molecular structure, that contribute to the electron donor nature of the other molecules²⁵. All of the four molecules show a reduction wave with the $E^{\text{red}}_{1/2}$ value of 1.10 V for **CS01**, **CS03**, and **LCS01**, reversible in all cases except **EP02**. The HOMO energy level obtained from $E^{\text{ox}}_{1/2}$ were found to be -5.01 eV, -4.81 eV, -5.36 eV and -5.16 eV, respectively for **CS01**, **CS03**, **EP02** and **LCS01**.

Design, synthesis and characterization of SMs for optoelectronic applications

Table 4.3: Oxidation potential, HOMO and LUMO energetic levels of benzothiadiazole-based molecules.

HTM	$E^{\text{ox}}_{1/2}$ (V)	E_{HOMO} (eV)	E_{LUMO} (eV)
CS01	0.21	-5.01	-3.00
CS03	0.02	-4.81	-2.88
EP02	0.57	-5.36	-3.02
LCS01	0.37	-5.16	-2.93
Spiro-OMeTAD ²⁶	0.58	-5.15	-2.05
PC₇₁BM ²⁷	-	-6.00	-4.00

The corresponding HOMO level of the four new molecules was higher than the valence band of the perovskite, so they can be used as hole transfer materials in perovskite solar cells. **LCS01** exhibited the same HOMO level than spiro-OMeTAD, which predicts an efficient hole transfer from the perovskite to the small molecule. LUMO level of the molecules was evaluated for using them as absorber for OSCs and PSCs. For all the new semiconductors, LUMO was approximately 1 V higher than the LUMO level of **PC₇₁BM**. Therefore, the fullerene can efficiently accept the photogenerated electrons.

4.2.3.3. Hole mobility measurements.

The analysis of the Space-Charge Limited Current (SCLC) is the most common technique to measure both hole and electron mobility on a single carrier device, as it was explained previously in Chapter 3. These devices were fabricated using one electrode hole-injection creating an ohmic contact that determines the performance of the device. This means that the recombination processes do not contribute to the performance of the device, but the mobility, electric fields and concentration of charges become the determinant factors.

Chapter 4

$$J_{\text{SCLC}} = \frac{9}{8} \epsilon_0 \epsilon_r \mu \frac{V_{\text{eff}}}{d^3} \quad \text{Equation 4.1}$$

Hole mobility values were obtained using the modified Mott-Gurney equation (Equation 4.1) when the voltage is higher than 2 or 3 V, which is the zone where the curves at 1 Sun and in dark conditions concur or are parallels. In this region, the photogenerated current has no influence on the overall current but is only due to the electric field. ϵ_0 is the electric constant, ϵ_r is the dielectric constant, μ corresponds to the hole mobility value, V_{eff} is the effective voltage and d is the thickness of the active layer. The J-V curves are shown in Figure 4.5.

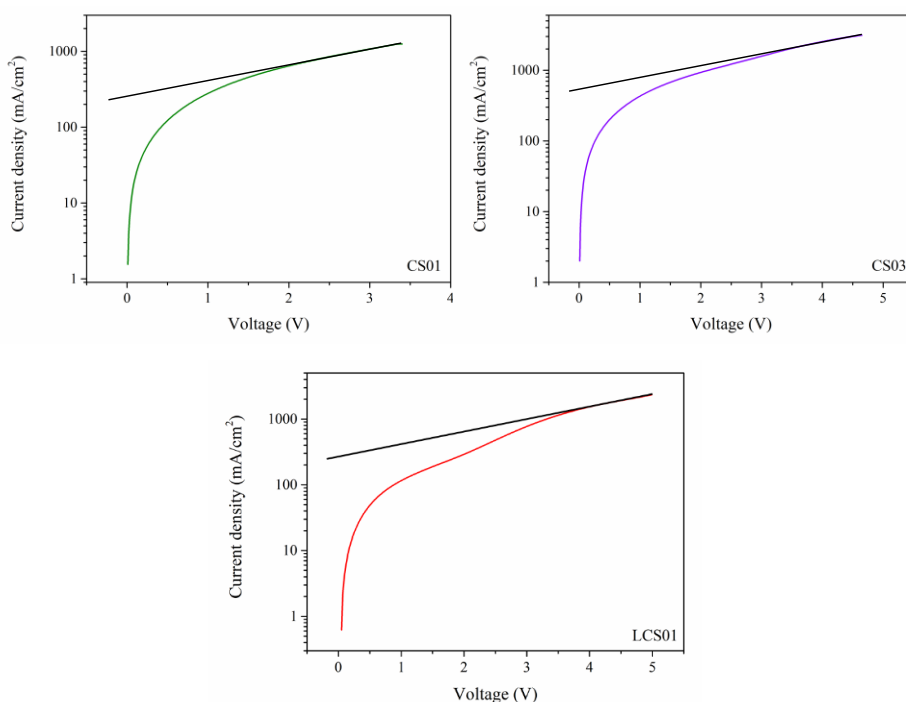


Figure 4.5: J–V curves for the hole only devices of **CS01**, **CS02**, **LCS01** and **EP02** using the SCLC method. The colour lines represent the IV curve of the device and the black lines correspond to an “eye-guide” for the zone of the J–V curve where it was done the fitting to Equation 4.1.

Design, synthesis and characterization of SMs for optoelectronic applications

The hole mobility is an important property to evaluate the competence of an HTM. Low hole mobility requires a very thin layer (< 100 nm) in order to have a good performance. After implementing the fitting of the Equation 4.1, we found the hole mobility values for three of the four molecules: $6.15 \cdot 10^4 \text{ cm}^2 \text{ V}^{-1} \text{ s}^{-1}$, $3.26 \text{ cm}^2 \text{ V}^{-1} \text{ s}^{-1}$ and $1.58 \text{ cm}^2 \text{ V}^{-1} \text{ s}^{-1}$ for **CS01**, **CS03** and **LCS01**, respectively. These mobilities corresponded to the doped small molecules. The dopant concentration used was 50 mol% of bis(trifluoromethane)sulfonimide lithium salt (LiTFSI) and 330 %mol of 4-tert-butylpyridine (*t*BP). According to the mobility values obtained, and comparing them with the most common electron donor material used to date in perovskite solar cells, spiro-OMeTAD, we might consider these new molecules excellent candidates as HTM for PSCs.

Table 4.4: Hole mobility values for the benzothiadiazole-based HTMs and spiro-OMeTAD.

	CS01	CS03	EP02	LCS01	Spiro-OMeTAD
$\mu \times 10^4$ ($\text{cm}^2 \text{V}^{-1} \text{s}^{-1}$)*	6.15	3.26	-	1.58	2.55 ²⁶

* μ corresponds to hole mobility. The values obtained are the average of minimum 5 measurements.

The hole mobility of **EP02** was not possible to measure because when applying high voltages, the temperature of the device increased making both the organic layer and the gold electrode melted (see Figure 4.6), probably caused by the presence and formation of shunting paths.

Chapter 4

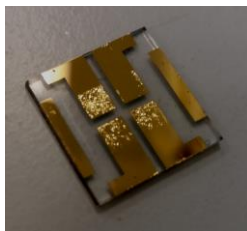


Figure 4.6: Picture of an only-hole device fabricated with **EP02** for hole mobility measurements.

Hole mobility measurements were carried out in the absence of additives. The results are shown below in Figure 4.7 and Table 4.5.

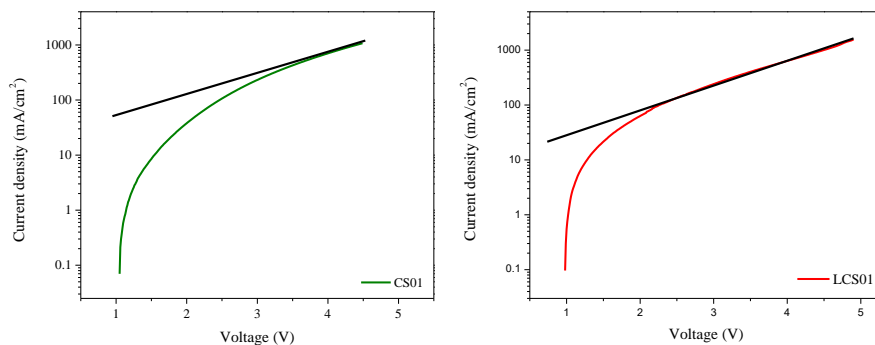


Figure 4.7: J–V curves for the hole only devices of undoped **CS01** and **LCS01** with no additives using the SCLC method. The colour lines represent the J–V curve of the device and the black line corresponds to an “eye-guide” for the zone of the J–V curve where was done the fitting to Equation 4.1.

Design, synthesis and characterization of SMs for optoelectronic applications

Table 4.5: Hole mobility values for **CS01**, **CS03** and **LCS01** in absence of additives.

SM	CS01	CS03	EP02	LCS01
$\mu \times 10^5 \text{ (cm}^2\text{V}^{-1}\text{s}^{-1}\text{)*}$	3.12	-	-	9.33

* μ is the hole mobility.

It can be seen that the values for hole mobility for **CS01** and **LCS01** are one order of magnitude smaller than with the use of additives. Although both molecules will be tested with and without the use of additives, based on these results, it is possible to think that they will have a better performance when the additives will be added to the solution. It was not possible to measure the hole mobility for **CS03** and **EP02** in absence of additives because the organic layer burnt in all the devices fabricated, as it is shown in Figure 4.8.

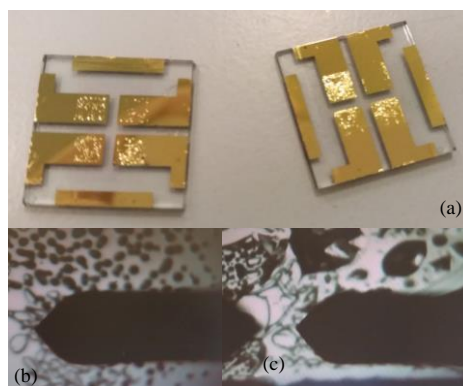


Figure 4.8: a) Hole mobility devices using **CS03** (left) and **EP02** (right) with no additives. b) Image the surface of a hole mobility device using **CS03** as hole transport material recorded with a profilometer. c) Image the

Chapter 4

surface of a hole mobility device using **EP02** as hole transport material recorded with a profilometer.

4.3. Triphenylamine and carbazole-based organic semiconductors.

The four molecules that will be described in this section were designed exclusively to be HTMs for PSCs. The aim was to synthesize low-cost and efficient hole conductors for highly efficient and stable PSCs. To date, spiro-OMeTAD is the best choice of small molecules for obtaining the best perovskite device performance despite of the difficulty of its synthesis and purification and its poor hole mobility ($2.55 \text{ cm}^2 \text{ V}^{-1} \text{ s}^{-1}$)²⁶, which makes necessary the use of dopants, decreasing the stability of long-term devices (in comparison with silicon-based solar cells). Therefore, the high production cost is so high that it is not the best option for large-scale production. To solve these inconveniences, many attempts have been done in the design and synthesis of new HTMs, changing the central core and introducing different donor moieties that lead into an appropriate HOMO level that matches with the valence band of the perovskite and hinders recombination processes.

In this work, TPA and carbazole units were chosen as electron donor groups, having in common the same substituent (1,3-dimethoxybenzene).

4.3.1. Donor units based on TPA and carbazole.

It is essential that HTMs include donor units in their molecular structure, such as triarylaminines and/or thiophenes moieties, among others. In this work, TPA and carbazole units have been used as substituents in the synthesis of the new molecules, as it is shown in Scheme 4.4. The nitrogen atom of the TPA acts as a doping site and can be stabilized through conjugation with neighbouring phenyl rings. It also helps to increase the intermolecular distance due to the non-

Design, synthesis and characterization of SMs for optoelectronic applications

planar configuration that increases the amorphous nature of the HTM layer, although it also reduces the hole mobility. For this reason, it is needed to balance these two properties, so the mobility could be high enough to transport the holes and the amorphous nature of the molecule can lead to a high glass transition temperature.

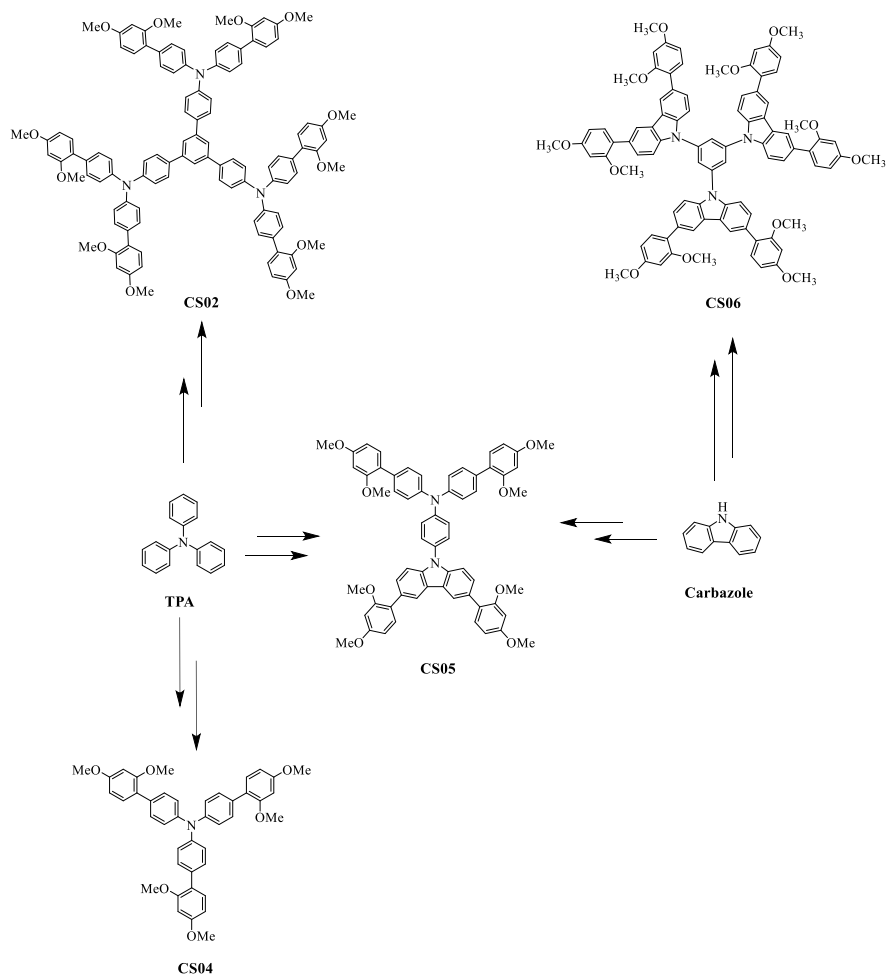
CS02 and **CS06** share the same central core, a phenyl ring which acts as a link between the donor units. **CS04** is a simple TPA-based HTM surrounded with 1,3-dimethoxybenzene and **CS05** is a combination of the TPA derivative used in all the molecules and the carbazole derivative.

As a result of the weak interaction between the donating moieties, it could be expected that this type of molecules will not absorb much in the visible range, yielding colourless solids that will not interfere with the light the perovskite collects.

4.3.2. Design and synthesis of triphenylamine and carbazole-based small molecules.

The general procedure for the preparation of 5'-(4-(bis(2',4'-dimethoxy-[1,1'-biphenyl]-4-yl)amino)phenyl)-N₄,N₄,N₄",N₄"-tetrakis(2',4'-dimethoxy-[1,1'-biphenyl]-4-yl)-[1,1':3',1"-terphenyl]-4,4"-diamine (**CS02**), tris(2',4'-dimethoxy-[1,1'-biphenyl]-4-yl)amine (**CS04**), N-(4-(3,6-bis(2,4-dimethoxyphenyl)-9H-carbazol-9-yl)phenyl)-N-(2',4'-dimethoxy-[1,1'-biphenyl]-4-yl)-2',4'-dimethoxy-[1,1'-biphenyl]-4-amine (**CS05**) and 1,3,5-tris(3,6-bis(2,4-dimethoxyphenyl)-9H-carbazol-9-yl)benzene (**CS06**) are shown in Scheme 4.4 and are described in detail in Section 4.4.

Chapter 4



Scheme 4.4: Scheme of the new hole transport materials based on a TPA (left centered) and carbazole (right centered).

The reactions involved in the synthesis of the TPA and carbazole derivative consisted first in the coupling of the 1,3-dimethoxybenzene units using Suzuki-coupling procedure in DMF and H₂O, followed by a bromination with (n-C₄H₉)₄NBr₃ in DMF only for the TPA derivative. After that, in order to obtain **CS05** and **CS06**, Buchwald-Hartwig amination between the carbazole and a halogen derivative were performed in toluene. The synthesis of **CS02** and **CS04**

Design, synthesis and characterization of SMs for optoelectronic applications

finish by the Suzuki cross-coupling reaction of the bromide-TPA derivative with 2-(2,4-dimethoxyphenyl)-4,4,5,5-tetramethyl-1,3,2-dioxaborolane.

4.3.3. Thermal, optical, electrochemical and hole mobility properties.

This section will address the main properties of the new four hole transport materials in order to know if they are good candidates to be used in perovskite solar cells.

4.3.3.1. Thermal properties.

The thermal behaviour of these small molecules was analysed by thermogravimetric analysis (TGA) and differential scanning calorimetry (DSC) measurements. All the data are collected in Table 4.6. From TGA, it was found that the four molecules have a higher decomposition temperature than Spiro-OMeTAD (417 °C), up to 464.2 °C, 445.7 °C, 451.7 °C and 465.2 °C for **CS02**, **CS04**, **CS05** and **CS06**, respectively. The high decomposition temperatures with a weight loss of 5 % indicate good thermal stability, required for photovoltaic devices. The TGA curves for all of them are depicted in Figure 4.9.

Chapter 4

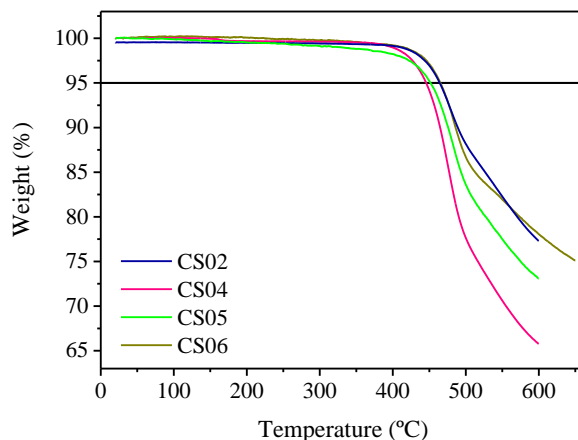
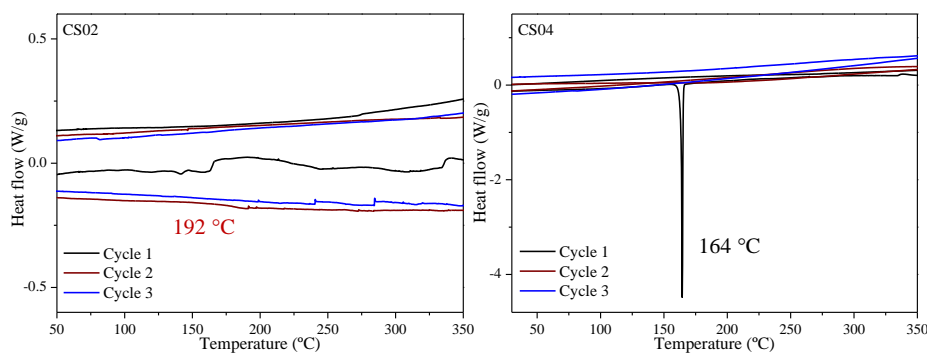


Figure 4.9: Thermal analysis of **CS02**, **CS04**, **CS05** and **CS06** at scan rate of 10 °C/min under N₂ atmosphere.

The thermal transitions were studied by DSC (Figure 4.10). During the first heating scan the melting transition temperatures of **CS04** and **CS06** were observed at 164 and 269 °C, respectively. After consecutive heating/cooling cycles no more melting or crystallization peaks were detected. During the second and third heating cycle their T_g was detected for **CS02** (192 °C), **CS05** (170 °C) and **CS06** (180 °C), indicating that the materials could exist in both crystalline and amorphous estates. **CS04** do not present T_g, which means it only exists with an amorphous phase.



Design, synthesis and characterization of SMs for optoelectronic applications

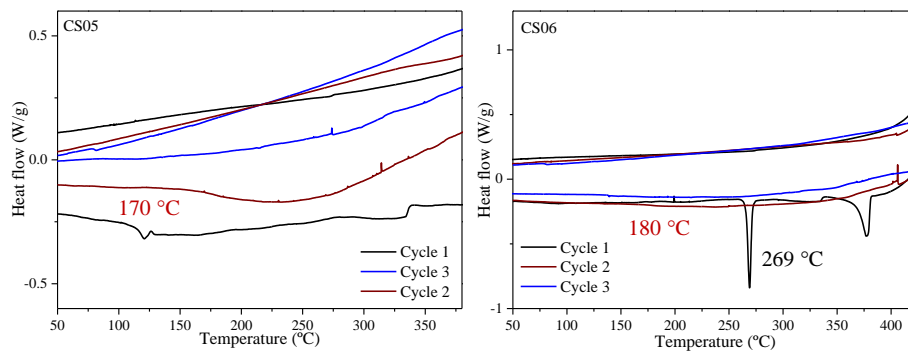


Figure 4.10: DSC experiment for **CS02**, **CS04**, **CS05** and **CS06** at scan rate of 10 °C/min under N₂ atmosphere.

The glass transition temperature of the Spiro-OMeTAD is 126 °C²⁸, lower than the values obtained for these molecules, indicating that they have more stabilized amorphous estate.

Table 4.6: Thermal properties of **CS02**, **CS04**, **CS05** and **CS06**.

SM	T _{des} (°C) ^[a]	T _m (°C) ^[b]	T _c (°C) ^[c]	T _g (°C) ^[d]
CS02	464.2	-	-	192
CS04	445.7	164	-	-
CS05	451.7	-	-	170
CS06	465.2	269	-	180
Spiro-OMeTAD	417	234	-	126

^[a] Decomposition temperature determined from TGA (5 % weight loss).

^[b] Melting temperature and ^[c] crystal temperature determined from the first cycle of DSC and ^[d] Glass transition temperature determine from the

Chapter 4

second cycle of DSC. All experiments were carried out under N₂ atmosphere at scan rate of 10 °C/min.

4.3.3.2. Optical and electrochemical properties.

The normalized UV-Vis absorption and emission spectra of the new small molecules (10⁻⁵ M) in DCM are shown in Figure 4.11. **CS02** and **CS04** have almost identical absorption band in the UV region with the absorption maximum wavelength ($\lambda_{\text{abs, max}}$) at 340.5 nm and 334.5 nm, respectively, while **CS05** and **CS06** have their maximum wavelength blue shifted, at 302.5 nm and 305.5 nm. This shift in the $\lambda_{\text{abs, max}}$ could be related to the incorporation of carbazole units to the molecular structure. The absorption bands that appear between 300 and 400 nm can be explained by the π - π^* transitions of the conjugated system. None of them shows absorption in the visible region of the spectrum. The emission spectra exhibit a maximum centred at 443.0 nm, 405.0 nm, 379.0 nm and 380.0 nm for **CS02**, **CS04**, **CS05** and **CS06**, respectively, when they are excited to the $\lambda_{\text{abs, max}}$.

The optical band gap corresponding to E₀₋₀ was determined at the intersection of the normalized absorption and emission for each molecule by applying the Equation 3.1 (see Table 4.7).

Design, synthesis and characterization of SMs for optoelectronic applications

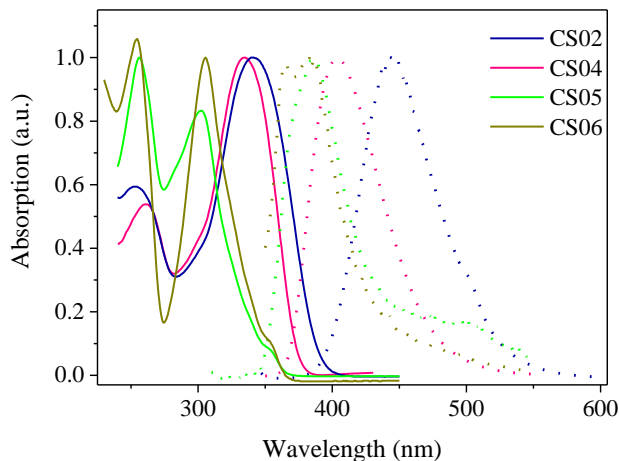


Figure 4.11: Absorption (solid line) and emission (dashed line) spectra of **CS02**, **CS04**, **CS05** and **CS06** in DCM at room temperature.

Table 4.7: Optical parameters of **CS02**, **CS04**, **CS05** and **CS06**.

SM	λ_{abs} (nm)	λ_{em} (nm)	ϵ ($\text{M}^{-1}\text{cm}^{-1}$)	E_{0-0} (eV)
CS02	340.5	443.0	21744	3.16
CS04	334.5	405.0	26797	3.54
CS05	302.5	379.0	13127	3.69
CS06	305.5	380.0	12838	3.60

Cyclic voltammetry was performed in order to estimate the energy levels HOMO and LUMO of the four new molecules (see Figure 4.12). The measurements were carried out in 0.1 M solution of (*n*-Bu)₄NPF₆ (TBAPF₆) in dry DCM and under argon atmosphere, using glassy carbon electrode as working electrode, Ag/Ag⁺ as reference electrode and platinum wire as counter electrode. Fc/Fc⁺ was used as internal standard. The data derived from the redox

Chapter 4

potentials with the HOMO energies estimated from the first half-wave oxidation potential ($E^{\text{ox}}_{1/2}$) and the LUMO energies are summarized in Table 4.8.

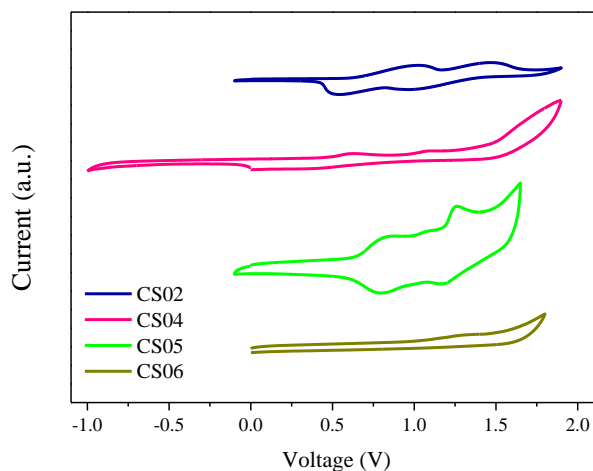


Figure 4.12: Cyclic voltammetry of **CS02**, **CS04**, **CS05** and **CS06**, measured using ferrocene as an internal reference at room temperature with a scan rate of 10 mV/s.

As it is shown in Figure 4.12, the new family of molecules are only active in the anodic region, although their electrochemical behaviour is entirely different. **CS02** and **CS05** exhibit two reversible oxidation waves with $E^{\text{ox}}_{1/2}$ value for the first wave of 0.57 V and 0.42 V vs vacuum, respectively. This oxidation waves can be assigned to consecutive extraction of one- and one-electron process from the TPA. **CS04** has one reversible wave at 0.07 V and another irreversible oxidation wave at 0.65 V and for **CS06**, the CV only revealed one irreversible wave at 0.76 V. The HOMO energy levels vs vacuum estimated from $E^{\text{ox}}_{1/2}$ using the Equation 3.2 from Chapter 3, were found to be -5.18 eV, -4.73 eV, -5.20 eV and -5.98 eV for **CS02**, **CS04**, **CS05**, and **CS06** respectively.

Design, synthesis and characterization of SMs for optoelectronic applications

Table 4.8: Oxidation potential and HOMO and LUMO energetic levels of **CS02**, **CS04**, **CS05** and **CS06**.

HTM	E^{ox}_{1/2} (V)	E_{HOMO} (eV)	E_{LUMO} (eV)
CS02	0.37	-5.18	-2.03
CS04	0.07	-4.73	-1.26
CS05	0.42	-5.20	-1.51
CS06	0.76	-5.98	-2.38
Spiro-OMeTAD	0.57	-5.15	-2.05

Only **CS04** exhibits a higher HOMO level (-4.73 eV) than spiro-OMeTAD (-5.15 eV). **CS02** and **CS05** present a similar value (-5.18 eV and -5.20 eV, respectively), whereas the HOMO value for **CS06** is considerably much lower than for any of the others small molecules in this family (-5.98 eV). It seems that the introduction of carbazole units in the molecular structure leads to a lower value of the HOMO level. Generally, when a conjugated molecule has electron withdrawing substituents attached to it, the electron density of the π -system decreases for that molecule. This means that the molecule is more stable and there is an increase in the oxidation potential corresponding to a shift of the HOMO level to lower energy. It was probed that substitutions in the 3 and 6 positions of the carbazole unit have stronger stabilizing effect that can explain the low value of HOMO obtained for **CS06** compared with the other three HTMs²⁹.

Chapter 4

4.3.3.3. Hole mobility measurements.

Hole mobility measurements were carried out following the Space-Charge Limited Current (SCLC) method, as it was described in Chapter 3. The results shown in Table 4.9 correspond to the doped layer of the hole transport small molecules. They were doped using 50 mol% of bis(trifluoromethane)sulfonimide lithium salt (LiTFSI) and 330 %mol of 4-tert-butylpyridine (*t*BP).

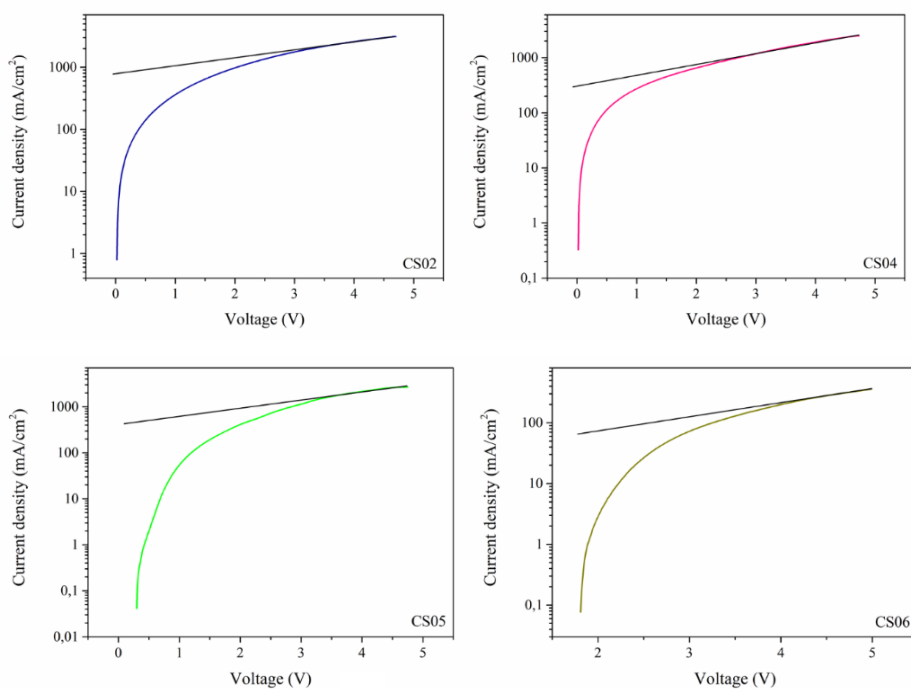


Figure 4.13: J–V curves for the hole only devices of doped **CS02**, **CS04**, **CS05** and **CS06** using the SCLC method. The colour lines represent the J–V curve of the device and the black line corresponds to an “eye-guide” for the zone of the J–V curve where was done the fitting to Equation 4.1.

Design, synthesis and characterization of SMs for optoelectronic applications

Table 4.9: Hole mobility values for doped **CS02**, **CS04**, **CS05** and **CS06** devices using SCLC method.

HTM	CS02	CS04	CS05	CS06	Spiro-OMeTAD
$\mu \times 10^4 \text{ (cm}^2\text{V}^{-1}\text{s}^{-1}\text{)}$	2.04	2.93	2.46	2.45	2.55

* μ : Hole mobility value. The results are the average of at least 5 measurements.

The hole mobility values and the J-V curves for these molecules in presence of additives are collected in Table 4.9 and shown in Figure 4.13 while in absence of additives are collected in Table 4.10 and in Figure 4.14. The values obtained correspond to the average of minimum 5 measurements. The hole mobilities of the four HTMs are in the same order of magnitude than spiro-OMeTAD, used as reference in PSCs, showing there are not significant differences that can affect the device performance. It can be seen that the hole mobility values of **CS02**, **CS04** and **CS05** are one order the magnitude smaller than when additives are added to the stock solution, while the value for **CS06** is two orders of magnitude lower. Based on the results obtained, it is plausible to think that devices based on these molecules will have better performance when use additives.

Table 4.10: Hole mobility values for **CS02**, **CS04**, **CS05** and **CS06** in absence of additives.

HTM	CS02	CS04	CS05	CS06
$\mu \times 10^5 \text{ (cm}^2\text{V}^{-1}\text{s}^{-1}\text{)}^*$	5.23	1.19	2.74	0.18

* μ is the hole mobility.

Chapter 4

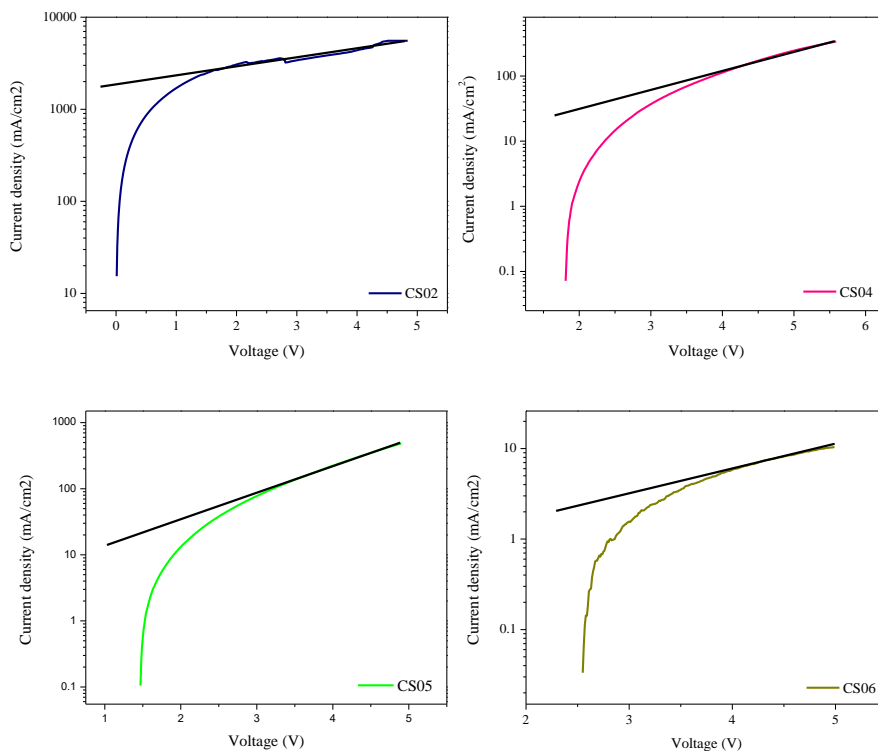


Figure 4.14: J–V curves for the hole only devices of undoped **CS02**, **CS04**, **CS05** and **CS06** with no additives using the SCLC method. The colour lines represent the J–V curve of the device and the black line corresponds to an “eye-guide” for the zone of the J–V curve where was done the fitting to Equation 4.1.

4.4. Conclusions.

In summary, a more rapid and efficient synthesis of two series of novel BT-, TPA- and carbazole-based compared with the polymers used in OSCs and with the spiro-OMeTAD was reported, which make them good alternates in PV devices. They are easily scalable and low the production costs. Molecules containing BT unit showed absorption in the visible range of the spectrum while

Design, synthesis and characterization of SMs for optoelectronic applications

the molecules based on TPA and carbazole groups only have absorption between 300 and 400 nm. The HOMO and LUMO levels of each compound based on CV, UV-Vis and PL spectra measurements, were found to be in agreement with the energy levels of the materials that will sandwich them, either in OSCs or PSCs. Hole mobility values for the molecules used as HTMs in PSCs are optimal to be used in presence of dopants.

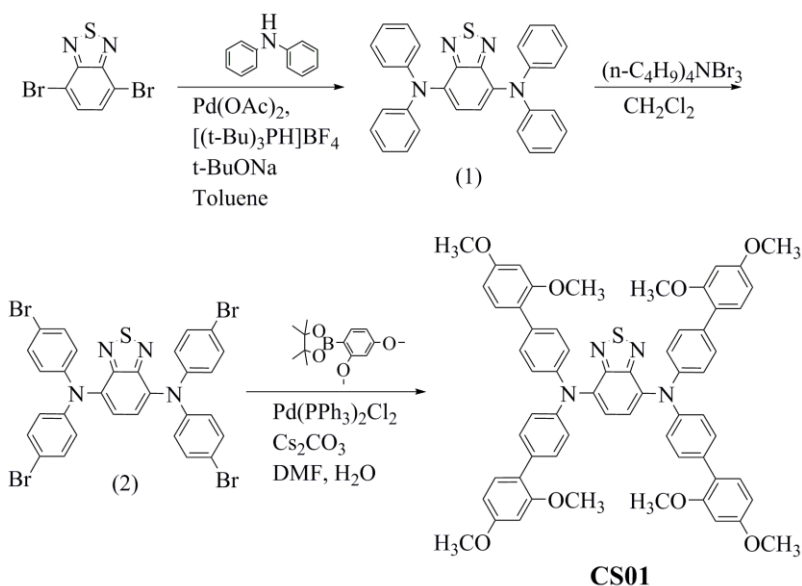
Chapter 4

4.5. Experimental procedures.

In the synthesis of new organic materials, the most common reactions used were the ones that allowed us to create new bonds between C-C, C-N or C-O, so it is possible to build bigger molecules including organic groups, as the ones mentioned previously in this Chapter, so they will have the properties needed for the applications they were designed for. This section will describe the synthetic procedures used in this work.

4.5.1 Benzothiadiazole-based small molecules.

4.5.1.1. Synthesis of CS01.



Scheme 4.5: Synthetic route of CS01.

Synthesis of N4,N4,N7,N7-tetraphenylbenzo[c][1,2,5]thiadiazole-4,7-diamine (1): 4,7-dibromobenzo[c][1,2,5]thiadiazole (479.3 mg, 1.63 mmol),

Design, synthesis and characterization of SMs for optoelectronic applications

diphenylamine (810 mg, 4.79 mmol), Pd(OAc)₂ (21.51 mg, 0.096 mmol), [(*t*-Bu)₃PH]BF₄ (83.44 mg, 0.29 mmol) and *t*-BuONa (3.45 g, 35.94 mmol) were dissolved in dry toluene (16 mL) and the mixture was stirred for 10 hours at 120°C under argon atmosphere. The product was extracted with toluene and dried over Na₂SO₄. The solvent was evaporated under vacuum and the residue was purified by silica-gel column chromatography using PE and DCM as eluents to obtain a pink solid (675.7 mg, 88 %). The spectroscopic data were in good agreement with those previously reported in the literature³⁰. ¹H-NMR (500 MHz, CDCl₃). δ_H: 7.29 (t, 8H); 7.11 (s, 2H); 7.10-7.02 (m, 12H).

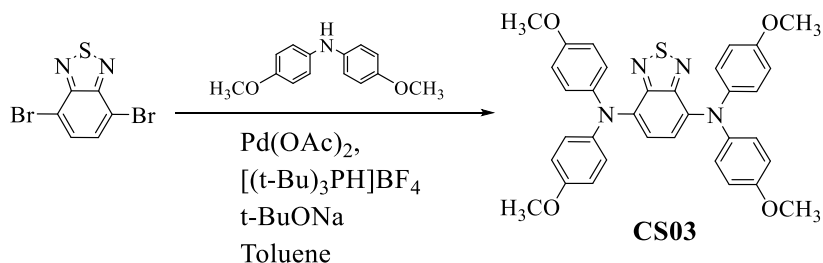
Synthesis of N₄,N₄,N₇,N₇-tetrakis(4-bromophenyl)benzo[*c*][1,2,5]thiadiazole-4,7-diamine (2): Compound (2) (550 mg, 1.17 mmol) was dissolved in DCM (180 mL) and (*n*-C₄H₉)₄Br₃ (5.63 g, 11.68 mmol) was added. The reaction mixture was stirred at room temperature for five hours. The mixture was extracted with DCM, dried with Na₂SO₄ and the solvent was removed under reduced pressure to yield a purple solid (778.69 mg, 85 %). ¹H NMR (500 MHz, CDCl₃). δ_H: 7.37 (d, *J* = 8.86 Hz, 8H); 7.10 (s, 2H); 6.93 (d, *J* = 8.86 Hz, 8H). ¹³C NMR (125 MHz, CDCl₃). δ_C: 152.20, 146.35, 135.39, 132.56, 125.34, 124.82, 116.43. HRMS (ESI⁺) *m/z* calcd for C₃₀H₁₈Br₄N₄S 781.7980, found 781.8004.

Synthesis of N₄,N₄,N₇,N₇-tetrakis(2',4'-dimethoxy-[1,1'-biphenyl]-4-yl)benzo[*c*][1,2,5]thiazole-4,7-diamine (CS01): N₄,N₄,N₇,N₇-tetrakis(4-bromophenyl)benzo[*c*][1,2,5]thiadiazole-4,7-diamine (2) (673.40 mg, 0.89 mmol), 2-(2,4-dimethoxyphenyl)-4,4,5,5-tetramethyl-1,3,2-dioxaborolane (2.35 g, 8.89 mmol) and Pd(PPh₃)₂Cl₂ (962.2 mg, 1.37 mmol) was dissolved in dry DMF (80 mL). Then, cesium carbonate (7.24 g, 22.23 mmol) and distilled water (32 mL) were added before degassing. The reaction mixture was stirred at 120°C overnight under nitrogen atmosphere. The mixture was extracted with DCM, dried with Na₂SO₄ and the solvent was removed under reduced pressure.

Chapter 4

The product was purified by silica-gel column chromatography using PE and EtOAc as eluents to obtain a purple product. After the recrystallization with MeOH, the solid obtained was dried under vacuum (500 mg, 49 %). ^1H NMR (500 MHz, CDCl_3). δ_{H} : 7.46 (d, $J = 8.47$ Hz, 8H); 7.31- 7.29 (m, 6H); 7.18 (d, $J = 8.47$ Hz, 8H); 6.60-6.58 (m, 8H); 3.87 (s, 12H); 3.84 (s, 12H). ^{13}C NMR (125 MHz, CDCl_3). δ_{C} : 160.0, 157.5, 152.9, 146.1, 135.8, 132.79, 131.1, 130.1, 125.6, 123.2, 123.0, 104.6, 99.0, 55.6, 55.4. HRMS (ESI $^+$) m/z calcd for $\text{C}_{62}\text{H}_{54}\text{N}_4\text{NaO}_8\text{S}$ 1037.3555, found 1037.3507.

4.5.1.2. Synthesis of CS03.



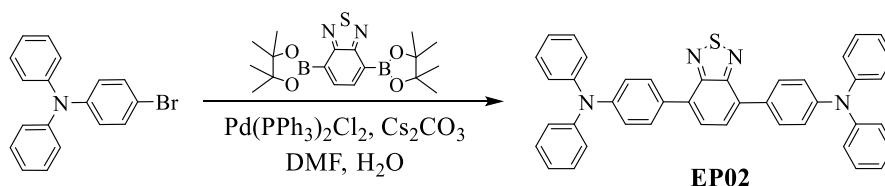
Scheme 4.6: Synthetic pathway of CS03.

Synthesis of N4,N4,N7,N7-tetrakis(4-methoxyphenyl)benzo[c][1,2,5]thiadiazole-4,7-diamine (CS03): 4,7-dibromobenzo[c][1,2,5]thiadiazole (170.00 mg, 0.58 mmol), bis(4-methoxyphenyl)amine (291.64 mg, 1.27 mmol), $\text{Pd}(\text{OAc})_2$ (5.61 mg, 0.03 mmol), $[(t\text{-Bu})_3\text{PH}]\text{BF}_4$ (22.05 mg, 0.08 mmol) and $t\text{-BuONa}$ (305.66 mg, 3.18 mmol) were dissolved in dry toluene (16 mL) and the mixture was stirring for 10 hours at 120°C under argon atmosphere. The product was extracted with toluene and dried over Na_2SO_4 . The solvent was evaporated under vacuum and the residue was purified by silica-gel column chromatography using PE and DCM as eluents to obtain a pink solid (211.20 mg, 62 %). ^1H NMR (500 MHz,

Design, synthesis and characterization of SMs for optoelectronic applications

CDCl_3). δ_{H} : 7.01 (d, $J = 8.96$ Hz, 8H); 6.90 (s, 2H); 6.83 (d, $J = 8.96$ Hz, 8H); 3.79 (s, 12H). ^{13}C NMR (125 MHz, CDCl_3). δ_{C} : 155.66, 152.24, 141.81, 135.87, 125.24, 122.96, 114.62, 55.61. HRMS (ESI⁺) m/z calcd for $\text{C}_{34}\text{H}_{30}\text{N}_4\text{NaO}_4\text{S}$ 613.1880, found 613.1883.

4.5.1.3. Synthesis of EP02.

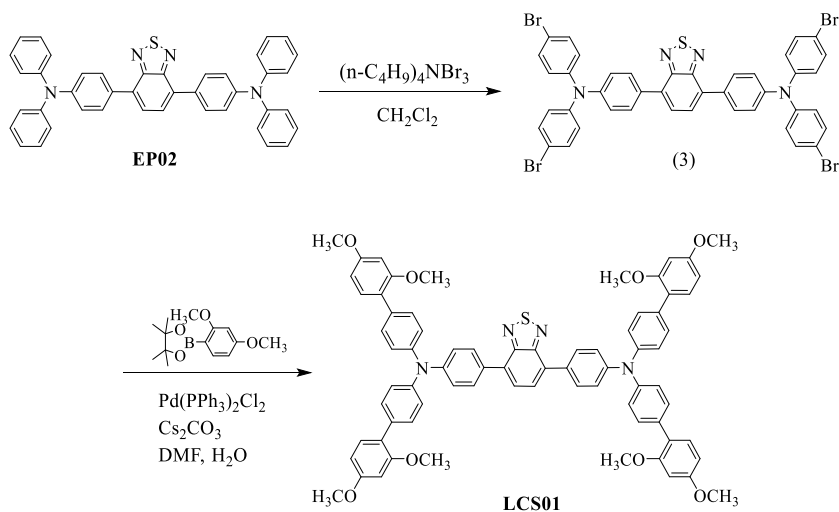


Scheme 4.7: Synthetic route of EP02.

Synthesis of 4,4'-(benzo[1,2,5]thiadiazole-4,7-diyl)bis(N,N-diphenylaniline): EP02: A solution of 4-bromo-N,N-diphenylaniline (1.17 g, 3.61 mmol); 4,7-di(1,3,2-dioxaborolan-2-yl)benzo[1,2,5]thiadiazole (500.00 mg, 1.29 mmol), bis(triphenylphosphine)palladium(II) dichloride (430.43 mg, 0.61 mmol) in dry DMF (100 mL) was degassed. Then, cesium carbonate (2.94 g, 9.02 mmol) and distil H₂O (13.5 mL) were added and the mixture was degassed again. The reaction mixture was stirred overnight at 120°C under nitrogen atmosphere. The orange crude was extracted into DCM and dried over magnesium sulfate. After removing the solvent under reduced pressure, the residue was purified by column chromatography using a gradient of PE and EtOAc as solvents to yield an orange solid, (681.98 mg, 85 %). The spectroscopic data were in good agreement with those previously reported in the literature³¹. ^1H NMR (500 MHz, CDCl_3). δ_{H} : 7.87 (d, $J = 8.8$ Hz, 4H); 7.73 (s, 2H); 7.27 (t, 8H); 7.20 (dd, $J = 7.5$ Hz, 8H); 7.17 (dd, $J = 7.5$ Hz, 8H); 7.05 (t, 4H). ^{13}C NMR (125 MHz, CDCl_3). δ_{C} : 154.30, 148.12, 147.64, 132.31, 131.15, 130.04, 129.50, 127.58, 125.03, 123.43, 123.08. MS (MALDI-TOF) m/z calcd for $\text{C}_{42}\text{H}_{30}\text{N}_4\text{S}$ 622.2191, found 622.2223.

Chapter 4

4.5.1.4. Synthesis of **LCS01**.



Scheme 4.8: synthetic pathway of **LCS01**.

Synthesis of 4,4'-(benzo[c][1,2,5]thiadiazole-4,7-diyl)bis(N,N-bis(4-bromophenyl)aniline) (3): ($n\text{-C}_4\text{H}_9$) $_4\text{NBr}_3$ (2.32 g, 4.01 mmol) was added to a solution of solution of 4,4'-(benzo[c][1,2,5]thiadiazole-4,7-diyl)bis(N,N-diphenylaniline) (300 mg, 0.40 mmol) in CH_2Cl_2 (60 mL). The reaction was stirred at room temperature for three hours. The crude mixture was extracted into DCM and the organic layer was washed with a saturated solution of NaHSO_4 , and water; and dried over sodium sulfate. Then, the solvent was evaporated and the residue was purified by column chromatography using PE and DCM as solvents to obtain a pink solid (404.87 mg, 90 %). The spectroscopic data were in good agreement with those previously reported in the literature³¹. $^1\text{H NMR}$ (500 MHz, CDCl_3) δ_{H} : 7.88 (d, $J = 8.8$ Hz, 4H); 7.73 (s, 2H); 7.37 (d, $J = 8.8$ Hz, 8H); 7.18 (d, $J = 8.8$ Hz, 4H); 7.02 (d, $J = 8.8$ Hz, 8H).

Design, synthesis and characterization of SMs for optoelectronic applications

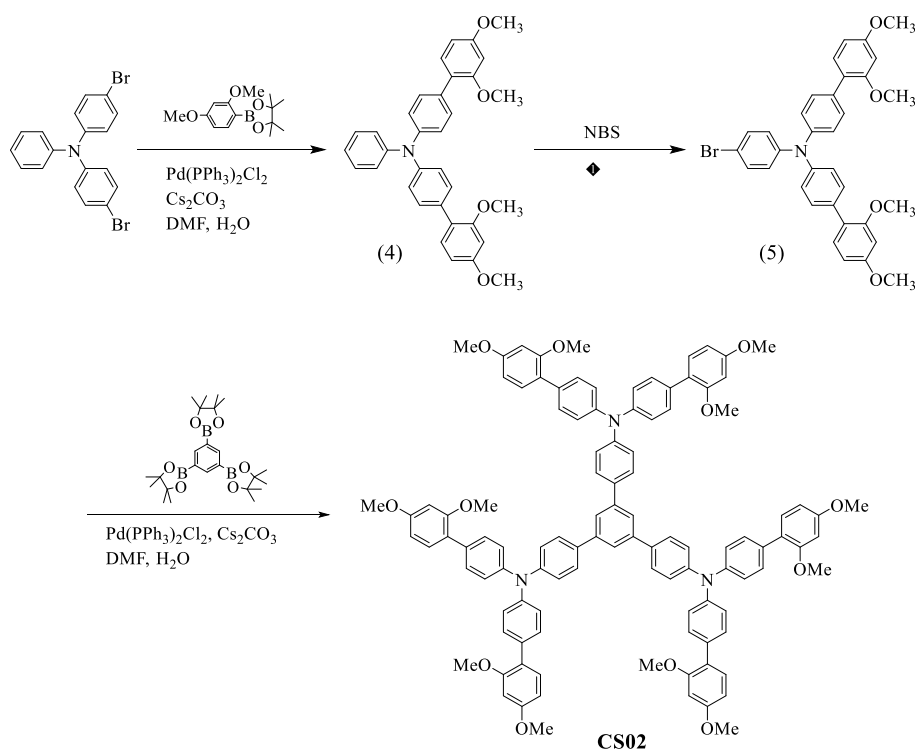
Synthesis of N,N'-(benzo[c][1,2,5]thiadiazole-4,7-diylbis(4,1-phenylene))bis(N-(2',4'-dimethoxy-[1,1'-biphenyl]-4-yl)-2',4'-dimethoxy-[1,1'-biphenyl]-4-amine): LCS01: A solution of 4,4'-(benzo[c][1,2,5]thiadiazole-4,7-diyl)bis(N,N-bis(4-bromophenyl)aniline) (303.00 mg, 0.39 mmol), 2-(2,4-dimethoxyphenyl)-1,3,2-dioxaborolane (647.09 mg, 3.11 mmol), Pd(PPh₃)₂Cl₂ (363.76 mg, 0.52 mmol) in dry DMF (70 mL) was degassed. Then, cesium carbonate (2.53 g, 7.77 mmol) in water (11 mL) was added to the mixture and degassed again. The reaction was stirred overnight at 120°C. The crude product was extracted into DCM, dried over MgSO₄ and the solvent was removed under reduced pressure. The crude was purified by silica-gel column chromatography using PE and ethyl acetate to yield an orange solid (294.82 mg; 65 %). ¹H NMR (500 MHz, CDCl₃) δH: 7.90 (d, J = 8.8Hz, 4H); 7.75 (s, 2H); 7.43 (d, J = 8.8Hz); 7.31 (d, J = 8.8Hz, 4H); 7.27 (d, J = 8.8Hz, 4H); 7.23 (d, J = 8.8Hz, 8H); 6.56 (m, 8H); 3.84 (s, 12H); 3.82 (s, 12H). ¹³C NMR (125 MHz, CDCl₃). δ_C: 160.24, 157.60, 154.35, 148.12, 145.89, 133.28, 132.33, 131.21, 131.12, 130.00, 127.59, 124.44, 123.55, 123.22, 104.79, 99.17, 55.68, 55.57. MS (MALDI-TOF) m/z calcd for C₇₄H₆₂N₄O₈S 1166.4288, found 1166.4422.

Chapter 4

4.5.2. Triphenylamine and carbazole-based Organic Semiconductors as Hole Transporting Materials.

In this case, the following materials that are going to be described have been exclusively used as HTMs for PSCs. They are TPAs and carbazole based HTMs.

4.5.2.1. Synthesis and characterization of CS02.



Scheme 4.9: Synthetic route for CS02.

Synthesis of N-(2',4'-dimethoxy-[1,1'-biphenyl]-4-yl)-2',4'-dimethoxy-N-phenyl-[1,1'-biphenyl]-4-amine (4): 4-bromo-N-(4-bromophenyl)-N-phenylaniline (3 g, 7.44 mmol), 2-(2,4-dimethoxyphenyl)-4,4,5,5-tetramethyl-

Design, synthesis and characterization of SMs for optoelectronic applications

1,3,2-dioxaborolane (5.5 g, 20.84 mmol) and Pd(PPh₃)₂Cl₂ (2.34 g, 3.33 mmol) were dissolved in dry DMF (320 mL). Cesium carbonate (16.97 g, 52.08 mmol) and distil water (75 mL) were added before degassing the mixture. The reaction mixture was stirring at 120°C overnight under nitrogen atmosphere. The mixture was extracted with DCM, dried with Na₂SO₄ and the solvent was removed under reduced pressure. The product was purified by silica-gel column chromatography using PE and EtAcO (3.59 g, 93 %). ¹H NMR (500 MHz, CDCl₃). δ_H: 7.41 (d, J = 8.7 Hz, 4H); 7.28 (d, J = 8.7, 4H); 7.26 (t, 2H); 7.21 (d, J = 8.7 Hz, 2H); 7.15 (d, J = 8.7 Hz, 4H); 3.86 (s, 6H); 3.83 (s, 6H). ¹³C NMR (125 MHz, CDCl₃). δ_C: 160.16, 157.57, 147.98, 146.28, 132.61, 130.21, 129.30, 124.62, 123.68, 123.29, 122.78, 104.76, 99.15, 55.66, 55.55. HRMS (ESI⁺) m/z calcd for C₃₄H₃₁NNaO₄ 540.2133, found 540.2145.

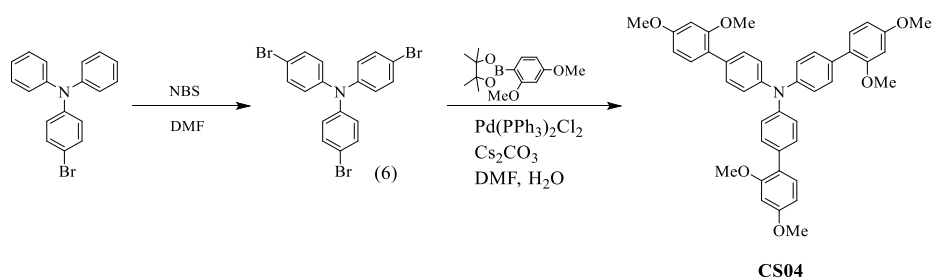
Synthesis of N-(4-bromophenyl)-N-(3',5'-dimethoxy-[1,1'-biphenyl]-4-yl)-2',4'-dimethoxy-[1,1'-biphenyl]-4-amine (5): 5,7-bis(4,4,5,5-tetramethyl-1,3,2-dioxaborolan-2-yl)-2,3-dihydrothieno[3,4-b][1,4]dioxine (4) (3.59 g, 6.94 mmol) was dissolved into DMF (100 mL). The solution was cooled to 0°C and NBS (1.36 g, 7.63 mmol) was added slowly. The mixture was stirring for 1 hour at 0°C and 2 hours at room temperature. Water was added to precipitate a white solid that was filtered off and washed with methanol to obtain the product (3.76 g, 91 %). ¹H-NMR (500 MHz, CDCl₃). δ_H: 7.39 (d, J = 8.6 Hz); 7.32 (d, J = 8.8 Hz, 2H); 7.23 (d, J = 8.8 Hz); 7.10 (d, J = 8.6 Hz, 4H); 6.54 (m, 4H); 3.83 (s, 6H); 3.80 (s, 6H). ¹³C NMR (125 MHz, CDCl₃). δ_C: 160.25, 157.54, 145.75, 133.22, 132.22, 131.16, 130.36, 130.29, 125.49, 123.97, 123.07, 114.79, 104.77, 99.13, 55.64, 55.55. HRMS (MALDI⁺) m/z calcd for C₃₄H₃₀BrNO₄ 595.1358, found 595.1348.

Synthesis of 5'-(4-(bis(2',4'-dimethoxy-[1,1'-biphenyl]-4-yl)amino)phenyl)-N4,N4,N4'',N4''-tetrakis(2',4'-dimethoxy-[1,1'-biphenyl]-4-yl)-[1,1':3,1''-terphenyl]-4,4''-diamine: CS02: N-(4-bromophenyl)-N-(3',5'-dimethoxy-

Chapter 4

[1,1'-biphenyl]-4-yl)-2',4'-dimethoxy-[1,1'-biphenyl]-4-amine (5) (273.02 g, 0.60 mmol), N-(4-bromophenyl)-N-(2',4'-dimethoxy-[1,1'-biphenyl]-4-yl)-2',4'-dimethoxy-[1,1'-biphenyl]-4-amine (2.5 g, 4.19 mmol) and Pd(PPh₃)₂Cl₂ (470.27 mg, 0.67 mmol) was dissolved in dry-DMF (150 mL). The mixture was degassed. Cesium carbonate (3.44 g, 10.48 mmol) and distilled water (15.2 mL) were added before degassing again. The reaction mixture was stirring at 120°C overnight under nitrogen atmosphere. The mixture was extracted with DCM, dried over Na₂SO₄ and the solvent was removed under reduce pressure. The product was purified by silica-gel column chromatography using PE and EtAcO to obtain a white solid (125 mg, 13 %). ¹H-NMR (400 MHz, CDCl₃). δ_H: 7.74 (s, 3H); 7.61 (d, J = 8.6 Hz, 6H); 7.44 (d, J = 8.6 Hz, 12H); 7.31 – 7.56 (m, 12H); 6.60 – 6.54 (m, 12H); 3.85 (s, 18H); 3.83 (s, 18H). ¹³C NMR (125 MHz, CDCl₃). δ_C: 160.20, 157.59, 146.10, 135.57, 134.34, 132.90, 131.24, 130.30, 130.26, 128.11, 124.33, 123.98, 123.26, 104.77, 99.15, 55.67, 55.56. HRMS (ESI⁺) m/z calcd for C₁₀₈H₉₃N₃O₁₂ 811.8374, found 811.8384.

4.5.2.2. Synthesis and characterization of CS04.



Scheme 4.10: Synthetic route for CS04.

Synthesis of tris(4-bromophenyl)amine (6): to a solution of 4-bromo-N,N-diphenylaniline (600.00 mg, 1.49 mmol) in DMF (26 mL) at 0°C, NBS (317.71 mg, 1.79 mmol) was added slowly. The mixture was stirring 1 hour at 0°C and another two hours at room temperature before adding distill water. It was

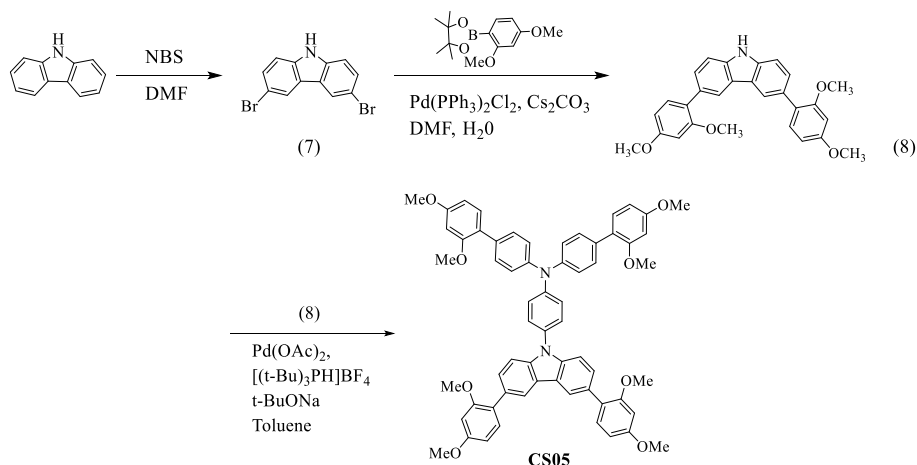
Design, synthesis and characterization of SMs for optoelectronic applications

extracted with DCM, dried over MgSO₄ and solvents were evaporated under reduced pressure. The product was crystallized from hexane to obtain a white solid (617.40 mg, 86 %). The spectroscopic data were in good agreement with those previously reported in the literature³². ¹H-NMR (500 MHz, CDCl₃). δ_H: 7.34 (d, J = 8.9 Hz, 6H); 6.91 (d, J = 8.9 Hz, 6H).

Synthesis of tris(2',4'-dimethoxy-[1,1'-biphenyl]-4-yl)amine: CS04: tris(4-bromophenyl)amine (9) (496.3 mg, 1.03 mmol), 2-(2,4-dimethoxyphenyl)-4,4,5,5-tetramethyl-1,3,2-dioxaborolane (950.87 mg, 3.60 mmol) and Pd(PPh₃)₂Cl₂ (404.99 mg, 0.58 mmol) were dissolved in dry-DMF (50 mL). Cesium carbonate (2.94 g, 9.01 mmol) and distilled water (9 mL) were added before degassing. The reaction mixture was stirring at 120°C, 48 hours under nitrogen atmosphere. The mixture was extracted with DCM, dried with Na₂SO₄ and the solvents were removed under reduce pressure. The product was purified by silica-gel column chromatography using a gradient of PE and EtAcO to obtain a white product (137.2 mg, 20 %). ¹H-NMR (500 MHz, CDCl₃). δ_H: 7.43 (d, J = 8.6 Hz, 6H); 7.28 (d, J = 8.9 Hz, 3H); 7.21 (d, J = 8.6 HZ; 6H); 6.61-6.53 (m, 6H); 3.85 (s, 9H); 3.83 (s, 9H). ¹³C NMR (125 MHz, CDCl₃). δ_C: 160.11, 157.54, 146.24, 132.57, 131.14, 130.17, 123.81, 123.28, 104.70, 99.09, 55.62, 55.50. HRMS (ESI⁺) m/z calcd for C₄₂H₃₉NNaO₆ 676.2670, found 676.2672.

Chapter 4

4.5.2.3. Synthesis and characterization of **CS05**.



Scheme 4.11: Synthetic pathway of **CS05**.

Synthesis of 3,6-dibromo-9H-carbazole (7): a solution of NBS (14.00 g, 78.94 mmol) in DMF (12.20 mL) was slowly added with stirring to a solution of 9H-carbazole (6.00 g, 35.90 mmol) in DMF (31.60 mL) inside an ice bath. After reacting for 2 hours at 0°C , the mixture was poured into ice water. The crude product was collected by filtration and washed with H_2O and EtOH to give a white powder (10.83 g, 93 %). The spectroscopic data were in good agreement with those previously reported in the literature³³. $^1\text{H-NMR}$ (500 MHz, CDCl_3). δ_{H} : 8.13 (d, $J = 1.8$ Hz, 2H), 8.09 (s, 1H), 7.52 (dd, $J = 8.6, 1.9$ Hz, 2H), 7.31 (d, $J = 8.6$ Hz, 2H). $^{13}\text{C NMR}$ (125 MHz, CDCl_3). δ_{C} : 138.52, 129.49, 124.27, 123.43, 112.81, 112.36.

Synthesis of 3,6-bis(2,4-dimethoxyphenyl)-9H-carbazole (8): 3,6-dibromo-9H-carbazole (5.687 g, 17.48 mmol), 2-(2,4-dimethoxyphenyl)-4,4,5,5-tetramethyl-1,3,2-dioxaborolane (8 g, 38.44 mmol) and $\text{Pd}(\text{PPh}_3)_2\text{Cl}_2$ (650.00 mg, 0.93 mmol) were dissolved in dry-DMF (250 mL). The mixture was degassed. Cesium carbonate (31.32 g, 96.11 mmol) and distilled water (65 mL)

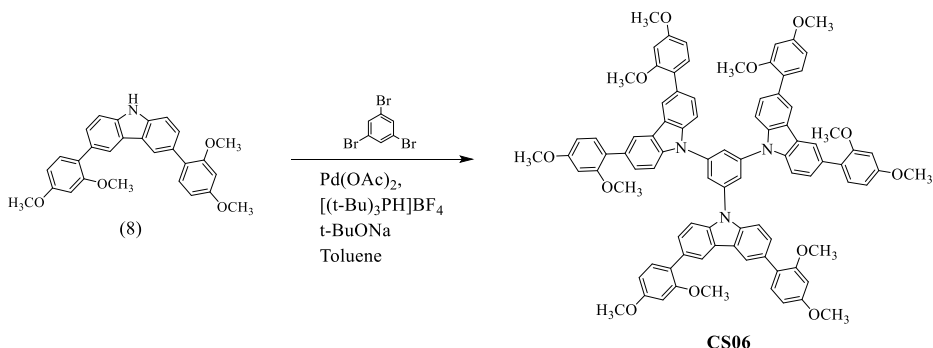
Design, synthesis and characterization of SMs for optoelectronic applications

were added before degassing again. The reaction mixture was stirring at 120°C overnight under nitrogen atmosphere. The mixture was extracted with DCM, dried with Na₂SO₄ and the solvents were removed under reduce pressure. The product was purified by silica-gel column chromatography using PE and EtAcO to obtain a white product (6.82 g, 90 %). ¹H-NMR (500 MHz, CDCl₃). δ_H: 8.17 (s, 2H); 8.04 (br s, 1H) 7.56 (dd, J = 8.4/1.7 Hz, 2H); 7.44 (d, J = 8.4 Hz, 2H); 7.35 (d, J = 8.9 Hz, 2H); 6.58 – 6.63 (m, 4H); 3.87 (s, 6H); 3.82 (s, 6H). ¹³C NMR (125 MHz, CDCl₃). δ_C: 160.01, 157.07, 138.93, 131.72, 129.83, 127.78, 124.69, 123.75, 121.30, 110.10, 104.76, 99.26, 55.80, 55.60. HRMS (ESI⁺) m/z calcd for C₂₈H₂₅N₃NaO₄ 462.1676, found 462.1673.

Synthesis of N-(4-(3,6-bis(2,4-dimethoxyphenyl)-9H-carbazol-9-yl)phenyl)-N-(2',4'-dimethoxy-[1,1'-biphenyl]-4-yl)-2',4'-dimethoxy-[1,1'-biphenyl]-4-amine: CS05: N-(4-bromophenyl)-N-(2',4'-dimethoxy-[1,1'-biphenyl]-4-yl)-2',4'-dimethoxy-[1,1'-biphenyl]-4-amine (8) (300 mg, 0.50 mmol), 3,6-bis(2,4-dimethoxyphenyl)-9H-carbazole (271.88 mg, 0.62 mmol) (11), Pd₃(dba)₂ (7.1 mg, 0.01 mmol), [(*t*-Bu)₃PH]BF₄ (4.38 mg, 0.02 mmol) and *t*-BuONa (156.13 mg, 1.62 mmol) were dissolved in dry toluene (10 mL) and the mixture was refluxing overnight under argon atmosphere. The product was extracted with EtOAc and dried over MgSO₄. The solvent was evaporated under vacuum and the residue was purified by silica-gel column chromatography using PE and EtOAc as eluents to obtain a solid (269.1 mg, 56 %). ¹H NMR (500 MHz, CDCl₃). δ_H: 160.24, 160.03, 157.67, 157.57, 147.05, 145.95, 140.43, 133.30, 131.79, 131.68, 131.19, 130.43, 130.11, 127.77, 124.62, 124.49, 124.23, 123.53, 123.13, 121.22, 109.42, 104.77, 99.24, 99.14, 55.76, 55.64, 55.56, 55.52. HRMS (ESI⁺) m/z calcd for C₆₂H₅₄N₂ O₈ 954.3875, found 954.3861.

Chapter 4

4.5.2.4. Synthesis and characterization of **CS06**.



Scheme 4.12: Synthetic route of **CS06**.

Synthesis of 1,3,5-tris(3,6-bis(2,4-dimethoxyphenyl)-9H-carbazol-9-yl)benzene: CS06: 1,3,5-tribromobenzene (100.00 mg, 0.32 mmol), 3,6-bis(2,4-dimethoxyphenyl)-9H-carbazole (**8**) (837.69 mg, 1.91 mmol), Pd(OAc)₂ (5.40 mg, 0.02 mmol), [(*t*-Bu)₃PH]BF₄ (13.83 mg, 0.05 mmol) and *t*-BuONa (183.16 mg, 1.91 mmol) were purged for 30 minutes under argon atmosphere before dissolved in dry toluene (15 mL). The mixture was stirring for 2 days at 120°C under argon atmosphere. The solvent was evaporated under vacuum and the residue was purified by silica-gel column chromatography using PE and DCM as eluents (v:v, 6 : 4). Finally, the solid was filtered off and washed with MeOH to obtain a white solid (121.3 mg, 27 %). ¹H NMR (400 MHz, CDCl₃). δ_H: 8.26 (s, 6H); 8.06 (s, 3H) 7.72 (d, J = 8.4 Hz, 6H); 7.62 (dd, J = 8.4/1.6 Hz, 6H); 7.37 (d, J = 8.9 Hz, 6H); 6.60 – 6.66 (m, 12H); 3.87 (s, 18H); 3.81 (s, 18H). ¹³C NMR (100 MHz, CDCl₃). δ_C: 160.21, 157.72, 141.11, 139.60, 131.68, 131.20, 128.31, 124.34, 122.86, 121.53, 109.38, 104.82, 99.28, 55.81, 55.62. HRMS (ESI⁺) m/z calcd for C₉₀H₇₅N₃O₁₂ 1389.5345, found 1389.5348.

Design, synthesis and characterization of SMs for optoelectronic applications

4.6. Annex.

In this section it is shown the NMRs, MS from the synthesis of the new molecules described above and hole mobility experiments in absence of additives.

4.6.1. NMRs.

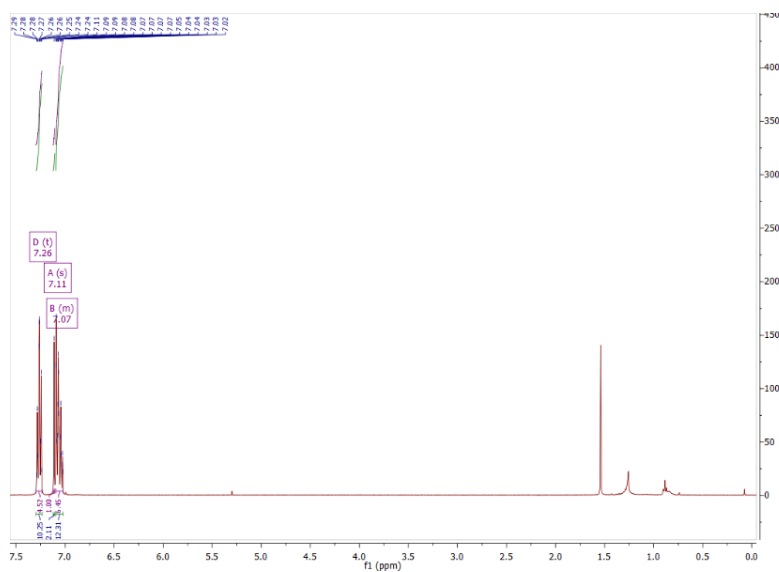


Figure A4.1: ^1H NMR of N₄,N₄,N₇,N₇-tetraphenylbenzo[c][1,2,5]thiadiazole-4,7-diamine (**1**).

Chapter 4

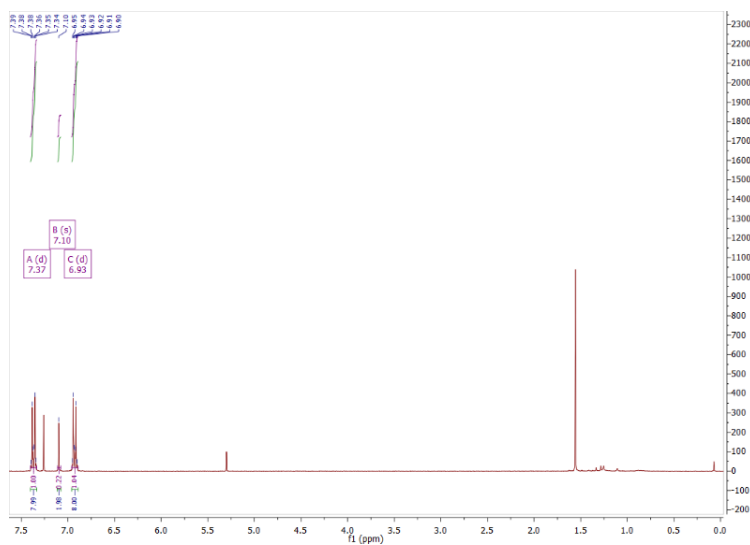


Figure A4.2: ^1H NMR of $\text{N}_4,\text{N}_4,\text{N}_7,\text{N}_7$ -tetrakis(4-bromophenyl)benzo[*c*][1,2,5]thiadiazole-4,7-diamine (**2**).

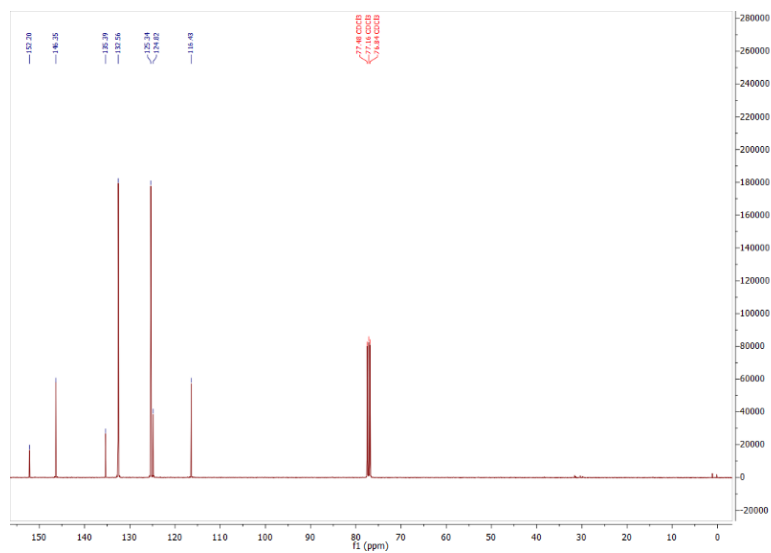


Figure A4.3: ^{13}C NMR of $\text{N}_4,\text{N}_4,\text{N}_7,\text{N}_7$ -tetrakis(4-bromophenyl)benzo[*c*][1,2,5]thiadiazole-4,7-diamine (**2**).

Design, synthesis and characterization of SMs for optoelectronic applications

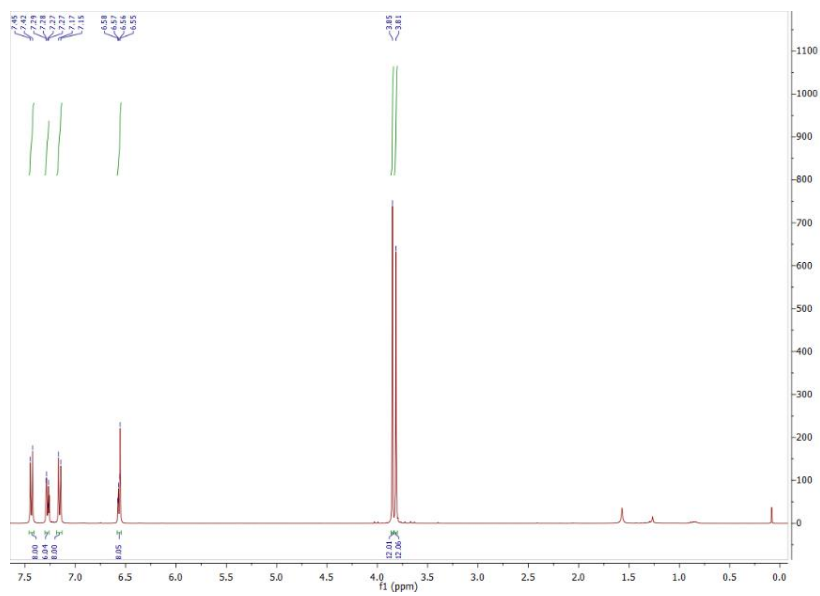


Figure A4.4: ¹H NMR of CS01.

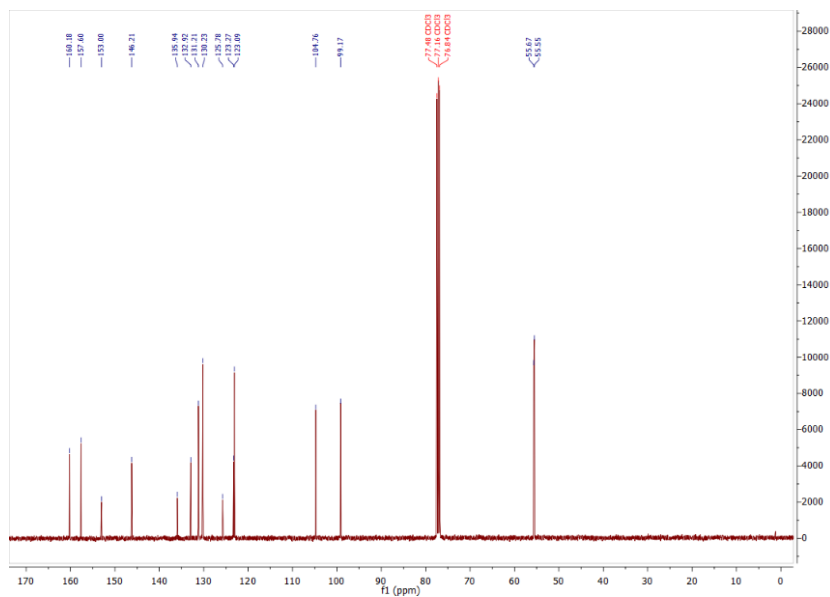


Figure A4.5: ¹³C NMR of CS01.

Chapter 4

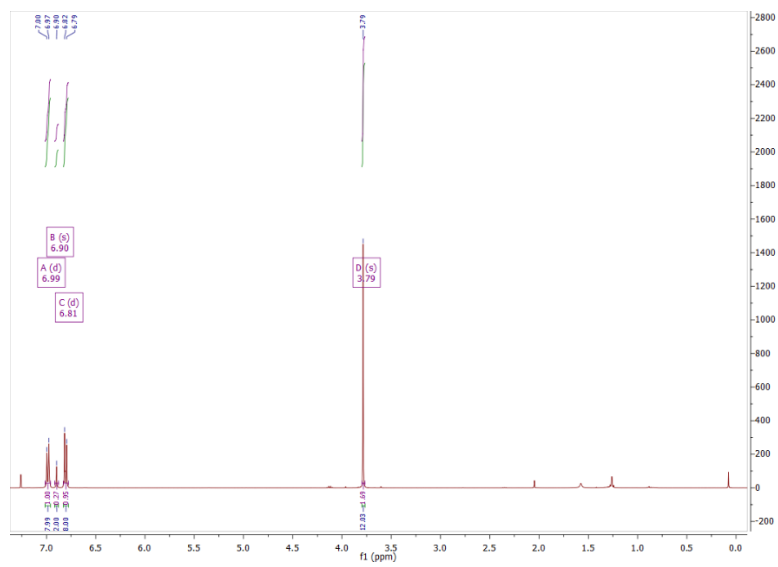


Figure A4.6: ^1H NMR of CS03.

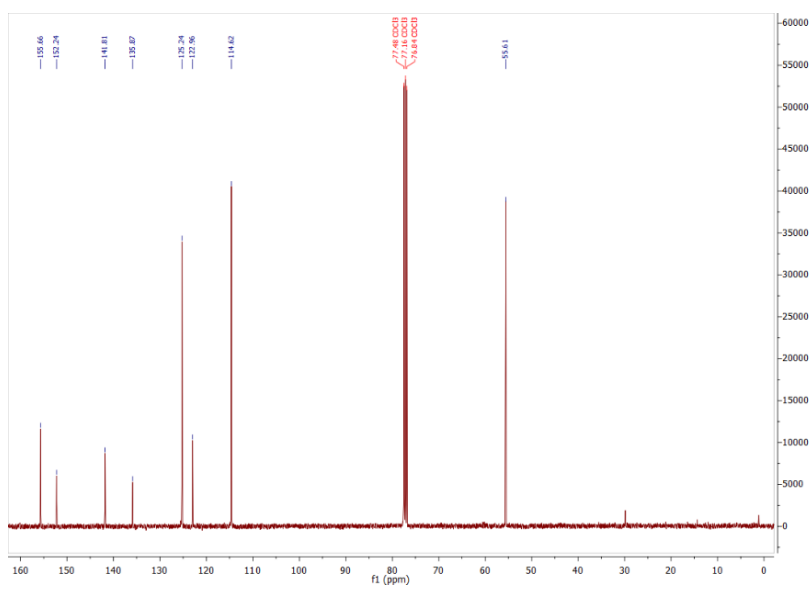


Figure A4.7: ^{13}C NMR of CS03.

Design, synthesis and characterization of SMs for optoelectronic applications

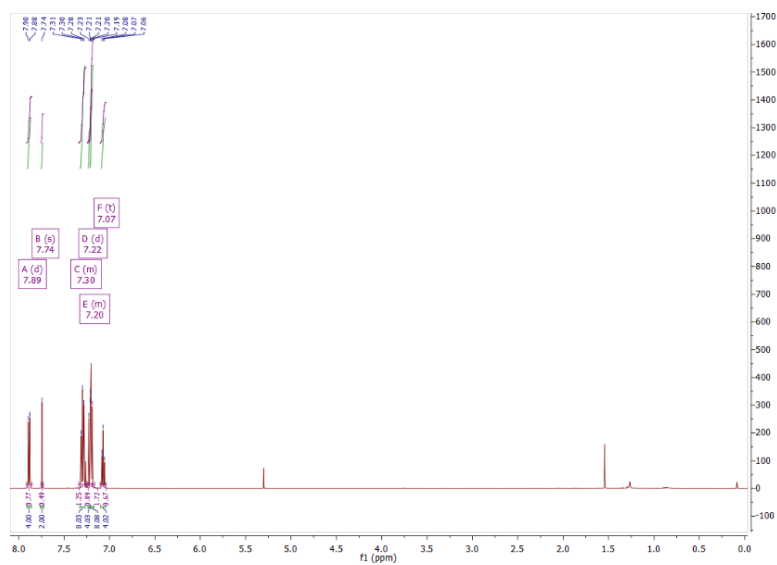


Figure A4.8: ^1H NMR of EP02.

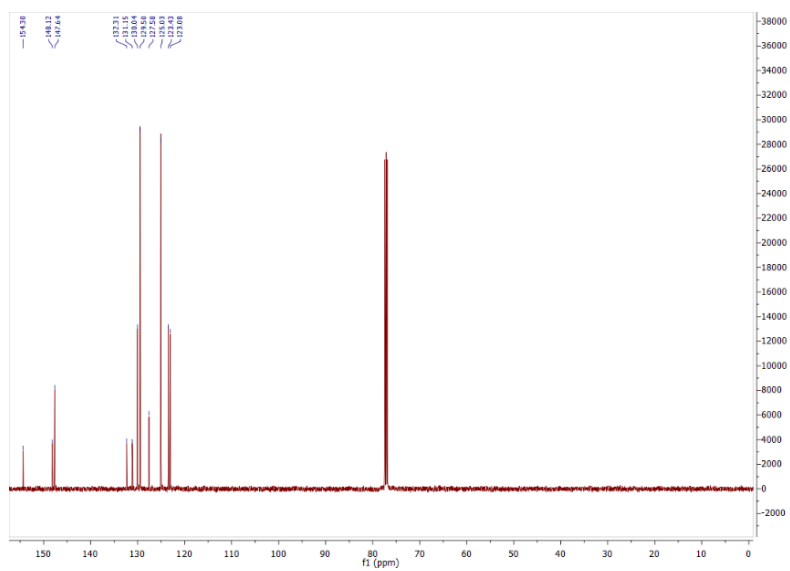


Figure A4.9: ^{13}C NMR of EP02.

Chapter 4

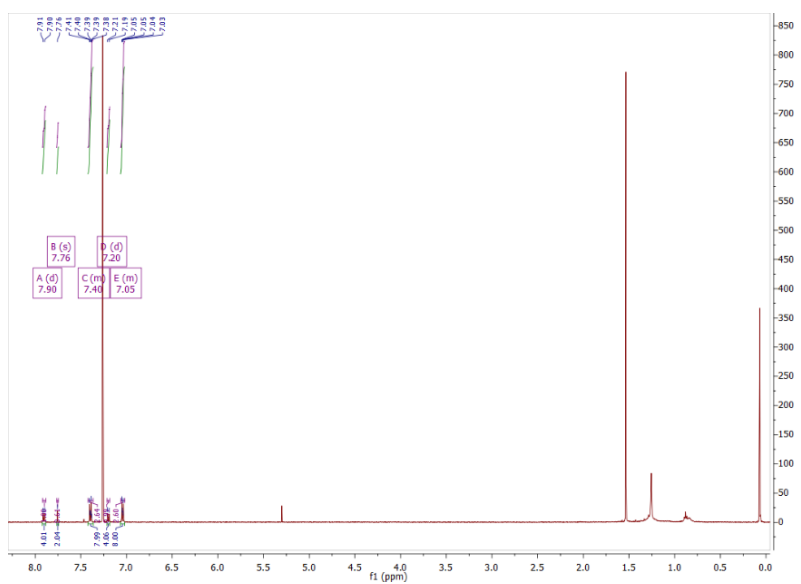


Figure A4.10: ^1H of 4,4'-(benzo[c][1,2,5]thiadiazole-4,7-diyl)bis(N,N-bis(4-bromophenyl)aniline)(3).

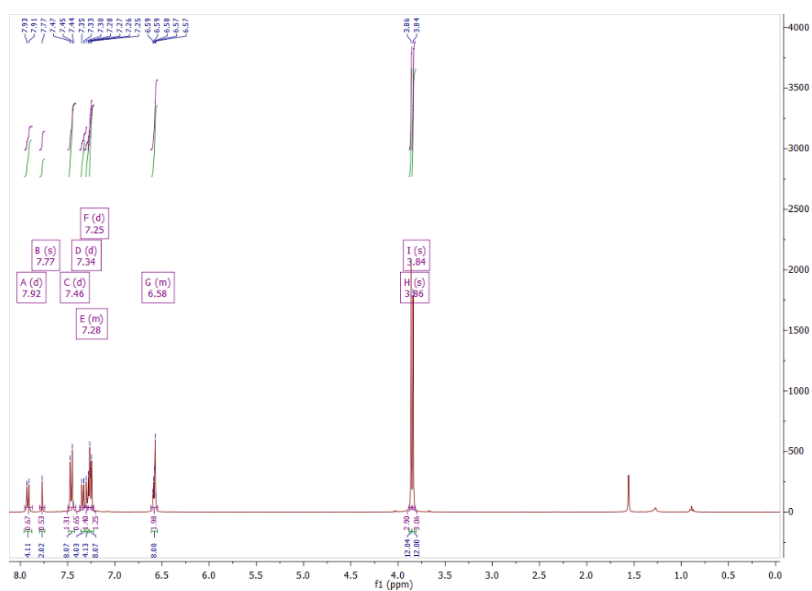


Figure A4.11: ^1H NMR of LCS01.

Design, synthesis and characterization of SMs for optoelectronic applications

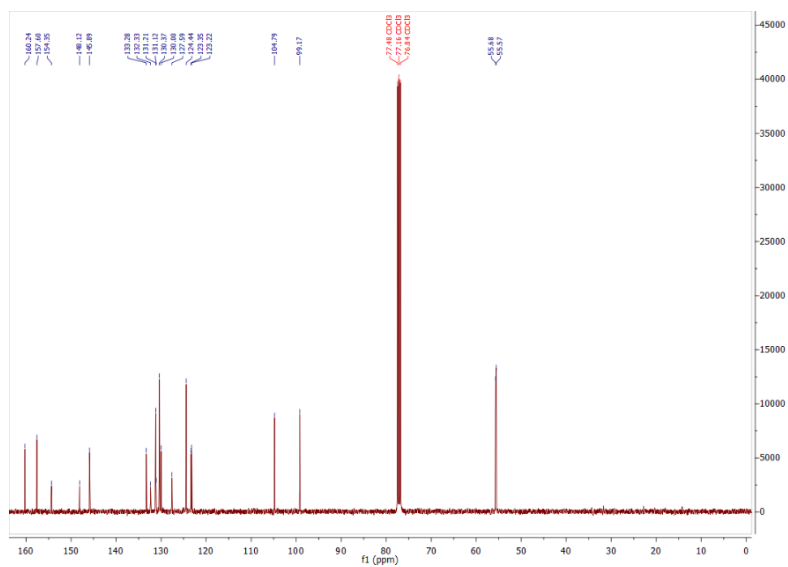


Figure A4.12: ^{13}C NMR of LCS01.

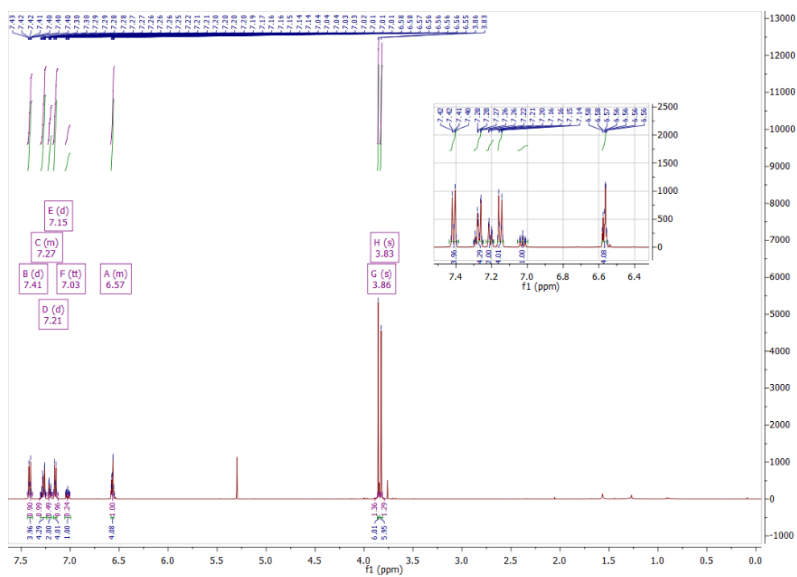


Figure A4.13: ^1H NMR of N-(2',4'-dimethoxy-[1,1'-biphenyl]-4-yl)-2',4'-dimethoxy-N-phenyl-[1,1'-biphenyl]-4-amine (**4**).

Design, synthesis and characterization of SMs for optoelectronic applications

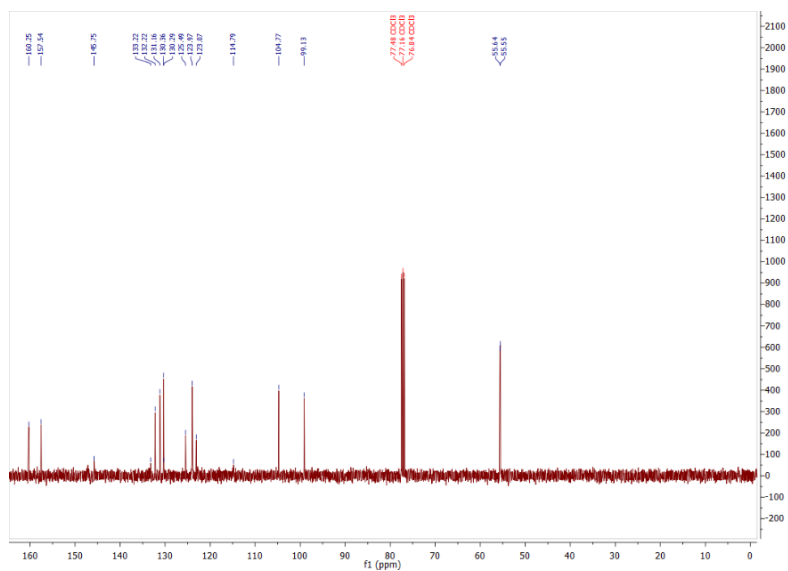


Figure A4.16: ^{13}C NMR of N-(4-bromophenyl)-N-(3',5'-dimethoxy-[1,1'-biphenyl]-4-yl)-2',4'-dimethoxy-[1,1'-biphenyl]-4-amine (**5**).

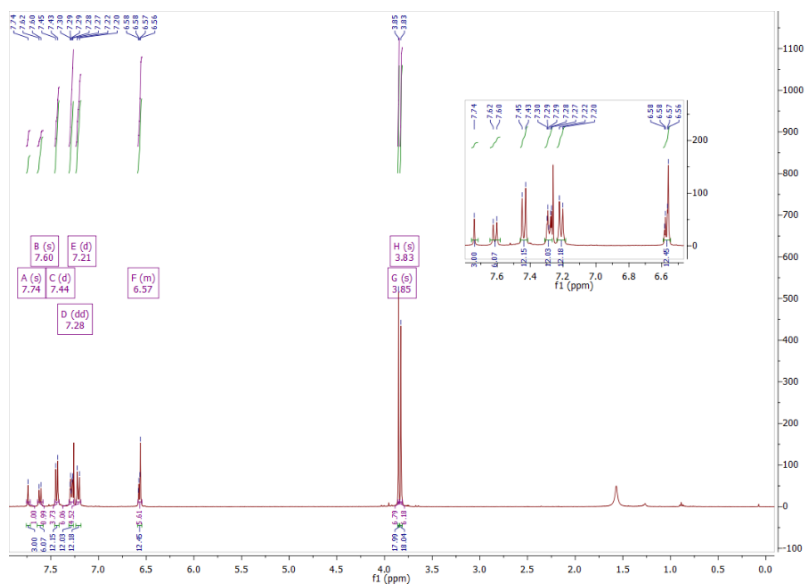


Figure A4.17: ^1H NMR of CS02.

Chapter 4

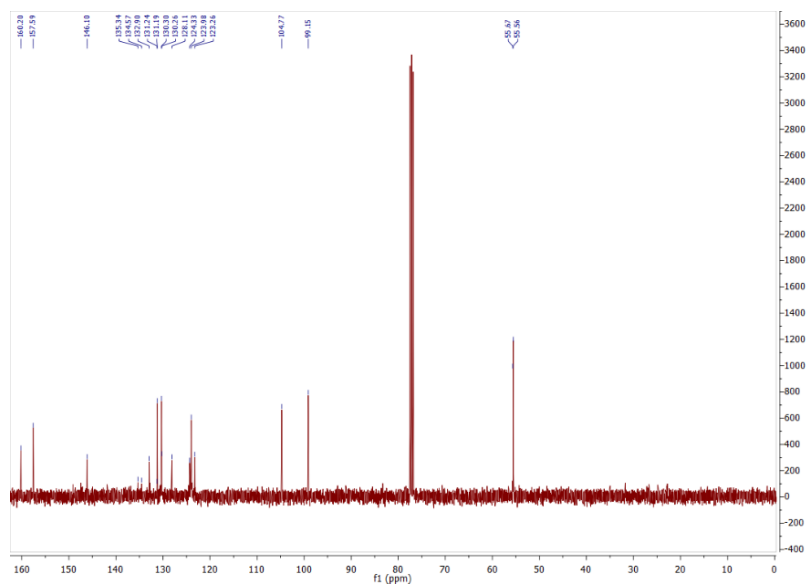


Figure A4.18: ^{13}C NMR of CS02.

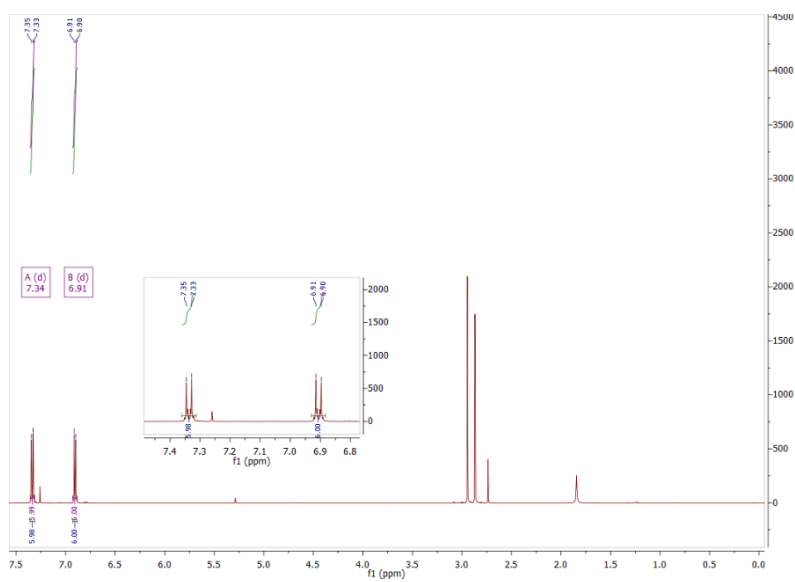


Figure A4.29: ^1H NMR of tris(4-bromophenyl)amine (**6**).

Chapter 4

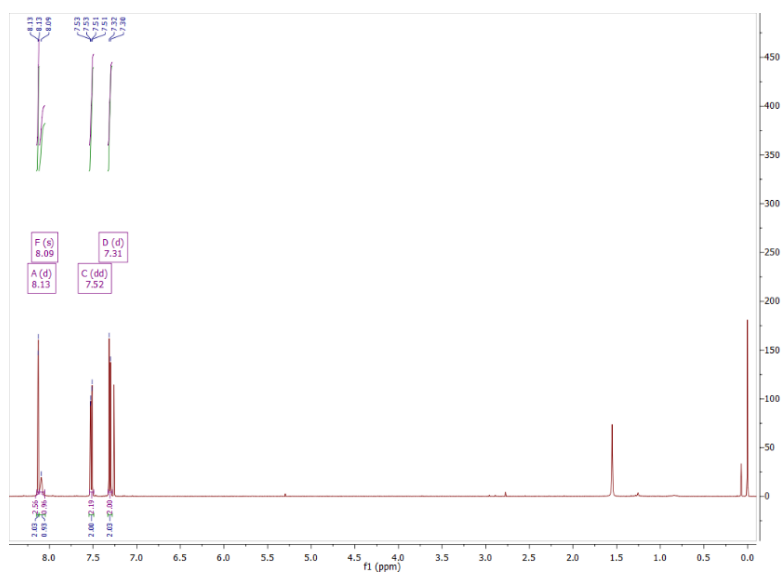


Figure A4.22: ¹H NMR of 3,6-dibromo-9H-carbazole (**7**).

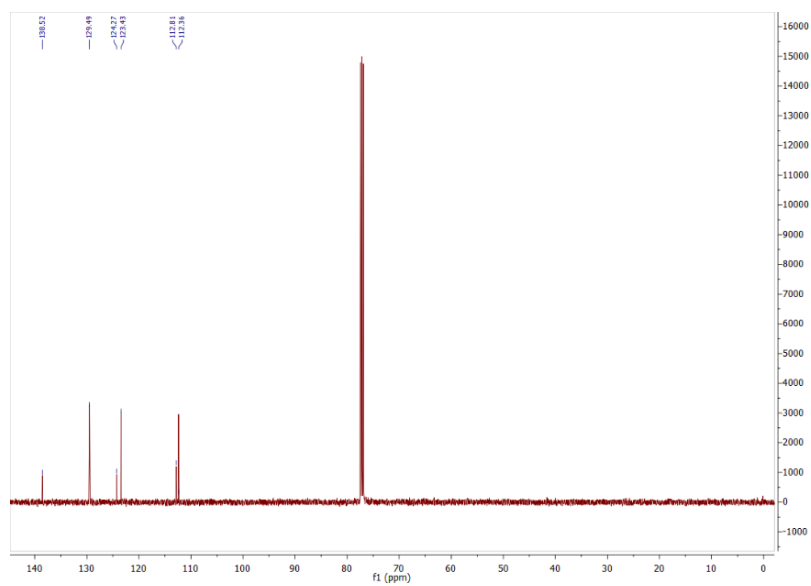


Figure A4.23: ¹³C NMR of 3,6-dibromo-9H-carbazole (**7**).

Design, synthesis and characterization of SMs for optoelectronic applications

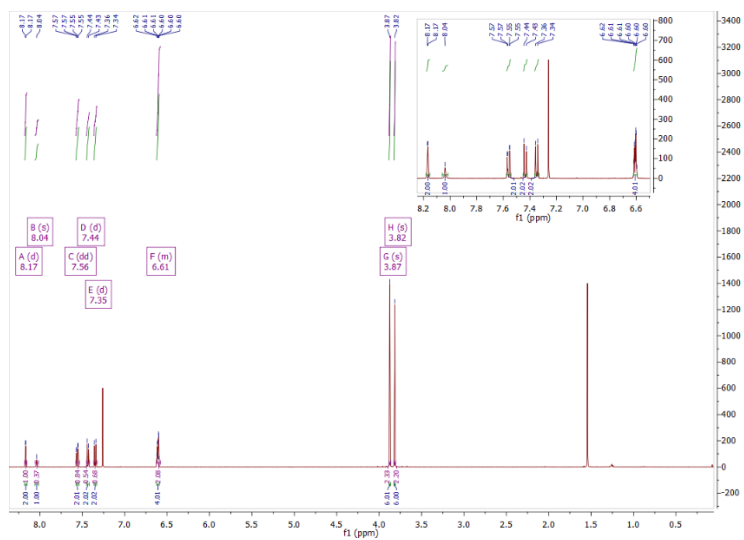


Figure A4.24: ^1H NMR of 3,6-bis(2,4-dimethoxyphenyl)-9H-carbazole (8).

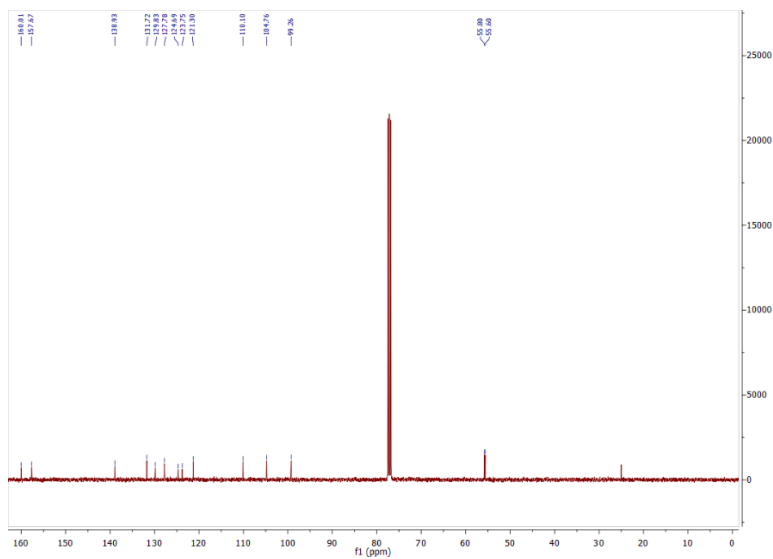


Figure A4.25: ^{13}C NMR of 3,6-bis(2,4-dimethoxyphenyl)-9H-carbazole (8).

Chapter 4

4.6.2. MS spectra.

Mass Spectrum SmartFormula Report

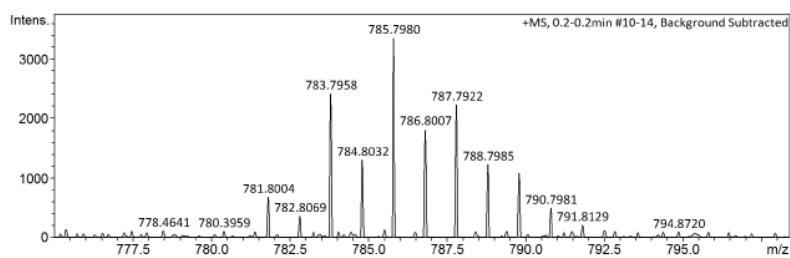
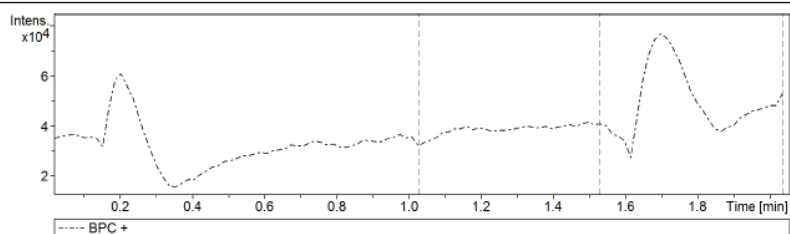
Analysis Info

Analysis Name W:\Data\180119\180119_CS114-1_RA2_01_17641.d
 Method tune_low_hplc-exactas2min.m
 Sample Name 180119_CS114-1
 Comment 0.1 PPM, MeOH injection

Acquisition Date 19/01/2018 12:28:57
 Operator ICIQ
 Instrument / Ser# micrOTOF 213750.10
 394

Acquisition Parameter

Source Type	ESI	Ion Polarity	Positive	Set Nebulizer	1.2 Bar
Focus	Active			Set Dry Heater	180 °C
Scan Begin	50 m/z	Set Capillary	4500 V	Set Dry Gas	8.0 l/min
Scan End	3000 m/z	Set End Plate Offset	-500 V	Set Divert Valve	Source



Meas. m/z	Ion Formula	m/z	err [ppm]	err [mDa]	mSigma	e ⁻ Conf	z
781.8004	C30H18Br4N4S	781.7980	3.0	2.4	103.3	odd	1+

Figure A4.26: MS spectrum of (2)

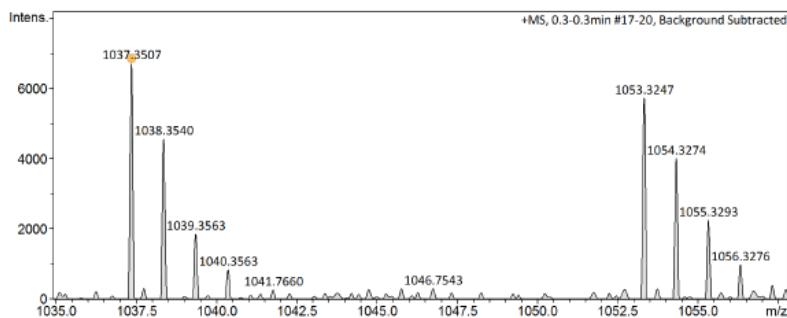
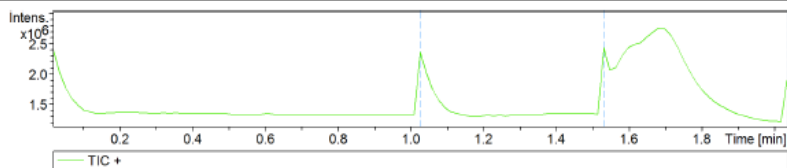
Design, synthesis and characterization of SMs for optoelectronic applications

Mass Spectrum SmartFormula Report

Analysis Info
 Analysis Name W:\Data\170316_newmethodpos\170316_cs01_RD3_01_14270.d
 Method tune_low_hplc-exactas2min.m
 Sample Name 170316_cs01
 Comment 0.1 ppm, MeOH injection
 Acquisition Date 16/03/2017 16:41:00
 Operator ICIQ
 Instrument / Ser# microTOF 213750.10
 394

Acquisition Parameter

Source Type	ESI	Ion Polarity	Positive	Set Nebulizer	1.2 Bar
Focus	Active			Set Dry Heater	180 °C
Scan Begin	50 m/z	Set Capillary	4500 V	Set Dry Gas	8.0 l/min
Scan End	3000 m/z	Set End Plate Offset	-500 V	Set Divert Valve	Source



Meas. m/z	Ion Formula	m/z	lerr [ppm]	err [mDa]	mSigma	e ⁻ Conf	z
1037.3507	C81H58NaO12S	1037.3541	3.3	3.4	13.7	even	1+
	C82H54N4NaO8S	1037.3555	4.6	4.8	17.8	even	1+

Figure A4.27: MS spectrum of CS01.

Chapter 4

Mass Spectrum SmartFormula Report

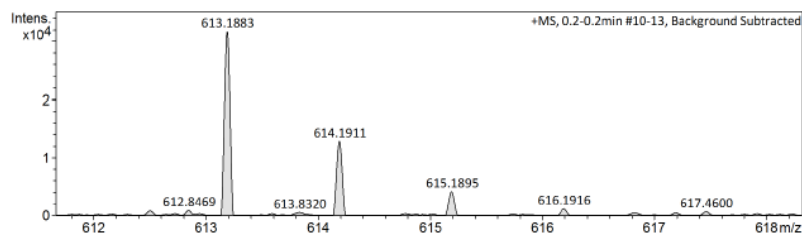
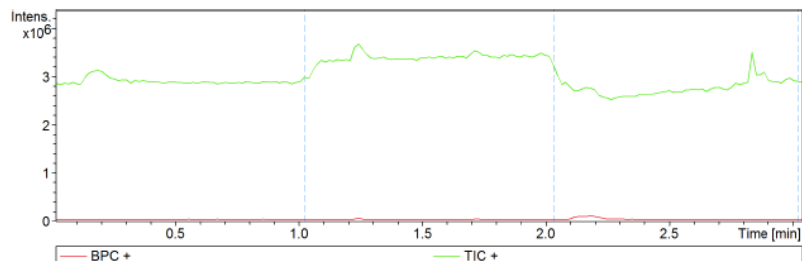
Analysis Info

Analysis Name W:\Data\161109\161109_CS03_RA5_01_12516.d
 Method tune_low_hplc-exactas3min-noe.m
 Sample Name 161109_CS03
 Comment 0.1 uL STARTING SOLUTION, Meoh INJ

Acquisition Date 09/11/2016 10:54:46
 Operator ICIQ
 Instrument / Ser# micrOTOF 213750.10
 394

Acquisition Parameter

Source Type ESI Ion Polarity Positive Set Nebulizer 1.2 Bar
 Focus Active Set Dry Heater 180 °C
 Scan Begin 50 m/z Set Capillary 4500 V Set Dry Gas 8.0 l/min
 Scan End 2000 m/z Set End Plate Offset -500 V Set Divert Valve Source



Meas. m/z	Ion Formula	m/z	err [ppm]	err [mDa]	mSigma	e ⁻ Conf	z
613.1883	C34H30N4NaO4S	613.1880	0.5	-0.3	6.6	even	1+

Figure A4.28: MS spectrum of CS03.

Design, synthesis and characterization of SMs for optoelectronic applications

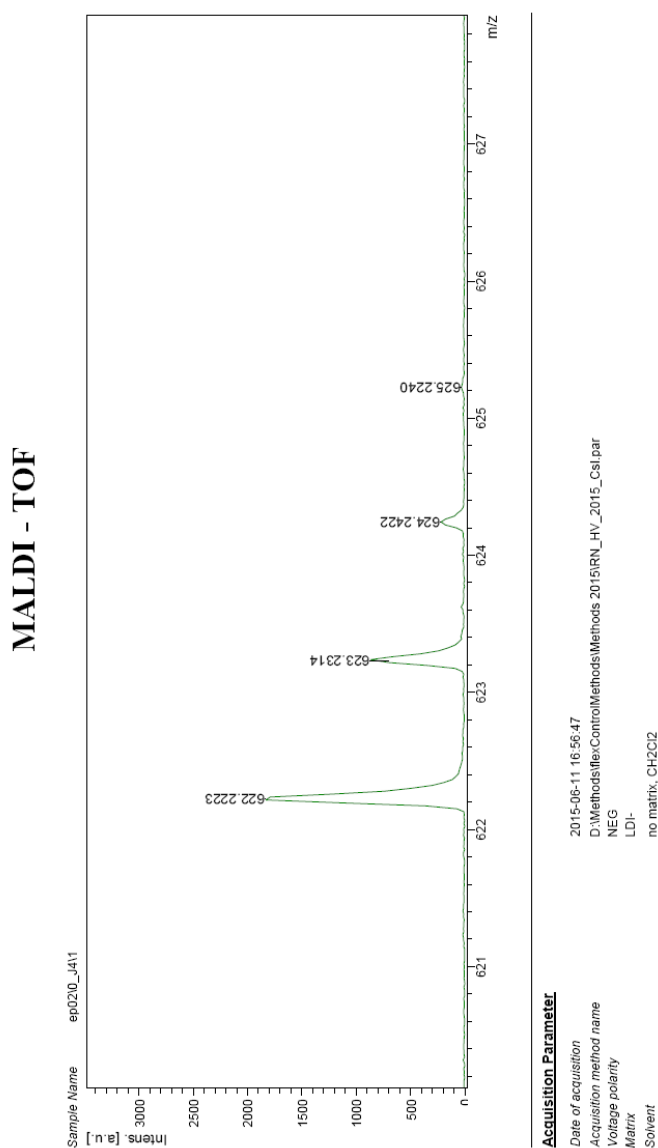


Figure A4.29: MS spectrum of EP02.

Chapter 4

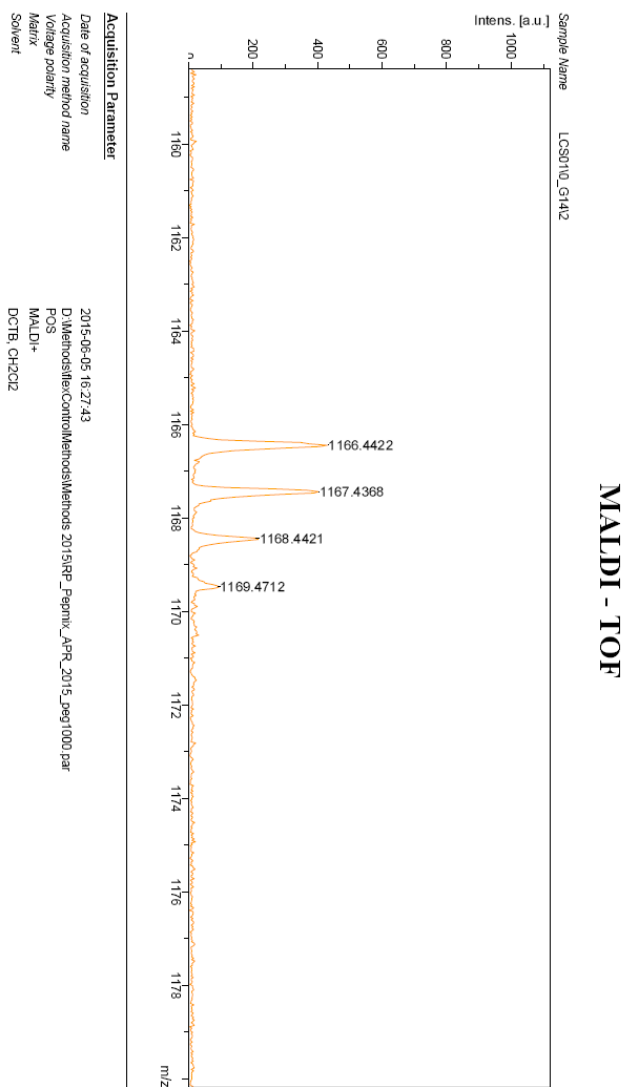


Figure A4.30: MS spectrum of LCS01.

Design, synthesis and characterization of SMs for optoelectronic applications

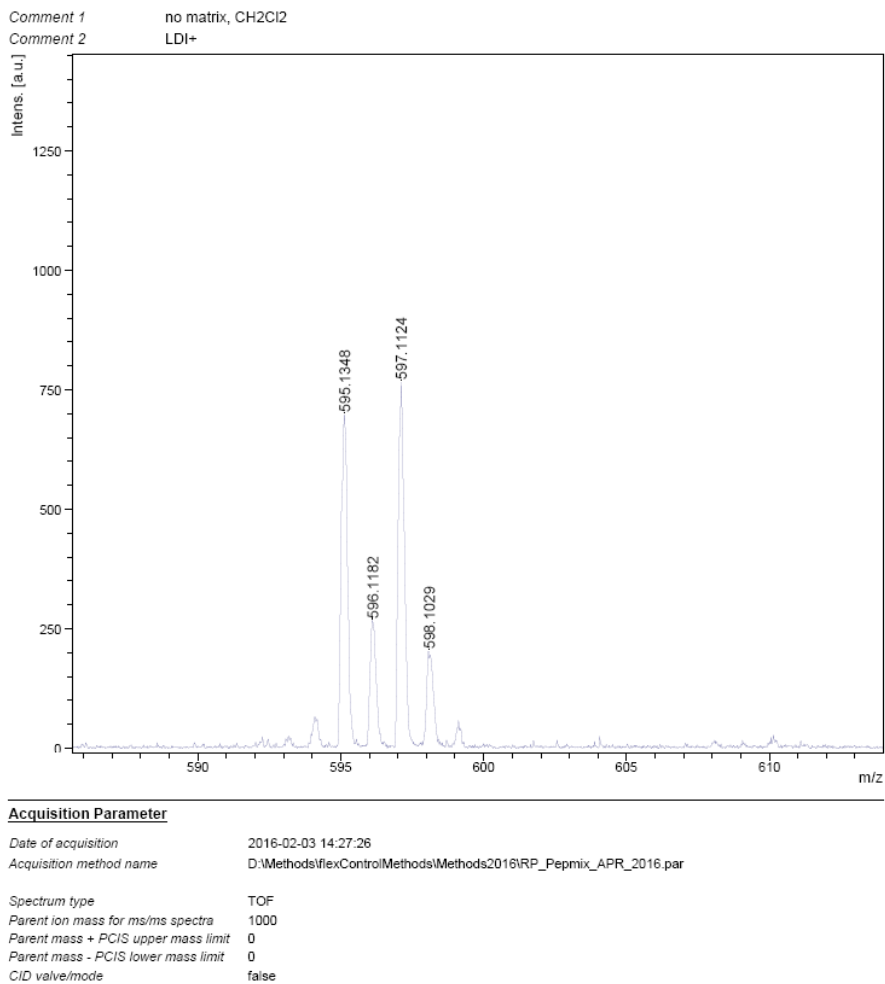


Figure A4.31: MS spectrum of (4).

Chapter 4

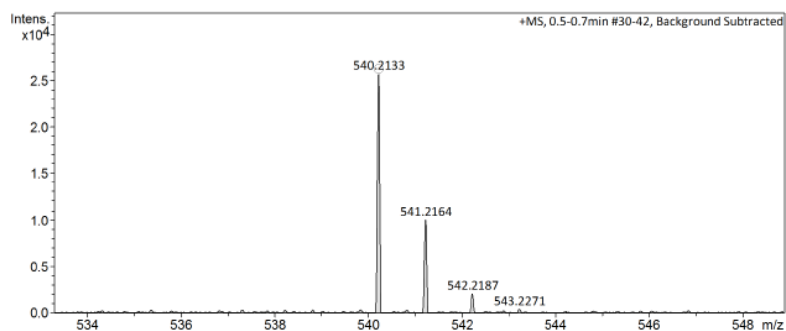
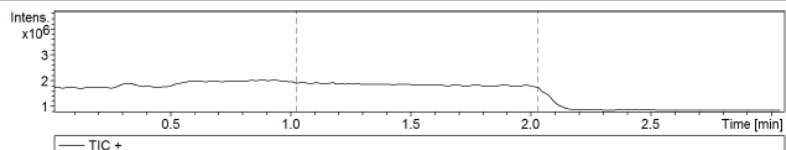
Mass Spectrum SmartFormula Report

Analysis Info

Analysis Name W:\Data\151117\151117_CS41-6_1-A,4_01_9082.d Acquisition Date 17/11/2015 13:49:10
 Method tune_low_hplc-exactas3min-noe.m Operator ICIQ
 Sample Name 151117_CS41-6 Instrument / Ser# microTOF 213750.10
 Comment 0.1 ppm MeOH 394

Acquisition Parameter

Source Type ESI Ion Polarity Positive Set Nebulizer 1.2 Bar
 Focus Active Set Dry Heater 180 °C
 Scan Begin 50 m/z Set Capillary 4500 V Set Dry Gas 8.0 l/min
 Scan End 2000 m/z Set End Plate Offset -500 V Set Divert Valve Source



Meas. m/z	Ion Formula	m/z	err [ppm]	err [mDa]	mSigma	e ⁻ Conf	z
540.2133	C ₃₄ H ₃₁ NNaO ₄	540.2145	2.2	-1.2	7.8	even	1+

Figure A4.32: MS spectrum of (5).

Design, synthesis and characterization of SMs for optoelectronic applications

Mass Spectrum SmartFormula Report

Analysis Info

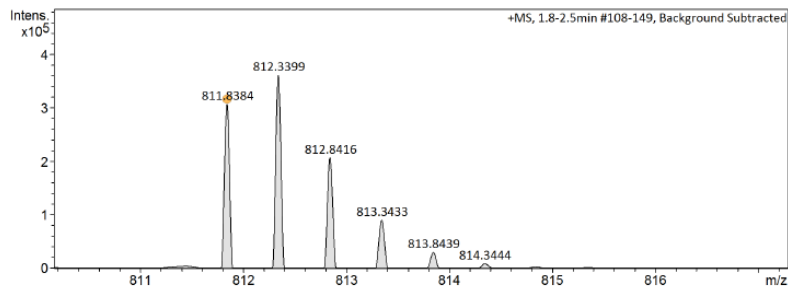
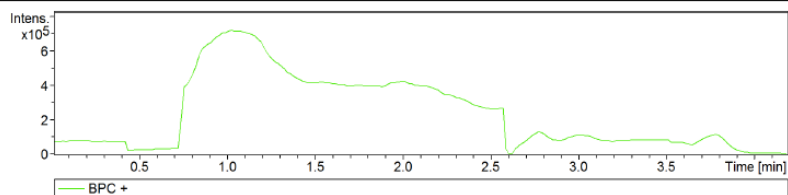
Analysis Name W:\Data\171006\171006M_CS02.d
 Method tune_low_hplc-exactas2min.m
 Sample Name 171006M_CS02
 Comment 0.5 ppm, MeCN injection

Acquisition Date 06/10/2017 17:57:45

Operator ICIQ
 Instrument / Ser# microTOF 213750.10
 394

Acquisition Parameter

Source Type	ESI	Ion Polarity	Positive	Set Nebulizer	0.4 Bar
Focus	Active			Set Dry Heater	180 °C
Scan Begin	50 m/z	Set Capillary	4500 V	Set Dry Gas	4.0 l/min
Scan End	3000 m/z	Set End Plate Offset	-500 V	Set Divert Valve	Source



Meas. m/z	Ion Formula	m/z	err [ppm]	err [mDa]	mSigma	e ⁻ Conf	z
811.8384	C108H93N3O12	811.8374	1.2	-1.0	16.4	even	2+

Figure A4.33: MS spectrum of CS02.

Chapter 4

Mass Spectrum SmartFormula Report

Analysis Info

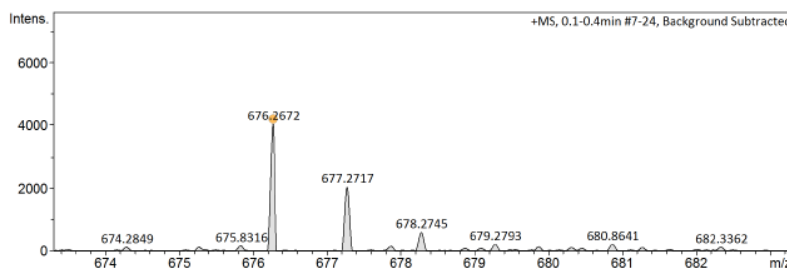
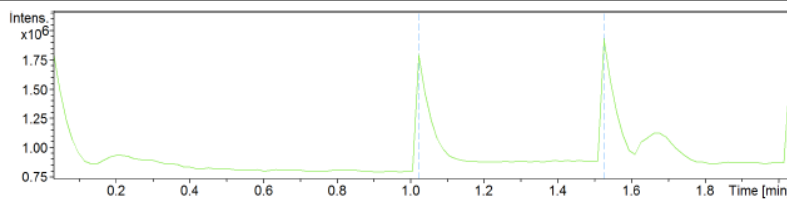
Analysis Name W:\Data\180702\180702_CS04_RE3_01_19817.d
 Method tune_low_hplc-exactas2min.m
 Sample Name 180702_CS04
 Comment 0.1 ppm, MeOH injection

Acquisition Date 02/07/2018 17:55:03

Operator ICIQ
 Instrument / Ser# microTOF 213750.10
 394

Acquisition Parameter

Source Type ESI Ion Polarity Positive Set Nebulizer 1.2 Bar
 Focus Active Set Dry Heater 180 °C
 Scan Begin 50 m/z Set Capillary 4500 V Set Dry Gas 8.0 l/min
 Scan End 3000 m/z Set End Plate Offset -500 V Set Divert Valve Source



Meas. m/z	Ion Formula	m/z	lerr [ppm]	err [mDa]	mSigma	e ⁻ Conf	z
676.2672	C41H33N8NaO	676.2670	0.4	0.3	30.2	odd	1+
	C42H39N8NaO6	676.2670	0.4	-0.3	31.9	even	1+
	C40H34N7O4	676.2667	0.8	0.6	34.0	even	1+
	C41H40O9	676.2667	0.8	0.6	36.6	odd	1+

Figure A4.34: MS spectrum of CS04.

Design, synthesis and characterization of SMs for optoelectronic applications

Analysis Info

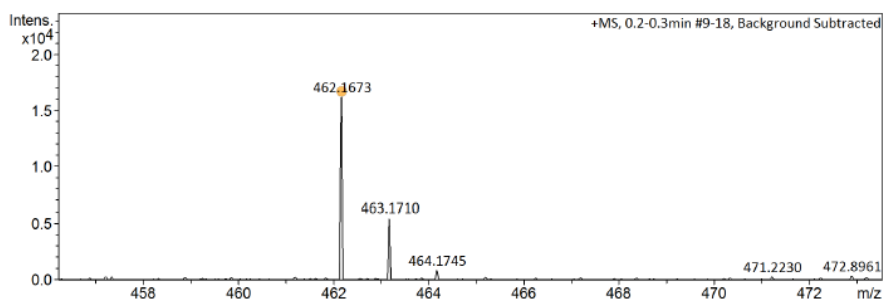
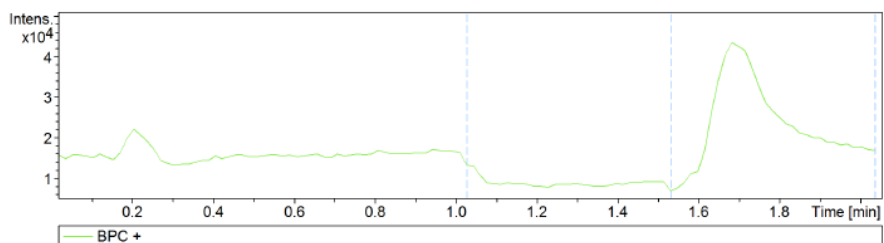
Analysis Name W:\Data\180702\180702_CARB3_RE2_01_19819.d
 Method tune_low_hplc-exactas2min.m
 Sample Name 180702_CARB3
 Comment 0.1 ppm, MeOH injection

Acquisition Date 02/07/2018 18:01:21

Operator ICIQ
 Instrument / Ser# micrOTOF 213750.10
 394

Acquisition Parameter

Source Type	ESI	Ion Polarity	Positive	Set Nebulizer	1.2 Bar
Focus	Active			Set Dry Heater	180 °C
Scan Begin	50 m/z	Set Capillary	4500 V	Set Dry Gas	8.0 l/min
Scan End	3000 m/z	Set End Plate Offset	-500 V	Set Divert Valve	Source



Meas. m/z	Ion Formula	m/z	err [ppm]	err [mDa]	mSigma	e ⁻ Conf	z
462.1673	C28H25NNaO4	462.1676	0.6	0.3	14.2	even	1+
	C26H20N7O2	462.1673	0.0	-0.0	14.6	even	1+
	C27H26O7	462.1673	0.0	-0.0	20.7	odd	1+

Figure A4.35: MS spectrum of (8).

Chapter 4

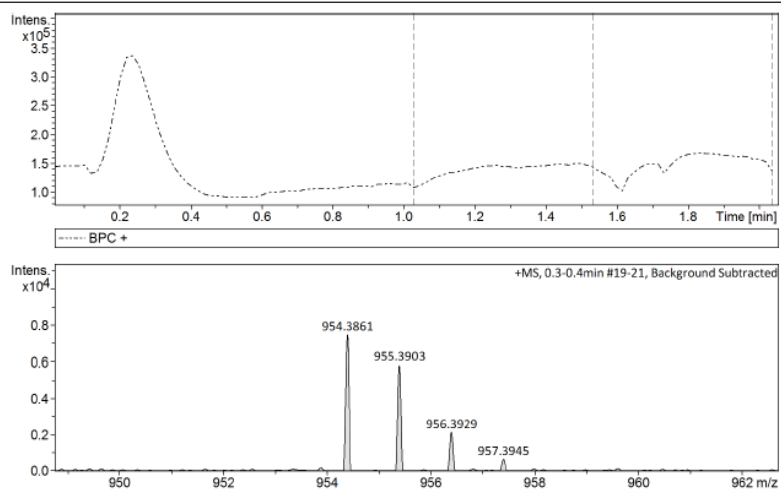
Mass Spectrum SmartFormula Report

Analysis Info

Analysis Name W:\Data\180830\180830_CSRP01-2_RA2_01_20595.d Acquisition Date 30/08/2018 11:44:58
 Method tune_low_hplc-exactas2min.m Operator ICIQ
 Sample Name 180830_CSRP01-2 Instrument / Ser# microTOF 213750.10
 Comment sample in acetonitrile, 5 ppm injection in MeOH 394

Acquisition Parameter

Source Type	ESI	Ion Polarity	Positive	Set Nebulizer	1.2 Bar
Focus	Active			Set Dry Heater	180 °C
Scan Begin	50 m/z	Set Capillary	4500 V	Set Dry Gas	8.0 l/min
Scan End	3000 m/z	Set End Plate Offset	-500 V	Set Divert Valve	Source



Meas. m/z	Ion Formula	m/z	err [ppm]	err [mDa]	mSigma	e ⁻ Conf	z
954.3861	C62H54N2O8	954.3875	1.4	-1.3	44.8	odd	1+

Figure A4.36: MS spectrum of CS05.

Design, synthesis and characterization of SMs for optoelectronic applications

Mass Spectrum SmartFormula Report

Analysis Info

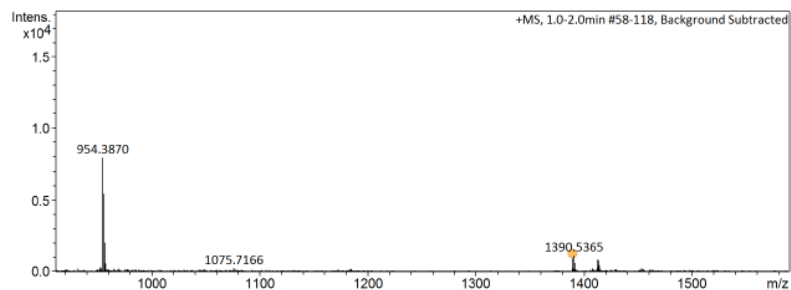
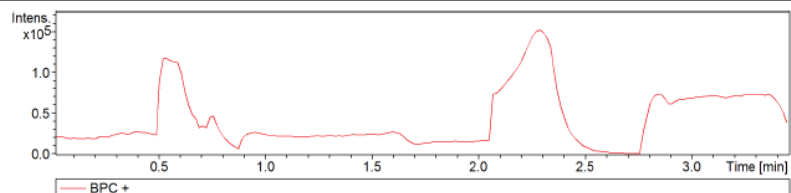
Analysis Name W:\Data\171006\171006M_CMR02.d
 Method tune_low_hplc-exactas2min.m
 Sample Name 171006M_CMR02
 Comment 0.5 ppm, MeCN injection

Acquisition Date 06/10/2017 17:47:13

Operator ICIQ
 Instrument / Ser# micrOTOF 213750.10
 394

Acquisition Parameter

Source Type	ESI	Ion Polarity	Positive	Set Nebulizer	0.4 Bar
Focus	Active			Set Dry Heater	180 °C
Scan Begin	50 m/z	Set Capillary	4500 V	Set Dry Gas	4.0 l/min
Scan End	3000 m/z	Set End Plate Offset	-500 V	Set Divert Valve	Source



Meas. m/z	Ion Formula	m/z	err [ppm]	err [mDa]	mSigma	e ⁻ Conf	z
1389.5348	C90H75N3O12	1389.5345	0.2	0.3	81.7	odd	1+

Figure A4.37: MS spectrum of CS06.

Chapter 4

4.7. References.

1. <https://www.nrel.gov/pv/cell-efficiency.html>.
2. Kippelen, B.; Brédas, J.-L., Organic photovoltaics. *Energy & Environmental Science* **2009**, 2 (3), 251-261.
3. Y. Cheng; A. Pascoe; F. Huang; Peng., Y., Print flexible solar cells. *Nature* **2016**, 539 (7630), 488-489.
4. Collins, S. D.; Ran, N. A.; Heiber, M. C.; Nguyen, T.-Q., Small is Powerful: Recent Progress in Solution-Processed Small Molecule Solar Cells. *Advanced Energy Materials* **2017**, 7 (10), 1602242.
5. Chen, C.-Y.; Chen, J.-G.; Wu, S.-J.; Li, J.-Y.; Wu, C.-G.; Ho, K.-C., Multifunctionalized Ruthenium-Based Supersensitizers for Highly Efficient Dye-Sensitized Solar Cells. *Angewandte Chemie International Edition* **2008**, 47 (38), 7342-7345.
6. Giannopoulos, P.; Raptis, D.; Theodosiou, K.; Andreopoulou, A. K.; Anastasopoulos, C.; Dokouzis, A.; Leftheriotis, G.; Lianos, P.; Kallitsis, J. K., Organic dyes end-capped with perfluorophenyl anchors: Synthesis, electrochemical properties and assessment of sensitization capacity of titania photoanodes. *Dyes and Pigments* **2018**, 148, 167-179.
7. Sun, H.; Li, P. a.; Liu, D.; Wang, T.; Li, W.; Hu, W.; Wang, L.; Zhou, X., Tuning photophysical properties via alkoxy groups in charge-separated triphenylamine sensitizers for dye-sensitized solar cells. *Journal of Photochemistry and Photobiology A: Chemistry* **2019**, 368, 233-241.
8. Ramasamy, S.; Gopi, P.; Raju, S.; Kathavarayan, S., Comparative analysis of fluorene and carbazole fused triphenylamine sensitizer donor units with new anchoring mode in dye-sensitized solar cells. *Reactive and Functional Polymers* **2018**, 122, 123-130.

Design, synthesis and characterization of SMs for optoelectronic applications

9. Krishna, A.; Grimsdale, A. C., Hole transporting materials for mesoscopic perovskite solar cells – towards a rational design? *Journal of Materials Chemistry A* **2017**, *5* (32), 16446-16466.
10. Jeon, N. J.; Lee, H. G.; Kim, Y. C.; Seo, J.; Noh, J. H.; Lee, J.; Seok, S. I., o-Methoxy Substituents in Spiro-OMeTAD for Efficient Inorganic–Organic Hybrid Perovskite Solar Cells. *Journal of the American Chemical Society* **2014**, *136* (22), 7837-7840.
11. Zhang, M.-D.; Zhao, D.-X.; Chen, L.; Pan, N.; Huang, C.-Y.; Cao, H.; Chen, M.-D., Structure-performance relationship on the asymmetric methoxy substituents of spiro-OMeTAD for perovskite solar cells. *Solar Energy Materials and Solar Cells* **2018**, *176*, 318-323.
12. Thelakkat, M., Star-Shaped, Dendrimeric and Polymeric Triarylamines as Photoconductors and Hole Transport Materials for Electro-Optical Applications. *Macromolecular Materials and Engineering* **2002**, *287* (7), 442-461.
13. Gozzo, F., Systemic Acquired Resistance in Crop Protection: From Nature to a Chemical Approach. *Journal of Agricultural and Food Chemistry* **2003**, *51* (16), 4487-4503.
14. Balasankar, T.; Gopalakrishnan, M.; Nagarajan, S., Synthesis and antibacterial activity of some 5-(4-biphenyl)-7-aryl[3,4-d] [1,2,3]-benzothiadiazoles. *European Journal of Medicinal Chemistry* **2005**, *40* (7), 728-731.
15. Neto, B. A. D.; Lapis, A. A. M.; da Silva Júnior, E. N.; Dupont, J., 2,1,3-Benzothiadiazole and Derivatives: Synthesis, Properties, Reactions, and Applications in Light Technology of Small Molecules. *European Journal of Organic Chemistry* **2013**, *2013* (2), 228-255.
16. Cabau, L.; Vijay Kumar, C.; Moncho, A.; Clifford, J. N.; López, N.; Palomares, E., A single atom change “switches-on” the solar-to-energy

Chapter 4

conversion efficiency of Zn-porphyrin based dye sensitized solar cells to 10.5%. *Energy & Environmental Science* **2015**, 8 (4), 1368-1375.

17. Kumar, N. S.; Ibrahim, A. A.; Dhar, A.; Vekariya, R. L., Optoelectrical characterization of different fabricated donor substituted benzothiazole based sensitizers for efficient DSSCs. *Journal of Photochemistry and Photobiology A: Chemistry* **2019**, 372, 35-41.

18. Revoju, S.; Biswas, S.; Eliasson, B.; Sharma, G. D., Phenothiazine-based small molecules for bulk heterojunction organic solar cells; variation of side-chain polarity and length of conjugated system. *Organic Electronics* **2019**, 65, 232-242.

19. Sagdullina, D. K.; Kuznetsov, I. E.; Akkuratov, A. V.; Kuznetsova, L. I.; Troyanov, S. I.; Troshin, P. A., New alternating thiophene-benzothiadiazole electron donor material for small-molecule organic solar cells and field-effect transistors. *Synthetic Metals* **2019**, 250, 7-11.

20. Mahesh, K.; Karpagam, S.; Putnin, T.; Le, H.; Bui, T.-T.; Ounnunkad, K.; Goubard, F., Role of cyano substituents on thiophene vinylene benzothiadiazole conjugated polymers and application as hole transporting materials in perovskite solar cells. *Journal of Photochemistry and Photobiology A: Chemistry* **2019**, 371, 238-247.

21. Wu, F.; Ji, Y.; Wang, R.; Shan, Y.; Zhu, L., Molecular engineering to enhance perovskite solar cell performance: Incorporation of benzothiadiazole as core unit for low cost hole transport materials. *Dyes and Pigments* **2017**, 143, 356-360.

22. Wu, F.; Ji, Y.; Zhong, C.; Liu, Y.; Tan, L.; Zhu, L., Fluorine-substituted benzothiadiazole-based hole transport materials for highly efficient planar perovskite solar cells with a FF exceeding 80%. *Chemical Communications* **2017**, 53 (62), 8719-8722.

Design, synthesis and characterization of SMs for optoelectronic applications

23. Gong, G.; Zhao, N.; Ni, D.; Chen, J.; Shen, Y.; Wang, M.; Tu, G., Dopant-free 3,3'-bithiophene derivatives as hole transport materials for perovskite solar cells. *Journal of Materials Chemistry A* **2016**, *4* (10), 3661-3666.
24. Chen, Y.-C.; Huang, S.-K.; Li, S.-S.; Tsai, Y.-Y.; Chen, C.-P.; Chen, C.-W.; Chang, Y. J., Facilely Synthesized spiro[fluorene-9,9'-phenanthren-10'-one] in Donor–Acceptor–Donor Hole-Transporting Materials for Perovskite Solar Cells. *ChemSusChem* **2018**, *11* (18), 3225-3233.
25. Dhingra, P.; Singh, P.; Rana, P. J. S.; Garg, A.; Kar, P., Hole-Transporting Materials for Perovskite-Sensitized Solar Cells. *Energy Technology* **2016**, *4* (8), 891-938.
26. Rodríguez-Seco, C.; Cabau, L.; Vidal-Ferran, A.; Palomares, E., Advances in the Synthesis of Small Molecules as Hole Transport Materials for Lead Halide Perovskite Solar Cells. *Accounts of Chemical Research* **2018**, *51* (4), 869-880.
27. Privado, M.; Seco, C. R.; Singhal, R.; Cruz, P. d. I.; Langa, F.; Sharma, G. D.; Palomares, E., Reduced Energy Offsets and Low Energy Losses Lead to Efficient (~10% at 1 sun) Ternary Organic Solar Cells. *ACS Energy Letters* **2018**, *3* (10), 2418-2424.
28. Rakstys, K.; Saliba, M.; Gao, P.; Gratia, P.; Kamarauskas, E.; Paek, S.; Jankauskas, V.; Nazeeruddin, M. K., Highly Efficient Perovskite Solar Cells Employing an Easily Attainable Bifluorenylidene-Based Hole-Transporting Material. *Angewandte Chemie International Edition* **2016**, *55* (26), 7464-7468.
29. Brunner, K.; van Dijken, A.; Börner, H.; Bastiaansen, J. J. A. M.; Kiggen, N. M. M.; Langeveld, B. M. W., Carbazole Compounds as Host Materials for Triplet Emitters in Organic Light-Emitting Diodes: Tuning the HOMO Level without Influencing the Triplet Energy in Small Molecules. *Journal of the American Chemical Society* **2004**, *126* (19), 6035-6042.

Chapter 4

30. Ni, F.; Wu, Z.; Zhu, Z.; Chen, T.; Wu, K.; Zhong, C.; An, K.; Wei, D.; Ma, D.; Yang, C., Teaching an old acceptor new tricks: rationally employing 2,1,3-benzothiadiazole as input to design a highly efficient red thermally activated delayed fluorescence emitter. *Journal of Materials Chemistry C* **2017**, *5* (6), 1363-1368.
31. Jun, L.; Yanxiang, C.; Zhiyuan, X.; Yanhou, G.; Lixiang, W.; Xiabin, J.; Fosong, W., White Electroluminescence from a Star-like Polymer with an Orange Emissive Core and Four Blue Emissive Arms. *Advanced Materials* **2008**, *20* (7), 1357-1362.
32. Shi, L.; He, C.; Zhu, D.; He, Q.; Li, Y.; Chen, Y.; Sun, Y.; Fu, Y.; Wen, D.; Cao, H.; Cheng, J., High performance aniline vapor detection based on multi-branched fluorescent triphenylamine-benzothiadiazole derivatives: branch effect and aggregation control of the sensing performance. *Journal of Materials Chemistry* **2012**, *22* (23), 11629-11635.
33. Bahamonde, A.; Murphy, J. J.; Savarese, M.; Brémond, É.; Cavalli, A.; Melchiorre, P., Studies on the Enantioselective Iminium Ion Trapping of Radicals Triggered by an Electron-Relay Mechanism. *Journal of the American Chemical Society* **2017**, *139* (12), 4559-4567.

5. ORGANIC SOLAR CELLS

Chapter 5

Table of contents

5.1. Introduction to Organic Solar Cells.....	177
5.2. Light harvesting materials for Organic Solar Cells.....	178
5.3. Benzothiadiazole-based Binary Bulk Heterojunction Organic Solar Cells using PC ₇₁ BM as acceptor.....	179
5.3.1. Devices fabrication.....	179
5.3.2. Results and discussion.....	181
5.3.2.1. Absorption and photoluminescence emission spectra.....	181
5.3.2.2 Photovoltaic measurements.....	184
6.3.3. Conclusions.....	195
6.4. Binary and Ternary Bulk Heterojunction Solar Cells with non-fullerene electron acceptor.	196
6.4.1. Introduction.....	196
6.4.2. Devices fabrication.....	197
6.4.3. CS01 and EP02 as electron donor and MPU3 as non-fullerene electron acceptor.	197
6.4.3.1. Absorption and photoluminescence spectra.....	199
6.4.3.2. Photovoltaic measurements.....	202
6.4.3.2. Ternary Organic Solar Cells.....	209
6.4.3.3. Conclusions.....	216
6.4.4. Binary and ternary bulk heterojunction organic solar cells with CS03 as electron donor and DPP8 as a non-fullerene electron acceptor.....	216
6.4.4.1. Device preparation.....	218
6.4.4.2. Absorption and photoluminescence spectra.....	218
6.4.4.3. Photovoltaic measurements.....	221
6.4.4.4. Conclusions.....	231
6.5. Conclusions.....	231
6.6. References.....	233

Chapter 5

5.1. Introduction to Organic Solar Cells.

The photoactive layer of bulk heterojunction organic solar cells (BHJ OSCs) is the most important component of it. As it was previously explained in detail in Chapter 1, the active layer is formed by one or more donor and/or acceptor materials. The electron donor or light harvesting materials described in this chapter will all be low-molecular weight (LMW) molecules based on the benzothiadiazole (BT) moiety. In this work, four donors with different substituents were tested and compared. All described compounds absorb in the visible range of the solar spectrum and their energetic levels match well with the other layers of the organic solar cell. We chose **PC₇₁BM** as the electron acceptor due to its physical properties such as high electron mobility and strong acceptor properties when paired with most donor materials because of its low lying LUMO energy level, efficient charge separation, excellent photostability and internal quantum efficiencies approaching unity¹.

Although, this type of devices are showing promising results regarding efficiency and stability, the morphology of each donor and acceptor moiety varies significantly from one material to another, especially in relation to domain size and degree of interpenetration between domains. This is important taking into account the limited lifetime of the excitons, leading to a diffusion length of around 10 nm². However, smaller domains will increase opportunities for bimolecular recombination between charge carriers. For this reason, optimization of the domain size for both donor and acceptor constituents facilitates the migration of excitons from the donor to the acceptor interface and their splitting into the free charge carriers, leading to efficient charge carrier extraction³. To this aim, we have used solvent vapour annealing method (SVA), which enhances the hole and electron mobility and the phase separation between the donor and acceptor, leading to higher efficiencies.

Chapter 5

Other attempts to improve the efficiency of OSCs has been via incorporating a third component by using two different acceptors mixed with a donor in the bulk to fabricate what is called ternary bulk heterojunction organic solar cells (TOHs). In this work, we found that the voltage and the efficiency of the organic solar cells increased when **PC₇₁BM** was replaced by a non-fullerene electron acceptor and when incorporating both acceptors to the mixture of the bulk while keeping the identity of the donor constant. This increase in efficiency is usually due to the increase in short circuit current (J_{sc}) since the two-electron acceptors and donor small molecules absorb at different wavelengths, nearly covering the whole range of the solar spectrum. Herein, a cascade-like energy level alignment is formed among these three materials which is beneficial for the charge transfer and collection. On top of that, it is possible to use the same optimizing strategies of BHJ organic solar cells, such as adjusting the ratio of donors and acceptors, controlling the morphology using solvent vapour annealing treatment. etc⁴.

5.2. Light harvesting materials for Organic Solar Cells.

Several organic semiconducting polymers have been used as donors in the fabrication of organic solar cells, as was explained in Chapter 1. However, they have some disadvantages such as the lack of batch-to-batch reproducibility, the difficulty in controlling their molecular weight and their purification. On the contrary, SMs require fewer synthetic steps and are easily isolated/purified⁵. For this reason, for different small molecules were synthesized bearing a push-pull D-A-D (donor-acceptor-donor) structure, commonly used in OPVs⁶. They all were synthesized with the same benzothiadiazole core (see Scheme 5.1), which has accepting properties and has been widely used in SMs and polymers for OSCs showing promising efficiencies⁷⁻¹⁰. The core was modified by changing the substituents that were based on di- and triphenylamine electron donating groups whose conjugation was extended by a phenyl spacer in different positions. The use of TPA moieties for organic semiconductor

materials is well known due to its favourable hole transporting and electron donating capabilities¹¹. The aim was to tune the HOMO energy level without changing the value of the LUMO. The HOMO and LUMO energy levels of these SMs indicate their suitability to serve as donors for the fabrication of SM-based OSCs along with **PC₇₁BM** and non-fullerene acceptors such as **MPU3** and **DPP8**, described later in this chapter.

5.3. Benzothiadiazole-based Binary Bulk Heterojunction Organic Solar Cells using PC₇₁BM as acceptor.

This section is based on partially published work (“Benzothiadiazole substituted semiconductor molecules for organic solar cells: the effect of the solvent annealing over the thin film hole mobility values.” J. Phys. Chem. C 2018, 122, 25, 13782 - 13789) as well as non-published work yet, in collaboration with the group of Prof. Sharma in Jaipur (India).

Nowadays, the BHJ structure has become the standard architecture to characterize organic solar cell materials. Power conversion efficiency (PCE) of BHJ solar cells has exceeded 11 %¹²⁻¹³ and 13 and 14 %¹⁴⁻¹⁷. In this chapter, the fabrication and characterization of BHJ OSCs based on four new SM donors and **PC₇₁BM** as electron acceptor will be described.

5.3.1. Devices fabrication.

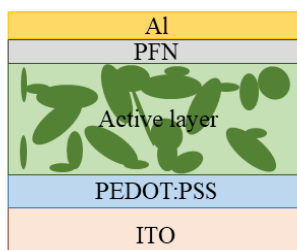
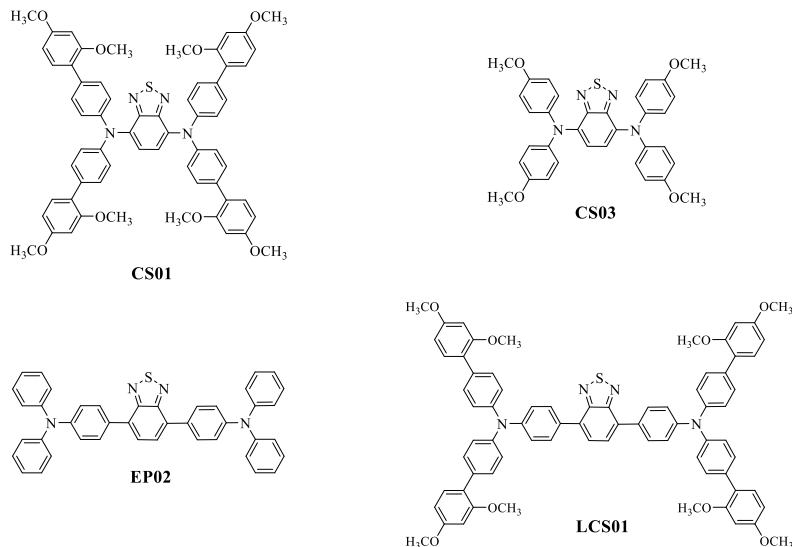


Figure 5.1: The architecture of the BHJ OSCs used in this work.

Chapter 5

OSCs were fabricated with a conventional structure of glass/ITO/PEDOT:PSS/**CS01**, **CS03**, **EP02** or **LCS01:PC₇₁BM**/PFN/Al, as it can be seen in Figure 5.1. The alcohol-soluble conjugated polymer, poly [(9,9-bis(32-(*N,N*-dimethylamino)propyl)-2,7-fluorene)-alt-2,7-(9,9-dioctylfluorene)] (PFN) was used as an cathode interfacial layer. The ITO coated glass substrates were cleaned by ultrasonic treatment in detergent, deionized water, acetone and isopropanol for 15 min each and subsequently dried in vacuum oven for 15 min at a temperature of 40° C. Then a thin layer of poly (3,4-ethylenedioxythiophene):(polystyrene sulfonate) (PEDOT:PSS) was spin-coated onto the pre-cleaned ITO coated glass substrate at 3500 rpm for 40 s and subsequently baked at 110° C for 20 min and allowed to cool to room temperature. In order to deposit the thin film of the active layer, a mixture of **CS01**, **CS03**, **EP02** or **LCS01** with PC₇₁BM with different weight ratios in chloroform (total concentration 16 mg/mL) was spin coated at 2000 rpm for 20 s on the top of the PEDOT:PSS substrate and then dried at room temperature. After the active spin coating, SVA was used to tune the morphology of the blend film. For SVA, the films were placed in a glass petri-dish, containing 1 mL carbon disulphide (CS₂) in the case of **CS01** and **CS03**, and 0.3 mL of THF for **EP02** and **LCS01**, during 40 s. The thickness of the active layers is 90 nm ± 5 nm. The thin PFN layer was spin coated from a 1.5 mg/mL solution in methanol at 3000 rpm for 30 s and dried in vacuum oven at room temperature for 90 s. Finally, an aluminium (Al) layer was deposited by thermal evaporation under vacuum (ca. 10⁻⁵ Pa) through a mask, yielding four individual devices with 16 mm² effective area for **CS01** and **CS03** and 20 mm² for **EP02** and **LCS01**. The devices for hole mobility measurement were fabricated under the same conditions with an architecture of ITO/PEDOT:PSS/SMs-donor:PC₇₁BM/Au.



Scheme 5.1: The chemical structure of **CS01**, **CS03**, **EP02** and **LCS01**.

5.3.2. Results and discussion.

5.3.2.1. Absorption and photoluminescence emission spectra.

The absorbance of **CS01**, **CS03**, **EP02** and **LCS01** in solution and in thin film (thickness 80 nm) are shown in Figure 5.2. The absorption spectra of all the absorbers in solution (concentration 1×10^{-5} M in chloroform) show a complete absorption from 300 nm to 500 nm and 550 nm for **EP02** and **LCS01** and from 350 nm to 650 nm and 700 nm for the case of **CS01** and **CS03**, respectively. The absorption band centred at 350 nm in the case of **LCS01** and **EP02** arises from the $n-\pi^*$ electronic transition of triphenylamine unit in the molecule, whereas the absorption band in 400- 550 nm corresponds to the intermolecular charge transfer (ICT) associated with push-pull effect between the donor and acceptor units in the molecular backbone. The ICT band of **LCS01** is slightly redshifted as compared to **EP02**, due to the strong push-pull effect and related to the strong electron donating nature of substituted triphenylamine in **LCS01**.

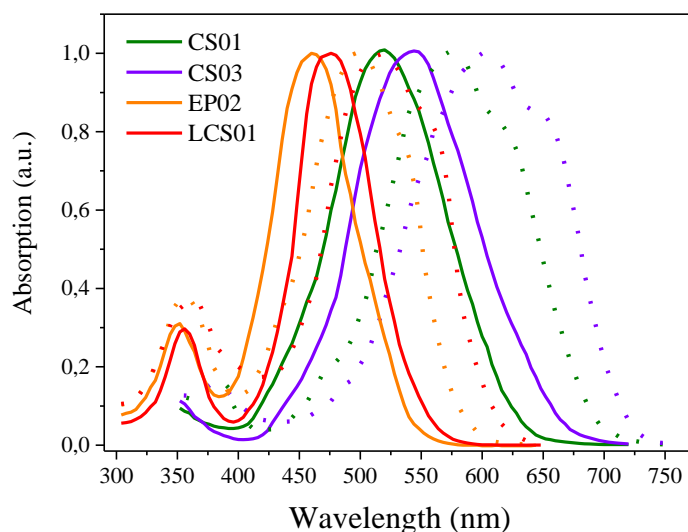


Figure 5.2: Absorption of **CS01**, **CS03**, **EP02** and **LCS01** in chloroform solution (line) and in thin films (dash line).

It also can be seen this red shift in **CS03** and **CS01**, being more noticeable for **CS03**. Moreover, an important red shift of the main absorption band with a noticeable shoulder can be monitored when the molecules are deposited in thin films attributed to the strong interactions originated from the ordered SM π - π packing¹⁸ and strong intermolecular interactions in solid state. This absorption shift is due to the formation of J-type aggregates¹⁹⁻²⁰ in the solid state. In fact, for the **CS03** and **LCS01** the formation of J-aggregates and intramolecular interaction seem favoured compared with the other two SMs, and a higher bathochromic shift is observed, and the absorption edge extended up to 750 nm and 650 nm respectively. The optical gap ($E_{\text{gap}}^{\text{opt}}$) was calculated from the onset of the absorption wavelength (λ_{onset}) in the thin films using $E_{\text{gap}}^{\text{opt}}=1241/\lambda_{\text{onset}}$, with values of 1.72 eV, 1.65 eV, 2.12 eV and 2.03 eV for **CS01**, **CS03**, **EP02** and **LCS01** respectively. It is noticeable than for the SMs that have a benzene ring between the benzothiadiazole core (BT), the optical band gap is larger than for the ones that have the nitrogen directly attached to the mentioned group; this is due to the higher electronegativity of the donor TPA, resulting in a

relatively higher oxidation potential²¹ and the wider separation between the donor and acceptor moiety.

The HOMO and LUMO energy levels of the SMs were measured by cyclic voltammetry (CV) in solution using dichloromethane as solvent, as showed in Chapter 5. The deeper HOMO value for **EP02** is beneficial for high value of V_{oc} for the corresponding OSC. The same trend is observed in the optical and electrochemical bandgap which indicates that bandgap decreases with the increased electron donating ability in donor-acceptor (D-A)²¹ conjugated SM, since the substituted TPA is stronger electron donor as compared to TPA. As the HOMO energy level is dependent on the electron donating moiety in D-A, therefore, the HOMO energy level of **LCS01** and **CS01** are up-shifted significantly compared with **EP02** and **CS03** respectively and attributed to the strong electron donating ability of the most substituted TPA and it has less effect on the LUMO energy level. The optical and electrochemical properties of these SMs suggest that these SMs can be employed as promising donor material for BHJ OSCs using either **PC₇₁BM** or low bandgap non-fullerene small molecule acceptors and possess sufficient LUMO and HOMO offset for exciton dissociation and charge transfer from donor to acceptor and vice-versa²².

The photoluminescence (PL) emission properties of the thin films were also measured. Figure 5.3 illustrates the PL spectrum upon excitation at $\lambda_{ex} = 529$ nm for **CS01**, $\lambda_{ex} = 543$ nm for **CS03**, $\lambda_{ex} = 460$ nm for **EP02** and $\lambda_{ex} = 473$ nm for **LCS01**. All PL spectra show the expected specular image of the absorption spectra. More interesting is the fact that, when the organic thin films contain the fullerene derivative **PC₇₁BM** in a ratio 1:2 the **CS01**, **CS03**, **EP02** and **LCS01** fluorescence is totally quenched. This observation indicates efficient electron transfer from the **CS01**, **CS03**, **EP02** and **LCS01** excited state to the fullerene and it is a first indication that all of them can be used in bulk-

heterojunction thin films, together with either **PC₇₁BM** or a low bandgap non-fullerene small molecule acceptors, in organic solar cells²².

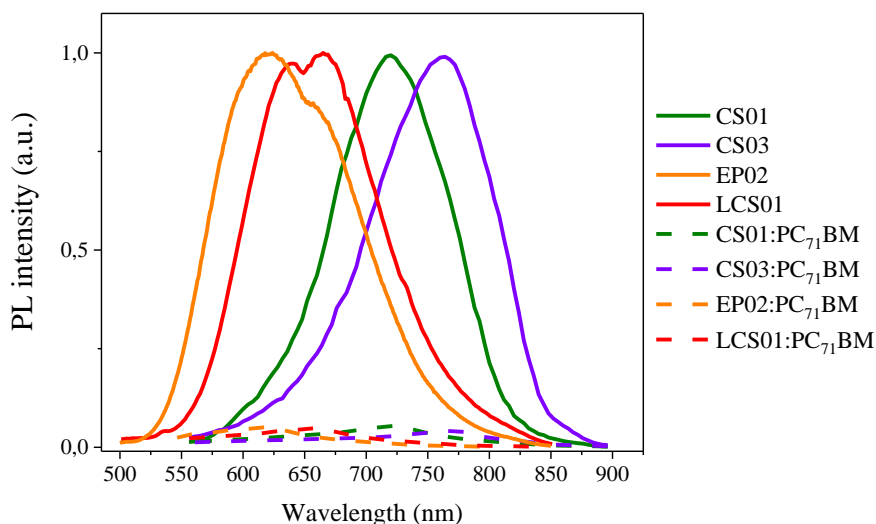


Figure 5.3: Fluorescence emission spectra for **CS01**, **CS03**, **EP02** and **LCS01** and the **CS01:PC₇₁BM**, **CS03:PC₇₁BM**, **EP02:PC₇₁BM** and **LCS01:PC₇₁BM** thin films.

6.3.2.2 Photovoltaic measurements.

In order to investigate the photovoltaic performance of these SMs, OSCs were fabricated with the following device structure ITO/PEDOT:PSS/**CS01**, **CS03**, **EP02** or **LCS01:PC₇₁BM**/PFN/Al. First of all, we have optimized the performance of OSCs through varying the D:A weight ratios in chloroform solution. It was found that the optimized weight ratio is 1:2 for all four SMs. The current-voltage (J-V) curves under illumination for the devices are shown in Figure 5.4 and photovoltaic parameters are listed in Table 5.1. The solar cells based on these SMs as cast based with **PC₇₁BM** as electron acceptor show an overall PCE of 2.03 %, 2.4 %, 2.84% and 3.20 % for **CS01**, **CS03**, **EP02** and **LCS01** respectively. The higher V_{oc} observed for **EP02** is due to the deeper relative HOMO energy value in comparison with the other SMs, besides we observe the V_{oc} gets higher depending on the energy value of the HOMO

following this trend: **CS03** < **CS01** < **LCS01** < **EP02**. As demonstrated previously, for equal recombination kinetics the V_{oc} of the organic solar cells can be correlated with the energy difference between the HOMO of the electron donor molecule and the LUMO energy level of the electron acceptor molecule. The differences in J_{sc} can be understood in terms of better light harvesting in the case of the **LCS01** and **CS03** thin films as already observed in Figure 5.2. Nonetheless, to reinforce our hypothesis we measured the incident photon to current conversion efficiency (IPCE) spectra for the OSCs (Figure 5.6). The IPCE spectrum is in perfect agreement with the absorption data and showed two bands, indicating that both **PC₇₁BM** and small molecule donors are contributing the exciton generation and subsequent dissociation in free charge carriers after the absorption of photons by the active layers. Moreover, the integration of the IPCE spectrum with respect to the 1.5 AM G sun spectra leads to values of J_{sc} very close (see Table 5.1) to the measured in the J-V curves.

The **CS01**, **CS03**, **EP02** and **LCS01** based OSCs without any treatment showed low PCE mainly due to the low values of both J_{sc} and FF and may be due to poor nanoscale morphology of the active layer which leads to undesirable charge recombination during their transportation towards electrodes. In order to improve the morphology of the active layer, we have adopted the solvent vapor annealing (SVA) treatment as reported in literature²³⁻²⁶. Solvent molecules interact with the surface of a material and may diffuse into it, depending on solvent material affinity, modifying the film and its morphology. The solvent causes intermolecular bonds (typically van der Waals and π - π interactions between conjugated building blocks) so the molecules become mobile and the material self-organizes itself into a more thermodynamic favourable state.²⁷ We have used CS₂ for SVA treatment^{25, 28} for **CS01** and **CS03** due to its high vapour pressure than other and these small molecules have medium solubility in CS₂. Moreover, **PC₇₁BM** exhibits better solubility in CS₂ as compared to other solvent such as THF. Therefore, the combination of high vapour pressure and medium solubility of the small molecule donor implies fast

Chapter 5

vapour penetration in the active layer. However, because of its hazard properties, we decided to use THF for **EP02** and **LCS01**. The current-voltage characteristics of the OSCs based on SVA treated active layer are shown in Figure 5.5 and the corresponding photovoltaic parameters are listed in Table 5.1. The photovoltaic performance of the OSCs has been significantly enhanced compared to as cast OSCs. With SVA treatment for 30 s, the OSCs based on **CS01**, **CS03**, **EP02** and **LCS01** showed overall PCE of 4.80 % ($J_{sc} = 10.48$ mA/cm², $V_{oc} = 0.79$ V and FF = 0.58), 5.32 % ($J_{sc} = 12.81$ mA/cm², $V_{oc} = 0.67$ V and FF = 0.62), 5.59 % ($J_{sc} = 10.54$ mA/cm², $V_{oc} = 0.93$ V and FF = 0.57) and 6.35 % ($J_{sc} = 12.97$ mA/cm², $V_{oc} = 0.79$ V and FF = 0.62) respectively. When the active layers are subjected to SVA treatment beyond 30 s, the both J_{sc} and FF drastically drops, while the V_{oc} remains almost constant or is slightly reduced which can be attributed to the enhanced crystalline ordering in the electron donor material or a lowering in the quasi-Fermi levels for electron and hole transport layer due to a depleted steady carrier density²⁹⁻³¹. Since the SVA treatment the crystallite of donor materials are grown, the SVA treatment of the longer time, these crystallites are over grown (> exciton diffusion length) and as large as the film thickness and the active layer no longer form the BHJ networks³²⁻³³. The large domains are not desirable for charge generation, leading to the reduction in both J_{sc} and FF and resulting reduction in the overall PCE.

The increase in the J_{sc} for the OSCs after the SVA treatment has been also confirmed from the IPCE spectra of devices (as shown in Figure 5.5). The values of IPCE for the SVA treated OSCs are higher than those for the as cast counterparts, indicating that the exciton generation and their dissociation into free charge carriers has been improved by the SVA treatment of active layer, related to the improved nanoscale morphology and phase separation.

Table 5.1: Photovoltaic parameters (J_{sc} , V_{oc} , FF, PCE for the different solar cells using **CS01**, **CS03**, **EP02** and **LCS01** as donor and **PC₇₁BM** as acceptor as cast and using SVA technique.

Active layer	J_{sc} (mA/cm ²)	V_{oc} (V)	FF	PCE (%)	J_{sc} (mA/cm ²) ^b
CS01: PC₇₁BM (as cast)	7.13	0.84	0.34	2.03 (1.93) ^a	7.01
CS01: PC₇₁BM (SVA)	10.48	0.79	0.58	4.80 (4.73) ^a	10.37
CS03: PC₇₁BM (as cast)	8.61	0.73	0.38	2.39 (2.32) ^a	8.49
CS03: PC₇₁BM (SVA)	12.81	0.67	0.62	5.32 (5.25) ^a	12.73
EP02:PC₇₁BM (as cast)	7.60	0.96	0.39	2.84 (2.77)	7.53
EP02:PC₇₁BM (SVA)	10.54	0.93	0.57	5.59 (5.50)	10.45
LCS01:PC₇₁BM (as cast)	9.08	0.82	0.43	3.20 (3.15)	9.01
LCS01:PC₇₁BM (SVA)	12.97	0.79	0.62	6.35 (6.28)	12.83

a Average of 10 devices.

b Calculated after the integration of IPCE spectra with respect to the 1.5 AM G solar spectrum.

Chapter 5

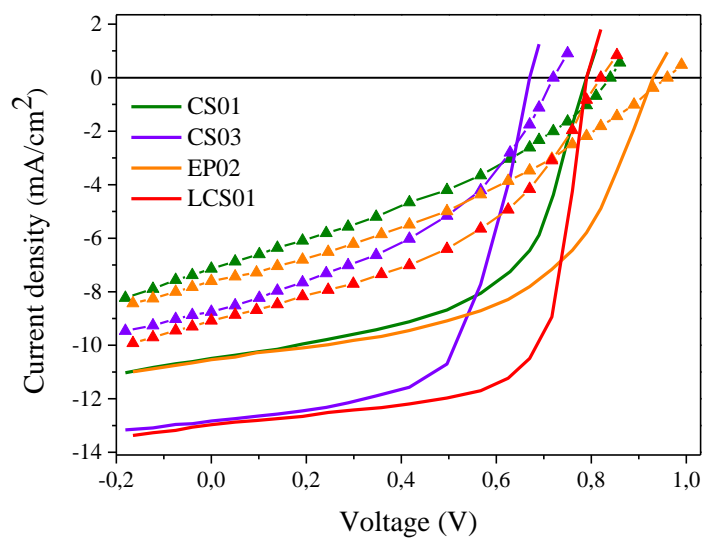


Figure 5.4: Photocurrent – voltage characteristics of the best BHJ solar cells based on **CS01**, **CS03**, **EP02** and **LCS01:PC₇₁BM** as an active layer as cast (coloured triangles) and after SVA (line).

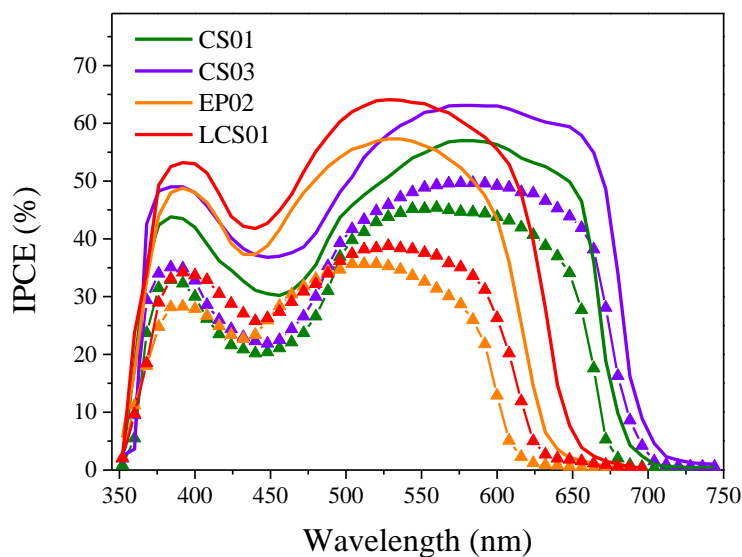


Figure 5.5: IPCE spectra of the organic solar cells based on **CS01**, **CS03**, **EP02** and **LCS01** as donor and **PC₇₁BM** as acceptor. Lines are for devices after SVA treatment and lines with coloured triangles for devices as cast.

The hole mobility of **CS01**, **CS03**, **EP02** and **LCS01** in the blend films were measured by the J-V characteristics on the hole only devices (Figure 5.6) and employing the space charge limited current (SCLC) model³⁴. The hole mobility values for as cast and SVA treated active layers are summarized in Table 5.2. The electron mobility in the as cast and SVA treated active layers were measured using electron only devices in similar manner as for hole mobility and compiled as well, in Table 5.2. There is a slight change in the electron mobility values after the SVA treatment. The improved hole mobility and better balance between the electrons and holes mobility after the SVA treatment promoted charge transport and reduced charge recombination, leading to improvement in J_{sc} and FF, and thereby PCE. Moreover, the hole mobility in **CS03** and **LCS01:PC₇₁BM** is higher than that for **CS01** and **EP02:PC₇₁BM** for as cast and SVA processing conditions, respectively; independently of the processing conditions, may be one the reasons for higher values of FF and PCE for former OSCs.

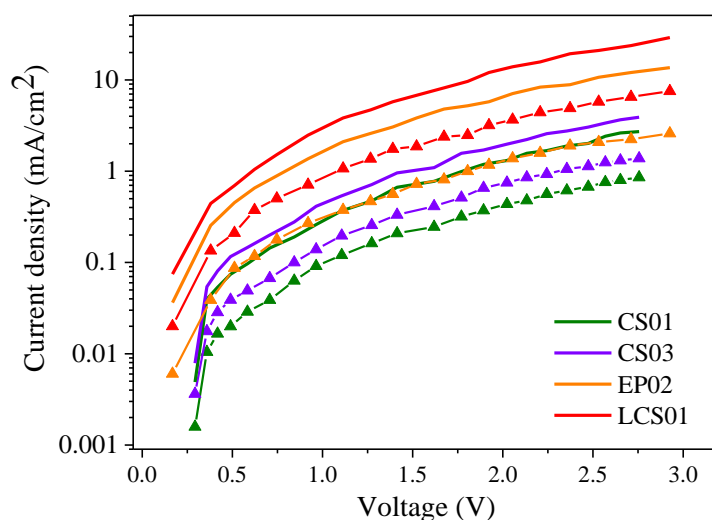


Figure 5.6: Photocurrent - voltage measurements for hole mobility using SCLC method. Lines are for devices after SVA treatment and lines with coloured triangles for devices as cast.

Chapter 5

Table 5.2: Solar cells carrier mobility measured using the Space Charge Limited Current (SCLC) model.

Active layer	Hole mobility (cm²/Vs)	Electron mobility (cm²/Vs)	Ratio
CS01:PC₇₁BM (as cast)	2.56 x10 ⁻⁵	2.13 x10 ⁻⁴	8.32
CS01:PC₇₁BM (SVA)	7.89 x10 ⁻⁵	2.42 x10 ⁻⁴	3.06
CS03:PC₇₁BM (as cast)	4.19x10 ⁻⁵	2.28 x10 ⁻⁴	5.44
CS03:PC₇₁BM (SVA)	9.87x10 ⁻⁵	2.48 x10 ⁻⁴	2.51
EP02:PC₇₁BM (as cast)	5.21 x10 ⁻⁵	2.19 x10 ⁻⁴	4.20
EP02:PC₇₁BM (SVA)	8.93 x10 ⁻⁵	2.29 x10 ⁻⁴	2.56
LCS01:PC₇₁BM (as cast)	2.11x10 ⁻⁵	2.26 x10 ⁻⁴	10.71
LCS01:PC₇₁BM (SVA)	1.04 x10 ⁻⁴	2.34 x10 ⁻⁴	2.25

Nonetheless, the solvent annealing process was indeed beneficial for the carrier collection. As illustrated in Figure 5.7 the photocurrent density (J_{ph}) plotted as a function of the effective voltage (V_{eff}) was used to get more information about the origin of the enhanced values of J_{sc} and FF. It shows significant differences between the solvent annealed thin films and the casted ones^{28, 35}. According to P.W.M. Blow et al.³⁶, the photocurrent density under AM 1.5 G light illumination (J_{ph}) can be expressed as the difference between the photogenerated current (J_{light}) and the current in the dark (J_{dark}):

$$J_{ph} = J_{light} - J_{dark}$$

Equation 5.1

$$V_{\text{eff}}=V_0-V_{\text{ext}}$$

Equation 5.2

The effective voltage (V_{eff}) also can be defined as the difference between the voltage, in which the J_{ph} is zero (V_0) and the external voltage applied (V_{ext})³⁶⁻³⁷. As can be seen from Figure 5.7, J_{ph} increases rapidly at low voltages, starts to saturate at an effective voltage at different values of V_{eff} and completely saturate at high value of V_{eff} . The early onset saturation of the J_{ph} observed for the **CS01** and **CS03** at $V_{\text{eff}} = 0.4$ V and for the **EP02** and **LCS01** at $V_{\text{eff}} = 0.6$ V based devices indicates that the internal electric field plays a minor role during the charge extraction and the charges are efficiently extracted by the electrodes.³⁶⁻³⁷ However, the as cast devices the value of J_{ph} saturate at high value of V_{eff} , indicating that large value of internal electric field is needed to extract the charge carriers and some of free charge carriers are lost prior to the collection by the respective electrode, resulting low value of FF³⁸. The ratio of the J_{ph} to the saturation current density (J_{phsat}) i.e. $J_{\text{ph}}/J_{\text{phsat}}$, under short circuit condition of the OSCs represents the exciton dissociation efficiency (P_{diss}) and the values of P_{diss} for the OSCs based on **CS01**, **CS03**, **EP02** and **LCS01** are about 0.89, 0.93, 0.93 and 0.95 respectively indicating that the exciton dissociation is more efficient for **LCS01** based device than **CS01**, **CS03** and **EP02** counterparts, following this order, due to the better phase separation. This indicates less geminate (when the electron-hole pair is still forming a weak bond) and bimolecular recombination for **LCS01**, **EP02** and **CS03** than for **CS01**, which is in agreement with the PCE values obtained. The $J_{\text{ph}}/J_{\text{phsat}}$ value at short circuit/maximum power point corresponds to the charge transport and collection efficiency (P_{coll}), which gives us information about the probabilities that the exciton dissociation occurs³⁹. The values found for P_{coll} are 0.73, 0.78, 0.67 and 0.69 for **CS01**, **CS03**, **EP02** and **LCS01** based OSCs respectively, suggesting that efficient charge transport and collection in the **CS03** based devices rather than the others. As shown in Figure 5.8 the as cast OSCs do not show any saturation region and the J_{ph} keeps on increasing with V_{eff} . At high V_{eff} , the J_{ph} for the as cast OSCs is almost same for the respective SVA treated

Chapter 5

OSCs indicating that the low values of J_{sc} measured for the as cast OSCs does not originate from the charge generation issues but rather from the poor charge extraction at the electrodes. The enhanced value of P_{coll} is also well supported by the increased value of FF.

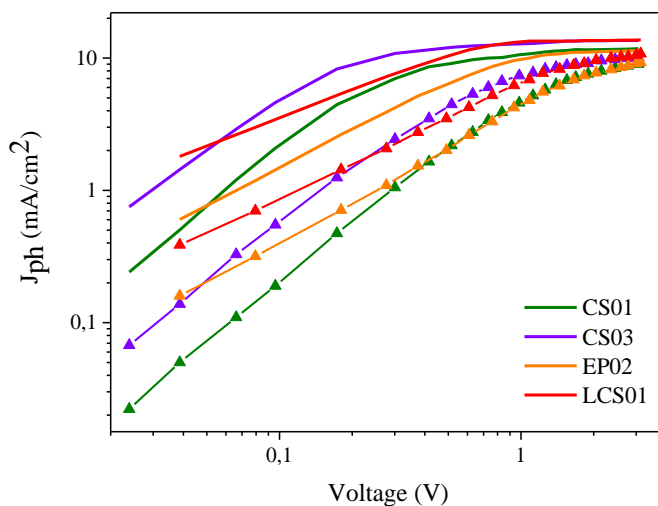


Figure 5.7: Variation of J_{ph} with the effective voltage (V_{eff}) for OSCs **CS01:PC₇₁BM**, **CS03:PC₇₁BM**, **EP02:PC₇₁BM** and **LCS01:PC₇₁BM** photoactive thin films with and without the solvent annealing process. Lines are for devices after SVA treatment and lines with coloured triangles for devices as cast.

In order to get the information about the difference in the photovoltaic performance OSCs based on **CS01**, **CS03**, **EP01** and **LCS01** as donor, X-ray diffraction measurements were applied to explore the crystallinity and molecular ordering in the optimized active layers (SVA treated active layers) for **CS01**, **CS03**, **EP02** and **LCS01** and shown in Figure 5.8. The **CS01** and **CS03** active layers showed a strong (100) diffraction peak at $2\theta = 4.89^\circ$, that corresponds to the lamellar distance of 1.98 nm. For **EP02** and **LCS01**, the diffraction peak is at $2\theta = 4.92^\circ$, so the lamellar distance is 1.93 nm. However, the (010) diffraction peak at $2\theta = 21.14^\circ$, 22.04° , 21.54° and 22.16° for **CS01**, **CS03**, **EP02** and **LCS01** corresponds to the π - π stacking distance of 0.46 nm,

0.43 nm, 0.44 nm and 0.43 nm, respectively. This suggests that **CS03** and **LCS01** form a denser molecular packing than **CS01** and **EP02**, which may induce a better nanoscale phase separation between donor and acceptor in the blend film. These factors may be responsible for the higher J_{sc} and FF. It can be seen from the XRD patterns that the **EP02** and **LCS01:PC₇₁BM** blend film showed stronger diffraction peaks correspond to (100) and (010) planes, which indicates that degree of crystalline nature is higher for **LCS01:PC₇₁BM** blend film than that for **CS01:PC₇₁BM** and **CS03:PC₇₁BM** which is beneficial for charge transport and collection. In addition to these two peaks in XRD, a weak diffraction peak also observed in all the blend films, corresponds to the PC₇₁BM⁴⁰.

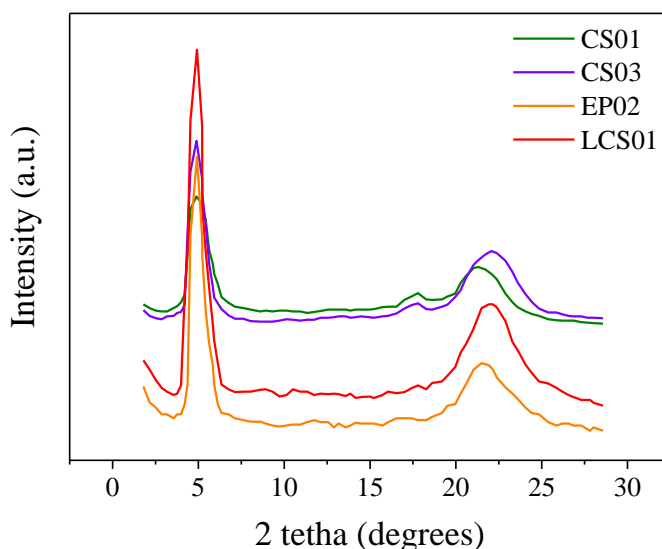
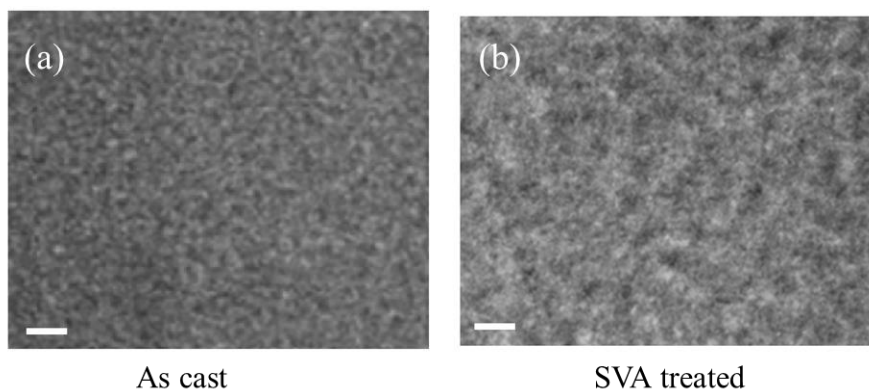


Figure 5.8: X-ray diffraction patterns of the optimized **CS01:PC₇₁BM**, **CS03:PC₇₁BM**, **EP02:PC₇₁BM** and **LCS01:PC₇₁BM** thin films after SVA treatment.

In order to get information about the influence of SVA (CS₂ and THF) on phase separation in the active layer, we have measured the transmission electron microscopy (TEM) images of the active layers before and after the SVA treatment and shown in Figure 5.9 (only for **CS03** and **LCS01:PC₇₁BM** active

Chapter 5

layers. Similar TEM images were also observed for **CS01** and **EP02:PC₇₁BM**. The black and white domains correspond to PC₇₁BM and donor small molecule regions, respectively. As it can be seen from the TEM images, as cast **CS03:PC₇₁BM** thin film did not showed any clear phase separation, which limits the charge transport within the active layer towards the electrodes, resulting low values of both J_{sc} and FF. However, the after the SVA treatment with CS₂, blend film showed larger domain (~20 nm) and clear phase separation compared to as cast, which form interpenetrating path ways for the electrons and holes transportation towards cathode and anode, respectively, leading to the increase in both J_{sc} and FF, resulting an improvement in PCE of the corresponding OSCs. Larger homogeneous with weak phase separated phase domains are observed in the case of as cast **LCS01:PC₇₁BM** thin films, however, the nano-phase separation with bi-continuous interpenetrating network is formed more efficiently in the active layer after SVA treatment, leading to the higher values of J_{sc} and FF of the corresponding OSCs.



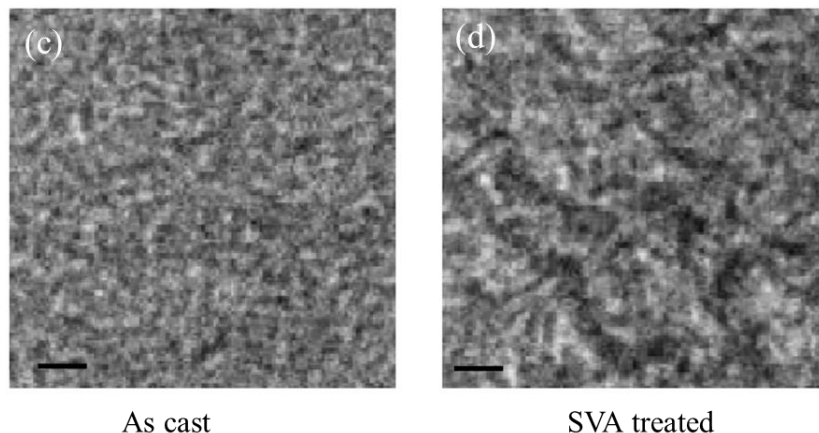


Figure 5.9: TEM images of as cast (a) and CS₂ SVA treated (b) CS03:PC₇₁BM (1:2) blended thin films and as cast (c) and THF SVA treated (d) LCS01:PC₇₁BM (1:2) blended thin films. Scale bar is 100 nm.

6.3.3. Conclusions.

In summary, we have synthesized four new low weight organic molecules that can be processed to form semiconductor organic thin films. The molecules show excellent absorption from the visible to the near IR region of the solar spectrum. These molecules show excellent interfacial electron transfer process when mixed in thin bulk-heterojunction films with the fullerene derivate PC₇₁BM. The optimization through solvent annealing of the photoactive films in solar cells with the standard configuration ITO/PEDOT:PSS/Photoactive film/PFN/Al leads to efficiencies of 4.80 %, 5.1 %, 5.59 % and 6.35 % for CS01, CS03, EP02 and LCS01, respectively. However, a deeper analysis of the photovoltaic parameters leads to the finding that the SVA processing implies the formation of an unbalanced processes between holes and electrons mobility. While the hole mobility property of the thin BHJ film improves noticeably, the electron mobility characteristics remains almost identical indicating the improved balanced charge transport. Nevertheless, the solvent annealing has positive effects on the film morphology that leads to better charge collection as measured by monitoring the changes in J_{ph} vs. V_{eff} leading to higher solar-to-energy conversion efficiencies over 6 % in the case of the

LCS01 molecule. These SMs can be also used as donor with the low bandgap non-fullerene acceptors as it will be analysed in the next section.

6.4. Binary and Ternary Bulk Heterojunction Solar Cells with non-fullerene electron acceptor.

6.4.1. Introduction.

Although impressive PCE values for binary OSCs have been achieved, there are numerous issues that must be resolved in order to further improve the PCE of OSCs. These issues include an increase in the light absorption by the active layer and better optimization of the donor/acceptor energy levels. Indeed, the large LUMO offset between many donors and acceptors can lead to significant energy loss due to the difference between the HOMO energy level of the acceptor and energy of the charge transfer state formed between the donor and the acceptor, which leads to low open circuit voltage⁴¹⁻⁴². On the other hand, a LUMO offset that is too low often limits the driving force for exciton dissociation and results in low short circuit current (J_{sc}) values.

One of the most promising strategies to overcome these issues is to employ a ternary active layer: two donors and one acceptor or one donor and two acceptors^{16, 43-46}. OSCs based on a ternary active layer harvest more photons and provide better PCE than OSCs based on binary active layers in some cases⁴⁷⁻⁴⁸.

Most of the efficient ternary OSCs investigated to date are based on a conjugated polymer as the donor. Ternary OSCs based on small molecule donor and acceptor have hardly been studied and their overall PCE values still are behind of those of their polymer counterparts. Nevertheless, in binary OSCs, small molecules display excellent efficiencies due to the known advantages over polymers, mentioned in the previous section⁴⁹⁻⁵². When studying non-

fullerene acceptors, it can be noticed that the absorption profile, molecular energy levels and molecular arrangement can be easily tuned by simple chemical modification, which makes non-fullerene small molecule acceptors ideal for the fabrication of binary and ternary OSCs.

In this section, BHJ OSCs based on new donor and acceptor small molecules, and ternary organic solar cells based on one donor and two acceptors, a fullerene (**PC₇₁BM**) and non-fullerene SM (**MPU3** and **DPP8**) will be described.

6.4.2. Devices fabrication.

The OSCs were fabricated with a conventional device arrangement: ITO/PEDOT:PSS/active layer/PFN/Al. The OSCs based on a 1:2 (donor:acceptor) weight ratio showed the best performance for binary active layers and 1:0.5:1.5 (donor:non-fullerene acceptor:**PC₇₁BM**) for the ternary counterpart in chloroform. In order to improve the efficiency, the active layers were treated by SVA treatment using tetrahydrofuran (THF) for two minutes. PFN was used as an interfacial layer.

6.4.3. CS01 and EP02 as electron donor and MPU3 as non-fullerene electron acceptor.

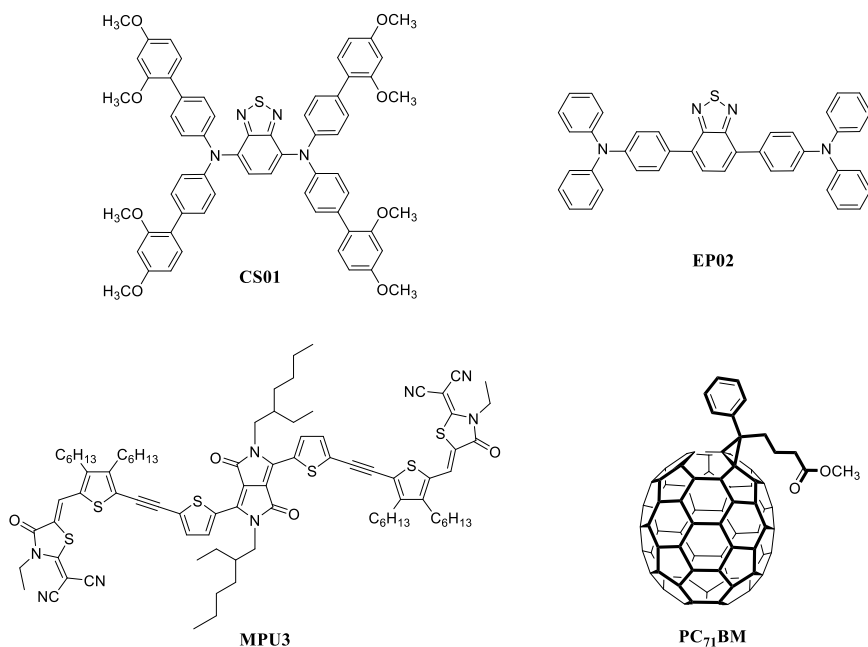
This section is based on partially published work (Efficient non-polymeric heterojunctions in ternary organic solar cells. ACS Appl. Energy Mater. 2018, 1, 8, 4203-4210), as well as not published work.

Recently, we reported two benzothiadiazole-substituted small molecule donor **CS01**⁵³ and **EP02** (Scheme 5.2) and used them as donors in conjunction with **PC₇₁BM** (see section 6.3) as an acceptor to give an overall PCE of 4.80% and 5.59 % respectively, after optimization of the binary BHJ active layer. The low

Chapter 5

PCE of this device is mainly due to the moderate J_{sc} value, which is related to the limited photoresponse range.

It was designed a non-fullerene small molecule acceptor, **MPU3**, by M. Privado, from Institute of Nanoscience, nanotechnology and Molecular Materials (INAMOL), that consists of a diketopyrrolopyrrole (DPP) central acceptor core coupled to terminal dicyanorhodanine acceptors via a thiophene ring and ethynyl linker (Scheme 5.2). This compound has previously been used as an acceptor along with a small molecule donor consisting of a 5,10-dihydroindolo [3,2-b]indole (DINI) central donor core and benzothiadiazole (BT) acceptor units. This system gave an overall PCE of 9.14% with a low energy loss of 0.54 eV.⁵⁴



Scheme 5.2: Chemical structures of **CS01**, **EP02**, **MPU3** and **PC₇₁BM**.

In the work reported here, we used **MPU3** as an acceptor and **CS01** and **EP02** as donors for the fabrication of binary BHJ OSCs and achieved a PCE of 7.81% and 8.91 %, with an energy loss of 0.48 eV and 0.47 eV, respectively, for the

optimized **CS01:MPU3** and **EP02:MPU3** active layers. These results are believed to be related to the low LUMO offset between the **CS01**, **EP02** and **MPU3**. The values obtained are higher than those of the fullerene-based counterpart.

6.4.3.1. Absorption and photoluminescence spectra.

The optical absorption spectra of these materials in thin film are shown in Figure 5.10. It can be seen from this figure that the donors **CS01** and **EP02** and the acceptor **MPU3** have complementary absorption spectra with different absorption bands centred at 574 nm, 498 nm and 702 nm, respectively.

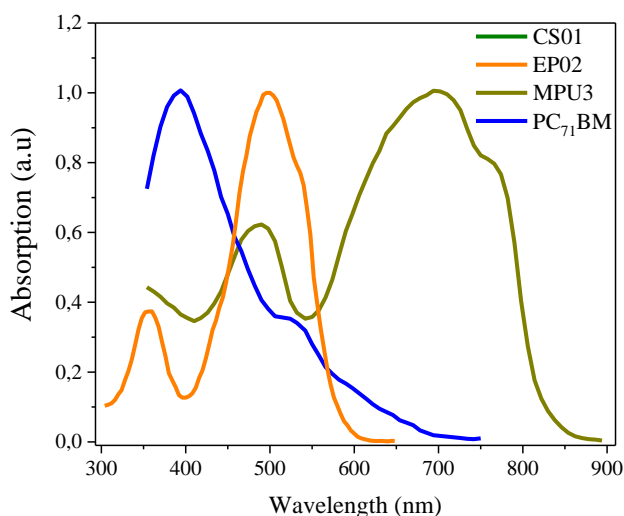


Figure 5.10: Normalized optical absorption spectra of **CS01**, **EP02**, **MPU3** and **PC₇₁BM** in thin film.

The HOMO/LUMO energy levels of **CS01**, **EP02** and **MPU3**, as determined from the electrochemical data, which was already explained in Chapter 4, are – 5.32/–3.60 eV, –5.36/–3.02 eV and –5.61/–3.74 eV, respectively (Figure 5.11).

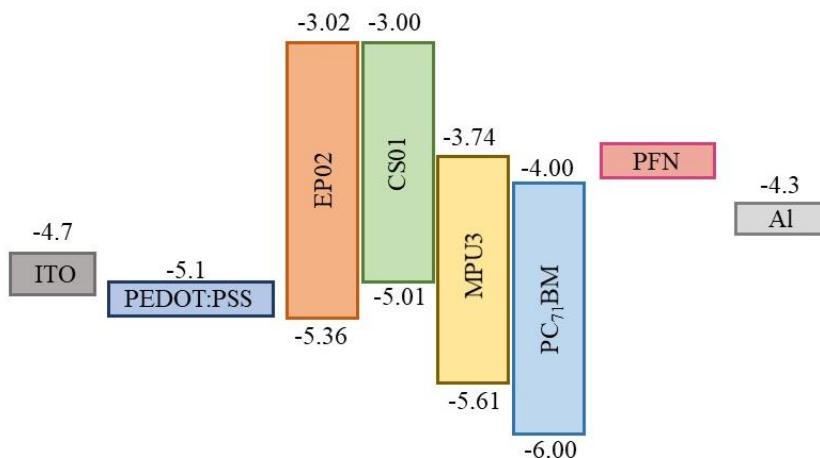


Figure 5.11: Energy level diagram of **CS01**, **EP02**, **MPU3** and **PC₇₁BM**.

The HOMO offset (ΔE_{HOMO}) between the **CS01** or **EP02** and **MPU3** is 0.29 eV and 0.25 eV (very close to the empirical threshold value of ~ 0.3 eV)⁵⁵, which is sufficient for efficient hole transfer from **MPU3** to **CS01** and **EP02**. On the other hand, the LUMO offset (ΔE_{LUMO}) between **CS01** and **MPU3** is only 0.14 eV, i.e., below the threshold value of 0.3 eV. In order to achieve high J_{sc} and V_{oc} values for OSCs, it is desirable to minimize the ΔE_{LUMO} between the donor and acceptor while still allowing efficient electron transfer from donor to acceptor. However, for **EP02** and **MPU3** also show a good performance being the value of the LUMO offset is 0.72 eV, as we confirmed from the photoluminescence (PL) data (Figure 5.12). In our OSCs based on a **CS01:MPU3** binary BHJ active layer, the electron transfer from **CS01** to **MPU3** is efficient, despite the small ΔE_{LUMO} value (0.14 eV), according to the PL. Therefore, we expect that an OSC based on a **CS01:MPU3** binary BHJ active layer may provide higher values for V_{oc} and J_{sc} than a **CS01:PC₇₁BM** counterpart. The results indicate that a ΔE_{LUMO} larger than 0.3 eV might not be an essential requirement for efficient dissociation and charge transfer in non-fullerene electron acceptors used in OSCs.

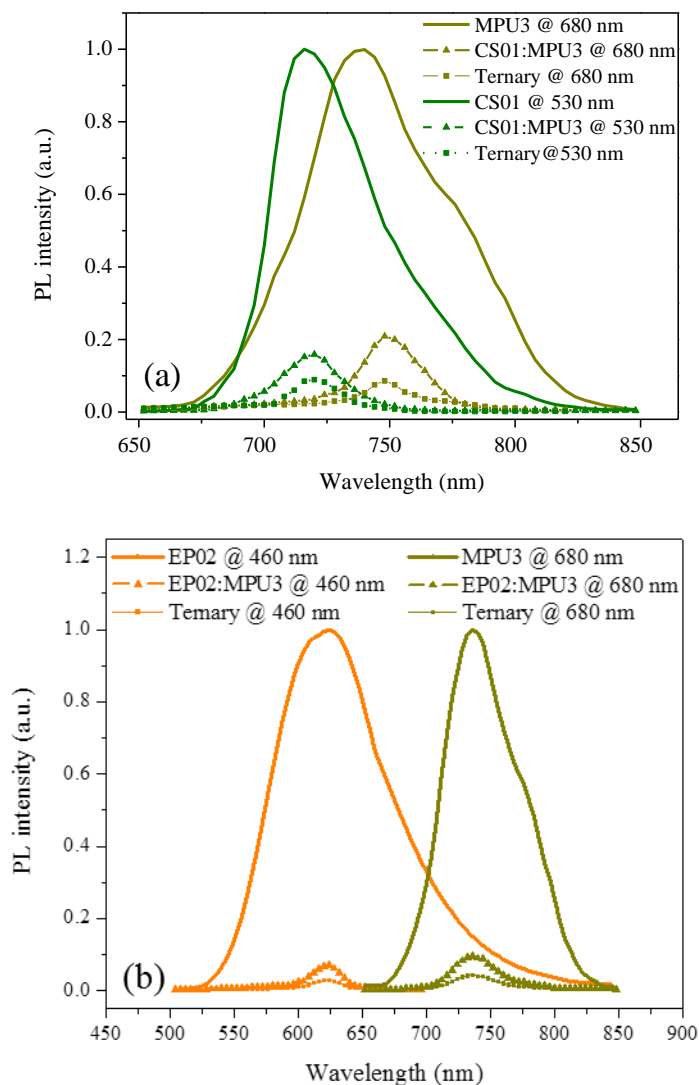


Figure 5.12: Photoluminescence spectra of (a) pristine **CS01**, **MPU3** and their binary and ternary blends in thin films and of (b) pristine **EP02**, **MPU3** and their binary and ternary blends with **PC₇₁BM** in thin films.

The PL spectra were recorded in order to investigate the charge transfer yield in the **CS01:MPU3**, **CS01:PC₇₁BM:MPU3**, **EP02:MPU3** and **EP02:PC₇₁BM:MPU3** thin films. The PL spectra of **CS01**, **EP02**, **MPU3** and their blended films are shown in Figure 5.12.

Chapter 5

The maximum absorption peaks of **CS01** (520 nm), **EP02** (490 nm) and **MPU3** (710 nm) were chosen to excite the **CS01**, **EP02** and **MPU3**, respectively. It can be seen that excitation at 520 nm led to significant quenching of the PL intensity of **CS01** for the **CS01:MPU3** blend, thus suggesting efficient electron transfer from **CS01** to **MPU3**. Similarly, excitation at 710 nm also led to quenching of the PL intensity of **MPU3** for the **CS01:MPU3** blend film. The same occurs when **EP02:MPU3** blend is excited at 490 nm and at 710 nm, indicating the effective photogenerated hole transfer from **MPU3** to **EP02** despite the low HOMO offset between them. These results demonstrate that efficient charge transfer is taking place at the D/A interfaces in the **CS01:MPU3** and **EP02:MPU3** active layers and the small molecules, **CS01**, **EP02** and **MPU3**, contribute to the photocurrent generation in these mixtures.

*6.4.3.2. Photovoltaic measurements.***Table 5.3:** Photovoltaic parameters of OSCs based on **CS01:MPU3** (as cast) with different weight ratio.

Weight ratio	J_{sc} (mA/cm ²)	V_{oc} (V)	FF	PCE (%)
1:0.5	7.48	1.09	0.31	2.53
1:1	8.78	1.10	0.31	2.99
1:2	9.48	1.10	0.32	3.34
1:2.5	8.93	1.11	0.31	3.07

In order to evaluate the photovoltaic properties of the OSCs based on **CS01:MPU3** and **EP02:MPU3** binary BHJ active layers, we initially screened (see the resume done for **CS01:MPU3** in Table 5.3) the performance of OSCs by varying the weight ratio of **CS01:MPU3** and **EP02:MPU3** using chloroform as solvent. The OSCs were fabricated with a conventional device arrangement, i.e., ITO/PEDOT:PSS/active layer/PFN/Al. The OSCs based on a 1:2 weight ratio (as cast) showed the best performance, with an overall PCE of 3.34 % (J_{sc}

= 9.48 mA/cm², V_{oc} = 1.10 V and FF = 0.32) and 4.70 % (J_{sc} = 11.45 mA/cm², V_{oc} = 1.08 V and FF = 0.38) for **CS01:MPU3** and **EP02:MPU3** respectively. After optimization of the **CS01:MPU3** and **EP02:MPU3** active layers by SVA treatment, the OSC behaviour was enhanced to give a PCE of 7.81 % (J_{sc} = 13.04 mA/cm², V_{oc} = 1.07 V and FF = 0.56) and 8.91 % (J_{sc} = 14.64 mA/cm², V_{oc} = 1.05 V and FF = 0.58). This PCE is higher than that of the **PC₇₁BM** counterpart processed under identical conditions (**CS01:PC₇₁BM**; PCE = 4.80 % and **EP02:PC₇₁BM**; PCE = 5.59 %), already showed in the previous section of this chapter. The current–voltage characteristics of the OSCs based on optimized **CS01:MPU3**, **CS01:PC₇₁BM**, **EP02:MPU3** and **EP02:PC₇₁BM** are shown in Figure 5.13 and the photovoltaic parameters are collected in Table 5.4.

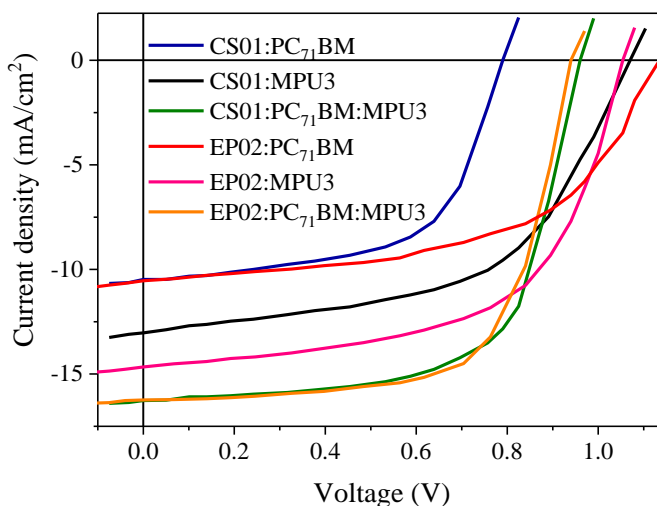


Figure 5.13: Current-Voltage (J - V) characteristics under illumination of the OSCs based on optimized **CS01:PC₇₁BM**, **CS01:MPU3**, **CS01:PC₇₁BM:MPU3**, **EP02:PC₇₁BM**, **EP02:MPU3**, **EP02:PC₇₁BM:MPU3**.

Chapter 5

Table 5.4: Photovoltaic parameters of the OSCs based on different active layers.

Active layer	J_{sc} (mA/cm ²)	J_{sc} (mA/cm ²) ^a	V_{oc} (V)	FF	PCE (%)
CS01:PC₇₁BM (as cast)	7.13	7.01	0.84	0.34	2.03 (1.95) ^b
CS01:PC₇₁BM (SVA)	10.48	10.39	0.79	0.58	4.80 (4.73) ^b
EP02:PC₇₁BM (as cast)	7.60	7.53	0.96	0.39	2.84
EP02:PC₇₁BM (SVA)	10.54	10.45	0.93	0.57	5.59
CS01:MPU3 (as cast)	9.48	-	1.10	0.32	3.34 (3.26) ^b
CS01:MPU3 (SVA)	13.04	12.95	1.07	0.56	7.81 (7.74) ^b
EP02:MPU3 (as cast)	11.45	11.34	1.08	0.38	4.70 (4.63) ^b
EP02:MPU3 (SVA)	14.64	14.57	1.05	0.58	8.91 (8.82) ^b
CS01:PC₇₁BM:MPU3 (as cast)	12.18	-	1.02	0.52	6.46 (6.41) ^b
CS01:PC₇₁BM:MPU3 (SVA)	16.27	16.22	0.97	0.63	9.94 (9.86) ^b
EP02:PC₇₁BM:MPU3 (as cast)	13.68	-	0.97	0.49	6.50 (6.43) ^b
EP02:PC₇₁BM:MPU3 (SVA)	16.24	16.12	0.94	0.63	9.62 (9.53) ^b

^aBased on IPCE measurements.

^bAverage of 8 devices

The V_{oc} values for OSCs based on the **MPU3** acceptor are higher than that obtained using **PC₇₁BM**, which was expected due to the higher LUMO energy level of **MPU3**. In addition, **MPU3**-based OSCs afford a higher J_{sc} value compared to **PC₇₁BM** counterparts. The J_{sc} of the OSCs is directly related to the light harvesting efficiency of the active layer and we therefore recorded the optical absorption spectra of the **CS01:MPU3**, **CS01:PC₇₁BM**, **EP02:MPU3** and **EP02:PC₇₁BM** blend thin films of the same thickness (see Figure 5.14).

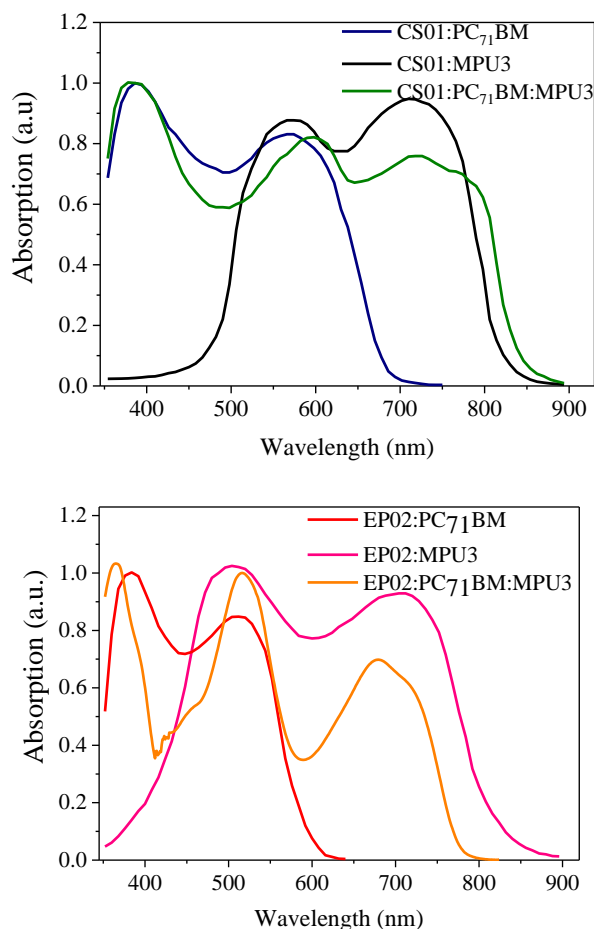


Figure 5.14: Optical absorption spectra of (a) binary and ternary active layers **CS01:PC₇₁BM**, **CS01:MPU3** and **CS01:PC₇₁BM:MPU3**, (b) binary active layers **EP02:PC₇₁BM** and **EP02:MPU3**.

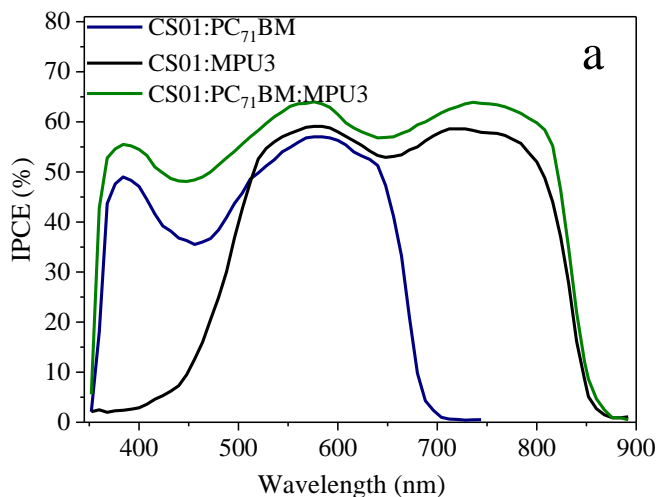
Chapter 5

The absorption spectra of the binary layers consisted in the two SMs with **PC₇₁BM** and **MPU3** are shown in Figure 5.14. It can be seen from this figure that the **EP02:MPU3** active layer showed a wide absorption profile from 400 to 870 nm whereas **EP02:PC₇₁BM** showed absorption only from 350 nm to 600 nm, indicating that employing **EP02:MPU3** active layer the light harvesting efficiency of the OSCs can be significantly improved which is beneficial for high value of J_{sc} . The same happens with **CS01:MPU3** active layer that shows an absorption spectrum from 400 nm up to 900 nm while **CS01: PC₇₁BM** presents an absorbance from 350 nm to 700 nm.

The higher V_{oc} value for the OSC based on an optimized active layer using **MPU3** as acceptor (1.07 V and 1.05 V for **CS01** and **EP02** respectively) when compared to the **PC₇₁BM** counterpart (0.79 V and 0.93 V) is attributed to the high lying LUMO of **MPU3** in comparison to **PC₇₁BM**, since in a BHJ OSC the V_{oc} is directly related to the energy difference between the LUMO of the acceptor and the HOMO of the donor materials used in the active layer.⁵⁶ It was reported that the V_{oc} values of such devices increase gradually with the decrease in the ΔE_{HOMO} between donor and non-fullerene acceptor ($HOMO_{donor} - HOMO_{acceptor}$)⁵⁷⁻⁵⁹. The ΔE_{HOMO} is lower for **CS01:MPU3** and **EP02:MPU3** than for **CS01:PC₇₁BM** or **EP02: PC₇₁BM**, and this difference can be attributed to the high V_{oc} of the former device as compared to latter. The low energy offsets, i.e., ΔE_{LUMO} and ΔE_{HOMO} , indicated a low energy loss for **MPU3** films when compared to their **PC₇₁BM** counterparts and this is beneficial for achieving a high V_{oc} .

The IPCE spectra of the devices based on the optimized **CS01:MPU3**, **EP02:MPU3**, **CS01:PC₇₁BM** and **EP02: PC₇₁BM** are shown in Figure 5.15. Both, the **CS01:MPU3** and **EP02:MPU3** devices showed a photo-response from 400 - 410 nm to 900 nm whereas the **CS01:PC₇₁BM** and **EP02:PC₇₁BM** devices showed a response only up to 700 nm, as it was illustrated previously in this chapter. The IPCE responses of the OSCs closely resemble the optical

absorption spectra of the corresponding active layers (Figure 5.15), which indicates that the donors (**CS01** and **EP02**) and acceptor (**PC₇₁BM** or **MPU3**) contribute to the photocurrent generation. Although the ΔE_{LUMO} for **CS01:MPU3** is very small (0.14 eV), the IPCE spectra indicate that there is sufficient driving force for the electron transfer to take place from the **CS01** to **MPU3**. The J_{sc} values estimated from the integration of the IPCE spectra of the OSCs are 10.39 mA/cm² and 12.95 mA/cm² for **CS01:PC₇₁BM** and **CS01:MPU3** active layers and 10.45 mA/cm² and 14.57 mA/cm² for **EP02:PC₇₁BM** and **EP02:MPU3** active layers, respectively. These results match well with the values obtained from the J - V measurements (Table 5.4).



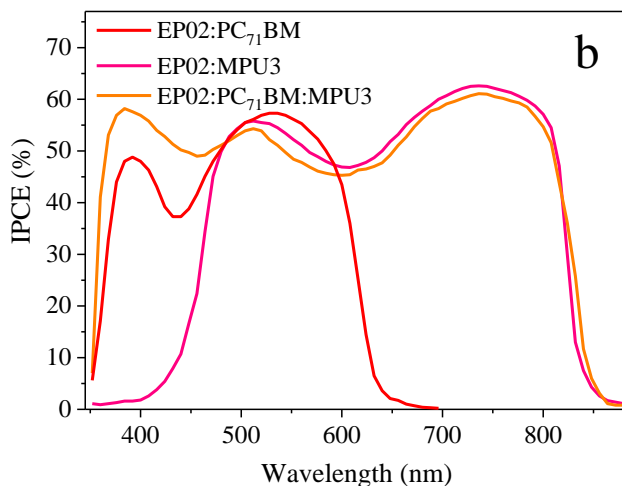


Figure 5.15: IPCE spectra of the OSCs based on optimized (a) **CS01:PC₇₁BM**, **CS01:MPU3** and **CS01:PC₇₁BM:MPU3** and (b) **EP02:PC₇₁BM**, **EP02:MPU3** and **EP02:PC₇₁BM:MPU3**.

One of the critical issues for OSCs is their relatively large energy loss (E_{loss}), defined as:

$$E_{\text{loss}} = E_g / q - V_{\text{OC}} \quad \text{Equation 5.3}$$

where E_g is the optical bandgap of the donor or acceptor (the smallest one), which is in the range of 0.7–1.0 eV⁵⁵. The energy loss of OSCs has three causes, including the unavoidably large driving force for exciton dissociation (≈ 0.2 –0.3 eV) and additional radiative and non-radiative recombination loss⁶⁰⁻⁶¹. The E_{loss} values for OSCs based on SVA-treated **CS01:MPU3**, **CS01:PC₇₁BM**, **EP02:MPU3** and **EP02:PC₇₁BM** are 0.45 eV 0.94 eV, 0.47 eV and 1.02 eV respectively. As the ΔE_{LUMO} for **CS01:MPU3** is very low (0.14 eV) compared to **CS01:PC₇₁BM** (0.73 eV), the radiative recombination loss may be attributed to the low E_{loss} ⁶²⁻⁶³. The reduced E_{loss} is the reason for the higher V_{oc} for the **CS01:MPU3**-based OSCs. It occurs the same in the case of the **EP02:MPU3**-based OSCs. ΔE_{LUMO} is lower (0.62 eV) than for **EP02:PC₇₁BM** (1.0 eV),

therefore the E_{loss} is also reduced and the V_{oc} obtained with the non-fullerene acceptor is higher.

6.4.3.2. Ternary Organic Solar Cells.

The active **CS01:MPU3** and **EP02:MPU3** layers showed poor absorption below 500 nm and it was therefore reasonable to incorporate **PC₇₁BM**, which exhibits strong absorption in the range of 300 – 500 nm, as a third component to improve the light harvesting efficiency of the active layer and thus increase the PCE of the corresponding device. Furthermore, the HOMO and LUMO energy levels of **PC₇₁BM** are lower than those of **MPU3** (Figure 5.11). This type of cascade energy level alignment improves the charge transfer. Initially, the weight ratio **MPU3** (acceptor 1):**PC₇₁BM** (acceptor 2) was carefully varied while the weight ratio of **CS01** or **EP02:(MPU3+PC₇₁BM)** was kept at 1:2 based on the binary OSCs. The best photovoltaic result was observed for the active layer **CS01** or **EP02:PC₇₁BM:MPU3** with a weight ratio of 1:0.5:1.5 (see Table 5.5 for **CS01**) in chloroform (PCE of 6.46 % with $J_{\text{sc}} = 12.18$ mA/cm², $V_{\text{oc}} = 1.02$ V and FF = 0.52 for **CS01** based devices and PCE of 6.50 % with $J_{\text{sc}} = 13.68$ mA/cm², $V_{\text{oc}} = 0.97$ V and FF = 0.49 for **EP02** based devices). A further increase in **PC₇₁BM** beyond 0.5 led to decrease in the J_{sc} value due to the insufficient absorption in the longer wavelength region. In order to improve PCE, the ternary active layer was treated by SVA using THF for 2 minutes. The J - V characteristics of the OSC based on the optimized ternary active layer are shown in Figure 5.14 and the photovoltaic parameters are provided in Table 5.4. The OSCs based on the optimized ternary active layer showed an overall PCE of 9.94 % with $J_{\text{sc}} = 16.27$ mA/cm², $V_{\text{oc}} = 0.97$ V and FF = 0.63 for **CS01:PC₇₁BM:MPU3** devices and of 9.62 % with $J_{\text{sc}} = 16.24$ mA/cm², $V_{\text{oc}} = 0.94$ V and FF = 0.63 for **EP02:PC₇₁BM:MPU3** devices. The increase in J_{sc} for the ternary active layer is due to the complementary absorption spectra when **PC₇₁BM** is included in the blend. The FF value of the ternary device also improved significantly in both cases and this is related to

Chapter 5

the morphology modulation and better charge balanced mobility due to the incorporation of **PC₇₁BM**, which plays a key role in the enhancement of the PCE. Both, J_{sc} and FF improved compared with the binary BHJ OSCs related to the broad absorption profile that improves the light harvesting efficiency of the active layer, and the increased the interfacial area in the D-A interfaces (**CS01** and **EP02/PC₇₁BM** and **CS01** and **EP02/MPU3**).

The increased D-A interfacial leads to more efficient exciton dissociation. The IPCE spectra of the optimized ternary OSC are shown in Figure 5.15. These closely resemble the absorption spectra of the ternary active layer (Figure 5.14) and this indicates that all components used in the ternary active layer contribute to the photocurrent generation. The J_{sc} value estimated from the IPCE spectra is 16.22 mA/cm² and 16.12 mA/cm² for **CS01** and **EP02** based devices respectively, and this is very close to the value obtained from the J - V characteristics under illumination.

Table 5.5: Photovoltaic parameters of OSCs based on **CS01:PC₇₁BM:MPU3** (as cast) with different weight ratio.

Weight ratio	J_{sc} (mA/cm ²)	V_{oc} (V)	FF	PCE (%)
1:0.2:1.8	11.03	1.01	0.50	5.58
1:0.5:1.5	12.18	1.02	0.52	6.46
1:0.8:1.2	11.73	0.99	0.49	5.69

The slight decrease in the V_{oc} for **CS01** and **EP02**-based devices after the incorporation of **PC₇₁BM** is due to the deeper LUMO energy level of **PC₇₁BM** when compared to **MPU3**, a difference that gives a lower energy offset with respect to the HOMO energy level⁶⁴. The values of ΔE_{LUMO} and ΔE_{HOMO} for the

CS01:MPU3 binary BHJ active layer are less than 0.3 eV and this may hinder the photoinduced charge transfer and also limit the PCE of the corresponding OSC. Compared to **MPU3**, **PC₇₁BM** has lower LUMO and HOMO energy levels and this difference acts as an energy driver to enhance the driving force for charge transfer⁶⁵. As a result, when compared to the OSC based on **CS01:MPU3** and **EP02:MPU3** with the optimized **CS01:PC₇₁BM:MPU3**-based and **EP02:PC₇₁BM:MPU3** counterparts showed an enhanced PCE of 9.84 % and 9.62 % with a small energy loss of 0.56 eV and 0.54 eV, and a high V_{oc} of 0.96 V and 0.93 V respectively.

As discussed above, the PL intensity of the **CS01:MPU3** blend is more quenched relative to pristine **CS01** and **MPU3**, respectively. The insufficient PL quenching of the **CS01:MPU3** may be attributed to the unsatisfactory driving force for charge transfer in the BHJ active layer. However, it was observed that in the optimized **CS01:PC₇₁BM:MPU3**, the PL intensity decreased compared to the pristine **CS01** and **MPU3**, respectively (as shown in Figure 5.13). The same results were found for **EP02:PC₇₁BM:MPU3**. The strong PL quenching indicates more efficient charge transfer from donor to acceptor and acceptor to donor. The enhanced IPCE response of **CS01**, **EP02** and **MPU3** in the **CS01** or **EP02:PC₇₁BM:MPU3** blend also suggests more efficient charge transfer from the donor to acceptor and acceptor to donor. The more efficient charge transfer in the ternary blend is attributed to the lower LUMO and HOMO energy levels of **PC₇₁BM** and this acts as an energy driver and leads to the enhancement in the J_{sc} and FF.

In an effort to obtain more information about the effect that the incorporation of **PC₇₁BM** has on the exciton generation and dissociation and on charge transport, the variation of photocurrent density (J_{ph}) with effective voltage (V_{eff}) in the OSCs were analysed, according to the equations 1 and 2, previously explained in this chapter.^{36, 66} The results are shown in Figure 5.11. It can be seen from the figure that J_{ph} for all the OSCs increases in a linear manner with

Chapter 5

voltage at low V_{eff} values and gradually approaches saturation at low V_{eff} values around 0.5 V.

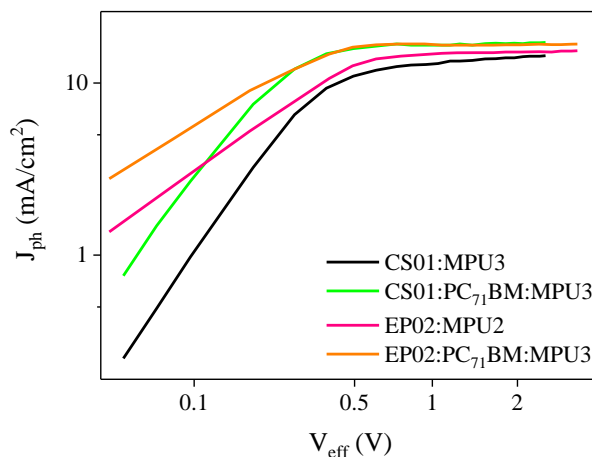


Figure 5.16: Variation of J_{ph} with V_{eff} for the devices based on optimized **CS01:MPU3**, **CS01:PC₇₁BM:MPU3**, **EP02:MPU3** and **EP02:PC₇₁BM:MPU3** active layers.

The saturation photocurrent density (J_{phsat}) for the ternary OSC is higher than those of the binary counterparts, which is consistent with the J_{sc} values. At high V_{eff} it is assumed that all the charge carriers are extracted and collected efficiently, in which case J_{phsat} is limited only by the exciton generation rate (G_{max}). The G_{max} is related to J_{phsat} as:

$$J_{\text{phsat}} = q \cdot L \cdot G_{\text{max}} \quad \text{Equation 5.4}$$

where q is the electronic charge and L is the thickness of the active layer. The value of G_{max} for ternary systems ($1.25 \times 10^{28} \text{ m}^{-3}\text{s}^{-1}$ for **CS01**-based devices and $1.22 \times 10^{28} \text{ m}^{-3}\text{s}^{-1}$ for **EP02**-based devices) is higher than that for binary OSCs ($1.05 \times 10^{28} \text{ m}^{-3}\text{s}^{-1}$ and $0.87 \times 10^{28} \text{ m}^{-3}\text{s}^{-1}$ for **CS01:MPU3** and **CS01:PC₇₁BM**, respectively and $1.13 \times 10^{28} \text{ m}^{-3}\text{s}^{-1}$ and $0.83 \times 10^{28} \text{ m}^{-3}\text{s}^{-1}$ for **EP02:MPU3** and **EP02:PC₇₁BM**). The high value of G_{max} for the ternary OSC is consistent with the absorption profile of the ternary blend and the IPCE

spectra of the corresponding OSCs. The probability of exciton dissociation (P_{diss}) and charge collection (P_{coll}) can be estimated by $J_{\text{ph}}/J_{\text{phsat}}$ at short circuit conditions and maximal power point conditions, respectively, as we explained before in this chapter⁶⁷. The $P_{\text{diss}}/P_{\text{coll}}$ values are 0.89/0.75, 0.91/0.79 and 0.95/0.81 for **CS01:PC₇₁BM**, **CS01:MPU3** and **CS01:PC₇₁BM:MPU3**, respectively. Both the P_{diss} and P_{cc} values for the ternary OSC are higher than those for binary counterparts, indicating that charge generation and transportation in the ternary OSCs is more efficient than in the binary OSCs. The values of $P_{\text{diss}}/P_{\text{coll}}$ for **EP02:PC₇₁BM**, **EP02:MPU3** and **EP02:PC₇₁BM:MPU3** are 0.93/0.67, 0.95/0.63 and 0.96/0.71, respectively. The same as for **CS01**-based devices, for **EP02** ternary OSCs the values of $P_{\text{diss}}/P_{\text{coll}}$ are higher than the binary based counterparts, which indicates that incorporation of **PC₇₁BM** is beneficial for exciton dissociation kinetics due to the increase D-A interfacial area (more D-A interfaces are created) in the ternary active layer.

In order to understand the improved PCE of the ternary OSCs, when compared to the binary counterparts, the charge carrier recombination actions in the devices were analysed by measuring the dependence of J_{sc} and V_{oc} on illumination intensity (P_{in}), since the charge recombination is a critical factor that significantly affects the performance of the OSCs.

Chapter 5

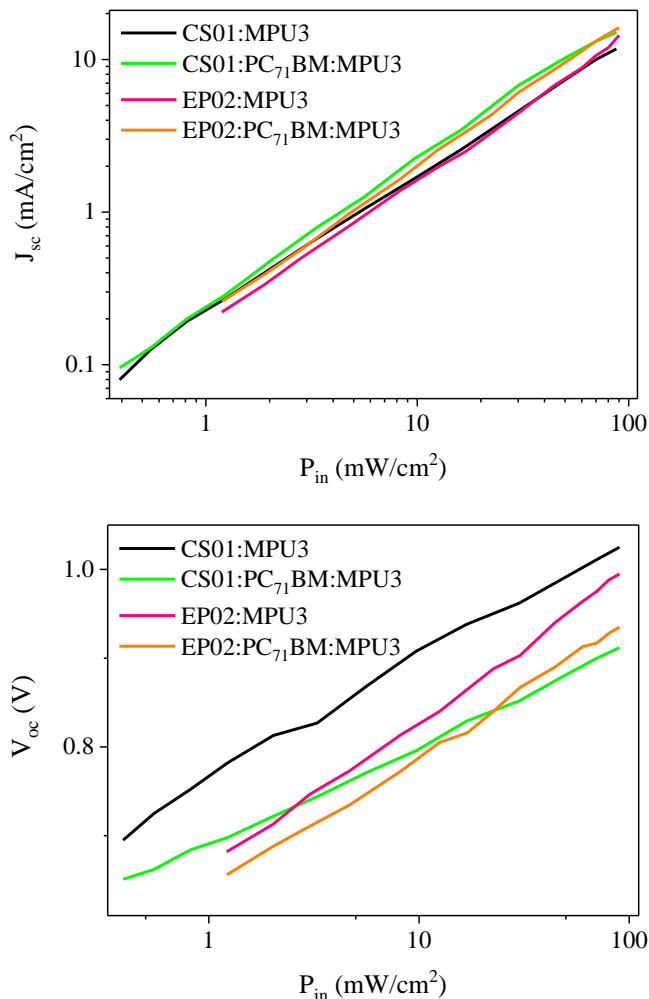


Figure 5.17: Variation of (a) J_{sc} and (b) V_{oc} with illumination intensity (P_{in}) for the OSCs based on optimized **CS01:MPU3**, **CS01:PC₇₁BM:MPU3**, **EP02:MPU3** and **EP02:PC₇₁BM:MPU3** active layers.

The variation of J_{sc} and V_{oc} for the OSCs is shown in Figures 5.17a and 5.17b, respectively, and this can be described by the power law:

$$J_{sc} \propto P_{in}^{\gamma} \quad \text{Equation 5.5}$$

where γ is the parameter that indicates the degree of bimolecular recombination⁶⁸⁻⁷⁰. When the value of γ is around unity, the photocurrent loss is minimal due to the negligible bimolecular recombination in the OSCs. Fitting the data shown in figure 12a with the power law (Equation 5.5) relationship gave γ values of 0.89, 0.91 and 0.95 for **CS01:PC₇₁BM**, **CS01:MPU3** and **CS01:PC₇₁BM:MPU3** based OSCs and 0.95 and 0.97 for **EP02:MPU3** and **EP02:PC₇₁BM:MPU3** based OSCs, respectively. Therefore, the improvement in the γ value with a higher P_{diss} for a ternary OSC, when compared to binary counterparts, indicates very weak bimolecular recombination and more efficient charge extraction⁷¹. The variation of V_{oc} with P_{in} for the OSCs is shown in Figure 5.18b. This relationship provides independent and complementary information about the charge recombination, under open circuit conditions, in which all of the photogenerated charge carriers should recombine within the device ($J = 0$). The relationship between V_{oc} and P_{in} can be expressed as it can be seen in the following equation:

$$V_{\text{oc}} \propto \left(\frac{nkT}{q} \right) \ln P_{\text{in}} \quad \text{Equation 5.6}$$

where k is the Boltzmann constant, T is the absolute temperature and q is the elementary charge⁷². When the parameter ‘ n ’ is close to unity then the bimolecular recombination becomes more dominant. However, if the value of ‘ n ’ is 2 then the trap-assisted recombination is more intense⁷²⁻⁷³. From Figure 5.13b it can be seen that the value of ‘ n ’ is about 1.45, 1.32 and 1.13 for **CS01:PC₇₁BM**, **CS01:MPU3** and **CS01:PC₇₁BM:MPU3** active layers and 1.43, 1.24 and 1.11 for **EP02:PC₇₁BM**, **EP02:MPU3** and **EP02:PC₇₁BM:MPU3** active layers, respectively. The lowest ‘ n ’ value for the ternary active layer based OSC indicates that the trap-assisted recombination was effectively suppressed in the optimized ternary active layer.

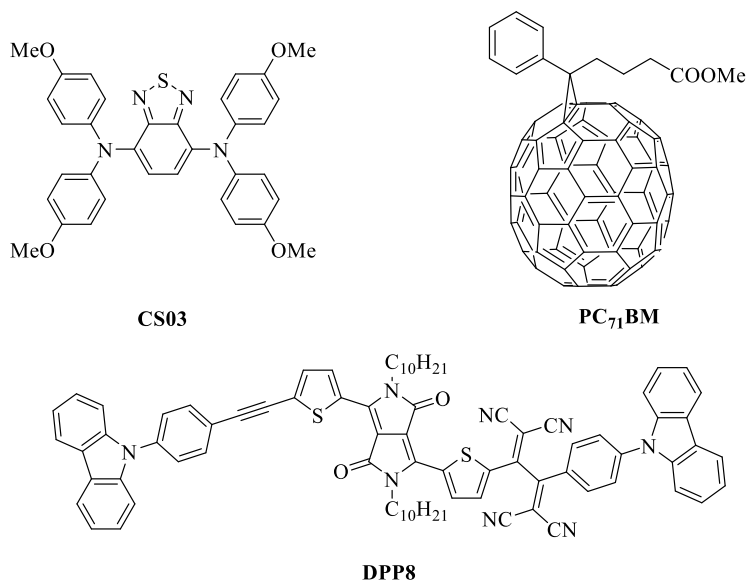
Chapter 5

6.4.3.3. Conclusions.

Small molecule OSCs have been fabricated with a low band gap non-fullerene acceptor, **MPU3** and a benzothiadiazole-substituted small molecule donors, **CS01** and **EP02**. After optimization of the **CS01** and **EP02:MPU3** active layers, the OSC showed an overall PCE of 7.81% and 8.91 %, respectively; which is higher than that of the **CS01** or **EP02:PC₇₁BM** counterparts processed under identical conditions. The higher LUMO energy of **MPU3** is beneficial for high V_{oc} and low energy loss while the low band gap and absorption profile, which extended up to 900 nm, are beneficial for higher J_{sc} . Finally, the OSC based on an optimized ternary **CS01** or **EP02:PC₇₁BM:MPU3** gave a PCE as high as 9.94% and 9.62 %. The increase in the PCE for ternary OSCs is attributed to the fact that **PC₇₁BM** acts as the energy driving force for the exciton dissociation due to the lower values of the HOMO and LUMO energy levels when compared to **MPU3** in the binary and the ternary OSC.

6.4.4. Binary and ternary bulk heterojunction organic solar cells with **CS03** as electron donor and **DPP8** as a non-fullerene electron acceptor.

Among some of the novel non-fullerene electron acceptors, the dihydropyrrolo[3,4-*c*]pyrrole-1,4-dione-based molecule containing a tetracyanobutadiene motif (**DPP8**) (Scheme 5.3) holds the promise to be a good alternative to the widely used **PC₇₁BM**⁷⁵. The **DPP8** UV-Visible absorption spectrum range, the HOMO and energy levels, and its solubility, can be easily tuned, which makes **DPP8** ideal for the designing of binary and ternary organic solar cells⁷⁶.



Scheme 5.3: The chemical structures of **CS03**, **DPP8** and **PC₇₁BM**.

In this work, we aim to take advantage of the TOHs and enlarge the photocurrent response of the solar cell by covering a wider range of the sun spectra and obtain higher open circuit voltage too. To this end, we incorporate **PC₇₁BM** into the binary blend of **DPP8** and the wide-band gap low molecular weight (LMW) electron donor **CS03**, to fabricate a ternary organic heterojunction/low molecular weight solar cell (TOH/LMW solar cell). The chemical structures of these organic materials are shown in Scheme 5.3. The TOH combines the advantages of **PC₇₁BM** (high electron mobility)¹ and **DPP8** (complementary and strong absorption beyond 650 nm to 950 nm⁷⁶, where the **CS03:PC₇₁BM** blend showed weak absorption). After the optimization of TOH, with solvent vapor treatment, the OSC showed overall PCE of 8.94 %, which is higher than that for binary organic heterojunctions BHJ consisting in a blend of **CS03**⁵³, with each individual electron acceptors being 7.44 % and 5.07 % for **CS03:DPP8** and **CS03:PC₇₁BM**, respectively. This enhancement is related to the wider absorption profile of TOH, improved energy levels alignment and better charge balance of electronic holes and electrons.

Chapter 5

6.4.4.1. Device preparation.

The solar cells efficiency of the binary and ternary blends were used in the following configuration: ITO/PEDOT:PSS/photoactive layer/PFN/Al. PFN was used as selective contact at the cathodic interfacial layer to improve carriers collection. The photoactive film of **CS03**, **PC₇₁BM**, and **DPP8** with various weight ratios and was fabricated using spin-casting from a chlorobenzene (CB) solution with a film thickness of 85 ± 5 nm. After the optimization of weight ratio of donor and acceptor, the binary active layer was exposed to the SVA for 40 seconds using tetrahydrofuran as solvent.

6.4.4.2. Absorption and photoluminescence spectra.

The syntheses, optical and electrochemical properties of **CS03** and **DPP8** have been already showed in the Chapter 4 and published elsewhere^{53, 75}. The UV-Visible absorption spectra of the individual thin films are shown in Figure 5.18.

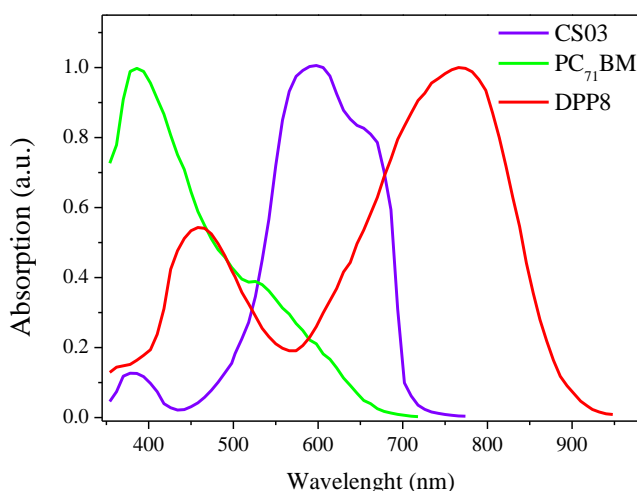


Figure 5.18: Normalized UV-Visible absorption spectra of **CS03**, **PC₇₁BM**, and **DPP8** individual thin films (thickness = 80 nm).

The UV-Visible-near IR absorption spectrum of **DPP8** shows maximum absorption at 764 nm with an onset that extends to 900 nm (optical band gap of 1.36 eV), which is complementary to both **CS03** and **PC₇₁BM**. The light absorption of **CS03** and **PC₇₁BM** is negligible in the near IR region, therefore it is reasonable to include **DPP8**, which exhibits its main absorption up to 950 nm, as third component to help the photon harvesting efficiency and further improve the efficiency of OSCs. The absorption spectra of the binary (**CS03:PC₇₁BM** and **CS03:DPP8**) and ternary (optimized **CS03:PC₇₁BM:DPP8**) thin films are shown in Figure 5.19.

As can be seen from Figure 5.16, the optical absorption of binary and ternary blend films are the grouping of the absorption profiles of individual components used in the active layers. We observed that the charge transfer absorption band of **DPP8**, in both binary and ternary blends, is blue-shifted due to the suppressed aggregation of **DPP8** in the blended films. Since the number of excitons depends upon the absorption profile of the active layer, the number of excitons generated in the **CS03:DPP8** film is higher than that in the **CS03:PC₇₁BM** film, which results in higher J_{SC} for the OSC based on the **CS03:DPP8** active layer.

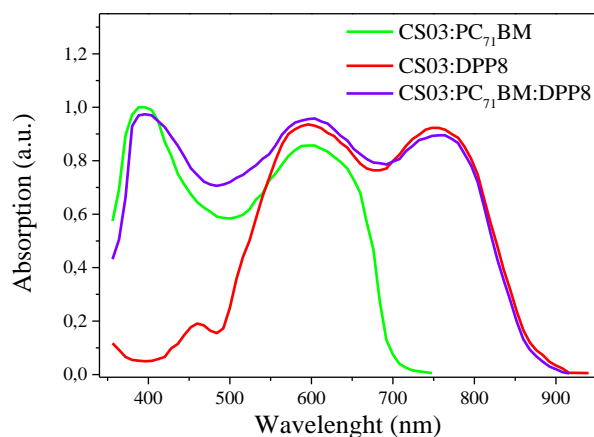


Figure 5.19: Normalized absorption spectra of **CS03:PC₇₁BM** (1:2), **CS03:DPP8** (1:2) and **CS03:PC₇₁BM:DPP8** (1:0.4:1.6) blend thin films.

Chapter 5

The HOMO/LUMO energy levels for **CS03** and **DPP8** are estimated from cyclic voltammetry and are $-5.13/-3.48$ and $-5.34/-3.81$ eV, respectively (Figure 5.20). The LUMO and HOMO energy offset between the **CS03** and **DPP8** suffices to become the driving force, after exciton dissociation at the donor-acceptor interface, for the interfacial electron transfer reaction to take place from **CS03** to **DPP8** and the subsequent hole transfer from **DPP8** to **CS03**.

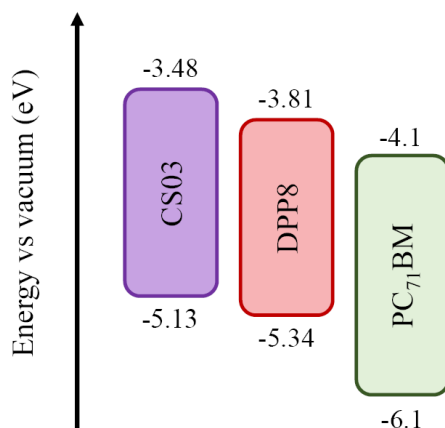


Figure 5.20. Graphical representation of the estimated energy levels for **CS03**, **DPP8** and **PC₇₁BM**.

The interfacial charge transfer efficiency in the photo-active layer was investigated by measuring the steady-state photoluminescence spectra (PL) of the pristine **CS03**, **DPP8** and the **CS03:DPP8** blended films photo-exciting at the wavelength of the corresponding maximum absorption of **CS03** (520 nm) and **DPP8** (750 nm) (as shown in Figure 5.18). Upon excitation at 520 nm, the emission of **CS03** centred at 720 nm was noticeably reduced (88%, against the initial emission yield) when **CS03** was mixed with **DPP8**. Upon excitation at 750 nm, the emission of **DPP8** peaked at 786 nm was also noticeably reduced (82%, against the initial emission yield) in the **CS03:DPP8** blend film. These results indicate that the interfacial charge transfer efficiency, i.e. electrons from

CS03 to **DPP8** and holes from the **DPP8** to **CS03**, is high even the HOMO offset between the **CS03** and **DPP8** is less than threshold value of 0.3 eV.

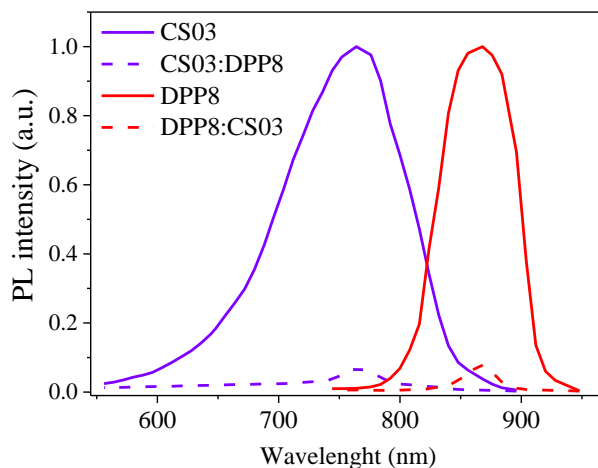


Figure 5.21: The steady-state photoluminescence (PL) spectra of (violet line) **CS03** excited at @520 nm, (violet dash) **CS03:DPP8** excited at @ 520 nm, (red line) **DPP8** excited at @750 nm and (red dash) **CS03:DPP8** excited at @750 nm.

6.4.4.3. Photovoltaic measurements.

We have optimized the photovoltaic results of OSCs based on the binary active layers, i.e. **CS03:PC₇₁BM** and **CS03:DPP8**, via varying the weight ratio between donor and acceptor and found that the optimized as cast **CS03:PC₇₁BM** (1:2) and **CS03:DPP8** (1:2) showed the best photovoltaic performance and showed overall PCE of efficiency of 2.45 % and 3.50 %, respectively. After the optimization of weight ratio of donor (**CS03**) and acceptor (**PC₇₁BM** or **DPP8**) the binary active layer was exposed to the SVA treatment for 40s using THF, to enhance the overall PCE of the OSCs. The current –voltage (*J-V*) characteristics of the OSCs based on optimized active layers, under 1 sun AM1.5 G illumination (100 mW/cm²), are shown in figure 19a and all relevant photovoltaic parameters are listed in Table 5.6.

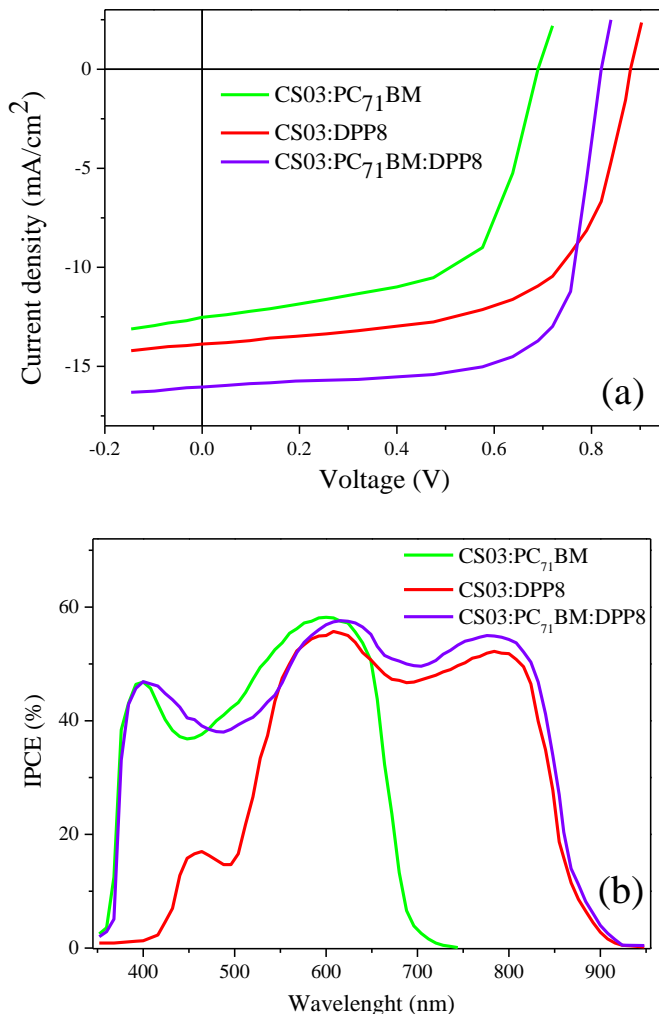


Figure 5.22: (a) The current–voltage characteristics under 1 sun illumination and (b) The IPCE spectra of OSCs based on SVA treated (black) **CS03:PC₇₁BM** (1:2), (red) **CS03:DPP8** (1:2) and (green) **CS03:PC₇₁BM:DPP8** (1:0.4:1.6) active layers.

After the SVA treatment of the active layer, the PCE is improved to 5.07 % and 7.44% for **CS03:PC₇₁BM** (1:2) and **CS03:DPP8** (1:2), respectively. The higher efficiency value for the OSC based on **CS03:DPP8** is attributed to its higher V_{OC} and J_{SC} values, which are originated from the high lying LUMO energy level of **DPP8**, in comparison to **PC₇₁BM**, and broader absorption of **DPP8** in the near IR region, respectively. Moreover, the solar cells photocurrent

is correlated with the film absorbance and, as shown in Figure 5.19b, the **CS03:DPP8** film showed strong absorption from $\lambda = 450$ nm to $\lambda = 900$ nm in which the absorption between 680 - 900 nm is due to the **DPP8**, whereas the **CS03:PC₇₁BM** film showed the absorption only up to 680 nm.

Table 5.6: Photocurrent at short circuit (J_{SC}), photovoltage at open circuit (V_{OC}), fill factor (FF) and overall efficiency (PCE) for the solar cell studied in this work.

Active layer	J_{sc} (mA/cm ²)	V_{oc} (V)	FF	PCE (%)
CS03:DPP8 (1:2) (as cast)	10.13	0.91	0.38	3.50 (3.43) ^a
CS03:DPP8 (1:2) (SVA)	13.86	0.88	0.61	7.44 (7.36) ^a
CS03: PC₇₁BM (1:2) (as cast)	8.61	0.73	0.39	2.45 (2.38) ^a
CS03:PC₇₁BM (1:2) (SVA)	12.46	0.69	0.59	5.07 (4.98) ^a
CS03:PC₇₁BM:DPP8 (1:0.4:1.6) (as cast)	12.52	0.85	0.51	5.43 (5.36) ^a
CS03:PC₇₁BM:DPP8 (SVA)	16.04	0.82	0.68	8.94 (8.87) ^a

^aAverage of 8 devices

The V_{OC} of the OSC for the optimized **CS03:DPP8** is $V_{OC} = 0.88$ V, which is higher than that for **CS03:PC₇₁BM** with $V_{OC} = 0.69$ V. The photon energy loss was calculated using Equation 5.3, as it was described before in this chapter^{42, 77}. The photon energy loss accounts for the loss in V_{OC} taking into account the optical band gap of the material. In our case, we have used the value of E_g for **CS03:PC₇₁BM** and **CS03:DPP8** as 1.65 eV (**CS03**) and 1.43 eV (**DPP8**) and

Chapter 5

the calculated values of E_{loss} are 0.96 eV and 0.55 eV, respectively. The smaller photon energy loss is one of the key reasons for the high V_{OC} for the **CS03:DPP8** OSC in addition to the higher LUMO energy level of **DPP8**.

After investigating in depth the **CS03:DPP8** films and devices, we turned into the improvement of the solar cell efficiency by using the TOHs composed by **CS03** as electron donor and **PC₇₁BM** and **DPP8** as acceptors. All photoactive materials are being low molecular weight organic molecules. We have incorporated **PC₇₁BM** into the **CS03:DPP8** as third component. In the TOHs, the overall weight ratio donor (**CS03**) to acceptor (**PC₇₁BM** and **DPP8**) was kept 1:2, whereas the weight ratio of the two acceptors was changed from 2:0 to 0:2. The optimum as cast active layer (**CS03:PC₇₁BM:DPP8**) consisted of 1:0.4:1.6 showing the best overall PCE of 5.43 %. After the SVA treatment of the active layer, the OSC showed the final PCE of 8.94 %. The photocurrent-voltage characteristics of the OSC based on the optimized active layer, under illumination are shown in Figure 5.22a and photovoltaic parameters are listed in Table 5.6. The photovoltaic parameters with different weight ratios are listed in Table 5.7. As seen in the mentioned table, the value of the V_{OC} decreases as the concentration of **PC₇₁BM** increases and approaches to 0.79 for **CS03:PC₇₁BM:DPP8** active layer with weight ratio of 1:2:0. Since the LUMO energy levels of **PC₇₁BM** and **DPP8** are -4.1 eV and -3.81 eV, the decreased value of V_{OC} may be attributed to the lower LUMO energy level of **PC₇₁BM**. The gradual decrease in the V_{OC} with the increased concentration of **PC₇₁BM**, but the increase of J_{SC} remains, which is consistent with the alloy model^{34, 78-79}. Therefore, both acceptors (**PC₇₁BM** and **DPP8**) in the ternary active layer form close electronic communication that shape material behaviour, forming an acceptor mixture with complementary absorption to improve the light absorption and enhancing the overall PCE. The enhancement in the J_{SC} is attributed the broader absorption profile of the ternary active layer (Figure 5.18). The higher value of FF for the TOH based OSC as compared to

CS03:DPP8 may be related to the fact that **PC₇₁BM** improves the electron transport.

Table 5.7: Photocurrent at short circuit (J_{sc}), photovoltage at open circuit (V_{oc}), fill factor and overall efficiency (PCE) for the solar cell with different concentration of **PC₇₁BM** in as cast ternary **CS03:DPP8:PC₇₁BM** active layer.

Weight ratio in CS03:PC₇₁BM:DPP8	J_{sc} (mA/cm ²)	V_{oc} (V)	FF	PCE (%)
1:0:2	10.13	0.91	0.38	3.50 (3.43) ^a
1:0.2:1.8	10.98	0.88	0.45	4.35 (4.29) ^a
1:0.4:1.6	12.52	0.85	0.51	5.43 (5.36) ^a
1:0.8:1.2	11.63	0.80	0.49	4.56 (4.48) ^a
1:1.2:0.8	9.31	0.76	0.46	3.25 (3.17) ^a
1:2:0	8.61	0.73	0.39	2.45 (2.38) ^a

^aAverage of 8 devices

In order to get information about the feasible interfacial charge transfer processes between **DPP8** and **PC₇₁BM**, we also fabricated the OSCs based on **DPP8:PC₇₁BM** (1:1) active layer and found that the device showed poor PCE of 0.64% ($J_{sc} = 3.28$ mA/cm², $V_{oc} = 0.63$ V and FF = 0.31). Even if the value of the efficiency is poor, this observation also confirmed the charge transfer at **DPP8:PC₇₁BM** blend film is favourable for the improved value of J_{sc} in OSCs based on ternary blend. The incident photons to current conversion efficiency (IPCE) spectra of the OSCs are depicted in Figure 5.22b. In the case of

Chapter 5

CS03:PC₇₁BM, the IPCE spectra of the OSC is limited up to 700 nm, whereas the **CS03:DPP8** based OSC showed an IPCE spectra from 450 to 900 nm and showed poorer values of IPCE in the wavelength region below 450 nm. When introducing **PC₇₁BM** into the ternary active layer, the light harvesting efficiency in the shorter wavelength region from 350-450 nm was improved due to the contribution from **PC₇₁BM**. The IPCE spectra of the optimized TOH based OSC is broader covering from 350 nm to 950 nm. The IPCE values at the near IR indicate improved charge generation and extraction in the **DPP8**, which we assign to the morphology modulation effect, arising from the incorporation of **PC₇₁BM** in the active layer. The J_{SC} values estimated from the integration of the IPCE spectra against the AM1.5 sun simulated spectra are 12.39, 13.74 and 15.89 mA/cm² for the optimized **CS03:PC₇₁BM**, **CS03:DPP8** and **CS03:PC₇₁BM:DPP8** based active layers, respectively, in perfect agreement with the J_{SC} values measured for the solar cells under 1 sun.

In our TOHs solar cells, the photo-generated holes will be transported along the domains made by the **CS03** donor and the photo-generated electrons will be transported along the networks formed by the **DPP8** and **PC₇₁BM**.

In order to get more information about the charge transport within the active layers with different optimized blends (i.e. binary and ternary), we have measured dark J - V characteristics of hole and electron only devices) and fitting these curves with space charge limited model (SCLC)⁸⁰ for the estimation of hole and electron mobility, as it is shown in Figure 5.23. The hole (μ_h)/electron (μ_e) mobilities of the SVA treated **CS03:PC₇₁BM** are estimated to be $9.73 \cdot 10^{-5}/2.45 \cdot 10^{-4}$ cm²/Vs with μ_e/μ_h ratio of 2.52, whereas **CS03:DPP8** active layer (SVA) exhibit hole (μ_h)/electron (μ_e) mobilities of $9.44 \cdot 10^{-5}/2.05 \cdot 10^{-4}$ cm²/Vs with μ_e/μ_h ratio of 2.17. The electron mobility and hole mobility of the as cast TOH was $\mu_{e-} = 2.24 \cdot 10^{-4}$ cm²/Vs and $\mu_{h+} = 1.09 \cdot 10^{-4}$ cm²/Vs, respectively. These values increased to $\mu_{e-} = 2.33 \cdot 10^{-4}$ cm²/Vs and $\mu_{h+} = 1.58 \cdot 10^{-4}$ cm²/Vs,

for optimized SVA TOH. The increase in the electron mobility of TOH as compared to **CS03:DPP8** may be due to the high electron mobility of **PC₇₁BM**. Therefore, the ratio of electron to hole mobility decreased from 2.04 cm²/Vs (as cast) to 1.47 cm²/Vs (SVA treated) indicating that photo-generated electron and hole transport becomes more balanced in the optimized SVA TOH layer which leads to an increase in the FF of the corresponding OSC.

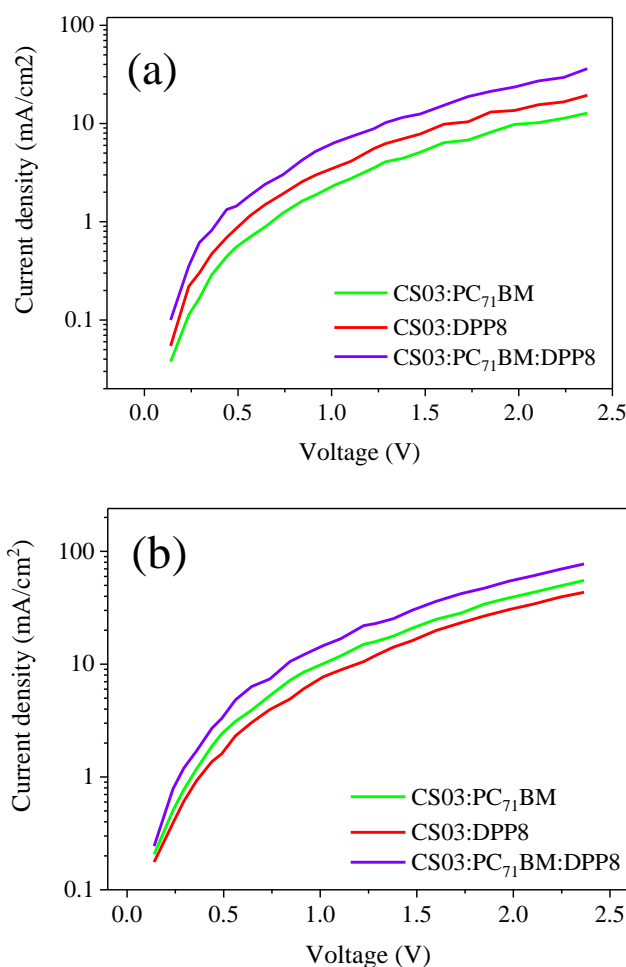
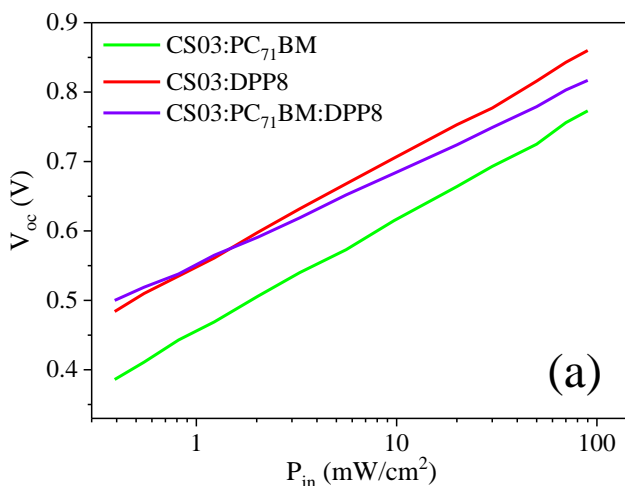


Figure 5.23: Dark J - V characteristics of the (a) hole only devices and (b) electron only devices based on optimized active layers.

We have calculated the values of J_{SC} and V_{OC} from the J - V characteristics of the OSCs under illumination at different intensities. The variation of V_{OC} with

Chapter 5

illumination intensity (P_{in}) is shown in Figure 5.24a and the relationship between V_{OC} and P_{in} for the OSCs is given by the Equation 5.6, which tells us that V_{OC} is proportional to $\ln P_{in}$.⁸¹ The values of ‘n’ estimated from Figure 24a are 1.37, 1.25 and 1.12 for the optimized **CS03:PC₇₁BM**, **CS03:DPP8** and **CS03:PC₇₁BM: DPP8** based OSCs, respectively. The lowest value of ‘n’ for the ternary OSC indicates that the trap assisted recombination can be minimized in this device as compared to the binary counterparts. Moreover, the dependence of J_{SC} on P_{in} was also investigated and can be expressed as $J_{sc} \propto P_{in}^{\gamma}$ and shown in Figure 5.24b. The fitted values of ‘ γ ’ for **CS03:PC₇₁BM**, **CS03:DPP8** and **CS03:PC₇₁BM: DPP8** based OSCs are 0.93, 0.95 and 0.97, respectively. The value of ‘ γ ’ is highest for ternary based OSCs and is very close to one, indicating that non-geminate recombination at short circuit is negligible.



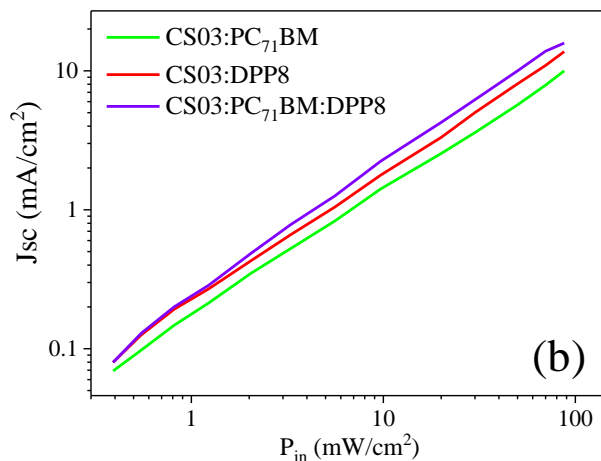


Figure 5.24: Variation of (a) V_{OC} and (b) J_{SC} for the OSCs based on SVA treated (black) **CS03:PC₇₁BM** (1:2), (red) **CS03:DPP8** (1:2) and (blue) **CS03:PC₇₁BM:DPP8** (1:0.4:1.6) active layers.

Furthermore, the exciton dissociation and charge collection efficiency in the OSCs was investigated via the variation of photocurrent density (J_{ph}) with the effective voltage (V_{eff}) (Figure 5.26). As it was mentioned before, J_{ph} is defined as the difference between the generated current at 1 sun and in dark (Equation 5.1), The V_{eff} is expressed as the voltage when $J_{light} = 0$ and the voltage applied (Equation 5.2). As it can be seen from Figure 5.25, J_{ph} shows linear dependence at low values of V_{eff} and reached to saturation value (J_{phsat}) at high voltage in all devices and independently of the applied voltage and only depends upon the number of photons captured by the film. At high V_{eff} , all the photogenerated excitons can be efficiently dissociated into free charge carriers and subsequently collected by the electrodes. The exciton dissociation (P_{diss}) and charge collection efficiency (P_{coll}) will be estimated from J_{SC}/J_{phsat} and J_{max}/J_{phsat} , respectively⁸². The J_{SC} and J_{max} are the photocurrent densities under short circuit and maximum power point conditions, respectively. The values of the P_{diss}/P_{coll} for SVA treated **CS03:PC₇₁BM**, **CS03:DPP8** and **CS03:PC₇₁BM:DPP8** are 0.93/0.78, 0.94/0.80 and 0.96/0.83, respectively. The values of both P_{diss} and P_{coll} are higher for TOHs OSCs as compared to the binary counterparts, indicating that exciton dissociation and charge collection

Chapter 5

efficiencies have been improved for the OSC based on the ternary active layer. The enhanced value of P_{coll} further confirmed the improved value of FF in ternary based OSC.

Since at higher V_{eff} , the J_{ph} is independent of applied voltage, we assume that photogenerated excitons are all dissociated into free charge carriers and the J_{phsat} is only limited to the total amount of photons. We have estimated the maximum exciton generation rate (G_{max}) using the Equation 5.4. The G_{max} values for optimized **CS03:PC₇₁BM**, **CS03:DPP8** and TOH active layer are 0.77×10^{28} , 0.97×10^{28} and $1.07 \times 10^{28} \text{ m}^{-3}\text{s}^{-1}\text{m}$, respectively. The value G_{max} for TOH is significantly higher than those for binary active layers, which is consistent with the IPCE spectra of corresponding OSCs.

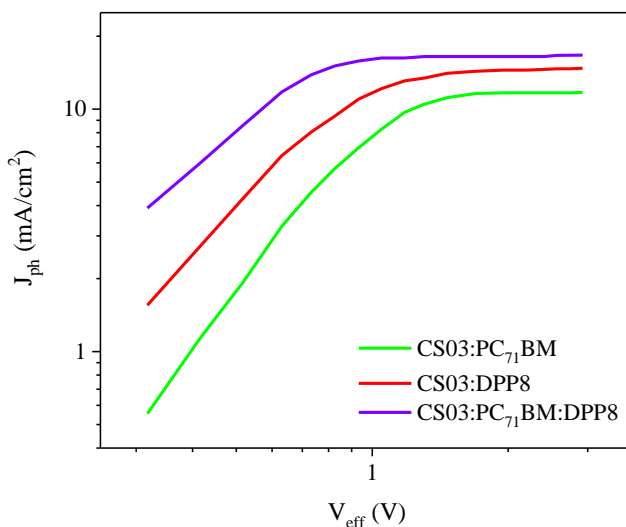


Figure 5.25: Variation of photocurrent (J_{ph}) with effective voltage (V_{eff}) for OSCs based on SVA treated (black) **CS03:PC₇₁BM** (1:2), (red) **CS03:DPP8** (1:2) and (blue) **CS03:PC₇₁BM:DPP8** (1:0.4:1.6) active layers.

6.4.4.4. *Conclusions.*

In summary, we have used a wide-band gap small molecule **CS03** and a narrow band gap, **DPP8** as non-fullerene acceptor, for the fabrication of all small molecule bulk heterojunction organic solar cells. After the optimization of donor to acceptor weight ratio and solvent vapor annealing treatment with THF, the OSCs showed overall PCE of 7.44% (with low energy loss of 0.55 eV), which is higher than that for the **PC₇₁BM** counterpart (5.07 %) with energy loss of 0.96 eV). The enhanced value of PCE of **DPP8** based OSCs is mainly related to the increased values of J_{SC} and V_{OC} , and related to more light harvesting efficiency of the **CS03:DPP8** active layer and up shifting of LUMO level of **DPP8** as compared to **PC₇₁BM**. Finally OSC based on the TOH **CS03:PC₇₁BM:DPP8** (1:0.4:1.6) cast from chloroform solvent showed an overall PCE of 5.43% which was further improved to 8.94 % when the ternary active layer was subjected to solvent vapor annealing in THF for 40 s. The improvement in the overall efficiency has been demonstrated to be related not only to the enhanced light harvesting efficiency, but also to the increased V_{OC} and to a better balanced charge transport to the selective contacts.

6.5. Conclusions.

In summary, we have synthesized a benzothiadiazole-based wide-band gap small molecule as donors (**CS01**, **CS03**, **EP02** and **LCS01**) for the fabrication of bulk heterojunction organic solar cells with **PC₇₁BM** as an electron acceptor. In order to increase the PCE, two non-fullerene acceptors, **MPU3** and **DPP8**, were used also in BHJ OSCs, achieving higher efficiencies than the **PC₇₁BM**-based OSCs, using identical conditions. We attributed this enhancement to the lower band gap and the absorption profile of both, that extends up to around 900 nm. Finally, we fabricated TOHs including a second electron acceptor to the active layer, **PC₇₁BM**, improving the overall efficiency due to the increase in the light harvesting and the V_{OC} , because of the absorption profile of the

Chapter 5

fullerene and the lower values of the LUMO energy level compared with the non-fullerene acceptors.

6.6. References.

1. Gasparini, N.; Wadsworth, A.; Moser, M.; Baran, D.; McCulloch, I.; Brabec, C. J., The Physics of Small Molecule Acceptors for Efficient and Stable Bulk Heterojunction Solar Cells. *Advanced Energy Materials* **2018**, *8* (12), 1703298.
2. Lu, L.; Zheng, T.; Wu, Q.; Schneider, A. M.; Zhao, D.; Yu, L., Recent Advances in Bulk Heterojunction Polymer Solar Cells. *Chemical Reviews* **2015**, *115* (23), 12666-12731.
3. Rafique, S.; Abdullah, S. M.; Sulaiman, K.; Iwamoto, M., Fundamentals of bulk heterojunction organic solar cells: An overview of stability/degradation issues and strategies for improvement. *Renewable and Sustainable Energy Reviews* **2018**, *84*, 43-53.
4. Huang, H.; Yang, L.; Sharma, B., Recent advances in organic ternary solar cells. *Journal of Materials Chemistry A* **2017**, *5* (23), 11501-11517.
5. Collins, S. D.; Ran, N. A.; Heiber, M. C.; Nguyen, T.-Q., Small is Powerful: Recent Progress in Solution-Processed Small Molecule Solar Cells. *Advanced Energy Materials* **2017**, *7* (10), 1602242-n/a.
6. Lin, Y.; Li, Y.; Zhan, X., Small molecule semiconductors for high-efficiency organic photovoltaics. *Chemical Society Reviews* **2012**, *41* (11), 4245-4272.
7. Fan, H.; Shang, H.; Li, Y.; Zhan, X., Efficiency enhancement in small molecule bulk heterojunction organic solar cells via additive. *Applied Physics Letters* **2010**, *97* (13), 133302.
8. Li, W.; Du, C.; Li, F.; Zhou, Y.; Fahlman, M.; Bo, Z.; Zhang, F., Benzothiadiazole-Based Linear and Star Molecules: Design, Synthesis, and Their Application in Bulk Heterojunction Organic Solar Cells. *Chemistry of Materials* **2009**, *21* (21), 5327-5334.
9. He, C.; He, Q.; He, Y.; Li, Y.; Bai, F.; Yang, C.; Ding, Y.; Wang, L.; Ye, J., Organic solar cells based on the spin-coated blend films of TPA-th-TPA and PCBM. *Solar Energy Materials and Solar Cells* **2006**, *90* (12), 1815-1827.

Chapter 5

10. Shang, H.; Fan, H.; Liu, Y.; Hu, W.; Li, Y.; Zhan, X., A Solution-Processable Star-Shaped Molecule for High-Performance Organic Solar Cells. *Advanced Materials* **2011**, *23* (13), 1554-1557.
11. Shang, H.; Fan, H.; Shi, Q.; Li, S.; Li, Y.; Zhan, X., Solution processable D-A-D molecules based on triphenylamine for efficient organic solar cells. *Solar Energy Materials and Solar Cells* **2010**, *94* (3), 457-464.
12. Yang, Y.; Zhang, Z.-G.; Bin, H.; Chen, S.; Gao, L.; Xue, L.; Yang, C.; Li, Y., Side-Chain Isomerization on an n-type Organic Semiconductor ITIC Acceptor Makes 11.77% High Efficiency Polymer Solar Cells. *Journal of the American Chemical Society* **2016**, *138* (45), 15011-15018.
13. Zhao, W.; Qian, D.; Zhang, S.; Li, S.; Inganäs, O.; Gao, F.; Hou, J., Fullerene-Free Polymer Solar Cells with over 11% Efficiency and Excellent Thermal Stability. *Advanced Materials* **2016**, *28* (23), 4734-4739.
14. Zhao, W.; Li, S.; Yao, H.; Zhang, S.; Zhang, Y.; Yang, B.; Hou, J., Molecular Optimization Enables over 13% Efficiency in Organic Solar Cells. *Journal of the American Chemical Society* **2017**, *139* (21), 7148-7151.
15. Cui, Y.; Yao, H.; Gao, B.; Qin, Y.; Zhang, S.; Yang, B.; He, C.; Xu, B.; Hou, J., Fine-Tuned Photoactive and Interconnection Layers for Achieving over 13% Efficiency in a Fullerene-Free Tandem Organic Solar Cell. *Journal of the American Chemical Society* **2017**, *139* (21), 7302-7309.
16. Zhang, S.; Qin, Y.; Zhu, J.; Hou, J., Over 14% Efficiency in Polymer Solar Cells Enabled by a Chlorinated Polymer Donor. *Advanced Materials* **2018**, *30* (20), 1800868.
17. Sun, J.; Ma, X.; Zhang, Z.; Yu, J.; Zhou, J.; Yin, X.; Yang, L.; Geng, R.; Zhu, R.; Zhang, F.; Tang, W., Dithieno[3,2-b:2',3'-d]pyrrol Fused Nonfullerene Acceptors Enabling Over 13% Efficiency for Organic Solar Cells. *Advanced Materials* **2018**, *30* (16), 1707150.
18. Badgular, S.; Lee, G.-Y.; Park, T.; Song, C. E.; Park, S.; Oh, S.; Shin, W. S.; Moon, S.-J.; Lee, J.-C.; Lee, S. K., Organic Solar Cells: High-Performance Small Molecule via Tailoring Intermolecular Interactions and its

Application in Large-Area Organic Photovoltaic Modules (Adv. Energy Mater. 12/2016). *Advanced Energy Materials* **2016**, *6* (12), n/a-n/a.

19. Würthner, F.; Kaiser, T. E.; Saha-Möller, C. R., J-Aggregates: From Serendipitous Discovery to Supramolecular Engineering of Functional Dye Materials. *Angewandte Chemie International Edition* **2011**, *50* (15), 3376-3410.

20. Wu, M.; Zhou, J.; Luo, Y.; Zheng, N.; Wang, C.; Liu, L.; Xie, Z.; Ma, Y., Construction of J-type aggregates as multi-functional interlayers for nonfullerene polymer solar cells. *Organic Chemistry Frontiers* **2018**, *5* (22), 3324-3330.

21. Xu, Z.; Du, H.; Yin, M.; Wang, B.; Zhao, J.; Xie, Y., Benzothiadiazole, hexylthiophen and alkoxy benzene based solution processable copolymer: Effect of the electron withdrawing substituents (fluorine atoms) on electrochemical, optical and electrochromic properties. *Organic Electronics* **2018**, *61*, 1-9.

22. Scharber, M. C.; Mühlbacher, D.; Koppe, M.; Denk, P.; Waldauf, C.; Heeger, A. J.; Brabec, C. J., Design Rules for Donors in Bulk-Heterojunction Solar Cells—Towards 10 % Energy-Conversion Efficiency. *Advanced Materials* **2006**, *18* (6), 789-794.

23. Wang, J.-L.; Wu, Z.; Miao, J.-S.; Liu, K.-K.; Chang, Z.-F.; Zhang, R.-B.; Wu, H.-B.; Cao, Y., Solution-Processed Diketopyrrolopyrrole-Containing Small-Molecule Organic Solar Cells with 7.0% Efficiency: In-Depth Investigation on the Effects of Structure Modification and Solvent Vapor Annealing. *Chemistry of Materials* **2015**, *27* (12), 4338-4348.

24. Kumar, C. V.; Cabau, L.; Viterisi, A.; Biswas, S.; Sharma, G. D.; Palomares, E., Solvent Annealing Control of Bulk Heterojunction Organic Solar Cells with 6.6% Efficiency Based on a Benzodithiophene Donor Core and Dicyano Acceptor Units. *The Journal of Physical Chemistry C* **2015**, *119* (36), 20871-20879.

25. Más-Montoya, M.; Janssen, R. A. J., The Effect of H- and J-Aggregation on the Photophysical and Photovoltaic Properties of Small

Chapter 5

Thiophene–Pyridine–DPP Molecules for Bulk-Heterojunction Solar Cells. *Advanced Functional Materials* **2017**, *27* (16), 1605779-n/a.

26. Fernandez, D.; Viterisi, A.; Challuri, V.; Ryan, J. W.; Martinez-Ferrero, E.; Gispert-Guirado, F.; Martinez, M.; Escudero, E.; Stenta, C.; Marsal, L. F.; Palomares, E., Understanding the Limiting Factors of Solvent-Annealed Small-Molecule Bulk-Heterojunction Organic Solar Cells from a Chemical Perspective. *ChemSusChem* **2017**, *10* (15), 3118-3134.

27. Amassian, A.; Pozdin, V. A.; Li, R.; Smilgies, D.-M.; Malliaras, G. G., Solvent vapor annealing of an insoluble molecular semiconductor. *Journal of Materials Chemistry* **2010**, *20* (13), 2623-2629.

28. Li, Y.; Lee, D. H.; Lee, J.; Nguyen, T. L.; Hwang, S.; Park, M. J.; Choi, D. H.; Woo, H. Y., Two Regioisomeric π -Conjugated Small Molecules: Synthesis, Photophysical, Packing, and Optoelectronic Properties. *Advanced Functional Materials* **2017**, *27* (33), 1701942-n/a.

29. Wang, J.-L.; Liu, K.-K.; Liu, S.; Xiao, F.; Liu, F.; Wu, H.-B.; Cao, Y., Developing High-Performance Electron-Rich Unit End-Capped Wide Bandgap Oligomeric Donor by Weak Electron-Deficient Central Core Strategy. *Solar RRL* **2018**, *2* (2), 1700212.

30. Xie, Y.; Zhou, W.; Yin, J.; Hu, X.; Zhang, L.; Meng, X.; Ai, Q.; Chen, Y., Post-annealing to recover the reduced open-circuit voltage caused by solvent annealing in organic solar cells. *Journal of Materials Chemistry A* **2016**, *4* (16), 6158-6166.

31. Li, G.; Yao, Y.; Yang, H.; Shrotriya, V.; Yang, G.; Yang, Y., “Solvent Annealing” Effect in Polymer Solar Cells Based on Poly(3-hexylthiophene) and Methanofullerenes. *Advanced Functional Materials* **2007**, *17* (10), 1636-1644.

32. Zhao, F.; Wang, C.; Zhan, X., Morphology Control in Organic Solar Cells. *Advanced Energy Materials* **2018**, *8* (28), 1703147.

33. Nelson, J., Polymer:fullerene bulk heterojunction solar cells. *Materials Today* **2011**, *14* (10), 462-470.

34. Khlyabich, P. P.; Rudenko, A. E.; Street, R. A.; Thompson, B. C., Influence of Polymer Compatibility on the Open-Circuit Voltage in Ternary Blend Bulk Heterojunction Solar Cells. *ACS Applied Materials & Interfaces* **2014**, *6* (13), 9913-9919.
35. Yu, J.; Yin, X.; Xu, Z.; Deng, P.; Han, Y.; Zhou, B.; Tang, W., Bisalkylthio side chain manipulation on two-dimensional benzo[1,2-b:4,5-b']dithiophene copolymers with deep HOMO levels for efficient organic photovoltaics. *Dyes and Pigments* **2017**, *136*, 312-320.
36. Mihailetchi, V. D.; Koster, L. J. A.; Hummelen, J. C.; Blom, P. W. M., Photocurrent Generation in Polymer-Fullerene Bulk Heterojunctions. *Physical Review Letters* **2004**, *93* (21), 216601.
37. Mihailetchi, V. D.; Wildeman, J.; Blom, P. W. M., Space-Charge Limited Photocurrent. *Physical Review Letters* **2005**, *94* (12), 126602.
38. Li, Y.; Ko, S.-J.; Park, S. Y.; Choi, H.; Nguyen, T. L.; Uddin, M. A.; Kim, T.; Hwang, S.; Kim, J. Y.; Woo, H. Y., Quinoxaline–thiophene based thick photovoltaic devices with an efficiency of ~8%. *Journal of Materials Chemistry A* **2016**, *4* (25), 9967-9976.
39. Varotto, A.; Nam, C.-Y.; Radivojevic, I.; P. C. Tomé, J.; Cavaleiro, J. A. S.; Black, C. T.; Drain, C. M., Phthalocyanine Blends Improve Bulk Heterojunction Solar Cells. *Journal of the American Chemical Society* **2010**, *132* (8), 2552-2554.
40. Chen, W.; Xu, T.; He, F.; Wang, W.; Wang, C.; Strzalka, J.; Liu, Y.; Wen, J.; Miller, D. J.; Chen, J.; Hong, K.; Yu, L.; Darling, S. B., Hierarchical Nanomorphologies Promote Exciton Dissociation in Polymer/Fullerene Bulk Heterojunction Solar Cells. *Nano Letters* **2011**, *11* (9), 3707-3713.
41. Di Nuzzo, D.; Wetzelaer, G.-J. A. H.; Bouwer, R. K. M.; Gevaerts, V. S.; Meskers, S. C. J.; Hummelen, J. C.; Blom, P. W. M.; Janssen, R. A. J., Simultaneous Open-Circuit Voltage Enhancement and Short-Circuit Current Loss in Polymer: Fullerene Solar Cells Correlated by Reduced Quantum Efficiency for Photoinduced Electron Transfer. *Advanced Energy Materials* **2013**, *3* (1), 85-94.
-

Chapter 5

42. Veldman, D.; Meskers, S. C. J.; Janssen, R. A. J., The Energy of Charge-Transfer States in Electron Donor-Acceptor Blend: Insight into the Energy Losses in Organic Solar Cells. *Adv. Funct. Mater.* **2010**, *19*, 1939-1948.
43. Chen, Y.-C.; Hsu, C.-Y.; Lin, R. Y.-Y.; Ho, K.-C.; Lin, J. T., Materials for the Active Layer of Organic Photovoltaics: Ternary Solar Cell Approach. *ChemSusChem* **2013**, *6* (1), 20-35.
44. Lu, L.; Kelly, M. A.; You, W.; Yu, L., Status and prospects for ternary organic photovoltaics. *Nature Photonics* **2015**, *9*, 491.
45. Naveed, H. B.; Ma, W., Miscibility-Driven Optimization of Nanostructures in Ternary Organic Solar Cells Using Non-fullerene Acceptors. *Joule* **2018**, *2* (4), 621-641.
46. Xu, X.; Bi, Z.; Ma, W.; Wang, Z.; Choy, W. C. H.; Wu, W.; Zhang, G.; Li, Y.; Peng, Q., Highly Efficient Ternary-Blend Polymer Solar Cells Enabled by a Nonfullerene Acceptor and Two Polymer Donors with a Broad Composition Tolerance. *Advanced Materials* **2017**, *29* (46), 1704271.
47. Dai, S.; Li, T.; Wang, W.; Xiao, Y.; Lau, T.-K.; Li, Z.; Liu, K.; Lu, X.; Zhan, X., Enhancing the Performance of Polymer Solar Cells via Core Engineering of NIR-Absorbing Electron Acceptors. *Advanced Materials* **2018**, *30* (15), 1706571.
48. Lu, H.; Xu, X.; Bo, Z., Perspective of a new trend in organic photovoltaic: ternary blend polymer solar cells. *Science China Materials* **2016**, *59* (6), 444-458.
49. Kan, B.; Li, M.; Zhang, Q.; Liu, F.; Wan, X.; Wang, Y.; Ni, W.; Long, G.; Yang, X.; Feng, H.; Zuo, Y.; Zhang, M.; Huang, F.; Cao, Y.; Russell, T. P.; Chen, Y., A Series of Simple Oligomer-like Small Molecules Based on Oligothiophenes for Solution-Processed Solar Cells with High Efficiency. *Journal of the American Chemical Society* **2015**, *137* (11), 3886-3893.
50. Lin, Y.; Zhan, X., Oligomer Molecules for Efficient Organic Photovoltaics. *Accounts of Chemical Research* **2016**, *49* (2), 175-183.
51. Yang, L.; Zhang, S.; He, C.; Zhang, J.; Yao, H.; Yang, Y.; Zhang, Y.; Zhao, W.; Hou, J., New Wide Band Gap Donor for Efficient Fullerene-Free

All-Small-Molecule Organic Solar Cells. *Journal of the American Chemical Society* **2017**, *139* (5), 1958-1966.

52. Zhou, J.; Zuo, Y.; Wan, X.; Long, G.; Zhang, Q.; Ni, W.; Liu, Y.; Li, Z.; He, G.; Li, C.; Kan, B.; Li, M.; Chen, Y., Solution-Processed and High-Performance Organic Solar Cells Using Small Molecules with a Benzodithiophene Unit. *Journal of the American Chemical Society* **2013**, *135* (23), 8484-8487.

53. Rodríguez-Seco, C.; Biswas, S.; Sharma, G. D.; Vidal-Ferran, A.; Palomares, E., Benzothiadiazole Substituted Semiconductor Molecules for Organic Solar Cells: The Effect of the Solvent Annealing Over the Thin Film Hole Mobility Values. *The Journal of Physical Chemistry C* **2018**.

54. Privado, M.; de la Cruz, P.; Biswas, S.; Singhal, R.; Sharma, G. D.; Langa, F., A non-fullerene all small molecule solar cell constructed with a diketopyrrolopyrrole-based acceptor having a power conversion efficiency higher than 9% and an energy loss of 0.54 eV. *Journal of Materials Chemistry A* **2018**, *6* (25), 11714-11724.

55. Janssen, R. A. J.; Nelson, J., Factors Limiting Device Efficiency in Organic Photovoltaics. *Advanced Materials* **2013**, *25* (13), 1847-1858.

56. Fan, Q.; Su, W.; Guo, X.; Guo, B.; Li, W.; Zhang, Y.; Wang, K.; Zhang, M.; Li, Y., A New Polythiophene Derivative for High Efficiency Polymer Solar Cells with PCE over 9%. *Advanced Energy Materials* **2016**, *6* (14), 1600430.

57. Bin, H.; Gao, L.; Zhang, Z.-G.; Yang, Y.; Zhang, Y.; Zhang, C.; Chen, S.; Xue, L.; Yang, C.; Xiao, M.; Li, Y., 11.4% Efficiency non-fullerene polymer solar cells with trialkylsilyl substituted 2D-conjugated polymer as donor. *Nature Communications* **2016**, *7*, 13651.

58. Gao, L.; Zhang, Z.-G.; Bin, H.; Xue, L.; Yang, Y.; Wang, C.; Liu, F.; Russell, T. P.; Li, Y., High-Efficiency Nonfullerene Polymer Solar Cells with Medium Bandgap Polymer Donor and Narrow Bandgap Organic Semiconductor Acceptor. *Advanced Materials* **2016**, *28* (37), 8288-8295.

59. Bin, H.; Zhang, Z.-G.; Gao, L.; Chen, S.; Zhong, L.; Xue, L.; Yang, C.; Li, Y., Non-Fullerene Polymer Solar Cells Based on Alkylthio and Fluorine

Chapter 5

Substituted 2D-Conjugated Polymers Reach 9.5% Efficiency. *Journal of the American Chemical Society* **2016**, *138* (13), 4657-4664.

60. Ran, N. A.; Love, J. A.; Takacs, C. J.; Sadhanala, A.; Beavers, J. K.; Collins, S. D.; Huang, Y.; Wang, M.; Friend, R. H.; Bazan, G. C.; Nguyen, T.-Q., Harvesting the Full Potential of Photons with Organic Solar Cells. *Advanced Materials* **2016**, *28* (7), 1482-1488.

61. Scharber, M. C., On the Efficiency Limit of Conjugated Polymer:Fullerene-Based Bulk Heterojunction Solar Cells. *Advanced Materials* **2016**, *28* (10), 1994-2001.

62. Liu, J.; Chen, S.; Qian, D.; Gautam, B.; Yang, G.; Zhao, J.; Bergqvist, J.; Zhang, F.; Ma, W.; Ade, H.; Inganäs, O.; Gundogdu, K.; Gao, F.; Yan, H., Fast charge separation in a non-fullerene organic solar cell with a small driving force. *Nature Energy* **2016**, *1*, 16089.

63. Li, W.; Hendriks, K. H.; Furlan, A.; Wienk, M. M.; Janssen, R. A. J., High Quantum Efficiencies in Polymer Solar Cells at Energy Losses below 0.6 eV. *Journal of the American Chemical Society* **2015**, *137* (6), 2231-2234.

64. Liu, T.; Guo, Y.; Yi, Y.; Huo, L.; Xue, X.; Sun, X.; Fu, H.; Xiong, W.; Meng, D.; Wang, Z.; Liu, F.; Russell, T. P.; Sun, Y., Ternary Organic Solar Cells Based on Two Compatible Nonfullerene Acceptors with Power Conversion Efficiency >10%. *Advanced Materials* **2016**, *28* (45), 10008-10015.

65. Cheng, P.; Zhang, M.; Lau, T.-K.; Wu, Y.; Jia, B.; Wang, J.; Yan, C.; Qin, M.; Lu, X.; Zhan, X., Realizing Small Energy Loss of 0.55 eV, High Open-Circuit Voltage >1 V and High Efficiency >10% in Fullerene-Free Polymer Solar Cells via Energy Driver. *Advanced Materials* **2017**, *29* (11), 1605216.

66. Blom, P. W. M.; Mihailetschi, V. D.; Koster, L. J. A.; Markov, D. E., Device Physics of Polymer:Fullerene Bulk Heterojunction Solar Cells. *Advanced Materials* **2007**, *19* (12), 1551-1566.

67. Strobel, T.; Deibel, C.; Dyakonov, V., Role of Polaron Pair Diffusion and Surface Losses in Organic Semiconductor Devices. *Physical Review Letters* **2010**, *105* (26), 266602.

68. Cowan, S. R.; Roy, A.; Heeger, A. J., Recombination in polymer-fullerene bulk heterojunction solar cells. *Physical Review B* **2010**, *82* (24), 245207.
69. Kyaw, A. K. K.; Wang, D. H.; Luo, C.; Cao, Y.; Nguyen, T.-Q.; Bazan, G. C.; Heeger, A. J., Effects of Solvent Additives on Morphology, Charge Generation, Transport, and Recombination in Solution-Processed Small-Molecule Solar Cells. *Advanced Energy Materials* **2014**, *4* (7), 1301469.
70. Kyaw, A. K. K.; Wang, D. H.; Gupta, V.; Leong, W. L.; Ke, L.; Bazan, G. C.; Heeger, A. J., Intensity Dependence of Current–Voltage Characteristics and Recombination in High-Efficiency Solution-Processed Small-Molecule Solar Cells. *ACS Nano* **2013**, *7* (5), 4569-4577.
71. Liu, X.; Wang, H.-Q.; Li, Y.; Gui, Z.; Ming, S.; Usman, K.; Zhang, W.; Fang, J., Regular Organic Solar Cells with Efficiency over 10% and Promoted Stability by Ligand- and Thermal Annealing-Free Al-Doped ZnO Cathode Interlayer. *Advanced Science* **2017**, *4* (8), 1700053.
72. Kyaw, A. K. K.; Wang, D. H.; Wynands, D.; Zhang, J.; Nguyen, T.-Q.; Bazan, G. C.; Heeger, A. J., Improved Light Harvesting and Improved Efficiency by Insertion of an Optical Spacer (ZnO) in Solution-Processed Small-Molecule Solar Cells. *Nano Letters* **2013**, *13* (8), 3796-3801.
73. Hu, L.; Wu, F.; Li, C.; Hu, A.; Hu, X.; Zhang, Y.; Chen, L.; Chen, Y., Alcohol-Soluble n-Type Conjugated Polyelectrolyte as Electron Transport Layer for Polymer Solar Cells. *Macromolecules* **2015**, *48* (16), 5578-5586.
74. Zhang, K.; Hu, Z.; Xu, R.; Jiang, X.-F.; Yip, H.-L.; Huang, F.; Cao, Y., High-Performance Polymer Solar Cells with Electrostatic Layer-by-Layer Self-Assembled Conjugated Polyelectrolytes as the Cathode Interlayer. *Advanced Materials* **2015**, *27* (24), 3607-3613.
75. Patil, Y.; Jadhav, T.; Dhokale, B.; Misra, R., Design and Synthesis of Low HOMO–LUMO Gap N-Phenylcarbazole-Substituted Diketopyrrolopyrroles. *Asian Journal of Organic Chemistry* **2016**, *5* (8), 1008-1014.

Chapter 5

76. Patil, Y.; Misra, R.; Keshtov, M. L.; Sharma, G. D., Small molecule carbazole-based diketopyrrolopyrroles with tetracyanobutadiene acceptor unit as a non-fullerene acceptor for bulk heterojunction organic solar cells. *Journal of Materials Chemistry A* **2017**, *5* (7), 3311-3319.
77. Ran, N. A.; Love, J. A.; Takacs, C. J.; Sadhanala, A.; Beavers, J. K.; Collins, S. D.; Huang, Y.; Wang, M.; Frined, R. H.; Bazan, G. C., Harvesting the Full Potential of Photons with Organic Solar Cells. *Adv. Mater.* **2016**, *28*, 1482-1488.
78. Street, R. A.; Davies, D.; Khlyabich, P. P.; Burkhart, B.; Thompson, B. C., Origin of the Tunable Open-Circuit Voltage in Ternary Blend Bulk Heterojunction Organic Solar Cells. *Journal of the American Chemical Society* **2013**, *135* (3), 986-989.
79. An, Q.; Zhang, F.; Yin, X.; Sun, Q.; Zhang, M.; Zhang, J.; Tang, W.; Deng, Z., High-performance alloy model-based ternary small molecule solar cells. *Nano Energy* **2016**, *30*, 276-282.
80. Koppe, M.; Egelhaaf, H. J.; Dennler, G.; Scharber, M. C.; Brabec, C. J.; Schilinsky, P.; Hoth, C. N., Influence of Polymer Compatibility of the Open-Circuit Voltage in Ternary Blend Bulk Heterojunction Solar Cells. *ACS Appl. Mater. Interfaces* **2014**, *6*, 9913-9919.
81. Wan, J.; Xu, X.; Zhang, G.; Li, Y.; Feng, K.; Peng, Q., Highly efficient halogen-free solvent processed small-molecule organic solar cells enabled by material design and device engineering. *Energy & Environmental Science* **2017**, *10* (8), 1739-1745.
82. Ma, X.; Zhang, F.; An, Q.; Sun, Q.; Zhang, M.; Miao, J.; Hu, Z.; Zhang, J., A liquid crystal material as the third component for ternary polymer solar cells with an efficiency of 10.83% and enhanced stability. *Journal of Materials Chemistry A* **2017**, *5* (25), 13145-13153.



6. PEROVSKITE SOLAR CELLS

Chapter 6

Table of contents

6.1. Introduction.....	247
6.2. Device fabrication.....	250
6.2.1. CsMAFAPbIBr perovskite solar cells.....	250
6.2.2. Perovskite solar cells using MAPbBr ₃ perovskite.....	251
6.3. Benzothiadiazole-based small molecules as hole transporting materials in perovskite solar cells.....	252
6.3.1. Optimization of the hole transporting layer.....	257
6.3.2. Device characterization.....	260
6.3.3. Conclusions.....	265
6.4. Triphenylamine and carbazole-based small molecules as hole transporting materials in Perovskite Solar Cells.....	266
6.4.1. Optimization of the hole transporting layer.....	270
6.4.2. Device characterization.....	272
6.4.3. CS06 as HTM using MAPBr ₃ perovskite solar cells.....	277
6.4.3. Conclusions.....	281
6.5. General conclusions.....	282
6.6. Annex.....	283
6.6.1. J-V parameters for devices using the novel HTMs comparing their performance with and in absence of additives.....	283
6.6.2. J-V curves and PV parameters of the optimization of the HTM layers for PSCs.....	285
6.7.3. Statistic values of PV parameters when using the new HTMs in PSCs.....	292
6.7.4. J-V curves in forward and reverse for the HTMs using in this work.....	293
6.7. References.....	295

Chapter 6

6.1. Introduction.

Perovskite solar cells (PSC) have emerged just few years ago competing with all third generation solar devices, Dye-Sensitized Solar Cells (DSSCs) and Organic Photovoltaics (OPVs), obtaining record efficiencies of 24.2 %¹ until now. The use this new material, called perovskite, and all the posterior optimization studies allow one of the fastest improvements, in terms of efficiency, from the early 3.8 %² in 2009 to efficiencies up to the one mentioned above in 2019.

Organic-inorganic hybrid halide perovskites is a group of materials represented by the general formula ABX_3 , where A is a small of organic methylammonium (MA) and/or formamidinium (FA) cation, B is a divalent cation (Pb^{+2} was used in this work) and X stands for halide anion (I^- , Br^- or Cl^-)³⁻⁴. The ideal structure has cubic-symmetry, where the A cation is 12-fold coordinated by the X anion in a cuboctahedral arrangement and the B cation is 6-fold coordinated by X in an octahedral configuration (Figure 6.1). Perovskites in the form of methylammonium lead triiodide ($MAPbI_3$) and methylammonium lead tribromide ($MAPbBr_3$) were used for the first time in 2009 as sensitizers in Dye-Sensitized Solar Cells (DSSCs⁵) replacing the organic dyes². This material was selected as an intrinsic semiconductor with outstanding light absorption capability and ambivalence electron and hole properties⁶. With the further development of the PSCs, more complex multi-cation composition and halides ration of perovskite have been used to improve some of their “original” properties. For example, some of these modifications were done to improve the light harvesting properties and get closer to the optimal band gap by the incorporation of the formamidinium cation (FA^+), obtaining $FA_{1-x}MA_xPbI_3$. Meanwhile, with Br^-/I^- anion mixture, the crystal quality was improved by reducing I^- concentration, that is considered the main responsible of the characteristic hysteretic behaviour of these kind of devices, limiting the famous “ion migration” process. Besides, it enhance the crystallinity and the diffusion

Chapter 6

length due to a decrease on the crystal defects⁷⁻⁸. Later on, other modifications in composition were made in order to increase the stability over time (regarding to temperature, solvent vapours or heating protocols), the quality of the films and reproducibility of the perovskite solar cells, by incorporating the cesium cation (Cs^+). The $\text{Cs}_{0.1}(\text{MA}_{0.15}\text{FA}_{0.85})_{0.9}\text{Pb}(\text{I}_{0.85}\text{Br}_{0.15})_3$ composition became standard for the further development of the perovskite solar cells⁹.

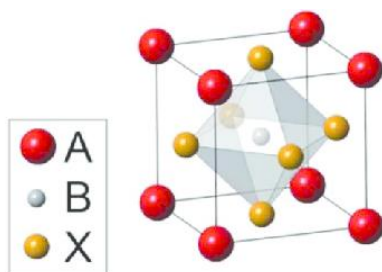


Figure 6.1: Perovskite general structure.

Regarding the aforementioned ambipolar behaviour of perovskites, it has made possible other device optimization strategies based on different architectures such as the mesoscopic or “regular”, planar or inverted structures¹⁰.

In this work, regular n-i-p structure has been utilized as it has been extensively studied and corresponds with the highest PCE reaching 24.2 %. This configuration consists in a transparent conductive oxide substrate, such as fluorine-doped tin oxide (FTO) on a glass – compact TiO_2 (c- TiO_2) blocking layer as electron-selective contact (n) – perovskite (i) (on mesoporous TiO_2 scaffold (m- TiO_2) in the case of the regular mesoporous cells) – positive-selective contact (p) (the HTM) and, finally, a metal electrode is evaporated, usually made of a high work function metal, such as Au or Ag. Regardless of device architecture, device performance strongly depends on the high quality of the perovskite film morphology. There are many factors that directly influence the final film morphology, such as the deposition method, material composition, the use of additives and film treatment among others. The

optimization of all these steps aim to promote a uniform growth of the perovskite crystals.

Moreover, studies based on the synthesis of new hole transporting materials (HTMs) become also an important area to explore in order to replace the most widely used HTM: Spiro-OMeTAD. This molecule plays an important role in the transportation of the holes to the counter-electrode in PSCs and it was used for the first time in solid state dye-sensitized solar cells (ss-DSSCs), where it was used as a solid electrolyte to regenerate the holes of the dye or photoactive material¹¹⁻¹². Spiro-OMeTAD has been the HTM's benchmark against other materials. Although its production cost is extremely high¹³ and it does not present outstanding properties (compared to other molecules), it is still the most currently used to make the best performance devices.

Moreover, the hole transporting layer (HTL), especially spiro-OMeTAD due to its low hole mobility, has to be heavily doped, traditionally with the bis(trifluoromethane)sulfonimide lithium salt (LiTFSI), 4-tert-butylpyridine (*t*BP), and tris(2-(1H-pyrazol-1-yl)-4-tert-butylpyridine)cobalt(III) tri[hexafluorophosphate] (FK209). *t*BP is commonly used as the HTL morphology controller, decreasing the aggregation, while LiTFSI and FK209 provide the necessary electrical conductivity¹⁴⁻¹⁵. However, the use of additives is not desirable, since the hygroscopic nature of the lithium salt makes the HTL highly hydrophobic and the Co(III) dopant tends to degrade chemically, influencing negatively the stability of the entire device¹⁶⁻¹⁷. Some examples of pristine HTL based devices have been published reaching 10 % with only very few examples over 15 %¹⁸⁻²⁰. For these reasons, it is of necessity to seek new materials that can compete with spiro-OMeTAD by reducing the overall price of the solar cell and enhance the stability.

In this work, the novel HTMs (described in Chapter 4) were tested for the first time in PSCs without using any additives. Most of the experiments in this work

Chapter 6

have been carried out using triple-cation perovskite^{9, 21}, $\text{Cs}_{0.1}(\text{MA}_{0.15}\text{FA}_{0.85})\text{Pb}(\text{I}_{0.85}\text{Br}_{0.15})_3$, to test **CS01**, **CS03**, **EP02**, **LCS01**, **CS02**, **CS04**, **CS05** and **CS06** HTMs. On the other hand, in the attempt to improve the efficiency of devices using **CS06**, and **CS05** for comparison, as HTM, the composition of the perovskite had to be changed to MAPbBr_3 providing a deeper HOMO level. This change in the energetics gave the possibility to improve the hole transfer efficiency, laying the HOMO levels in a more suitable position.

These studies were carried out at Prof. M. K. Nazeeruddin's laboratory at EPFL (Sion, Switzerland) and the whole work will be reported in scientific journals.

6.2. Device fabrication.

6.2.1. CsMAFAPbIBr perovskite solar cells.

Solar cell devices were fabricated onto conductive FTO coated glass substrates. The substrates were cut and cleaned by sequential treatment with 2 % aqueous Helmanex solution, acetone and isopropanol in an ultrasonic bath for 10 minutes respectively, followed by a 15 minutes UV-ozone exposure. The titania blocking layer was applied by spray pyrolysis from a precursor solution of titanium diisopropoxide bis(acetylacetonate) in ethanol at 450°C in ambient atmosphere. Mesoporous TiO_2 layer was deposited spin coating a 30 nm titanium dioxide particle (30 NR-D) paste from Dyesol diluted in ethanol at 3000 rpm for 30 s. The substrates were gradually heated under air flow at 125°C for 20 minutes, 250°C for 10 minutes, 350°C for 10 minutes, 450°C for 10 minutes and 500° for 30 minutes. After cooling down the substrates, SnO_2 layer was deposited spin coating a solution of SnCl_4 anhydrous in deionized water at 5000 rpm for 20 s, followed by a sintering step at 390°C for one hour. The perovskite layer was applied by one step spin coating procedure, reported by Michael Saliba et al.⁹, from a precursor solution of

$\text{Cs}_{0.1}(\text{MA}_{0.15}\text{FA}_{0.85})\text{Pb}(\text{I}_{0.85}\text{Br})_3$. The spin coating sequence includes two steps: 2000 rpm for 12 s with an acceleration of 200 rpm s^{-1} and 5000 rpm for 25 s with an acceleration of 2000 rpm s^{-1} . Prior to the end of the second step $100 \mu\text{L}$ of chlorobenzene are poured onto the spinning substrate. At the end of the spin program the substrate is immediately transferred onto a hotplate set at 100°C and is kept at that temperature for one hour under nitrogen atmosphere. The HTMs were deposited from solutions in chlorobenzene and also by spin coating. The thickness of this layer was optimized to obtain the best device performance for each molecule, changing spin coating conditions and solution concentrations. Also the concentration of additives that were added to the solutions of **CS02**, **CS04** and **CS05** were individually optimized. tBP, Li-TFSI and cobalt complex FK209 were added as additives to Spiro-OMeTAD, **CS01**, **CS03**, **EP02**, **LCS01** and **CS06**: 330 mol% tBP, 50 mol% Li-TFSI from a 1.8 M stock solution in acetonitrile and 10 mol% FK209 from a 0.25 M stock solution in acetonitrile. Finally, the gold electrode was deposited by thermal evaporation 70 nm layer of gold with 0.09 cm^2 using a shadow mask under high-vacuum conditions.

6.2.2. Perovskite solar cells using MAPbBr_3 perovskite solar cells.

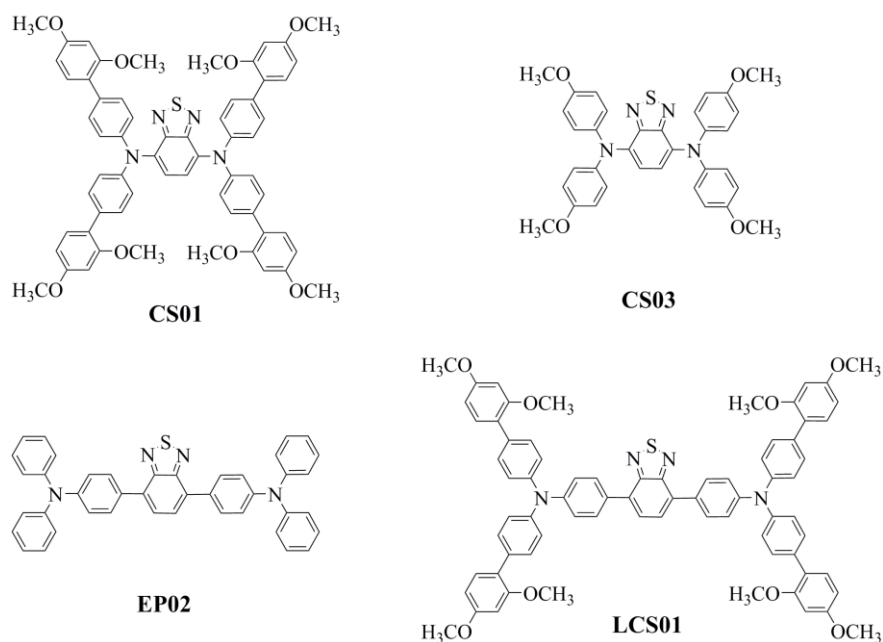
Solar cell devices were fabricated onto conductive FTO coated glass substrates. The substrates were cut and cleaned by sequential treatment with 2 % aqueous Helmanex solution, acetone and isopropanol in an ultrasonic bath for 10 minutes respectively, followed by a 15 minutes UV-ozone exposure. The titania blocking layer was applied by spray pyrolysis from a precursor solution of titanium diisopropoxide bis(acetylacetonate) in ethanol at 500°C in ambient atmosphere. Mesoporous TiO_2 layer was deposited spin coating a 30 nm titanium dioxide particle (30 NR-D) paste from Dyesol diluted in ethanol. The substrates were heated at 500° for 30 minutes. After cooling down the substrates and applying UV-ozone treatment for 15 minutes, SnO_2 layer was deposit the by spin coating a solution of SnCl_4 anhydrous 0.1 M in deionized

Chapter 6

water at 3000 rpm for 30 s, followed by a sintering step at 390°C for one hour. Right after another UV-ozone treatment of 15 minutes, the perovskite layer was applied spin coating a precursor solution of MAPbBr₃, 1.3 M, in DMF:DMSO 4:1, described in detail in Chapter 3. The spin coating sequence includes two steps. Prior to the end of the second step 100 µL of chlorobenzene are poured onto the spinning substrate. At the end of the spin program the substrate is immediately transferred onto a hotplate set at 100°C and is kept at that temperature for one hour under nitrogen atmosphere. Spiro-OMeTAD and PTAA were deposited on top of the perovskite layer by spin coating at 4000 rpm for 30 s. In the case of **CS05** and **CS06** were deposited at 2000 rpm for 30 s. tBP, LiTFSI and cobalt complex FK209 were added as additives to all HTMs: 330 mol% tBP, 50 mol% Li-TFSI from a 1.8 M stock solution in acetonitrile and 10 mol% FK209 from a 0.25 M stock solution in acetonitrile. Finally, the gold electrode was deposited by thermal evaporation of 70 nm layer of gold using a mask under high-vacuum conditions (10⁻⁵ Pa).

6.3. Benzothiadiazole-based small molecules as hole transporting materials in perovskite solar cells.

The BT-based **CS01**, **CS03**, **EP02** and **LCS01** molecules, all substituted by different di- and triphenylamines (see Scheme 6.1) were used as HTMs in triple-cation PSCs. This work consisted in a study of the influence of HTMs the molecular structure on the solar cell performance in order to enlighten the different roles of all individual molecular moieties. The ultimate goal of this work is then, to help in the development of new strategies to design novel high-efficiency HTMs.



Scheme 6.1: Molecular structure of **CS01**, **CS03**, **EP02** and **LCS01**.

The main differences between them, in terms of molecular structure, are the number of phenyl linkers added to extend the conjugation. **CS01** includes one phenyl group between the amine and the methoxy-substituted ring in comparison with **CS03**. While in the case of **LCS01**, the phenyl group is included between the BT and the two amines. These modifications were thought to have an influence in the HOMO energy level maintaining the LUMO. The optical, electrochemical and photophysical properties of these molecules have been addressed previously in Chapter 4. Table 6.1 shows a resume of them.

Chapter 6

Table 6.1: Resume of the optical, electrochemical and photophysical properties of BT-based HTMs.

HTM	CS01	CS03	EP02	LCS01	Spiro-OMeTAD
T_g (°C) ^[a]	168	81.5	99	155	125
$\lambda_{\max, \text{abs}}$ (nm)	529	543	460	473	386
λ_{em} (nm)	705	743	621	669	419
E_{HOMO} (eV)	-5.01	-4.81	-5.36	-5.16	-5.16
E_{LUMO} (eV)	-3.00	-2.88	-3.02	-2.93	-2.11
$\mu^{[b]} \times 10^4$ ($\text{cm}^2 \text{V}^{-1} \text{s}^{-1}$)	6.15	3.26	-	1.58	2.55

^[a] Glass transition temperature determine from the second cycle of DSC. All experiments were carried out under N₂ atmosphere at scan rate of 20 °C/min. ^[b] Hole mobility calculated with the SCLC method.

All these molecules exhibit a suited band alignment with the valence band edge of the perovskite (Figure 6.2), which led not only in an effective hole extraction from the perovskite to the HTM but also an optimal electron blocking capability. **LCS01** presents same HOMO level than spiro-OMeTAD although a much deeper LUMO in comparison. **CS01** and **EP02** exhibit deeper energetic values for HOMO, being the **EP02** the deepest and for **CS03**, the highest. It is also important to notice that in all the cases LUMO levels are around 1 eV deeper than Spiro-OMeTAD LUMO which increase the risk of a charge leakage²² throughout the HTM.

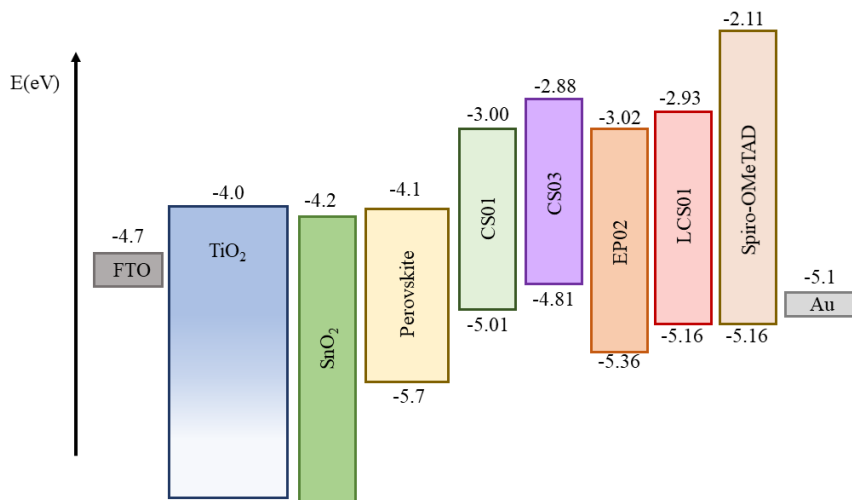


Figure 6.2: Energetic levels of the BT-based HTMs with the rest of the layers that form the device.

Considering the TGA and DSC experiments, **CS01** and **LCS01** are thermally stable. **CS03** and **EP02**, in contrast, presented some stability issues when they are tested in PSCs considering that they do not have a high value of T_g (81.5°C and 99°C, respectively) and it is very close to the operating temperature of a device at 1 Sun, which is around 60 - 100°C¹³.

Regarding the mobility measurements, as it can be seen in the Table 6.1, the hole mobility values of all the HTMs are about the same order of magnitude than the reported value for doped Spiro-OMeTAD²³. Notice that it was not possible to measure the hole mobility of **EP02**, the devices could not stand the measurement conditions (see Chapter 4). Lower conductivities require thinner layers (< 100 nm) in order to avoid transport losses and, thus, obtain good performances. Nevertheless, using a thinner HTM layer is more likely to generate shunting paths due to, for example, poorer coverages provoked by the roughness of the perovskite layer which is reflected in low performances and reproducibility of the devices. In addition, also related with the coverage, it is needed to avoid direct contact between the perovskite layer and the counter electrode, because it is well known that the counter electrode reacts with iodide

Chapter 6

ion in perovskite and quickly degrades the devices²⁴. Likewise, a thicker HTM layer (> 100 nm) allows usually a favourable reproducibility by covering the perovskite surface uniformly. However, extremely thicker HTL increase the probability to create high series resistance²⁵.

In sum and considering all these characteristics, it is possible to say that all of them can be good candidates as HTMs for perovskite solar cells as they present favourable energy levels and hole transport properties will not be a limiting factor in the working device.

In order to determine the thickness of each layer and the quality of the aforementioned coverage, high resolution scanning electron microscopy (SEM) cross-section image of spiro-OMeTAD based device is shown in Figure 6.3. As it can be seen, it is possible to easily identify the different layers of the device and their thicknesses: 30 nm of compact TiO_2 blocking layer, 180 nm of mesoporous TiO_2 , 40 nm of SnO_2 , 470 nm of perovskite, 200 nm of the Spiro-OMeTAD and 70 nm of the gold electrode.

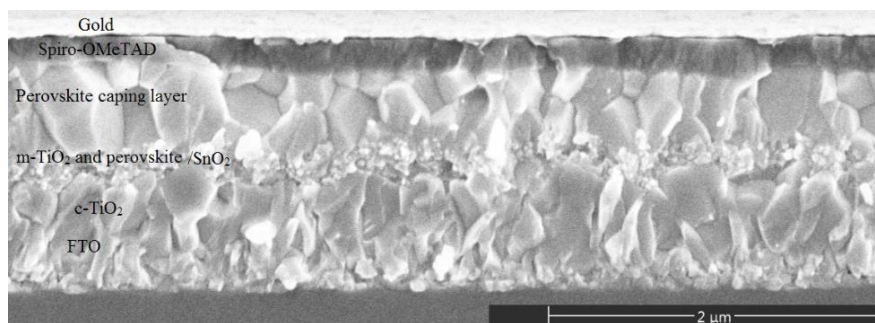


Figure 6.3: Cross-sectional SEM image of an optimized PSC device with Spiro-OMeTAD as HTM.

The BT-based HTM layers were optimized starting from the same conditions than that used for spiro-OMeTAD.

6.3.1. Optimization of the hole transporting layer.

In this section, the optimization process is described. To this aim, in the first test the devices were fabricated under the same conditions of deposition and solution concentrations for each HTM with and without additives. From that, the HTM concentrations and the deposition speed of the HTM solutions deposited on top of the perovskite layer were changed.

In order to test the effect of the additives in the BT-based HTMs, as the ones reported before with this chemical group²⁶⁻²⁸, a set of devices with and without them were fabricated, with no further optimization. Table 6.2 resumes all the results obtained. The J-V curves are displayed in the annex (Figure A6.1).

Table 6.2: J-V data for PSCs using **CS01**, **CS03**, **EP02** and **LCS01** solutions with and in the absence of additives.

HTM	Dopants	Concentration (mg/mL)	PCE (%)
CS01	x	25	9.91
CS01	-	25	0.70
CS03	x	25	7.72
CS03	-	25	2.08
EP02	x	20	7.69
EP02	-	20	5.85
LCS01	x	25	14.06
LCS01	-	25	2.83

As it can be seen in Table 6.2 the overall efficiency drops significantly for **CS01**, **CS03** and **LCS01** when no additives were added to the solution, whereas for **EP02** the decrease in efficiency is not as dramatic. For this reason, in the following tests for the three first HTMs mentioned above, devices were

Chapter 6

fabricated including additives into the HTM solution. The influence of the additives was not clear for **EP02** thus more tests were performed. In Table A6.3 it is summarized the optimization that was done for **CS01**. The J-V curves and device parameters are collected in the annex of this chapter (Figure A6.3).

In general, for all the molecules, two parameters were changed to optimize the hole transporting layer: the concentration of the HTM solution and the deposition speed. A thicker layer was obtained when the spinning speed was reduced and/or the concentration was increased: 75 nm, 80 nm, 140 nm and 70 nm for **CS01**, **CS03**, **EP02** and **LCS01**. By increasing the thickness of the layer, it is less likely to generate pinholes, so the perovskite layer would be completely covered and not in contact with the gold electrode. In addition, the hole mobility value of **CS01**, **CS03** and **LCS01** (6.15 , 3.26 and $1.58 \times 10^{-4} \text{ cm}^2 \text{ V}^{-1} \text{ s}^{-1}$ respectively) is in the same order of magnitude as spiro-OMeTAD ($2.55 \times 10^{-4} \text{ cm}^2 \text{ V}^{-1} \text{ s}^{-1}$) to allow the increase of the thickness.

The optimal concentration for **CS01** was 20 mg/mL and the speed of the deposition, 2000 rpm.

The J-V curves and the PV parameters for **CS03** are collected in the annex (Figure A6.3) and in Table A6.4. **CS03**-based devices have better efficiency when the layer is deposited at a slower speed (2000 rpm) with a concentration of 20 mg/mL, with a thickness of 80 nm (Figure 6.8). In later tests PCE record for this HTM (13.31 %) was obtained.

CS01 and **CS03** showed higher efficiencies when the speed of the spinning was reduced from 4000 rpm to 2000 rpm getting thicker devices (from 50 nm to 80 nm for a 20 mg/mL stock solution of **CS03**). On the contrary, **EP02** did not work efficiently using these conditions, a thinner layer of 60 nm was needed to achieve better reproducibility and device performance, as shown in the Table

A6.5 (see Figure 6.3). There were no important differences in PCE when additives were added to the solution under mentioned conditions.

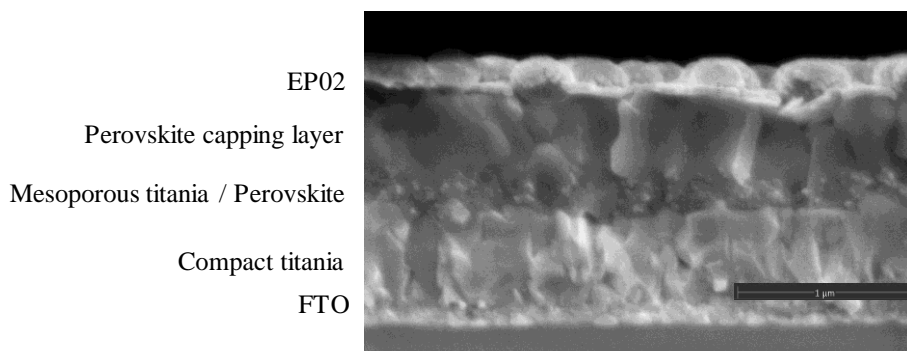


Figure 6.4: Cross-sectional SEM image of a PSC device with **EP02** as HTM, deposited at 2000 rpm.

In the SEM image (Figure 6.4), it was possible to identify the **EP02** layer and it can be seen some formed semi spherical domains on top of the perovskite layer with a poor coverage, which led to have poor reproducibility and low efficiencies. Trying to achieve better results, the speed of the spin coater was increased and the concentration of the solution was decreased in order to deposit a thinner layer. The optimal PCE (around 10 % without further optimization) was found using solutions at 10 mg/mL.

LCS01-based devices were prepared changing the concentration from 20 to 25 mg/mL and the speed the layer was deposited, being the optimal thickness 70 nm. The same as occurred with **CS01** and **CS03** the best results were obtained for the lowest concentration and speed of deposition.

Having optimized the conditions for each HTM of this family, a large set of devices was prepared and characterized for each of them. A table summarizing the optimal conditions is shown below:

Chapter 6

Table 6.3: Optimized parameters for the HTMs layer.

HTM	Concentration (mg·mL ⁻¹ / mM)	Spin coater conditions (rpm, rpm/s, s)	Thickness (nm)
CS01	20 / 19.7	2000, 2000, 30	75
CS03	20 / 33.9	2000, 2000, 30	80
EP02	10 / 16.1	4000, 2000, 30	60
LCS01	20 / 17.1	2000, 2000, 30	70

6.3.2. Device characterization.

The photovoltaic performance of the devices was measured under AM 1.5 G conditions and J-V curves were recorded by applying a forward and reverse bias with a scan rate of 10 mV s⁻¹ in order to minimize the hysteresis effects stemming from the perovskite material²⁹. Forward J-V curves of the four HTMs and the reference (spiro-OMeTAD) for comparison are shown in Figure 6.5. Forward and reverse J-V curves of all of them are collected in the annex (see Figure A6.6).

The PV parameter of the optimized PSCs devices using BT family as HTMs are shown in Table 6.4. **CS01** and **LCS01** show excellent PCEs up to 17.84 % and 18.09 % respectively. The V_{OC} is around 1 V for both compounds, only 0.1 V less than the voltage obtained for the reference (1.12 V). Figure 6.5 shows the J-V curves of the best device using these four HTMs and spiro-OMeTAD. The J_{SC} of **LCS01** and **CS01** (around 23.5 mA/cm²) are very close to the value of spiro-OMeTAD and all of them are above 20 mA/cm². J_{SC} values obtained by J-V measurements with the solar simulator matched well with the ones calculated from the integral external quantum efficiency (EQE) measurements (23.40 mA/cm² for **CS01**, 20.25 mA/cm² for **CS03**, 22.14 mA/cm² for **EP02** and 21.48 mA/cm² for **LCS01**), depicted in Figure 6.6.

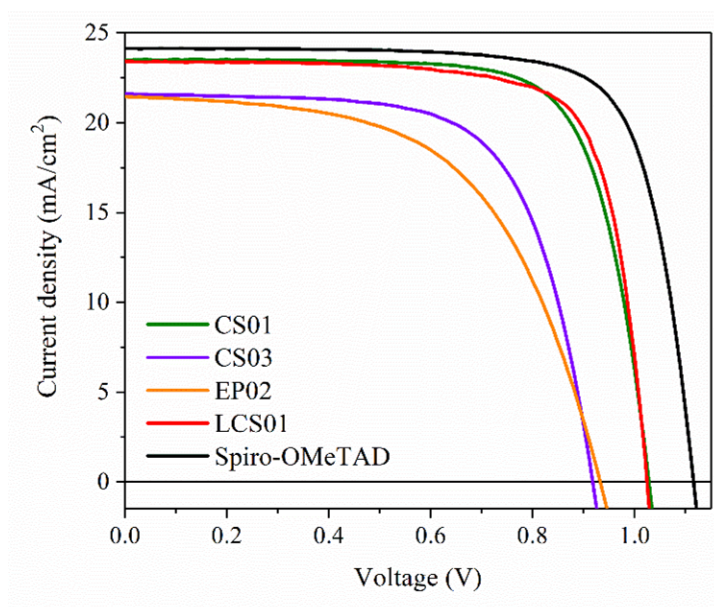


Figure 6.5: J-V curves of triple-cation mix PSCs devices using CS01, CS03, EP02, LCS01 and Spiro-OMeTAD as HTMs.

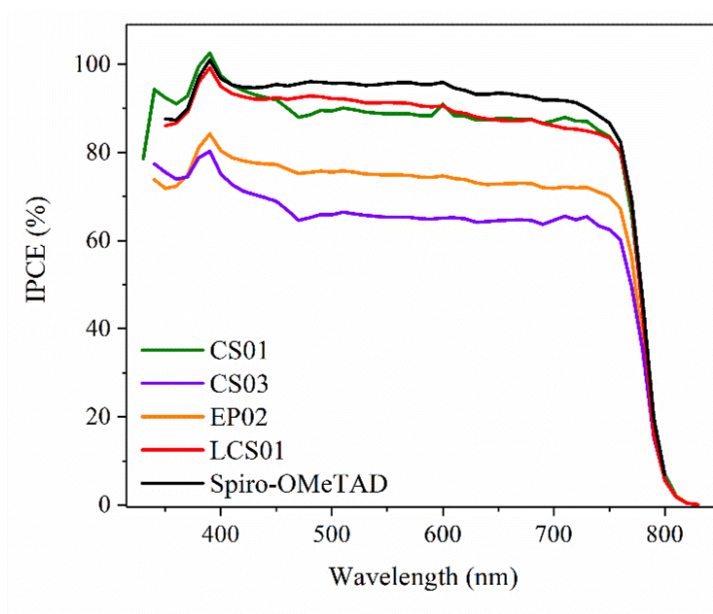


Figure 6.6: IPCE spectrum for devices based on CS01, CS03, EP02, LCS01 and Spiro-OMeTAD as HTMs.

Chapter 6

On the contrary, devices with **EP02** and **CS03** do not show efficiencies as high as the other molecules. Comparing the results with **CS01** and **LCS01**, the differences in V_{OC} and FF are noticeable. While **CS01** and **LCS01** have a V_{OC} around 1 V, **EP02** and **CS03** are below 0.85 V although no significant differences in the HOMO energy levels of these molecules can be appreciated. In DSSCs, the V_{OC} could be predicted by the difference in the HOMO energy levels of the electrolyte and the Fermi level of the TiO_2 layer³⁰. This observation is of high importance as indicates that the values from UV-Vis absorbance, luminescence and electrochemical potential are not sufficient to determine the HOMO and LUMO energy levels of the HTMs when deposited on top of the perovskite layer³¹⁻³². Moreover, it has been discussed the origin of the V_{OC} could be related with the non-radiative recombination of free carriers that takes place in the perovskite and its interfaces, but also with the charge accumulation³³. It has been found that the energy losses of the perovskite bulk and the hole- and electro- selective interfaces limit the value of the V_{oc} in PSCs³⁴.

The main reason for the lower performance of **CS03** and **EP02** is the FF (0.56 for **CS03** and 0.51 for **EP02**), that limits the PCE. FF is limited by the formation of the hole transport layer on top of the perovskite layer leading higher series resistance and low shunt resistance that decrease the FF³⁵⁻³⁶. The performance of **CS03** can also be explained by looking at its molecular structure (see Scheme 6.1), due to the π -conjugation is not as extended as for **CS01** or **LCS01**, achieving a PCE of 13.31 %. Nevertheless, the π -conjugation for **CS01** was extended by adding a phenyl ring next to each diphenylamine and for **LCS01**, by adding an additional one between the BT and the amines. This fact allowed **CS01** and **LCS01** to compensate the photogenerated charge more efficiently, obtaining an important enhance of the PCE compared to **CS03**.

Table 6.4: PV parameters showing the performance of the best PSCs devices prepared by using **CS01**, **CS03**, **EP02** and **LCS01**.

HTM	V _{oc} (V)	J _{sc} (mA/cm ²)	FF (%)	PCE (%)
CS01	1.03	23.49	0.74	17.84
CS03	0.92	21.53	0.67	13.31
EP02	0.93	21.45	0.56	11.29
LCS01	1.02	23.41	0.76	18.09
Spiro-OMeTAD	1.12	24.13	0.76	20.42

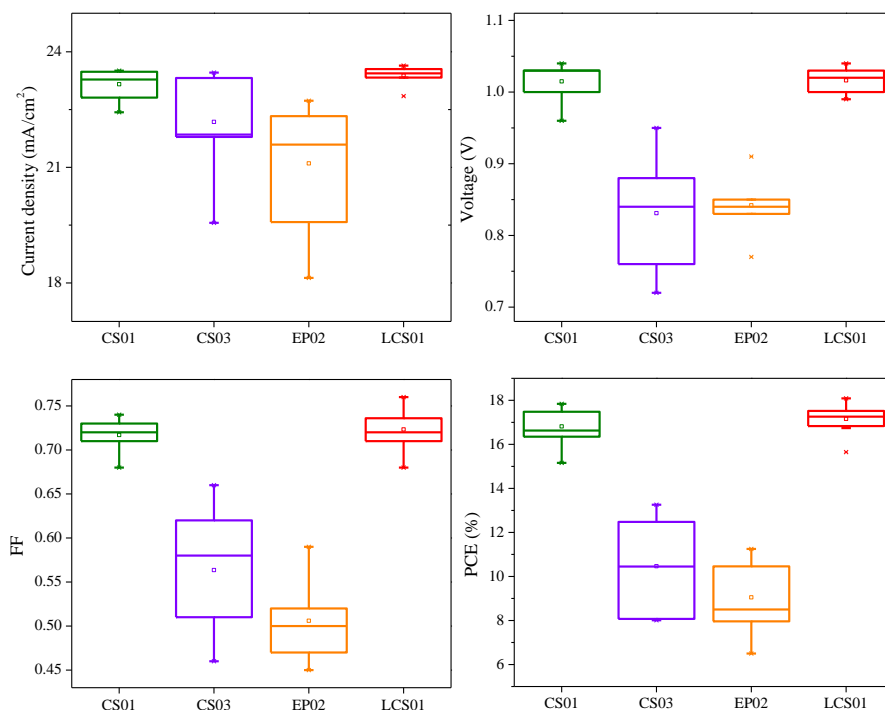


Figure 6.7: Statistic of PV parameter when BT-based HTMs were used in PSCs.

Chapter 6

The average PCEs of 16.82 ± 0.83 % for **CS01** and 17.16 ± 0.66 % for **LCS01** indicate good reproducibility, better than for **CS03** and **EP02** (10.47 ± 2.31 % and 9.05 ± 1.54 %, respectively) as it has been exposed before.

Despite having obtained better performance after the optimization of devices using **EP02** as HTM, solar cells efficiencies (11.25 %) cannot compete with spiro-OMeTAD or with the other HTMs of this family. The layer of this organic semiconductor was deposited by decreasing the concentration from 20 to 10 mg/mL and the thickness of the layer (by increasing the speed of the spinning to 4000 rpm), obtaining better reproducibility and uniformity of the film. However, when a cross-section SEM image (Figure 6.8) was performed, it showed a very thin layer of 60 nm that did not covered completely the perovskite layer. It was also observed in a top view SEM image (Figure 6.9) the same semi sphere structures in the surface as appeared in thicker (215 nm of diameter) films, indicating the issue was not solve by reducing the concentration and increasing the speed of the deposition and, thus, reducing the thickness. This could be explained because **EP02** has not methoxy groups or alkyl chains, making it less soluble and with more tendency to form aggregates. Although it was probed that the incorporation of methoxy groups is not completely essential to obtain good efficiencies^{13, 37}, it is desirable to include them in the molecular structure, not only to increase the solubility, but also to help to increase the electron donating properties of the molecule (when they are located in *ortho* or *para* position)³⁸.

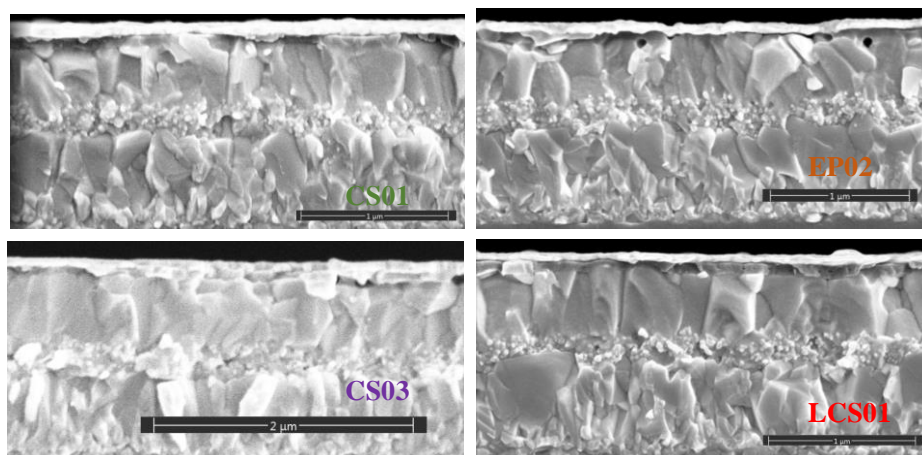


Figure 6.8: Cross-section SEM images for triple mix-perovskite champion devices based on **CS01**, **CS03**, **EP02** and **LCS01** as HTMs.

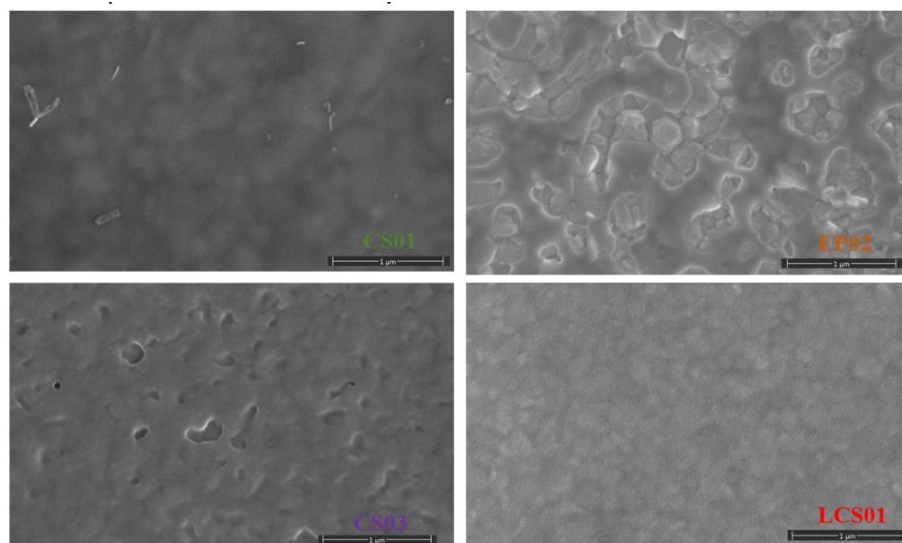


Figure 6.9: Top view SEM images for triple-cation mixed perovskite champion devices based on **CS01**, **CS03**, **EP02** and **LCS01** as HTMs.

6.3.3. Conclusions.

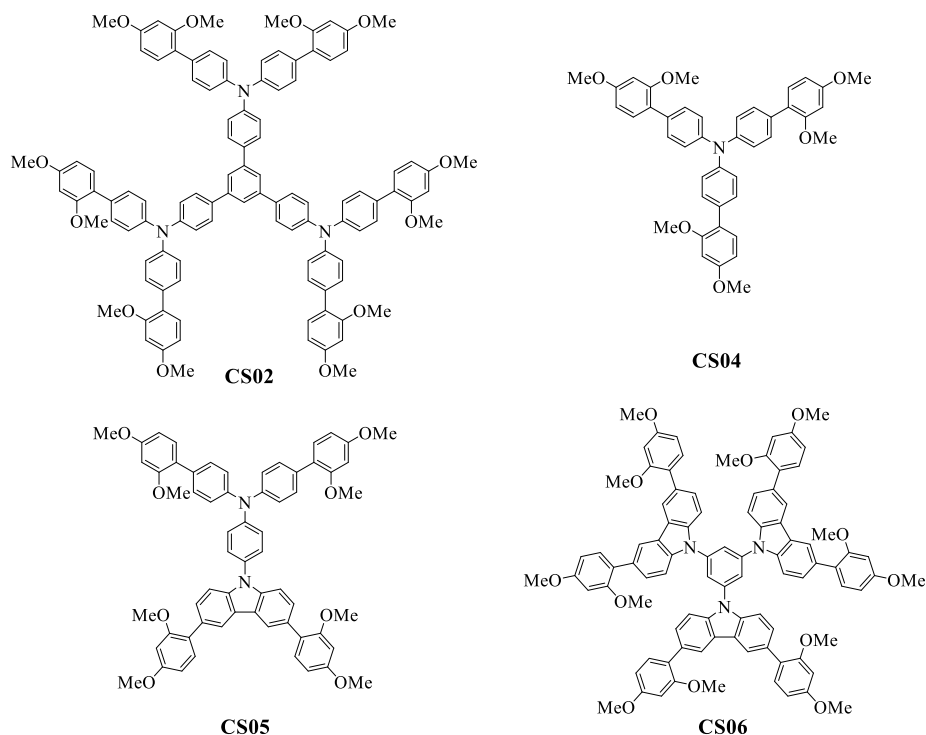
In summary, a rapid and efficient synthesis of a series of novel benzothiadiazole HTMs with methoxyphenyl substituents have been reported. These HTMs are obtained from simple and inexpensive starting materials, scalable in one, two

Chapter 6

or three synthetic steps, with the potential of low production costs in comparison with the most widely used, spiro-OMeTAD. Looking at the measurements of UV-Vis, CV and PL spectra, the HOMO and LUMO levels of each compound were found to be in good alignment with perovskite's. Remarkable power conversion efficiencies were obtained for **LCS01** and **CS01** as HTMs (18.05 % and 17.84 %, respectively) in comparison with **CS03** and **EP02** (13.31 % and 11.25 %), which does not show good performance due to the lack of aromatic rings that can compensate the electron acceptor nature of the BT group, for **CS03**, and also the absence of alkyl chains or methoxy groups that makes **EP02** not being soluble enough and forming aggregates in the surface of the perovskite layer. This work demonstrates the importance of the molecular structure in the design and synthesis of new HTMs and the deposition conditions of the hole transport layer.

6.4. Triphenylamine and carbazole-based small molecules as hole transporting materials in Perovskite Solar Cells.

These novel organic compounds constitute a new family of ease to prepare HTMs based on TPA and carbazole groups with *o,p*-dimethoxybenzene as substituents (Scheme 6.2). These molecules were specifically designed to be used as HTMs for PSCs due to the greater electron donating properties of their moieties.



Scheme 6.2: Molecular structure of the triphenylamines/carbazole-based organic semiconductors used as HTMs for PSCs in this work.

The optical, electrochemical and photophysical properties of these HTMs have been described previously in Chapter 4. In Table 6.5, a resume of the main properties is shown.

As it can be seen in Table 6.5, **CS04** does not present a value of T_g , which means that the organic material is amorphous and directly melts at 164 °C). In addition, the T_g of other HTMs are equal or above 170 °C, higher than for spiro-OMeTAD (125 °C), so it can be assumed they will be thermally stable when they will be used in an operating device.

Chapter 6

Table 6.5: Summary of the main thermogravimetric, optical, electrochemical and photophysical characteristics of **CS02**, **CS04**, **CS05** and **CS06**.

HTM	CS02	CS04	CS05	CS06	Spiro-OMeTAD
T_g (°C) ^[a]	192	-	170	180	125
λ_{max, abs} (nm)	340.5	334.5	302.5	305.5	386
λ_{em} (nm)	443.0	405.0	379.0	380.0	419
E_{HOMO} (eV)	-5.18	-4.73	-5.20	-5.98	-5.16
E_{LUMO} (eV)	-2.03	-1.26	-1.51	-2.38	-2.11
Hole mobility					
value 10⁴	2.04	2.93	2.46	2.45	2.55
(cm²V⁻¹s⁻¹) ^[b]					

^[a] Glass transition temperature determine from the second cycle of DSC. All experiments were carried out under N₂ atmosphere at scan rate of 20 °C/min.

^[b] Calculated with the SCLC method.

According to the results of hole mobility, estimated with the SCLC method, the values are in the same range as the reference ($2.55 \times 10^{-4} \text{ cm}^2\text{V}^{-1}\text{s}^{-1}$) indicating that this parameter will not be a limiting factor to determine the final optimal thickness. Nevertheless, a thinner hole transport layer (around 100 nm) have been deposited, allowing us to achieve high efficiencies and optimal reproducibility, as it can be seen in the cross-section image of devices based in these HTMs (see Figure 6.10)

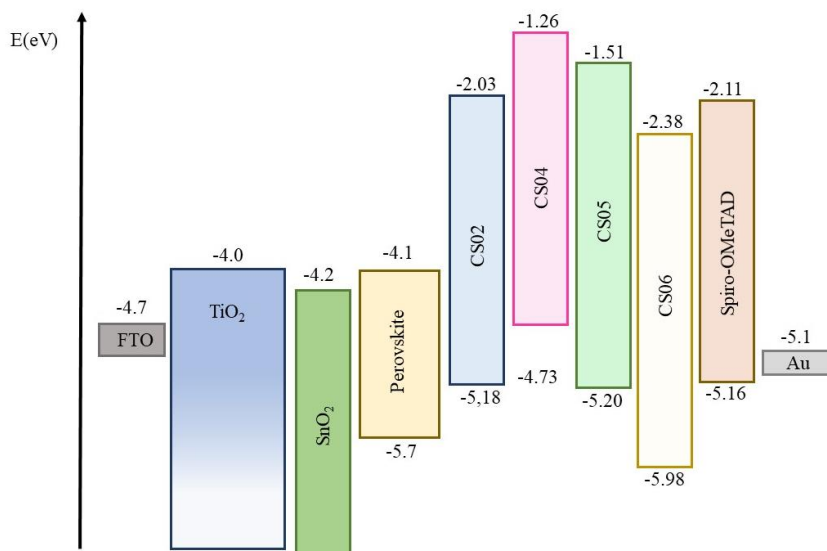


Figure 6.10: Energetic levels of all components of the PSC device and the HTMs used in this study.

HOMO and LUMO energetic levels of **CS02**, **CS04** and **CS05** properly match with the valence band edge of the perovskite, leading to an effective hole extraction from the HTM to the perovskite, but also an effective electron-blocking due to higher levels. However, the HOMO level of **CS06** was found to be deeper than that of the perovskite and the already mentioned hole extraction is not allowed. With this last observation, a functional PSCs using **CS06** and the triple-cation mixed perovskite cannot be expected. Even though, few tests were carried out to verify the result, specially, since it has been demonstrated that the use of additives and the layer conformation strongly affect the energy levels of the materials provoking substantial shifting³³.

The molecules synthesized in this work were tested with triple mix-perovskite obtaining PCEs in the range of 15.40 % to 19.38 % under AM 1.5 G for three of them (**CS02**, **CS04** and **CS05**). These efficiencies are comparable to those obtained using spiro-OMeTAD, which point them out as promising candidates to be used as easily attainable and cost-effective alternatives for PSCs.

6.4.1. Optimization of the hole transporting layer.

In this section, it will be explained briefly, the optimization carried out to obtain the best device performance for each HTM. In order to achieve it, a first test was done preparing devices under the same conditions but changing the HTMs layers and adding or not, the corresponding additives to the stock solutions. The efficiency of the aforementioned devices are shown in Table 6.6. In this previous test, devices were fabricated with no further optimization, and in all cases the use of additives substantially improved the device performance, for example achieving an efficiency of 17.64 % (from 1.38 % without additives) using **CS05**. With **CS02** and **CS04** the gain in efficiency was also significant reaching 11.86 % (from 0.04 %) and 13.54 % (from (3.31 %)), respectively. Moreover, as we predicted and mentioned before, **CS06** does not permit an efficient hole injection from the perovskite with or without additives obtaining extremely low performances in both cases.

Table 6.6: Efficiencies for PSCs devices using **CS02**, **CS04**, **CS05** and **CS06** as HTMs with and without the use of additives.

HTM	Dopants	Concentration (mg/mL)	PCE (%)
CS02	x	50	11.86
CS02	-	50	0.04
CS04	x	25	13.54
CS04	-	25	3.31
CS05	x	25	17.64
CS05	-	25	1.38
CS06	x	20	0.56
CS06	-	20	0.09

To carry on with the optimization, the solution concentration of the HTMs and additives were varied, maintaining the speed conditions at 2000 rpm, continuing using the optimal conditions found for the BT-based family of HTMs. The results are summarized in Table 6.7.

In this family of HTMs, not only the concentration was modified, but also the amount of additives used in the solution. For **CS02**, the optimal efficiency was found at 50 mg/mL, the highest compared with the other HTMs of this family. When the concentration of additives is doubled respect to the reference (which means, 100 mol% of LiTFSI from a 1.8 M stock solution in ACN, 660 mol% of *t*BP and 20 mol% of FK409 from a 0.25 M stock solution in ACN), the highest PCE of 15.40% was achieved (see Table A6.8). In this case, even obtaining considerable high efficiencies including the additives, **CS02** could not be the best candidate as, ideally, the new HTMs should dispense with the additives or maximally reduce them in order to prevent or retard the degradation¹⁵⁻¹⁶.

Table 6.7: Optimized parameter for the HTMs layer.

HTM	Concentration (mg·mL ⁻¹ / mM)	Spin coater conditions (rpm, rpm/s, s)	Thickness (nm)
CS02	20 / 19.7	2000, 2000, 30	75
CS04	20 / 33.9	2000, 2000, 30	80
CS05	25 / 26.2	4000, 2000, 30	60
CS06	20 / 17.1	2000, 2000, 30	70

CS04 was tested from solutions at two different concentrations and at two different ratio of additives. Comparing the results showed in Table A6.9, it can be seen that the less concentrated solution (20 mg/mL) showed higher efficiencies, which means also the thinner layers (95 nm versus 105 nm). This

Chapter 6

fact could be understood as a hole mobility issue thus, if it is very low, it is not possible to deposit a thick layer. However, the hole mobility value for **CS04** ($2.46 \cdot 10^{-4} \text{ cm}^2\text{V}^{-1}\text{s}^{-1}$) is the same as the value for spiro-OMeTAD ($2.55 \cdot 10^{-4} \text{ cm}^2\text{V}^{-1}\text{s}^{-1}$) or the other HTMs studied in this work, so we can say that this is not only parameter responsible for the device efficiency. The best efficiency (18.05 %) was found when the additives were used in the same ratio as they are used for spiro-OMeTAD.

The highest value of PCE (19.38 %) was obtained with 25 mg/mL solution concentration of **CS05** in CB and doubled the concentration of the additives. In this particular case, a colour change in the solution colour from transparent to green was observed when the cobalt complex (FK209) was added at 20 %mol, making evidencing the oxidation of the HTM. On the contrary, the colour remained unaltered when 10 %mol of FK209 was added. Increasing the concentration up to 50 mg/mL led into a decrease in the overall efficiency (Table A6.10).

In the case of **CS06**, it was previously demonstrated that, in spite of its favourable optical, electrochemical and photophysical characteristics, no efficient hole injection occurs, so all tests using this HTM are shown in detail in the annex. The conclusion is that this HTM is not suitable for the triple-cation mix-perovskite. In order to overcome this issue, **CS06** was also tested with MAPbBr₃, which has a lower HOMO level that could enhance the hole transfer. The results using this configuration will be shown further in this chapter.

6.4.2. Device characterization.

The photovoltaic performance of the devices was measured under AM 1.5 G conditions and J-V curves were recorded by applying a forward and reverse bias with a scan rate of 10 mV s^{-1} for each HTM (see Figure A6.6 in the annex). The champion J-V curves for the four HTMs recorded under reverse bias are

shown in the Figure 6.11 and the corresponding PV parameters are summarized in Table 6.8.

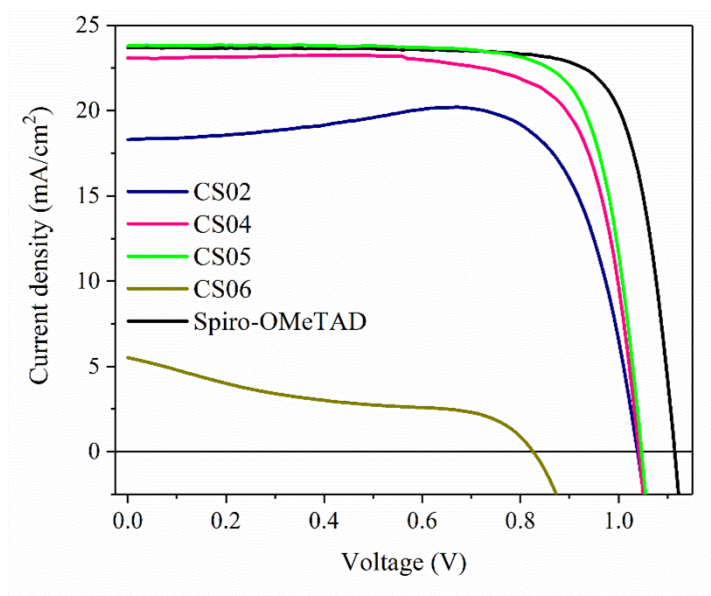


Figure 6.11: J-V curves measured in reverse bias of triple mix-perovskite devices using **CS02**, **CS04**, **CS05**, **CS06** and Spiro-OMeTAD as HTMs.

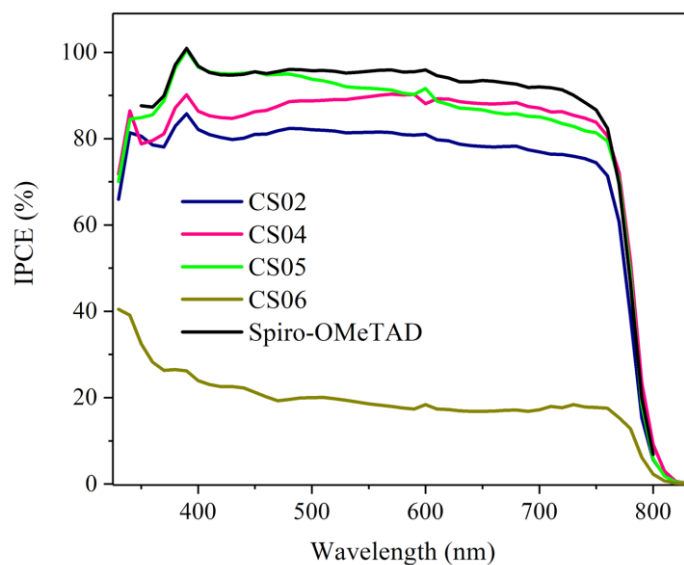


Figure 6.12: IPCE spectrum for devices based on **CS02**, **CS04**, **CS05**, **CS06** and Spiro-OMeTAD as HTMs.

Chapter 6

The results show excellent performances for **CS02**, **CS04** and **CS05** HTMs, this last one with the highest efficiency. Comparing the results obtained for the three derivatives (**CS06** will not be taken in consideration in this discussion), the main difference when using **CS02** is the lower J_{sc} (18.15 ± 1.89 mA/cm²). The value of J_{sc} for **CS05** is very close to those obtained with the Spiro-OMeTAD reference. All of them present voltages above 1.00 V or very close (1.00 ± 0.03 V, 0.99 ± 0.04 V and 1.04 ± 0.00 V for **CS02**, **CS04** and **CS05** respectively).

Table 6.8: PV parameters showing the performance of best PSCs devices by using **CS02**, **CS04**, **CS05** and **CS06** as HTMs.

HTM	V _{oc} (V)	J _{sc} (mA/cm ²)	FF (%)	PCE (%)
CS02	1.04	18.30	0.81	15.40
CS04	1.04	23.09	0.75	18.05
CS05	1.05	23.80	0.78	19.38
CS06	0.815	4.42	0.48	1.74
Spiro-OMeTAD	1.15	24.13	0.80	20.97

The J_{sc} obtained from J-V measurements match well with the ones calculated from the IPCE measurements (20.5 mA/cm², 22.78 mA/cm², 22.20 mA/cm², 4.31 mA/cm² and 22.6 mA/cm² for **CS02**, **CS04**, **CS05**, **CS06** and spiro-OMeTAD, respectively). The IPCEs of the PSCs devices as a function of wavelength also shows that the devices with **CS04** and **CS05**, as well as spiro-OMeTAD, exhibits an IPCE value above 90 %, covering the region from 400 nm up to 800 nm. The high fill factor may be attributed to a lower series resistance³⁶ that can be favoured by the thin HTM layers of 108 nm, 95 nm and

110 nm, for **CS02**, **CS04** and **CS05**, respectively, (see Figure 6.13). As a general trend, the presented chemical structures of **CS04** and **CS05** seem to favour the formation of homogeneous thin films with a good morphology and hole mobility, which lead to excellent FF values ($> 70\%$), comparable to those obtained for spiro-OMeTAD. **CS05** has a more rigid molecular structure which may lead to a better π - π stacking of the HTL, thus, better performance. In Figure 6.13 and 6.14, the cross-section and top view images of the four HTMs are shown. **CS05** shows a good coverage of the perovskite layer, while **CS04** shows “spheres” that could be related with the formation of aggregates, which could lead to amorphous domains in the film.

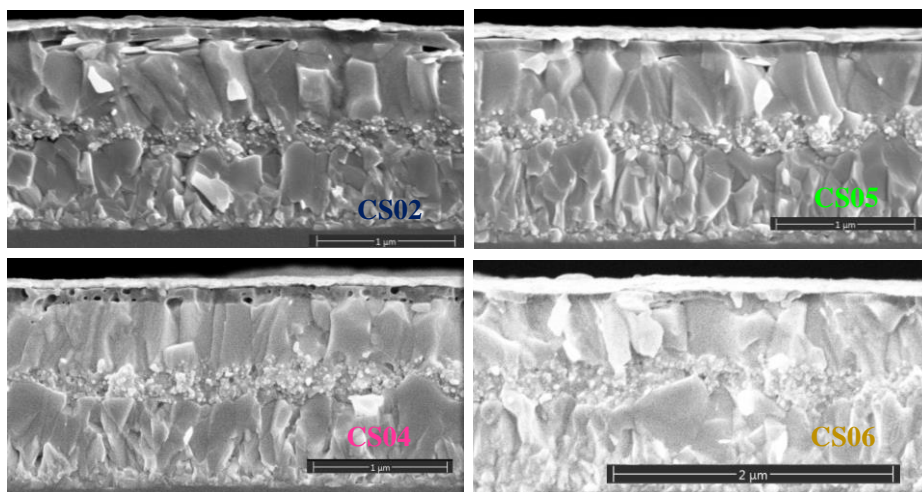


Figure 6.13: Cross-section images for triple mix-perovskite champion devices based on **CS02**, **CS04**, **CS05** and **CS06** as HTMs.

The statistic distribution of the PV parameters of 10 devices fabricated with these four HTMs are shown in Figure 6.15. The PCE average of $18.67 \pm 0.45\%$ for **CS05** indicates a very good reproducibility for this molecule, as well as for the J_{SC} , V_{OC} and FF. **CS04**-based devices also shows good reproducibility although the average PCE is lower (14.60 %).

Chapter 6

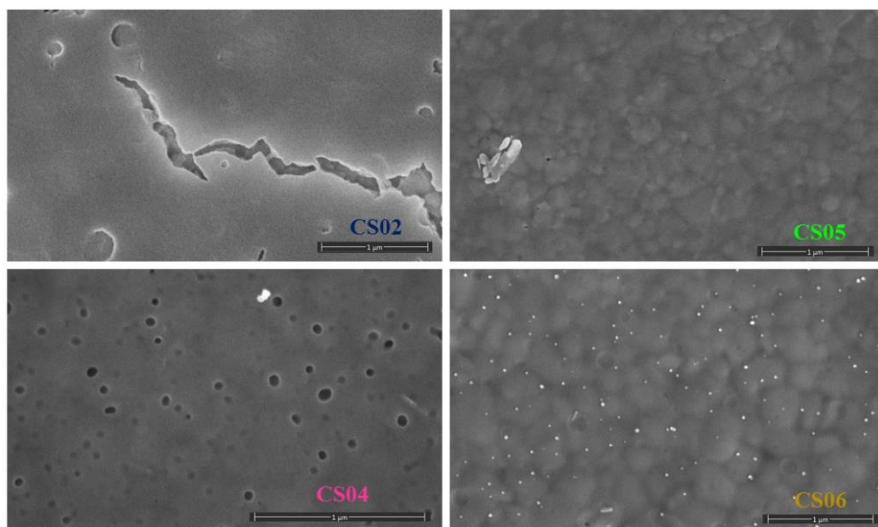


Figure 6.14: Top view SEM images for triple-cation mixed perovskite champion devices based on CS02, CS04, CS05 and CS06 as HTMs.

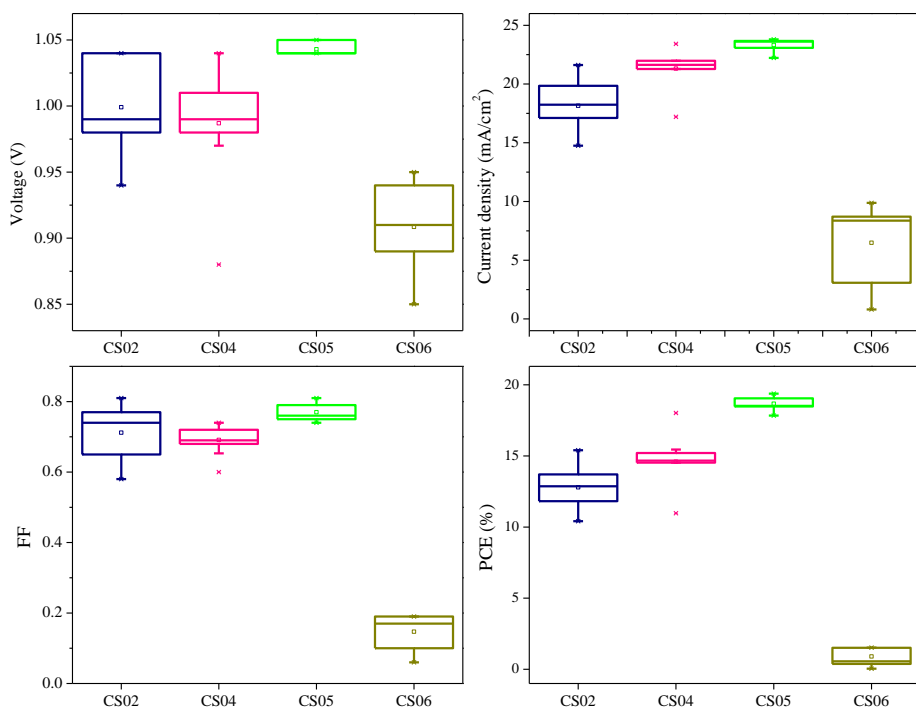


Figure 6.15: Statistical distribution of at least ten devices of PSCs using TPA and carbazole-based HTMs.

6.4.3. CS06 as HTM using MAPBr₃ perovskite solar cells.

Several types of perovskite, in terms of composition, have been tested in devices depending on the application or the final use³⁹. It is well known that it is possible to tune the band gap⁴⁰⁻⁴¹ of the perovskite by changing the ratio of the anions (I⁻ or Br⁻) used. For example, it has been demonstrated that by increasing the amount of bromine in the precursor solution the band gap widens⁴¹⁻⁴². Even so, the precise value for the HOMO and LUMO energy levels of MAPbBr₃ perovskite are not perfectly determined. P. Schulz et al. calculated a HOMO level (see Figure 6.16) of -5.9 eV⁴³, J. Das et al. reported a value of -6.5 eV⁴⁴ and J. H. Noh et al., of -5.44 eV⁴⁰ despite using the same technique to do the characterization (ultraviolet photoelectron spectroscopy, UPS). A direct and accurate determination of the perovskites' electronic structures and of their interface energetics is fundamental to help with the design and optimization of perovskite-based structures and of the materials at the interfaces. To date, the effects taking place at the interface between the HTM and the perovskite have been studied, such as an interface dipole, that could change the position of the HOMO level of the organic molecule relative to the valence band maximum of the perovskite, which may impede hole extraction or lead to an energy loss in the hole transfer⁴³.

Chapter 6

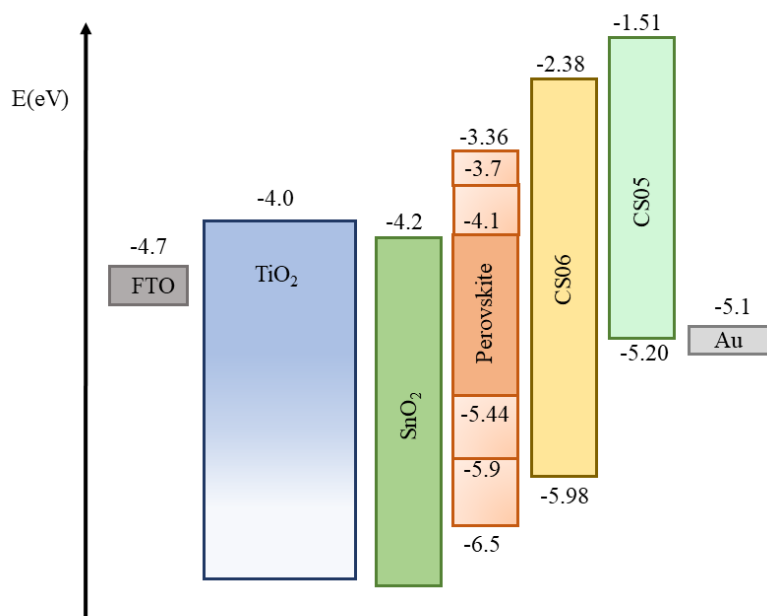
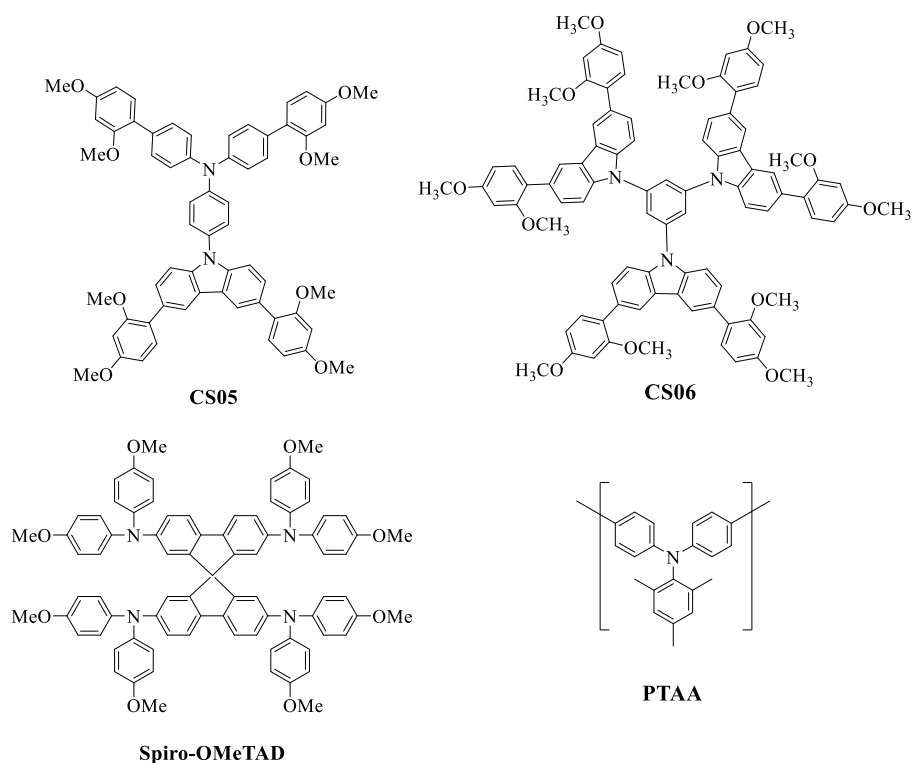


Figure 6.16: Energy diagram of the different components in the PSC device. The difference in the orange tones of the perovskite charts corresponds to the different values reported for the perovskite composition MAPbBr_3 .

Based in the molecular structure (Scheme 6.3) and due to its optical and electrochemical characteristics, **CS06** was designed to be a good electron donor semiconductor which can be used as a HTM in PSCs. However, as it has been mentioned before, the hole injection from the perovskite (triple-cation mix-perovskite) to this HTM is compromised due to its deeper HOMO level. In order to solve that issue, MAPbBr_3 was chosen to replace the triple-cation mix perovskite, since it presents also a deeper HOMO level that could match with **CS06**.



Scheme 6.3: Molecular structure of the HTMs used with MAPbBr₃ PSCs.

MAPbBr₃ PSCs were fabricated using **CS05**, **CS06**, spiro-OMeTAD and Poly[bis(4-phenyl)(2,4,6-trimethylphenyl)amine] (PTAA) (see Scheme 6.3) as HTM. The photovoltaic performance of the devices was measured under AM 1.5 G conditions and I-V curves were recorded by applying a reverse bias with a scan rate of 10 mV s⁻¹ and are shown in Figure 6.17.

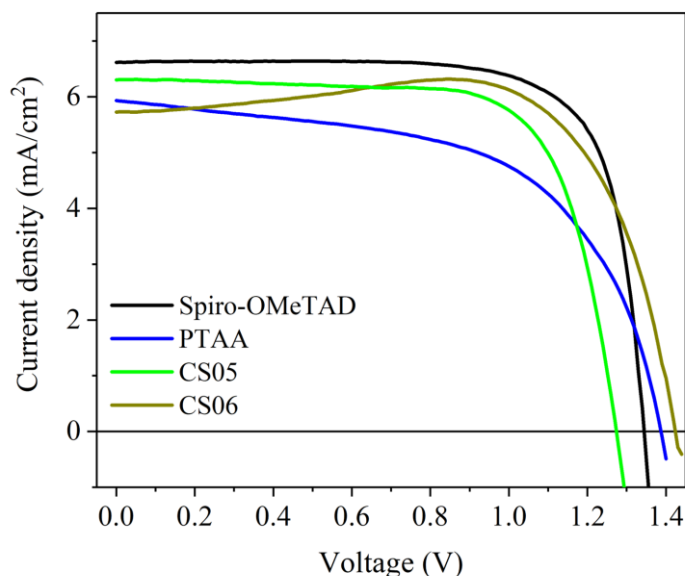


Figure 6.17: J-V curves showing the performance of MAPbBr_3 perovskite devices prepared by using **CS05**, **CS06**, Spiro-OMeTAD and TPAA as HTMs.

With this perovskite composition, and the results obtained from the J-V curves, it evidences that the hole transfer from **CS06** takes place, indicating that the HOMO energy levels of the HTMs can be well-aligned with the MAPbBr_3 valence band. **CS05** and **CS06** exhibited PCE of 5.76 % and 6.28 %, respectively. Devices using **CS05** show a V_{OC} (1.33 V) which is on par with that of Spiro-OMeTAD (1.34 V). On the other hand, **CS06** exhibited a noteworthy higher V_{OC} of 1.43 V. The differences in J_{SC} of **CS06** and Spiro-OMeTAD lead to the small difference in PCE between them. The bump of the J-V curve for **CS05** and **CS06** might be attributed to a not very efficient charge extraction in the interface between the HTM and the perovskite²⁹.

Table 6.9: PV parameters of the best MAPBr₃ devices using **CS05**, **CS06**, spiro-OMeTAD and PTAA as HTMs.

HTM	V _{oc} (V)	J _{sc} (mA/cm ²)	FF (%)	PCE (%)
CS05	1.27	6.30	0.72	5.77
CS06	1.43	5.73	0.77	6.28
Spiro-OMeTAD	1.34	6.62	0.75	6.70
PTAA	1.39	5.93	0.58	4.77

The mentioned S-shape of the J-V curve for **CS05** could justify the overestimated FF, indicating there might be a charge accumulation issue at the interface of the HTM and the perovskite.

More experiments are being carried out to further optimize the device structure and improve the efficiencies using this configuration.

6.4.3. Conclusions.

Four novel HTMs have been synthesized, three of them based on TPA group (**CS02**, **CS04** and **CS05**) and one (**CS06**) based on carbazole: all of them substituted with methoxyphenyl rings. The energy levels of **CS02**, **CS04** and **CS05** show a good alignment with those of the cesium mix perovskite. The HTM named **CS05** exhibited an outstanding PCE of 19.38 %, compared with spiro-OMeTAD (20.36 %). The only difference between them is the slightly smaller V_{oc} obtained for **CS05** (1.05 V). **CS04** and **CS05** show J_{sc} as high as the devices using the reference.

Chapter 6

CS06 was tested with two different perovskite compositions. Its HOMO level was too deep to allow the hole transfer to the triple-cation mixed perovskite, so the MAPBr₃ composition was used leading to a PCE of 6.28 %. The high voltage values and the excellent efficiencies obtained announced that CS06 can compete with the most widely used HTM (spiro-OMeTAD, 6.70 %) in this perovskite composition.

6.5. General conclusions.

Two new families of HTMs were synthesized to study the influence of the chemical structure in the performance of PSCs. It was concluded that when there is an electron acceptor group (like BT) in the molecule, it is desirable to have an extended π -conjugation system around it to compensate the electron accepting nature of BT, as **CS01** or **LCS01**. In addition, when alkyl chains are not linked, the molecule tends to be less soluble and forms aggregates in the surface of the perovskite layer. Even though, four HTMs exhibited excellent PCEs, as **CS01**, **LCS01**, **CS04** and **CS05** (17.84 %, 18.09 %, 18.05 % and 19.38 % respectively). The chemical group they have in common is TPA with *o,p*-methoxybenzene substituents. The synthesis consisted in two or three steps and is cheaper than that of spiro-OMeTAD, which make them good candidates to replace it as HTM in PSCs. Finally, in a particular case, **CS06** was needed to be tested with MAPBr₃ perovskite devices because of its deep HOMO level obtaining competitive results (6.28 %) when compared with the reference (6.70 %).

6.6. Annex.

In this section, there will be described in details the results obtained in this work.

6.6.1. J-V parameters for devices using the novel HTMs comparing their performance with and in absence of additives.

Table A6.1: PV parameters of the first tests of PSCs devices (best result) by using BT-based molecules as HTMs with and without additives.

HTM	Additives				No additives			
	V _{oc} (V)	J _{sc} (mA/cm ²)	FF	PCE (%)	V _{oc} (V)	J _{sc} (mA/cm ²)	FF	PCE (%)
CS01	0.91	21.47	0.51	9.91	0.58	6.24	0.19	0.70
CS03	0.75	13.96	0.74	7.72	0.69	13.87	0.17	1.66
EP02	0.93	13.60	0.61	7.69	0.89	17.60	0.37	5.85
LCS01	0.95	20.11	0.74	14.06	0.96	15.90	0.19	2.83

Chapter 6

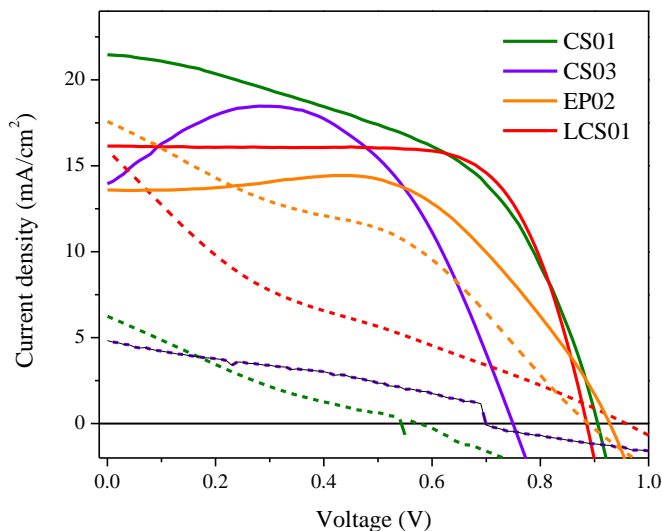


Figure A6.2: J-V curves of BT-based PSCs devices. Lines correspond to measurements at 1 Sun in the presence of additives and dashes in the absence of them.

Table A6.2: PV parameters of the champion PSCs devices (best result) by using TPA and carbazole-based molecules as HTMs with and without additives.

HTM	Additives				No additives			
	V _{oc} (V)	J _{sc} (mA/cm ²)	FF	PCE (%)	V _{oc} (V)	J _{sc} (mA/cm ²)	FF	PCE (%)
CS02	0.92	22.27	0.58	11.79	0.84	0.69	0.08	0.04
CS04	0.97	20.68	0.68	13.54	0.97	14.12	0.24	3.31
CS05	1.05	22.44	0.75	17.64	0.92	7.08	0.14	0.91
CS06	0.94	6.12	0.10	0.56	0.69	5.47	0.11	0.40

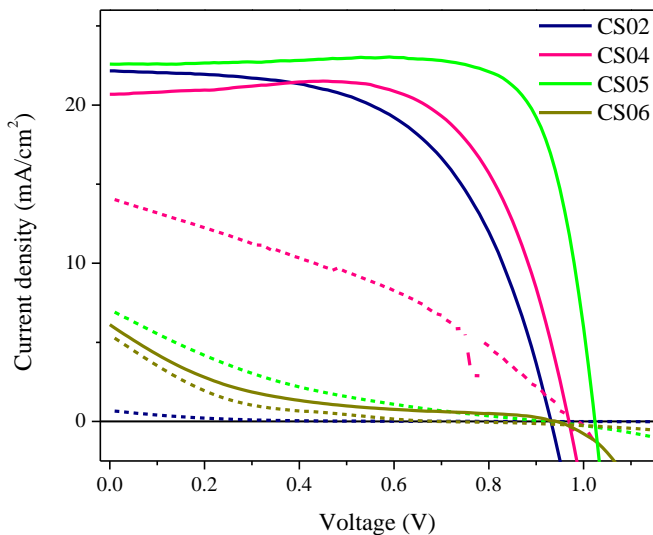


Figure A6.2: J-V curves of PSCs devices using **CS02**, **CS04**, **CS05** and **CS06** as HTMs with (lines) and without (dashes) dopants without further optimization.

6.6.2. J-V curves and PV parameters of the optimization of the HTM layers for PSCs.

Table A6.3: Description of the fabrication and PCE of devices using **CS01** as HTM in PSCs.

HTM	Concentration (mg·mL ⁻¹ / mM)	Spin coater conditions (rpm, rpm/s, s)	PCE (%)	Device
CS01	15 / 14.8	4000, 2000, 30	12.21	1
CS01	20 / 19.7	4000, 2000, 30	9.92	4
CS01	25 / 24.6	2000, 2000, 30	9.91	2
CS01	50 / 49.3	2000, 2000, 30	12.47	5
CS01	20 / 19.7	2000, 2000, 30	17.84	3

Chapter 6

Table A6.4: Description of the fabrication parameters and PCE of devices using **CS03** as HTM in PSCs.

HTM	Concentration (mg·mL ⁻¹ / mM)	Spin coater conditions (rpm, acc. rpm, s)	PCE (%)	Device
CS03	20 / 33.9	4000, 2000, 30	7.05	1
CS03	25 / 40.3	2000, 2000, 30	7.97	3
CS03	20 / 33.9	2000, 2000, 30	8.37	2

Table A6.5: Description of the fabrication parameters and PCE of devices using **EP02** as HTM in PSCs.

HTM	Concentration (mg·mL ⁻¹ / mM)	Spin coater conditions (rpm, acc. rpm, s)	PCE (%)	Device
EP02	25 / 40.2	2000, 2000, 30	1.73	6
EP02	20 / 32.1	2000, 2000, 30	2.02	2
EP02	20 / 32.1	4000, 2000, 30	7.69	1
EP02*	10 / 16.07	4000, 2000, 30	8.59	4
EP02	10 / 16.07	4000, 2000, 30	10.47	3
EP02	5 / 8.04	4000, 2000, 30	6.02	5

Table A6.6: Parameters optimized and PCE for **LCS01**-based devices.

HTM	Concentration ($\text{mg}\cdot\text{mL}^{-1}$ / mM)	Spin coater	PCE (%)	Device
		conditions (rpm, acc. rpm, s)		
LCS01	20 / 17.1	4000, 2000, 30	15.95	3
LCS01	25 / 21.4	2000, 2000, 30	10.23	1
LCS01	20 / 17.1	2000, 2000, 30	18.09	2

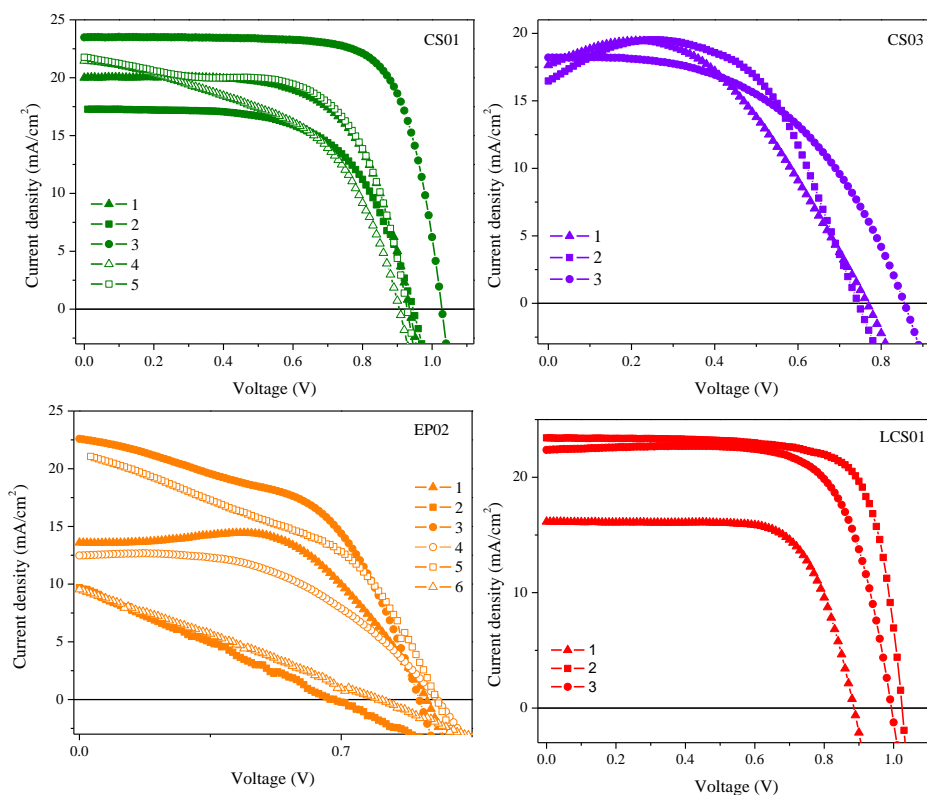


Figure A6.3: J-V curves of the optimization process of the HTM layers for the BT-based PSCs devices. Each line corresponds to a different deposition condition.

Chapter 6

Table A6.7: PV data of the optimization process of the HTM layers for the BT-based PSCs devices.

HTM	Device	V _{OC} (V)	J _{sc} (mA/cm ²)	FF (%)	PCE (%)
CS01	1	0.93	20.00	0.65	12.21
	2	0.91	21.47	0.51	9.91
	3	1.03	23.49	0.74	17.84
	4	0.94	17.28	0.61	9.92
	5	0.93	21.77	0.62	12.47
CS03	1	0.77	17.64	0.52	7.05
	2	0.74	16.47	0.68	8.37
	3	0.86	18.21	0.51	7.97
EP02	1	0.93	13.60	0.61	7.69
	2	0.80	9.54	0.26	2.02
	3	0.91	22.59	0.51	10.47
	4	0.93	21.06	0.44	8.59
	5	0.97	12.47	0.50	6.02
	6	0.68	9.69	0.26	1.73
LCS01	1	0.89	16.15	0.72	10.23
	2	1.02	23.41	0.76	18.09
	3	0.99	22.37	0.72	15.95

Table A6.8: Parameters optimized in the preparation of PSCs using **CS02** as HTM.

HTM	Concentration (mg·mL ⁻¹ / mM)	Additives ratio vs reference	PCE (%)	Device
CS02	20 / 12.3	2	8.09	3
CS02	25 / 15.4	2	9.08	1
CS02	50 / 30.8	2	12.86	4
CS02	50 / 30.8	1	10.61	2

Table A6.9: Optimized parameters for devices of PSCs using **CS04** as HTM.

HTM	Concentration (mg·mL ⁻¹ / mM)	Additives ratio vs reference	PCE (%)	Device
CS04	20 / 30.6	2	16.65	1
CS04	25 / 38.2	2	13.54	3
CS04	20 / 30.6	1	18.05	2

Table A6.10: Parameters changed to optimize PSCs devices using **CS05** as HTM.

HTM	Concentration (mg·mL ⁻¹ / mM)	Additives ratio vs reference	PCE (%)	Device
CS05	25 / 26.2	2	19.05	3
CS05	20 / 20.1	2	18.05	1
CS05	50 / 52.4	2	11.01	4
CS05	25 / 26.2	1	17.05	2

Chapter 6

Table A6.11: Parameters optimized in the fabrication of devices of PSCs using CS06 as HTM.

HTM	Concentration (mg·mL ⁻¹ / mM)	PCE (%)	Device
CS06	20 / 14.4	1.51	1
CS06	25 / 18.0	1.52	2

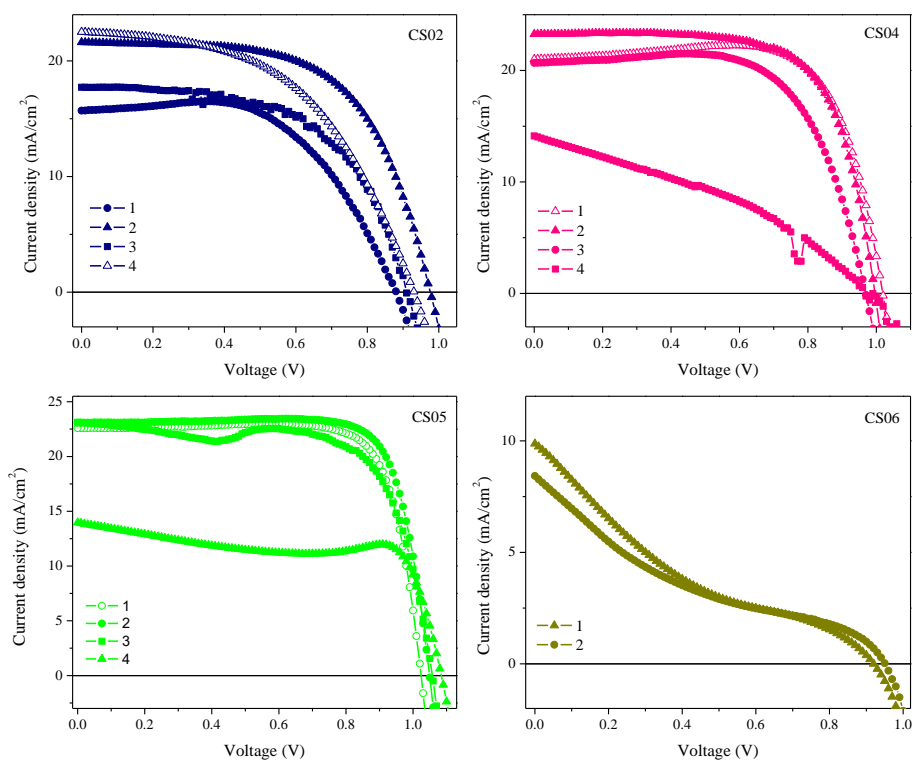


Figure A6.4: J-V curves of the optimization process of the HTM layers for the TPA and carbazole-based PSCs devices.

Table A6.12: PV data of the optimization process of the HTM layers for the TPA and carbazole-based PSCs devices.

HTM	Device	V _{oc} (V)	J _{sc} (mA/cm ²)	FF (%)	PCE (%)
CS02	1	0.91	17.73	0.56	9.08
	2	0.93	22.51	0.51	10.61
	3	0.88	15.71	0.59	8.09
	4	0.98	21.62	0.61	12.86
CS04	1	1.02	21.01	0.75	16.06
	2	1.00	23.26	0.69	16.06
	3	0.97	20.68	0.68	13.54
	4	0.97	14.12	0.24	3.31
CS05	1	1.02	22.59	0.78	18.05
	2	1.06	23.13	0.70	17.05
	3	1.05	23.08	0.79	19.05
	4	1.08	13.97	0.73	11.01
CS06	1	0.92	9.88	0.17	1.51
	2	0.95	8.43	0.19	1.52

Chapter 6

6.7.3. Statistic values of PV parameters when using the new HTMs in PSCs.

Table A6.13: PV parameters of the PSCs devices using BT-based HTMs. Values are the average obtained by at least 10 devices.

HTM	V _{oc} (V)	J _{sc} (mA/cm ²)	FF (%)	PCE (%)
CS01	1.02 ± 0.03	23.16 ± 0.37	0.71 ± 0.02	16.82 ± 0.83
CS03	0.83 ± 0.08	22.18 ± 1.24	0.56 ± 0.07	10.47 ± 2.31
EP02	0.84 ± 0.04	21.10 ± 1.76	0.51 ± 0.05	9.05 ± 1.54
LCS01	1.02 ± 0.02	23.38 ± 0.25	0.72 ± 0.02	17.16 ± 0.66
Spiro-OMeTAD	1.11 ± 0.03	23.62 ± 0.45	0.77 ± 0.01	20.28 ± 0.48

Table A6.14: PV parameters of the Cs-mix PSCs devices using **CS02**, **CS04**, **CS05** and **CS06**. Averaged values obtained by at least 10 devices.

HTM	V _{oc} (V)	J _{sc} (mA/cm ²)	FF (%)	PCE (%)
CS02	1.00 ± 0.03	18.15 ± 1.89	0.71 ± 0.08	12.80 ± 1.36
CS04	0.99 ± 0.04	21.32 ± 1.85	0.69 ± 0.04	14.60 ± 1.85
CS05	1.04 ± 0.00*	23.33 ± 0.51	0.77 ± 0.02	18.67 ± 0.45
CS06	0.91 ± 0.03	6.49 ± 3.36	0.15 ± 0.05	0.90 ± 0.65
Spiro-OMeTAD	1.11 ± 0.02	23.55 ± 0.31	0.77 ± 0.02	20.10 ± 0.39

* Real value: 0.00483.

6.7.4. J-V curves in forward and reverse for the HTMs using in this work.

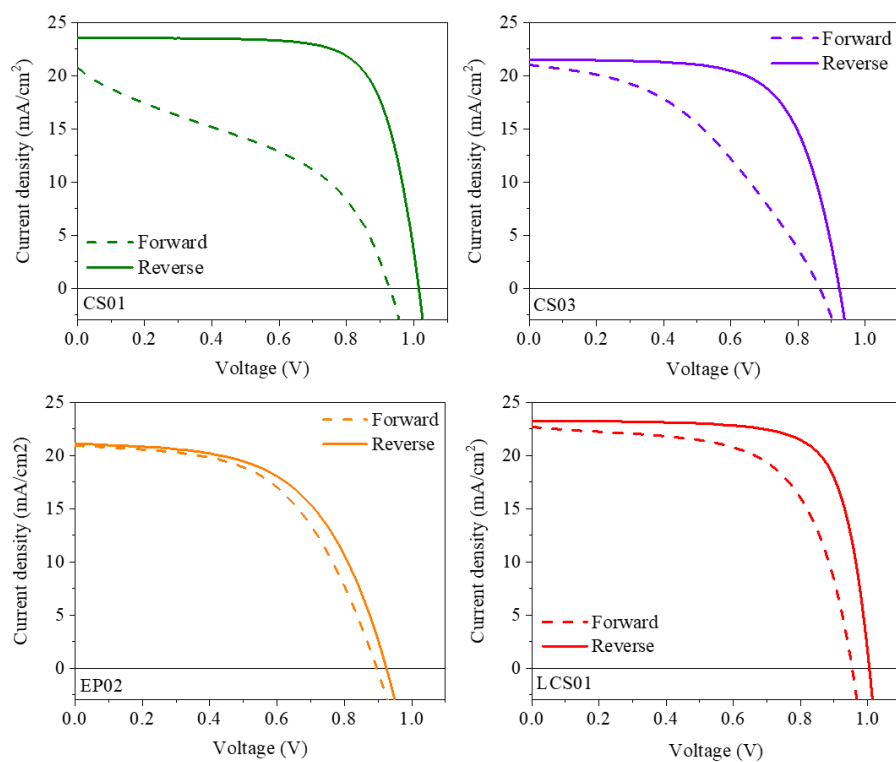


Figure A6.5: J-V curves in forward and reverse using BT-based HTM in PSCs.

Chapter 6

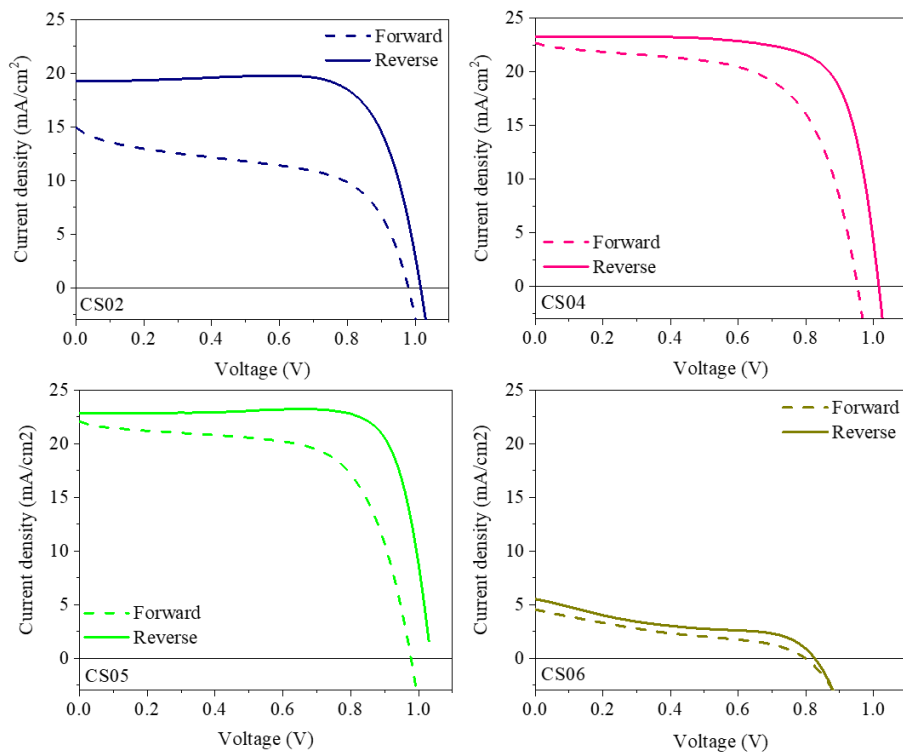


Figure A6.6: J-V curves in forward and reverse using TPA and carbazole-based HTM in PSCs.

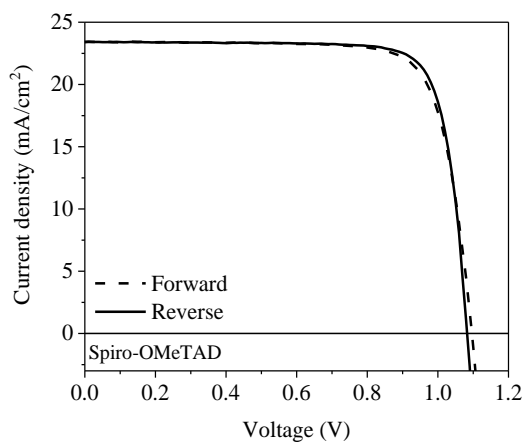


Figure A6.7: J-V curve in forward and reverse using **spiro-OMeTAD** as HTM in PSCs.

6.7. References.

1. <https://www.nrel.gov/pv/cell-efficiency.html>.
2. Kojima, A.; Teshima, K.; Shirai, Y.; Miyasaka, T., Organometal Halide Perovskites as Visible-Light Sensitizers for Photovoltaic Cells. *Journal of the American Chemical Society* **2009**, *131* (17), 6050-6051.
3. Yoon, S. J.; Stamplecoskie, K. G.; Kamat, P. V., How Lead Halide Complex Chemistry Dictates the Composition of Mixed Halide Perovskites. *The Journal of Physical Chemistry Letters* **2016**, *7* (7), 1368-1373.
4. Stoumpos, C. C.; Kanatzidis, M. G., Halide Perovskites: Poor Man's High-Performance Semiconductors. *Advanced Materials* **2016**, *28* (28), 5778-5793.
5. Swetha, T.; Singh, S. P., Perovskite solar cells based on small molecule hole transporting materials. *Journal of Materials Chemistry A* **2015**, *3* (36), 18329-18344.
6. Liu, D.; Yang, J.; Kelly, T. L., Compact Layer Free Perovskite Solar Cells with 13.5% Efficiency. *Journal of the American Chemical Society* **2014**, *136* (49), 17116-17122.
7. Jeon, N. J.; Noh, J. H.; Yang, W. S.; Kim, Y. C.; Ryu, S.; Seo, J.; Seok, S. I., Compositional engineering of perovskite materials for high-performance solar cells. *Nature* **2015**, *517*, 476.
8. Pellet, N.; Gao, P.; Gregori, G.; Yang, T.-Y.; Nazeeruddin, M. K.; Maier, J.; Grätzel, M., Mixed-Organic-Cation Perovskite Photovoltaics for Enhanced Solar-Light Harvesting. *Angewandte Chemie International Edition* **2014**, *53* (12), 3151-3157.
9. Saliba, M.; Matsui, T.; Seo, J.-Y.; Domanski, K.; Correa-Baena, J.-P.; Nazeeruddin, M. K.; Zakeeruddin, S. M.; Tress, W.; Abate, A.; Hagfeldt, A.; Grätzel, M., Cesium-containing triple cation perovskite solar cells: improved stability, reproducibility and high efficiency. *Energy & Environmental Science* **2016**, *9* (6), 1989-1997.

Chapter 6

10. Liu, T.; Chen, K.; Hu, Q.; Zhu, R.; Gong, Q., Inverted Perovskite Solar Cells: Progresses and Perspectives. *Advanced Energy Materials* **2016**, *6* (17), 1600457.
11. Lee, M. M.; Teuscher, J.; Miyasaka, T.; Murakami, T. N.; Snaith, H. J., Efficient Hybrid Solar Cells Based on Meso-Superstructured Organometal Halide Perovskites. *Science* **2012**, *338* (6107), 643.
12. Kim, H.-S.; Lee, C.-R.; Im, J.-H.; Lee, K.-B.; Moehl, T.; Marchioro, A.; Moon, S.-J.; Humphry-Baker, R.; Yum, J.-H.; Moser, J. E.; Grätzel, M.; Park, N.-G., Lead Iodide Perovskite Sensitized All-Solid-State Submicron Thin Film Mesoscopic Solar Cell with Efficiency Exceeding 9%. *Scientific Reports* **2012**, *2*, 591.
13. Krishna, A.; Grimsdale, A. C., Hole transporting materials for mesoscopic perovskite solar cells – towards a rational design? *Journal of Materials Chemistry A* **2017**, *5* (32), 16446-16466.
14. Juarez-Perez, E. J.; Leyden, M. R.; Wang, S.; Ono, L. K.; Hawash, Z.; Qi, Y., Role of the Dopants on the Morphological and Transport Properties of Spiro-MeOTAD Hole Transport Layer. *Chemistry of Materials* **2016**, *28* (16), 5702-5709.
15. Wang, S.; Sina, M.; Parikh, P.; Uekert, T.; Shahbazian, B.; Devaraj, A.; Meng, Y. S., Role of 4-tert-Butylpyridine as a Hole Transport Layer Morphological Controller in Perovskite Solar Cells. *Nano Letters* **2016**, *16* (9), 5594-5600.
16. Leijtens, T.; Giovenzana, T.; Habisreutinger, S. N.; Tinkham, J. S.; Noel, N. K.; Kamino, B. A.; Sadoughi, G.; Sellinger, A.; Snaith, H. J., Hydrophobic Organic Hole Transporters for Improved Moisture Resistance in Metal Halide Perovskite Solar Cells. *ACS Applied Materials & Interfaces* **2016**, *8* (9), 5981-5989.
17. Niu, G.; Guo, X.; Wang, L., Review of recent progress in chemical stability of perovskite solar cells. *Journal of Materials Chemistry A* **2015**, *3* (17), 8970-8980.

18. Franckevičius, M.; Mishra, A.; Kreuzer, F.; Luo, J.; Zakeeruddin, S. M.; Grätzel, M., A dopant-free spirobi[cyclopenta[2,1-b:3,4-b']dithiophene] based hole-transport material for efficient perovskite solar cells. *Materials Horizons* **2015**, *2* (6), 613-618.
19. Zhang, F.; Zhao, X.; Yi, C.; Bi, D.; Bi, X.; Wei, P.; Liu, X.; Wang, S.; Li, X.; Zakeeruddin, S. M.; Grätzel, M., Dopant-free star-shaped hole-transport materials for efficient and stable perovskite solar cells. *Dyes and Pigments* **2017**, *136*, 273-277.
20. Zhao, X.; Zhang, F.; Yi, C.; Bi, D.; Bi, X.; Wei, P.; Luo, J.; Liu, X.; Wang, S.; Li, X.; Zakeeruddin, S. M.; Grätzel, M., A novel one-step synthesized and dopant-free hole transport material for efficient and stable perovskite solar cells. *Journal of Materials Chemistry A* **2016**, *4* (42), 16330-16334.
21. Rakstys, K.; Paek, S.; Grancini, G.; Gao, P.; Jankauskas, V.; Asiri, A. M.; Nazeeruddin, M. K., Low-Cost Perovskite Solar Cells Employing Dimethoxydiphenylamine-Substituted Bistricyclic Aromatic Enes as Hole Transport Materials. *ChemSusChem* **2017**, *10* (19), 3825-3832.
22. Zuo, L.; Yao, J.; Li, H.; Chen, H., Assessing the origin of the S-shaped I-V curve in organic solar cells: An improved equivalent circuit model. *Solar Energy Materials and Solar Cells* **2014**, *122*, 88-93.
23. Snaith, H. J.; Grätzel, M., Enhanced charge mobility in a molecular hole transporter via addition of redox inactive ionic dopant: Implication to dye-sensitized solar cells. *Applied Physics Letters* **2006**, *89* (26), 262114.
24. Wang, S.; Jiang, Y.; Juarez-Perez, Emilio J.; Ono, Luis K.; Qi, Y., Accelerated degradation of methylammonium lead iodide perovskites induced by exposure to iodine vapour. *Nature Energy* **2016**, *2*, 16195.
25. Kim, G.-W.; Shinde, D. V.; Park, T., Thickness of the hole transport layer in perovskite solar cells: performance versus reproducibility. *RSC Advances* **2015**, *5* (120), 99356-99360.

Chapter 6

26. Choi, H.; Ko, H. M.; Ko, J., Stable and efficient star-shaped hole transporting materials with EDOT moiety as side arm for perovskite solar cells. *Dyes and Pigments* **2016**, *126*, 179-185.
27. Wu, F.; Ji, Y.; Wang, R.; Shan, Y.; Zhu, L., Molecular engineering to enhance perovskite solar cell performance: Incorporation of benzothiadiazole as core unit for low cost hole transport materials. *Dyes and Pigments* **2017**, *143*, 356-360.
28. Wu, F.; Ji, Y.; Zhong, C.; Liu, Y.; Tan, L.; Zhu, L., Fluorine-substituted benzothiadiazole-based hole transport materials for highly efficient planar perovskite solar cells with a FF exceeding 80%. *Chemical Communications* **2017**, *53* (62), 8719-8722.
29. Tress, W.; Marinova, N.; Moehl, T.; Zakeeruddin, S. M.; Nazeeruddin, M. K.; Grätzel, M., Understanding the rate-dependent J–V hysteresis, slow time component, and aging in CH₃NH₃PbI₃ perovskite solar cells: the role of a compensated electric field. *Energy & Environmental Science* **2015**, *8* (3), 995-1004.
30. Cabau, L.; Pellejà, L.; Clifford, J. N.; Kumar, C. V.; Palomares, E., Light soaking effects on charge recombination and device performance in dye sensitized solar cells based on indoline–cyclopentadithiophene chromophores. *Journal of Materials Chemistry A* **2013**, *1* (31), 8994-9000.
31. Jiménez-López, J.; Cambarau, W.; Cabau, L.; Palomares, E., Charge Injection, Carriers Recombination and HOMO Energy Level Relationship in Perovskite Solar Cells. *Scientific Reports* **2017**, *7* (1), 6101.
32. Ravishankar, S.; Gharibzadeh, S.; Carmona, C.; Grancini, G.; Lee, Y.; Ralaiarisoa, M.; Asiri, A. M.; Koch, N.; Bisquert, J.; Nazeeruddin, M., *Influence of Charge Transport Layers on Open-Circuit Voltage and Hysteresis in Perovskite Solar Cells*. 2018; Vol. 2.
33. Prochowicz, D.; Tavakoli, M. M.; Solanki, A.; Goh, T. W.; Sum, T. C.; Yadav, P., Correlation of recombination and open circuit voltage in planar heterojunction perovskite solar cells. *Journal of Materials Chemistry C* **2019**, *7* (5), 1273-1279.

34. Stolterfoht, M.; Caprioglio, P.; Wolff, C.; Marquez-Prieto, J.; Nordmann, J.; Zhang, S.; Rothhardt, D.; Hörmann, U.; Redinger, A.; Kegelmann, L.; Albrecht, S.; Kirchartz, T.; Saliba, M.; Unold, T.; Neher, D., *The perovskite/transport layer interfaces dominate non-radiative recombination in efficient perovskite solar cells*. 2018.
35. Wu, N.; Wu, Y.; Walter, D.; Shen, H.; Duong, T.; Grant, D.; Barugkin, C.; Fu, X.; Peng, J.; White, T.; Catchpole, K.; Weber, K., Identifying the Cause of Voltage and Fill Factor Losses in Perovskite Solar Cells by Using Luminescence Measurements. *Energy Technology* **2017**, *5* (10), 1827-1835.
36. Kiermasch, D.; Gil-Escrig, L.; Bolink, H. J.; Tvingstedt, K., Effects of Masking on Open-Circuit Voltage and Fill Factor in Solar Cells. *Joule* **2019**, *3* (1), 16-26.
37. Hu, Z.; Fu, W.; Yan, L.; Miao, J.; Yu, H.; He, Y.; Goto, O.; Meng, H.; Chen, H.; Huang, W., Effects of heteroatom substitution in spiro-bifluorene hole transport materials. *Chemical Science* **2016**, *7* (8), 5007-5012.
38. Jeon, N. J.; Lee, H. G.; Kim, Y. C.; Seo, J.; Noh, J. H.; Lee, J.; Seok, S. I., o-Methoxy Substituents in Spiro-OMeTAD for Efficient Inorganic–Organic Hybrid Perovskite Solar Cells. *Journal of the American Chemical Society* **2014**, *136* (22), 7837-7840.
39. Chen, Q.; De Marco, N.; Yang, Y.; Song, T.-B.; Chen, C.-C.; Zhao, H.; Hong, Z.; Zhou, H.; Yang, Y., Under the spotlight: The organic–inorganic hybrid halide perovskite for optoelectronic applications. *Nano Today* **2015**, *10* (3), 355-396.
40. Noh, J. H.; Im, S. H.; Heo, J. H.; Mandal, T. N.; Seok, S. I., Chemical Management for Colorful, Efficient, and Stable Inorganic–Organic Hybrid Nanostructured Solar Cells. *Nano Letters* **2013**, *13* (4), 1764-1769.
41. Prathapani, S.; Bhargava, P.; Mallick, S., Electronic band structure and carrier concentration of formamidinium–cesium mixed cation lead mixed halide hybrid perovskites. *Applied Physics Letters* **2018**, *112* (9), 092104.
42. Zhang, X.; Liu, J.; Song, Z.; Zuo, W.; Fan, Z.; He, X.; Luo, K.; Ye, Q.; Liao, C., Tuning Bandgap of Mixed-Halide Perovskite for Improved

Chapter 6

Photovoltaic Performance Under Monochromatic-Light Illumination. *physica status solidi (a)* **2019**, *216* (4), 1800727.

43. Eperon, G. E.; Stranks, S. D.; Menelaou, C.; Johnston, M. B.; Herz, L. M.; Snaith, H. J., Formamidinium lead trihalide: a broadly tunable perovskite for efficient planar heterojunction solar cells. *Energy & Environmental Science* **2014**, *7* (3), 982-988.

44. Das, J.; Bhaskar Kanth Siram, R.; Cahen, D.; Rybtchinski, B.; Hodes, G., Thiophene-modified perylenediimide as hole transporting material in hybrid lead bromide perovskite solar cells. *Journal of Materials Chemistry A* **2015**, *3* (40), 20305-20312.

7. CONCLUDING REMARKS AND PERSPECTIVE

Chapter 7

7.1. Concluding remarks.

The synthesis and characterization of novel electron donor and low-molecular weight hole transporting materials (HTMs) have been described as well as their application in OSCs and PSCs. The general aim was to investigate the relationship between the molecular structure and its influence on the device performance. The understanding of this relationship will lead to a more rational design in future synthesis of new organic p-type semiconductors. To that aim, small modifications in the molecular structure of the two families of small molecules were carried out.

In Chapter 4, the synthetic pathways and the characterization of the two novel families of organic HTMs (for PSCs) and absorbers (for OSCs) were described. Based on absorption and emission spectroscopy and CV measurements, it has been demonstrated that the BT family of molecules obtained had suitable energy levels to be used in both kind of devices (OSCs and PSCs) and TPA- and carbazole-based as HTMs for PSCs.

In Chapter 5, the device performance of binary and ternary BHJ OSCs by using the new BT family of donor was investigated. Binary active layers consisted in a blend of a BT donor with the fullerene **PC₇₁BM** or with two different non-fullerene electron acceptors (**DPP8** and **MPU3**). Efficiencies up to 6.35 % and 5.59 % were achieved for **LCS01/EP02:PC₇₁BM** active layer respectively. When the active layer contained the BT molecules blended with one of the non-fullerene electron acceptors (**DPP8** or **MPU3**), PCEs arrived to 7.81 % and 8.91 %, for **CS01/EP02:MPU3**, respectively; and to 7.40 % for **CS03:DPP8**. An increase in the voltage was observed for all of them when compared with **PC₇₁BM**-based devices due to the higher LUMO level of **MPU3** and **DPP8**. When ternary BJH OSCs were fabricated by using one donor and two acceptors, the current density was enhance leading to higher PCEs

Chapter 7

(9.94 % **CS01:PC₇₁BM:MPU3**, 9.62 % for **EP02:PC₇₁BM:MPU3** and 8.94 % for **CS03:PC₇₁BM:DPP8**-based devices). This can be attributed to the addition of a third component into the active layer that has a complementary absorption in the visible range of the solar spectrum contributing to the photogenerated electrons. Solvent vapour annealing was applied to control the morphology of the active layer in all the configurations.

In Chapter 6, the device optimization and performance of PSCs using the eight HTMs synthesized during this thesis have been described. The optimization process indicated that the thickness of the hole transport layer plays an important role in PSCs, even with relative high hole mobilities. **CS01** and **LCS01** showed the best efficiencies (18.09 % and 17.84 %, respectively) when compared with the other molecules of the BT family. It can be justified because of their more extended π -conjugated system and the introduction of methoxy substituents in *ortho* and *para* positions. **CS05** is the champion molecule with a PCE of 19.38 %, which includes in its structure TPA and carbazole moieties. The introduction of the carbazole group, in this case, was an excellent approach. Likewise, **CS02** and **CS04** efficiencies were 15.40 % and 18.05 %, respectively, showing that the introduction of the substituted TPA has a positive effect due to its electron donor properties. **CS06** showed no hole injection when tested with the triple-cation mixed perovskite ((CsPbI₃)_{0.05}(FAPbI₃)_{0.85}(MAPbBr₃)_{0.15}). Nevertheless, MAPbBr₃ perovskite-based devices employing the mentioned molecule achieved an exceptional PCE of 6.28 % (6.70 % and 4.77 % for the reference cell using spiro-OMeTAD and PTAA respectively).

7.2. Perspective.

As it was explain above, the introduction of the TPA and carbazole groups in the synthesis of new HTMs reports in high efficiencies. In our group, new HTMs based on these structures will be synthesized trying to reduce the preparation cost and by using new cores.

To overcome the solubility and aggregation issues of **EP02**-based PSCs when the HTL was deposited by solution process, more test will be done depositing the layer by thermal evaporation. The thickness of the HTM layer will be optimized to achieve an optimal coverage of the perovskite surface and avoid short-circuits.

Due to the promising results obtained with **CS06**-based devices using MAPbBr_3 , more tests will be carried out optimizing the hole transport layer. Three new asymmetric molecules using the same core are being synthesized in order to compare the effect in the HOMO level and thus, in the hole injection and efficiency that those changes in the molecular structure may have.

Chapter 7



EPFL



UNIVERSITAT
ROVIRA i VIRGILI